Model-based analyses of spatiotemporal brain activity during resting-state and low-level states of consciousness

Ane López-González

TESI DOCTORAL UPF / any 2021

DIRECTORS DE LA TESI

Dr. Adrián Ponce Alvarez and Prof. Dr. Gustavo Deco

DEPARTMENT

Department of Experimental and Health Sciences

Gizonen lana jakintza dugu: ezagutuz aldatzea,
Naturarekin bat izan eta harremanetan sartzea.
Eta indarrak ongi errotuz gure sustraiak lurrari
lotuz, bertatikan irautea: ezaren gudaz baietza
sortuz, ukazioa legetzat hartuz beti aurrera joatea.

Xabier Lete,
Bigarren poema liburua (1974)

Agradecimientos

El trabajo que presento aquí es el resultado de un largo camino que no habría sido posible sin el apoyo y la ayuda de muchas personas. En primer lugar quiero agradecer a mis supervisores, Adrián y Gustavo, por las oportunidades que me habéis ofrecido, especialmente por abrirme la puerta a la investigación, por los consejos oportunos y la confianza que habéis depositado en mi. También por vuestra cercanía y mejores deseos. También quiero agradecer a Gorka y Matthieu por el tiempo que me habéis dedicado y por compartir vuestro conocimiento conmigo.

This thesis would not be possible without the support and resources of the Sinergia group. I would like to thank the Sinergia group to give me this opportunity, specially, to Patric Hagmann for his generosity and values. I want to also thank our collaborators in Liège, especially Raja and Jitka. I feel very lucky to have the opportunity to work with such amazing data that has allowed me to research what motivated me to start the PhD and work with you, support each other and exchange our knowledge.

Sin duda alguna quiero agradecer particularmente a los que han hecho que la rutina de ir al CBC fuese un momento para recibir cariño y compartir risas; gracias Gonzalo por tu amabilidad y presencia tan agradable y gracias Marc por las entrañables conversaciones. A Manel, muchas gracias por compartir tantas experiencias conmigo, algunas muy agradables, viajes, comidas y conversaciones infinitas, y otras que sin tu apoyo y presencia hubiesen sido muchísimo más difíciles; el hecho de que no se necesitan palabras para entenderse creo que es un claro reflejo de esta amistad. Y Konstantina, mi gran amiga y compañera, que ha estado acompañándome durante todo este proceso, siempre ayudándome, protegiéndome y cuidándome con tu mejor intención, pasase lo que pasase. Muchas gracias a todos.

Y junto con el despacho, es imposible no recordar los momentos de tomar café y las comidas con todas las personas que han tenido un aporte en este doctorado; Jessica, Andrea, Vicente, Anira, Silvana, Laura, Katerina, Xenia, David e Irene Vigue. También Iñigo Romero-Arandia por iluminarme el camino con su experiencia y amistad, y a Leire Zamora y Leire Kaiero por estar presentes y haber compartido este proceso conmigo. También me

siento muy agradecida por las clases de Jon Baltza, el profesor de filosofía (de vida) en el instituto, que despertaron mi inquietud y anhelo por el conocimiento que me llevaron a hacer este trabajo. Eskerrik asko!

Por último, agradecer de corazón a mi familia, a mis padres, Iñigo y Julia, a mis hermanos Xabi y Pablo, por estar en todo momento apoyándome y por todo vuestro amor incondicional. Y a Sam, por estar presente en cada momento de esta etapa a mi lado. Me siento muy, muy afortunada. Muchas gracias.

Ane López

Abstract

The brain's resting-state activity displays complex spatiotemporal patterns of activity that are constantly formed and dissolved. The study of these dynamic collective patterns has increased our understanding of the brain's organization principles during function and dysfunction. However, the underlying mechanisms remain unknown. Theoretical whole-brain models explore this question by combining neural networks and brain activity/connectivity data. In the present thesis, I studied whole-brain models of resting-state activity during conscious wakefulness and low-level states of consciousness. I analyzed neuroimaging data (fMRI and EEG) from subjects during wakefulness and anesthesia, and from patients with disorders of consciousness due to brain lesions. I interpreted the results using diverse models to disentangle the contribution of brain dynamics, network connectivity, and temporal scales. The results suggest that loss of consciousness is driven by altered network interactions, more homogeneous and structurally constrained local dynamics, and less stability of the network's topological core compared to conscious states.

Keywords— Whole-brain spatiotemporal activity; Consciousness; Disorders of Consciousness; Anesthesia; Whole-brain modelling

Resumen

La actividad cerebral en reposo muestra patrones espacio-temporales complejos que se forman y desvanecen constantemente. El estudio de estos patrones ha impulsado nuestro conocimiento sobre la organización del cerebro durante su función y disfunción. Sin embargo, los mecanismos subyacentes aún no han sido revelados. Los modelos teóricos cerebrales a gran escala exploran esta cuestión combinando redes neuronales y datos de actividad/conectividad. Aquí, examino modelos cerebrales de actividad en reposo durante estados de vigilia y baja conciencia. Específicamente, analizo datos de neuroimagen (fMRI y EEG) de sujetos durante estados conscientes y anestesiados, y pacientes con deórdenes de conciencia provocados por lesiones. Interpreto estos resultados usando diversos modelos que disocian contribuciones dinámicas, de conectividad y escala temporal. Los resultados sugieren que la pérdida de conciencia es debida a alteraciones en las interacciones de la red, a dinámicas locales más homogéneas y acotadas a la estructura, y a una menor estabilidad del núcleo topológico.

Palabras clave— Actividad cerebral espaciotemporal a gran escala; Conciencia; Desórdenes de conciencia; Anestesia; Modelos a gran escala

Preface

The brain and the nervous system are the central processing core of behaviour and cognition, which are implemented by the brain's neuronal mechanisms and reflected in its dynamics. Understanding the brain's complex features is a research direction that has been largely investigated for thousands of years, first with philosophy, then more quantitatively, and that led to the emergence of the discipline called neuroscience, as a specific research field.

Technological advancements have allowed the recording of brain activation from the microscopic level to the macroscopic whole-brain level, extending our knowledge of brain organization and function. The study of spontaneous brain activation has shed light on understanding collective features, which are not explained by the dynamics of specific elements but by the interplay (e.g. temporal correlation between the activation time courses) between neuronal populations across the whole brain. In particular, it has been shown that brain dynamics is described by patterns of activation characterized by specific spatial maps and temporal structure. These patterns constantly change in time and represent the 'repertoire of states' of the brain dynamics. The spatial organization of the collection of collective activity patterns has been largely studied, but the characterization of the temporal structure is still under research. Indeed, the temporal organization of the repertoire of patterns is altered in different behavioural conditions, such as under altered states of consciousness, which suggest that consciousness is not a localized property of the brain, but a collective emergent property.

Even if the study of the dynamical properties and spatiotemporal repertoire of brain activity has increased our understanding of alterations thereof, it remains unclear how the brain mechanisms can generate the diversity of experimentally observed patterns. In other words, the mere observation of coordination patterns does not explain the mechanism underlying these emergent phenomena. In theoretical neuroscience, the idea of a deeper understanding of brain dynamics using computational models has aroused, yielding a powerful tool for investigating the brain's collective activity patterns and modeling the dynamics of neuronal populations for distinct brain regions. In this thesis, I present three studies that apply whole-brain

models to uncover the brain mechanism that is involved in the emergence of collective activity patterns and modulation of consciousness. To do so, I use data from healthy participants which I also compare with patients that suffered from brain injuries that lead to disorders of consciousness and healthy participants that undergo propofol sedation.

In Chapter 1, the specific concepts for understanding the computational framework developed in the following chapters will be explained. In particular, I present evidence for the relevance of the brain dynamics during spontaneous activation, combined with the description of the brain dynamics in low-level states of consciousness and, finally, the use of computational models to explain the brain mechanism underlying the dynamics.

Chapter 2 and 3 share the purpose of describing how the brain subnetworks are altered in low-level states of consciousness, described by the hemodynamic response measured by functional magnetic resonance. In particular, Chapter 2 addresses the question of the dynamical and structural alterations at the global and local level that are reflected in the mechanism and network properties. The characterization of the local properties allow the investigation of the spatial distribution of the parameters across the brain. Chapter 3 focuses on investigating the modifications in the brain properties of specific connections that impair the propagation of information flow through the subnetwork. Chapter 4 aims to identify the relevant temporal scale for the emergence of spatiotemporal properties of the spontaneous activity of healthy participants. For this, we studied how the collective activity patterns recorded with electroencephalography changes at the whole-brain level across temporal scales.

Finally, Chapter 5 will put the previous chapters' results into a unifying global perspective. Additionally, I discuss the possible neurobiological mechanism and the limitations faced in the studies presented, to provide an outlook of my work in the field of cognitive neuroscience.

Outcomes of the thesis:

- Escrichs, A., Sanjuán, A., Atasoy, S., **López-González, A.**, Garrido, C.,Cḿara, E., Deco, G. (2019). *Characterizing the Dynamical Complexity underlying Meditation.* Frontiers in Systems Neuroscience,13, 27. 10.3389/fnsys.2019.00027
- Kobeleva, X., **López-González, A.**, Kringelbach, M., Deco, G. (2020). *Spatiotemporal scales of dynamical functional networks - using whole-brain modelling to identify the optimal resolution.* bioRxiv, 10.1101/2020.09.12.277699
- **López-González, A.***, Panda, R.*, Ponce-Alvarez, A., Zamora-López, G., Escrichs, A., Martial, C., Thibaut, A., Gosseries, O., Kringelbach, M.L., Annen, J., Laureys, S., Deco, G (2020). *Loss of consciousness reduces the stability of brain hubs and the heterogeneity of brain dynamics.* Accepted in *Nature Communications Biology.* (**Chapter 2**)
- Panda, R.*, **López-González, A.***, Zamora-López, G., Gilson, M., Gosseries, O. Frasso, G., Cecconi, B., Thibaut, A., Escrichs, A., Laureys, S., Deco, G., Annen, J. *Brain ignition and information flow characterize pathological state of consciousness: a computational modelling framework* (in preparation). (**Chapter 3**)
- **López-González, A.**, Seeber, M., Rubega, M., Carboni, M., Vulliemoz, S., Michel, C., Deco, G., Ponce-Alvarez, A. *Extracting the temporal scale of the brain dynamics from EEG recordings using dynamical repertoire and spin glass models* (in preparation). (**Chapter 4**)
- Panda, R., Thibaut, A., **López-González, A.**, Hillebrand, A., Stam, C.J., Escrichs, A., Deco, G., Laureys, S., Gosseries, O., Annen, J., Tewarie, P. *Brain structural-functional network dynamics characterize pathological loss of consciousness* (in preparation).

Contents

List of Figures

List of Tables

CHAPTER 1

Introduction

"I guess I've had only one question all my life. Why do emergent selves pop up all over the place creating worlds, whether at the mind/body level, the cellular level, or the transorganism level? This phenomenon is something so productive that it doesn't cease creating entirely new realms: life, mind, and societies. That, to me, is a key and eternal question."
Francisco Varela, 1996

The brain is a complex system composed of billions of neurons. Neurons create specific conglomerates that can show synchronous firing, i.e. correlated activity, during spontaneous activity or in response to a stimuli. This correlated activation is observed at various scales, from local microcircuits to cortical columns at the mesoscopic scale, and brain regions at the macroscopic level. Indeed, a large number of studies have shown that, at the whole-brain level, the activation of distributed brain regions displays different coordinated patterns (Biswal et al., 1995; Greicius et al., 2009; Damoiseaux et al., 2006). These collective patterns are formed, dissolved, and re-formed over time, and emerge from the interactions between brain regions (Ponce-Alvarez et al., 2015). It is assumed that the collective

spatiotemporal patterns are key to understand how the brain undergoes qualitatively different brain states characterized at the behavioural level by different cognition states and levels of consciousness (e.g. wakefulness, sleep, coma, anesthesia and psychedelic states) (Tagliazucchi et al., 2013; Carhart-Harris et al., 2014; Boveroux et al., 2010; Barttfeld et al., 2015; Demertzi et al., 2019). This assumption, supported by the increasing evidence, consolidated the idea that consciousness is not a localized property of the brain, but a collective emergent property.

However, the mere observation of the spatiotemporal patterns in the brain does not explain the mechanism underlying the emergence of these collective phenomena. By combining concepts of physics, information theory and neurophysiology, theoretical models are a powerful tool for investigating the mathematical principles of brain collective activity. One of the challenges these theoretical models face is understanding how structural, dynamic, local and network properties interplay in the brain, which allow going beyond the phenomenological study of statistical relationships between those ingredients.

This thesis aims to explore the mechanisms underlying brain dynamics of healthy subjects and how they change in different brain states involving levels of consciousness. In the following chapters, I will present a collection of studies that aim to investigate the mechanism of brain dynamics and its alteration in different context (i.e. brain states and temporal scales) using dynamical and statistical models. Before diving into these studies, I will contextualize the topics addressed in this dissertation within the current state-of-the-art. This introduction will first describe the framework of resting-state activity and neuroimaging methods, and review the most important concepts for understanding the collective features that characterize the whole-brain activity (e.g. describing the spatiotemporal patterns, their temporal structure, the organization of the brain networks, etc.). I will also describe the observed brain dynamics during brain states associated with a reduction or loss of consciousness at the behavioural level. In particular, in this thesis, such brain states have been defined for patients that suffered from brain injuries that lead to disorders of consciousness (DOC) and healthy patients that undergo transient states of anesthesia, which will be studied in Chapters 2 and 3. Finally, I will

present the need to use computational models to address our questions.

1.1. Resting-state and network neuroscience

1.1.1. Resting-state changes the paradigm

The focus of human neuroscience has evolved over the decades with the development of recording techniques. These techniques have allowed going from the study of behavioural aspects until the description of the coordinated brain activation patterns. For many years, brain dynamics were interpreted within a *localizationist* approach. In this view, brain dynamics can be understood by studying the functional properties of specific anatomical brain regions. To prove that hypothesis, the experiments followed an input-output scheme, where the focus was to determine the neural activation in specific brain regions when a given stimulus was presented or when the participants performed a given cognitive task (Friston et al., 1998; Cabeza and Nyberg, 2000). Pioneer studies based their protocols on the difference between task-induced activation and baseline activity (i.e., no task, with eyes open and fixed or closed) and identified regions with increased activity during the task (Cordes et al., 2000). These experiments were motivated by the development of neuroimaging methods that allowed for a very precise spatial localization of the activity in the cortex. This new approach of linking the regions that show higher activation in each task determined many of the studies in the following years (Friston et al., 1998; Lotze et al., 1999). Indeed, such studies allowed for the association of specific functions in particular brain regions over decades, see Review (Sutterer and Tranel, 2017).

Implicitly, these studies assumed that baseline brain activity represents noise without structure. This assumption started to fall in the 1990s when more generalized and systematic studies quantified the structure of the spontaneous ongoing activity, then coined as resting-state activity, i.e. when the participant is not engaged in any specific task (Biswal et al., 1995). Notably, resting-state activity accounts for about 20 % of the total oxygen consumption of a person at rest. The pioneer studies of resting-state brain activity pointed out that even with eyes closed, brain activity shows slow oscillations (Biswal et al., 1995; Fox and Raichle, 2007).

Furthermore, these studies indicated that the resting-state activity shows coordination patterns among brain regions distributed across the brain, i.e. spatial patterns of activation that emerged at the whole-brain level, see Figure 1.1 A.

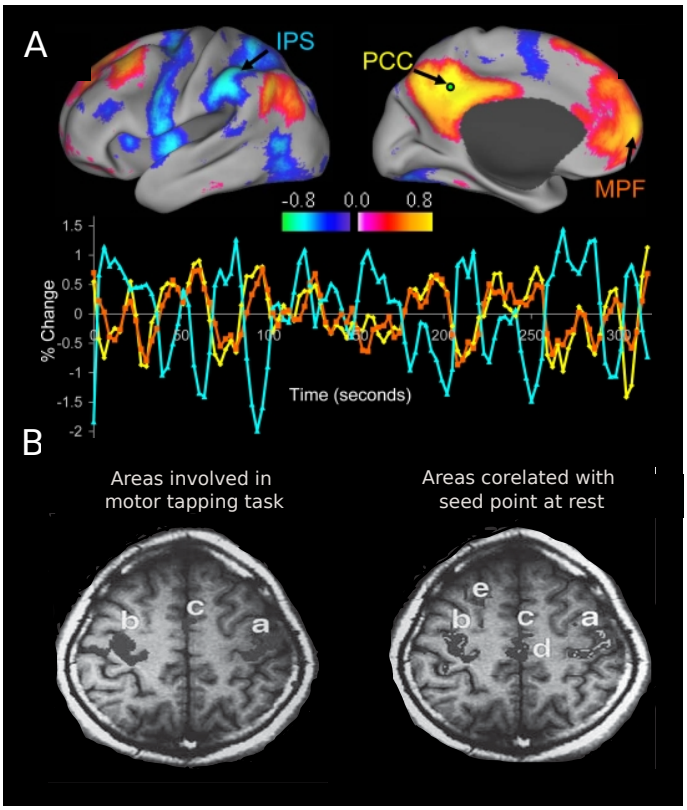

Figure 1.1: **Brain activation at rest shows slow oscillations and long-range coordination patterns. A)** Correlation in the BOLD fluctuations during resting-state activity between the posterior cingulate cortex (PCC) and the rest of the voxels show both positive and negative values spread across the cortex (upper panel). The BOLD fluctuations are similar for the PCC and medial pre-frontal cortex (MPF), suggesting correlated activity among them, and anticorrelated fluctuations between PCC and intraparietal sulcus (IPS) (lower panel). Figure edited from (Fox et al., 2005). **B)** Study of the activation of brain areas in response to a finger movement task (left) compared to the areas activated in rest (right). The areas a, b and c show statistically similarity between the task and resting condition, whereas d and e were present only during rest. Figure edited from (Biswal et al., 1995).

These patterns were obtained by measuring the correlation between neuroimaging signals from different brain regions (Greicius et al., 2009) or by studying the evolution of the extreme values of the fluctuating signals across time (Lehmann et al., 1987). Interestingly, the spatial patterns of correlations between distant cortical areas observed in resting-state activity were similar to the activation patterns observed in different cognitive tasks (Biswal et al., 1995; Raichle, 2009), suggesting that resting-state activity encloses by itself the principle of brain function, see Figure 1.1 B.

Currently, understanding the origin and function of resting-state activity is considered crucial to understand the constant computations of the brain (e.g. reorganizing its internal model of the world or having self-referential thoughts) (Deco et al., 2013a). Since its discovery, many studies have attempted to clarify the origin of these fluctuations (Biswal et al., 1997; Raichle, 2001; Greicius et al., 2003; Mantini et al., 2007; Greicius et al., 2009; Fox and Raichle, 2007; Honey et al., 2009). Moreover, the observed brain dynamics are not described purely by the anatomical links, but they result from an interplay between the brain dynamics and structure that remains largely unknown.

1.1.2. Whole-brain dynamics and structure

The discovery of resting-state activity and the spatiotemporal patterns led to a change in the paradigm of neuroscientific studies during the last decades (Raichle, 2009). As previously mentioned, this was due to the substantial development in neuroimaging methods applied to study the human brain. This development allowed for capturing a high-quality description of the macroscopic properties at the whole-brain level. Concerning brain activity, these advancements arise mainly in three non-invasive neuroimaging methods; electroencephalography, EEG, functional magnetic resonance imaging, fMRI, and magnetoencephalography, MEG (see Table 1.1 for a detailed description of the methods). These methods allowed the exploration and understanding of the properties of spontaneous brain activity. One can find a large number of studies describing the resting-state activity using fMRI (Raichle, 2001; Logothetis et al., 2001), EEG (Olejniczak, 2006; Lehmann et al., 1998; Mantini et al., 2007) and MEG (Brookes et al., 2011). Each neuroimaging technique has developed its

context and framework, but due to the difference in the measured physical variables and spatial and temporal resolutions, it is hard to merge the observations between techniques, see Table 1.1.

Neuroimaging technique	**Measured biological variable/mechanism**	**Spatial resolution**	**Temporal resolution**
Electroencephalography (EEG)	Records the dynamic synchronous polarization of spatially aligned neurons in extended gray matter networks	Source modelling is needed to localize the origins of the measured brain activity	Very high temporal resolution (milliseconds)
Functional Magnetic Resonance Imaging (fMRI)	Detects the changes in the blood oxygenation that partly follows from neuronal activity	Very high spatial resolution (millimeters)	Very low temporal resolution ($\sim$ seconds)
Magnetoencephalography (MEG)	Records the magnetic field produced by electrical currents occurring in the brain	Very high spatial resolution (millimeters)	Very high temporal resolution (milliseconds)
Diffusion Magnetic Resonance Imaging (diffusion MRI)	Detects the white matter pathways via the diffusion of water molecules in the axons	Very high spatial resolution (millimeters)	Static

Table 1.1: **Summary of the neurogimaging methods.** Information about the neuroimaging methods used for capturing information from human brains containing the measured variables and spatial and temporal resolutions.

Concerning the anatomical organization of the brain, the researchers developed techniques for obtaining data on the brain anatomy and its physical substrate. In humans, the development of diffusion MRI (dMRI) (Hagmann, 2005) allowed estimating the brain's anatomical connectivity at a the mesoscopic and macroscopic levels. Based on the data acquired by dMRI, Diffusion Tensor Imaging (DTI) estimates the main direction and strength of anisotropic diffusion in each voxel (Hagmann et al., 2008), see Table 1.1, which relate to the fibre tracts connecting different brain regions.

1.2. Understanding brain connectivity

All these neuroimaging methods provided a huge amount of data that quantify the brain activation fluctuations and its topological structure. The complexity of these data brought the need of developing new tools for studying the network effects and interactions, by applying *graph theory* and information-theoretical measures (Rubinov and Sporns, 2010; Sporns

et al., 2005; Zamora-López et al., 2011). Based on this framework, the brain can be described as a *network* composed of elements or *nodes*, such as the brain regions, that are interconnected by *links* or *edges*, that may refer to anatomical links, statistical dependencies or directed interactions, see Figure 1.2. As shown below, this framework demonstrates that the brain networks show complex structure with non-trivial topological features (van den Heuvel and Hulshoff Pol, 2010; Zamora-López et al., 2011; Sporns et al., 2005; Bullmore and Sporns, 2009).

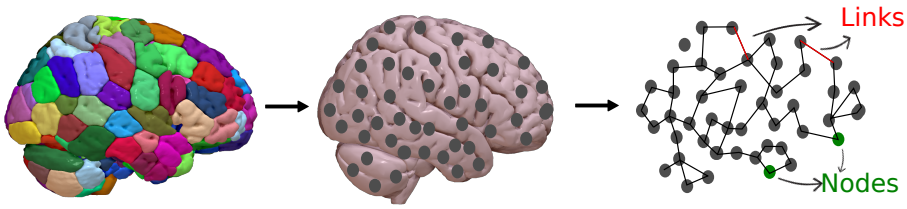

Figure 1.2: **Schematic representation of brain network reconstruction.** The data captured from the neuroimaging methods are described in the brain anatomy based on a parcellation, which describes the brain regions, spatial distribution and location. Each of the region-of-interest (ROI) described by the parcellation is considered a node in a network comprising the brain (or in some cases, the brain cortex). The links among nodes may refer to anatomical links, statistical dependencies or directed interactions.

The links between the nodes create the *connectivity* of the network, which usually is described by a matrix, $\mathbf{M}$, of size NxN, where N is the number of nodes. The element M_{ij} corresponds to the link between the nodes i and j. Depending on the types of interactions and the neuroimaging data used to define the networks, four families of connectivity measures have emerged:

- **Functional connectivity (FC):** Functional connectivity is obtained by extracting the structure of the correlation of activity time courses. Typically, FC measures the statistical dependencies of signals from predefined brain regions (Achard et al., 2006; van den Heuvel and Hulshoff Pol, 2010), calculated using the Pearson correlation (the most common one), Granger causality or mutual informa-

tion, see Figure 1.3 a. The resulting matrix is a static representation of the correlation structure of brain activity.

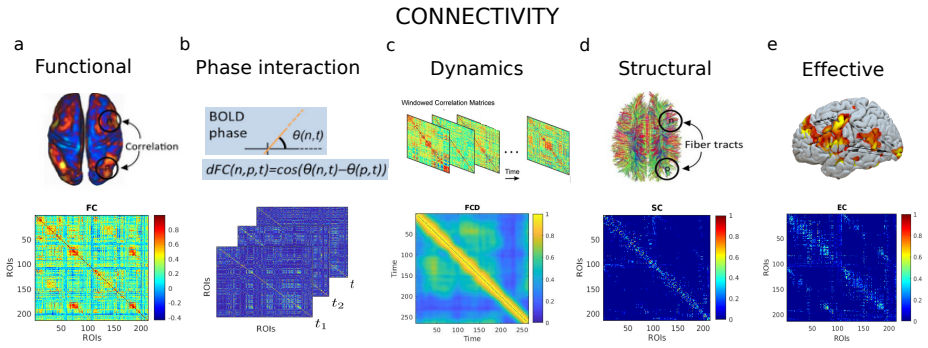

Figure 1.3: **Connectivity matrices and their description. a)** Functional Connectivity (FC) matrix characterizes the functional networks of the brain. In this panel case, the FC reflects the Pearson correlation between the whole BOLD signals of the brain regions. **b)** Phase-interaction matrices computed using the phase differences extracted from BOLD signals. **c)**The functional Connectivity Dynamics (FCD) describes the similarity between the FC matrices computed in sliding windows extracted from the BOLD timeseries. **d)** Structural Connectivity (SC) matrix captured from the DTI describes the connections of the brain anatomy. In this panel, the SC reflects the links density among brain regions . **e)** Effective Connectivity (EC) captures the influence one neural system exerts over another. Figure adapted from (Cabral et al., 2011; Kafashan et al., 2016).

- **Phase-interaction matrices:** Phase-interaction matrices can be seen as a subtype of FC for oscillatory signals. The phase-interaction matrices evaluate the level of synchrony by studying the phase relationship between signals typically filtered within a narrow frequency band, Figure 1.3 b. Typically, phases are calculated using the Hilbert transform of narrow-band filtered data or using wavelets. The benefit of using the phase-interaction matrices is that they allow describing the time series' spatiotemporal properties with a high temporal resolution (Ponce-Alvarez et al., 2015).

- **Dynamical functional connectivity (dFC):** The primary motivation for using this connectivity is to evaluate the presence of repeating patterns and to consider the time dimension by tracking correlations that could change over time. The dynamical functional connectivity (dFC) is obtained by calculating the correlation across time of the FC matrices computed in short time windows (Hansen et al., 2015), Figure 1.3 c.

- **Structural connectivity (SC):** The connections or fibres between different brain regions are thought to determine the anatomical structure, or connectome, of the brain (Sporns, 2011), Figure 1.3 d. The study of network structural connectivity (SC) matrices allows determining the organization of the brain's network topology (Sporns, 2018; van den Heuvel and Sporns, 2019; Zamora-López et al., 2009).

- **Effective connectivity (EC):** In a given neural network, Effective Connectivity (EC) captures the influence one neural system exerts over another (Friston et al., 2003), which explains how the activity patterns are generated, Figure 1.3 e. The original concept comes from electrophysiology (Aertsen et al., 1989) where the EC was introduced to quantify how the stimulation of a neuron affects a target neuron, independently of the anatomical links. At the whole-brain level, the EC usually describes statistical relationships among brain regions that determine the observed activity (e.g. in BOLD or EEG signals). The EC shows alterations when changing the local (e.g. excitability) and network (e.g. synaptic efficacy) properties of the neurons or neural populations.

All these connectivity matrices described the collective activity in brain networks, each considering different statistical properties of the functional time series or the physical substrate. These matrices contain the essential information for describing the brain's spatiotemporal dynamics at the whole-brain level. The following section will present the basic features captured from these brain network descriptions of resting-state activity.

1.3. Organization principles of brain activity and structure

The representation of the brain networks in the connectivity families enables the description of collective features of the resting-state activity at whole-brain level. As explained in the previous section, it is hypothesized that resting-state activation encloses the basic mathematical principles of brain activity. Moreover, the similarity between resting-state patterns and functional/structural networks indicates that spontaneous activity is key to understanding the brain's structure-function relationship. On the other hand, studies of brain networks' anatomical organization have shed light on the graphs' properties that ensure robustness and efficiency. Finally, these networks can also represent the synchronization between brain regions and their effective connectivities, which is considered crucial for explaining the brain mechanism for propagating neural signals and for communication throughout the network. This section will review what is already known about resting-state and will serve as the basis for our studies in chapter 2, 3 and 4.

1.3.1. Spatiotemporal patterns in whole-brain activity

Large-scale functional brain networks have been captured using different neuroimaging methods such as fMRI (Fox et al., 2005; Damoiseaux et al., 2006; De Luca et al., 2006; van den Heuvel et al., 2009), EEG (Lehmann et al., 1987; Laufs et al., 2003; Michel and Koenig, 2018) and MEG (Mantini et al., 2007; de Pasquale et al., 2010; Brookes et al., 2011). The fMRI patterns are captured by applying dimensionality reduction techniques in the whole-brain time series of resting-state activity (Fox et al., 2005; Damoiseaux et al., 2006; De Luca et al., 2006). The extracted (e.g. principal or independent) components are usually mapped to the cortical surface, and are referred to as the resting-state networks (RSNs). Several studies have investigated the functionally relevant RSNs in fMRI recordings (Fox et al., 2005; Damoiseaux et al., 2006; De Luca et al., 2006; Greicius et al., 2009). Interestingly, the RSNs have specific spatial distributions across the brain cortex and are constantly reshaped over time (Wackermann et al., 1993; Greicius, 2008). The ensemble of patterns that the system visits is called the 'dynamical repertoire' of the

brain (Tononi, 2004; Ghosh et al., 2008). These networks are similar to the spatial activation patterns observed during cognitive tasks requiring visual, sensorimotor, salience, attention and executive control processing (Greicius et al., 2003; Damoiseaux et al., 2006), see Figure 1.4 A. In addition to these networks, the default mode network (DMN), or task-negative network, has been widely studied due to its activation in self-referential operations(Fransson, 2005; Mason et al., 2007), and during consciousness of the environment (Fernández-Espejo et al., 2012) and of the self (Spreng and Grady, 2010; Qin and Northoff, 2011).

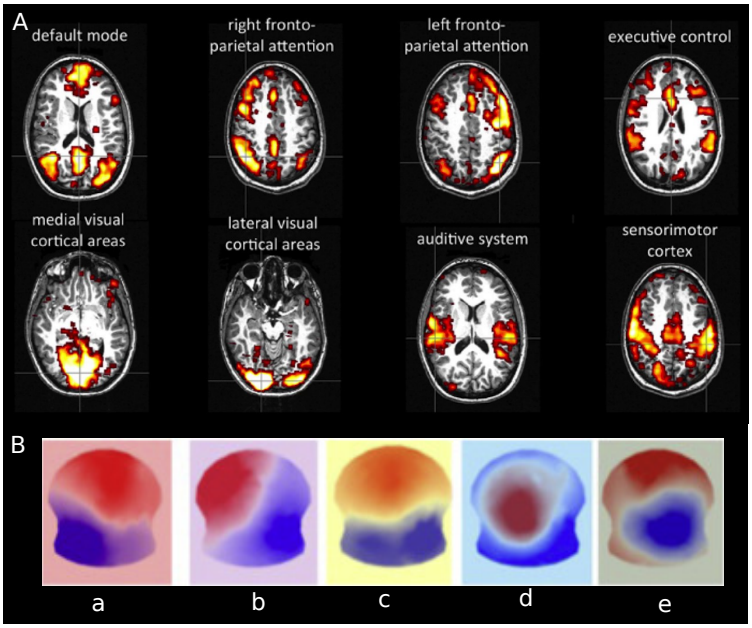

Figure 1.4: **Functional networks described from the activation of whole-brain timeseries using fMRI and EEG. A)** Major functional networks extracted through seed-based spatial coherence from fMRI BOLD signals recorded during rest. Those functional networks are usually referred as resting-state Networks (RSNs). Figure edited from (Storti et al., 2013). **B)** The scalp topographies termed as 'microstates' obtained from the EEG signals. Figure edited from (Britz et al., 2010).

EEG studies evaluating the correlations among amplitude fluctuations showed that a limited number of scalp potential topographies describe the

brain dynamics (Lehmann et al., 1987, 2005; Michel and Koenig, 2018). These topographies remain stable for a short period ($\sim$ 60 - 120 ms) before rapidly changing to another topography (Michel and Koenig, 2018). These discrete, limited, and distinguishable stable scalp potential maps have been defined as 'microstates' (Lehmann et al., 1987), see Figure 1.4 B. Some studies focused on the microstates' spatial distribution have shown that EEG microstate closely relate to RSNs captured in the BOLD-fMRI signals (Musso et al., 2010; Britz et al., 2010; Yuan et al., 2012).

In the last decade, there has been a growing interest in the temporal courses of activity patterns and the transitions among them (Chang and Glover, 2010; Kiviniemi et al., 2011; Allen et al., 2014; Ponce-Alvarez et al., 2015). The temporal transitions between patterns have also been captured in brain states for which the level of consciousness is reduced, e.g. in patients with disorders of consciousness or under anesthesia (Hudetz, 2012; Ghosh et al., 2008; Demertzi et al., 2015). This suggests that the transitions are not likely to be produced by a transition between different mental states. Thus, these transitions might be an emergent property of the complex brain network. Indeed, the functional networks and the transitions among them may be a consequence of *metastability* in the brain (Ponce-Alvarez et al., 2015; Deco et al., 2017a).

Metastability is the property of dynamic systems that display a set of states that can persist for some time before switching to another state. A system showing metastable patterns is a favourable functional scenario since it permits the flexible exploration of the dynamic repertoire as a response to incoming stimuli, while also ensuring the presence of a given pattern for some time. Indeed, the diversity of the accessible patterns and the transitions among them are thought to be essential for optimal conscious information processing (Tononi and Koch, 2008; Deco and Kringelbach, 2014). These properties have been proved to be fundamental for the adaptation to cognitive demands during tasks (Garrett et al., 2013; He, 2013).

Metastable patterns typically arise in systems that operate in a regime between phases of order and disorder, also known as critical points, where complex patterns of fluctuations characterize the system's dynamics (Werner, 2007; Beggs, 2008; Kitzbichler et al., 2009; Deco and Jirsa, 2012; Tagli-

azucchi et al., 2012). Indeed, the emerging hypothesis in the neuroscientific community is that the brain activity self-organize to operate close to a phase transition or critical point (Beggs and Plenz, 2003; Mazzoni et al., 2007; Pasquale et al., 2008; Friedman et al., 2012; Hahn et al., 2010; Tagliazucchi et al., 2012; Priesemann et al., 2014). Working in the critical regime is especially beneficial for the brain since it ensures an optimal balance between stability (system's resilience to perturbations) and flexibility (responsiveness and adaptation to stimuli) (Munoz, 2017). Furthermore, theoretical work shows that working in this regime optimizes several brain functions such as information transmission within the network, input sensitivity, and dynamic range (Shew and Plenz, 2013; Schneidman et al., 2006; Beggs and Plenz, 2003; Kinouchi and Copelli, 2006; Haldeman and Beggs, 2005).

The hypothesis of the brain working close to an order-disorder phase transition is gaining interest in the field. One can find multiple studies that suggest signs of criticality using different neural signals, such as LFPs *in vitro* (Beggs and Plenz, 2003; Mazzoni et al., 2007; Pasquale et al., 2008; Friedman et al., 2012), LFPs *in vivo* (Hahn et al., 2010), BOLD signals (Tagliazucchi et al., 2012), voltage imaging (Scott et al., 2014), and calcium imaging (Priesemann et al., 2014; Bellay et al., 2015; Hahn et al., 2017; Ponce-Alvarez et al., 2018). Evidence of criticality comes mainly from the study of sequences of activation called 'neural avalanches' (Beggs and Plenz, 2003; Mazzoni et al., 2007; Pasquale et al., 2008; Friedman et al., 2012; Hahn et al., 2010; Tagliazucchi et al., 2012; Priesemann et al., 2014; Ponce-Alvarez et al., 2018), which are defined as sequences of time bins during which at least one neuron is active (Marshall et al., 2016), and from probabilistic models developed in a statistical physics approach to describe emergent macroscopic properties of the data (Schneidman et al., 2006; Tkacik et al., 2009; Tkačik et al., 2013; Ponce-Alvarez et al., 2018).

Even if the transitions and temporal structure of the activity patterns have been largely investigated, the temporal scale that describe the repertoire of states is still unknown. In Chapter 4, I studied how the functionally-relevant collective features of EEG resting-state signals change at different

temporal scales. For this, I investigate not only the network organization of the collective spatiotemporal patterns, but also the transition among them and the information about the collective dynamics, e.g. critical dynamics. This study describes the spatiotemporal dynamical repertoires for different temporal scales and provides a theoretical justification for using temporal scales in the characterization of EEG patterns.

1.3.2. Organization of functional and anatomical networks

Graph theory tools have also increased the understanding of the organization of brain networks. The brain network organization displays multiple features of an efficient and functional communication network (van den Heuvel and Hulshoff Pol, 2010; Bullmore and Sporns, 2012). In particular, to minimize the physical and metabolic cost of the wiring, the healthy brain promotes the formation of specialized compact network communities, also known as modules, which have been observed both in anatomical and functional networks (van den Heuvel et al., 2009; Zamora-López et al., 2010; Sporns, 2013). On the other hand, to ensure global communication and functional integration, the brain needs to invest resources, i.e. wiring, to create long-range links that integrate the information from spatially distant regions. These two major competing topological properties, i.e. segregation and integration, have been reported to reach a balance in healthy conscious subjects, see Figure 1.5. This balance is disrupted in different low-level states of consciousness (Monti et al., 2013; Rizkallah et al., 2019), suggesting that maintaining this organization is a signature of consciousness (Tononi and Edelman, 1998).

Interestingly, many of those long-range connections are maintained by central hub regions, i.e. brain regions that are densely interconnected to the rest of the network (Zamora-López et al., 2010; Senden et al., 2014; Grayson et al., 2014). Furthermore, these hub regions tend to be connected densely to each other, forming a central 'core' or 'rich club' in the network (van den Heuvel and Sporns, 2011; Gollo et al., 2015; Gollo, 2019; Margulies et al., 2016). These regions require high energy cost but possess highly efficient brain information transfer in the network. The differentiation between a network core with a few densely connected nodes and

the majority belonging to the network periphery suggest a *core-periphery* architecture in the brain (Csermely, 2018). This network organization has been proposed to play an important role in the development of fast and efficient responses (May, 1972), flexibility-robustness trade-offs (Kitano, 2004) and learning (Bassett et al., 2013), among others.

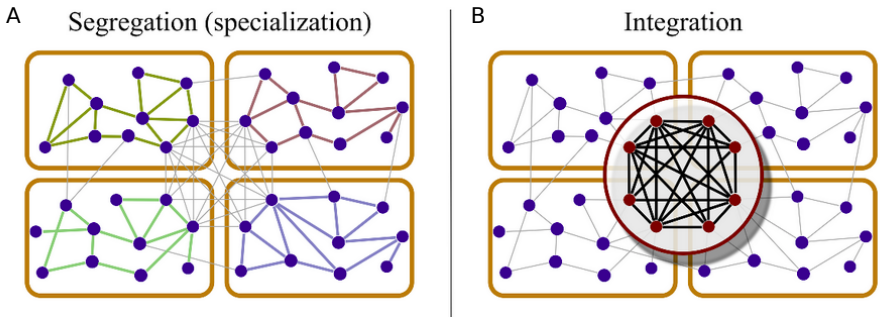

Figure 1.5: **Segregation and integration as the two major dispositions of the topological organization. A)** Brain networks are organized into modules composed of regions with specific brain functions. This modular organization ensure the parallel processing of different brain functions. **B)** Specific brain regions form a central module that can communicate between different modules and integrate multisensory information. Figure modified from (Zamora-López et al., 2011).

1.3.3. Neural communication

Network-oriented analyses can also be used to study how distant brain regions communicate and exchange information. Propagation of brain activation is key for the emergence of behaviour, memory, and conscious processing. Consequently, most theories of consciousness postulate a central role of information integration among brain regions (Dehaene et al., 1998, 2014; Tononi and Edelman, 1998; Northoff and Lamme, 2020). The neural mechanisms that ensure effective communication and transmission of information in the brain have been widely studied (Fries, 2005; Deco and Kringelbach, 2016; Friston et al., 1993; Gilson et al., 2016). One can find in the literature several attempts to explain the neural coupling mechanism that gates communication, such as the 'Communication Through Coherence' (CTC) (Fries, 2005).

The application of external stimulation also contributes to understanding the propagation of inputs in the brain networks. Many attempts have focused on externally perturbing the brain with artificial inputs applying interventions such as transcranial magnetic stimulation (TMS) (Siebner et al., 2009) or deep brain stimulation (DBS) (Kringelbach et al., 2007). Studies have investigated the combination of these external stimulations with neuroimaging methods, such as EEG or fMRI, which allows measuring the spatiotemporal propagation of the perturbations within the brain network (Massimini et al., 2005; Casali et al., 2013). Among them, one can find the seminal study by Massimini et al. (Massimini et al., 2005), where the changes in the global EEG signals after applying a TMS perturbation were investigated. The same authors defined the Perturbative Complexity Index (PCI) that quantifies the effect of the perturbation in the network. As it will be explained later in the next section, the PCI is used as biomarker that characterize different levels of consciousness.

The following section will introduce the relevance of comparing the brain dynamics on different brain states. In particular, we will cover the research in low-level states of consciousness characterized by a loss of consciousness.

1.4. Brain states and low-level states of consciousness

The study of the collective whole-brain patterns of the resting-state brain activity in healthy participants has offered the opportunity to describe the baseline brain functional and structural network organization to maintain normal brain functions, e.g. to perform usual tasks. Recent studies have focused on studying the alterations in the resting-state activity patterns during cognitive tasks and altered states of consciousness (Gilson et al., 2018; Tagliazucchi et al., 2013; Hudetz, 2012; Demertzi et al., 2015; Deco and Kringelbach, 2017; Luppi et al., 2019). This procedure allows explaining the neural mechanism underlying conscious and healthy processing and understanding the origin of alterations in cognition and diseases. In particular, one of the focus of this thesis is the study of the neural dynamics in altered states of consciousness, specifically in pathologically and phys-

iologically originated low-level states of consciousness. These conscious states show alterations in the levels of consciousness caused by an imbalance between the dimensions of awareness and wakefulness (see Figure 1.6), that will be explained in detail in the following subsections.

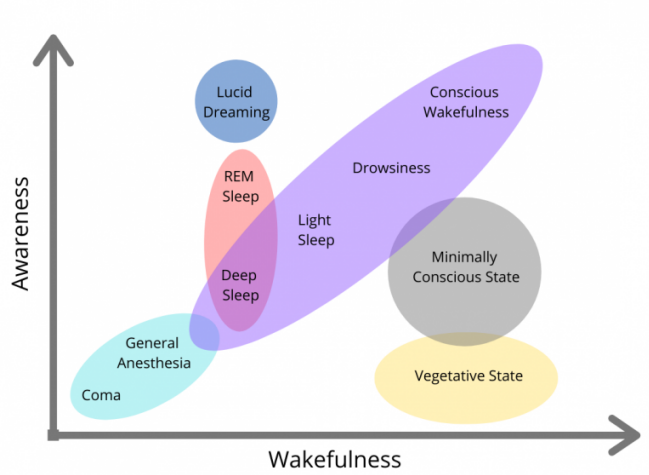

Figure 1.6: **States of consciousness according to the two main dimension; awareness and wakefulness.** The states of consciousness are classified according to the level of awareness (ability to communicate and respond to external inputs) and wakefulness (level of processing of conscious content). Conscious wakefulness shows high level of awareness and wakefulness, while the rest of the conscious states show alteration in one of both dimensions. Figure extracted from (Laureys, 2005).

The study of the consciousness in the brain, its origin, and its manifestation in brain dynamics have been broadly discussed during many centuries. Historically, the subjectivity of the experience and the variety of theories around this topic have placed the study of consciousness far from the scientific research (Storm et al., 2017). Recently, even with the uncertainty surrounding the topic, Neuroscience has started approaching the search of *neural correlates of consciousness* (Koch et al., 2016). The neural correlates of consciousness are the experimental observables that correlate with conscious experiences (e.g. visual perception) (Crick and Koch, 1990). One approach to use these confounds consists of the study of

consciousness as a temporally extended state, such as contrasting wakefulness vs. states of diminished consciousness (Laureys et al., 2010; Demertzi et al., 2015). The most basic assumption is the presence of subjective experiences during normal wakefulness that disappear or are changed when we lose or alter consciousness (e.g. during sleep, anesthesia, DOC or under psychedelic drugs) (Dehaene and Changeux, 2011; Tononi et al., 2016; Bayne and Carter, 2018). For example, during sleep, participants are unaware of the environment and cannot respond to external stimuli.

To facilitate the study of consciousness in the brain, the multi-faceted concept of consciousness has been reduced into two main dimensions: **awareness** of the environment (i.e. the ability to communicate and respond to external inputs) and/or of the self (i.e. rumination, thoughts and the internal awareness of body) and **wakefulness** (i.e. the level of consciousness) (Storm et al., 2017; Laureys, 2005). Other dimensions can be also considered to characterize consciousness as a multidimensional construct (Bayne et al., 2016), such as visual perception, cognition or/and experience of unity, which are important to describe brain states characterized by altered consciousness, such as psychedelic states or meditation (Bayne and Carter, 2018). However, the brain states define here will depend on the level of these two dimensions, see Figure 1.6.

Low-level states of consciousness are characterised by a reduction in awareness and wakefulness comparing with conscious wakefulness or resting-state, see Figure 1.6. The level of consciousness is reduced in three different contexts; (i) in a *pathological* context, where general injuries affecting cortical and subcortical regions or relatively localised traumatic brain injuries led to a disorder of consciousness (DOC) where the patients show alterations in the level of wakefulness or/and awareness, (ii) *pharmacological* interventions, such as the administration of anesthesia, which induce transient states of reduced consciousness and (iii) *physiological* alterations occurring naturally or without external manipulations such as sleep stages or meditation. All these states of reduced consciousness share a common feature: lack or distortion of reported subjective experience that leads to alterations in the level of awareness and wakefulness, see Figure 1.6.

In chapter 2 and 3, I present two studies where the neural mechanism of

loss or reduction of consciousness is studied in patients that show a loss of consciousness due to severe brain damage and which lead to disorder of consciousness (DOC) and in healthy participants that were induced in temporally states of propofol-induced sedation. In the next two sections, I will introduce the experimentally observable changes characterizing the brain dynamics of DOC patients and states of induced sedation. These alterations can be determined using the observations described in the previous section, such as changes in the organization of the functional and structural networks and alterations in the connectivity or complexity, among others.

1.4.1. Disorders of consciousness

Most people who suffered severe brain damage fall into a coma within the first days after injury. During coma, patients show an absence of awareness of self and surroundings and no signs of wakefulness; thus, one can define coma state as a state characterized by the absence of consciousness. After coma, there are multiple options for the patients' evolution; in the most extreme cases, the patients suffer a brain death, i.e. they lose all the brainstem function and demonstrate continuing apnoea. In the cases where the patients recover some or ultimately brain function, there is typically a progression through different stages, see Figure 1.7; in the first stage, Unresponsive Wakefulness Syndrome (UWS) (Laureys, 2005), the patients are awake but unaware of themselves or their environments. Patients in this state can be defined as 'an organic body capable of growth and development but devoid of sensation and thought' (Jennett and Plum, 1972). Next, the patients can progress to the state of Minimal Conscious States (MCS), where the patients show limited but clear evidence of awareness of themselves or/and their environment, expressed as responding to simple commands, gestural or verbal yes/no response, intelligible speech or purposeful behaviour (Laureys et al., 2004; Giacino et al., 2002). DOC patients (i.e. UWS and MCS) can partly recover consciousness and remain in a Locked-in Syndrome, characterized by sustained eye-opening and awareness of the environment, but they are parallelized with aphonia or quadriplegia. In the best of the cases, the patients can fully recover consciousness, a state that is characterized by the patients' ability to use objects functionally (Laureys et al., 2004). The recovery of cognitive and

motor functions of these patients, including additional states of emergence from MCS or levels of disability, is shown in Figure 1.7.

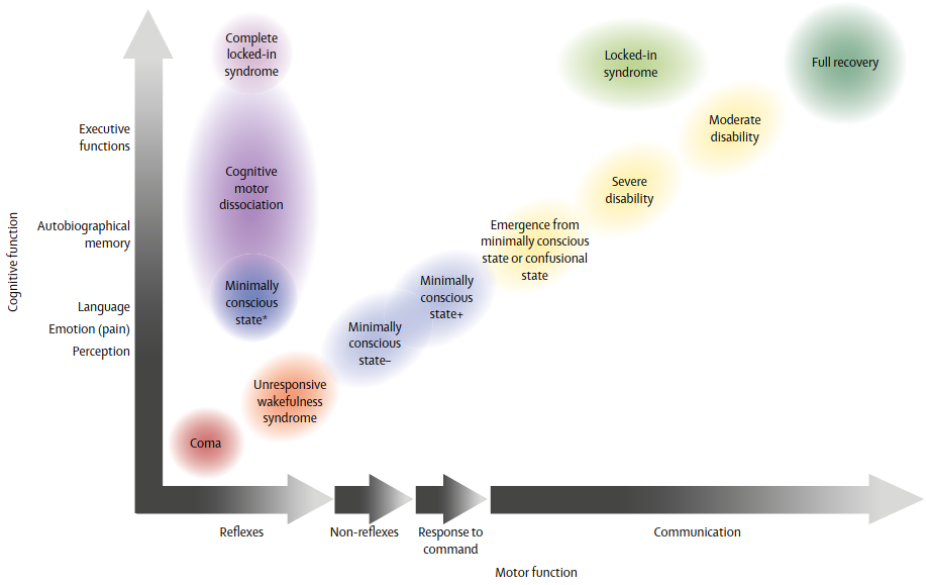

Figure 1.7: **Evolution in the cognitive and motor skills of the possible states from coma until full recovery.** Red circles represent patients who are unconscious with only reflexive movements. Blue circles represent patients in a minimally conscious state. The yellow circles represent the states when functional communication is detected. Patients emerge from the minimally conscious state and can evolve to a confusional state or severe or moderate disability, before a full recovery (dark green circle). Dissociations between motor and cognitive functions exist in locked-in syndrome (light green circle), cognitive motor dissociation (dark purple circle), and minimally conscious state* (dark blue circle). In rare cases, the diagnosis of complete locked-in syndrome (light purple circle) can be done through neuroimaging examinations. The black-to-white gradient represents the evolution from absence (black) to the recovery of a behaviour (white). Figure extracted from (Thibaut et al., 2019).

The study of brain dynamics in DOC patients is key to understand the mechanism of consciousness in the brain, because it allows disentangling between the dimensions of wakefulness and awareness. Nevertheless, the investigation with DOC patients is remarkably controversial due to its re-

lation with end-of-life decisions in permanently unconscious patients and with major philosophical, sociological, political, and religious questions of humankind (Laureys et al., 1999). In the following paragraphs, I will present some studies investigating the brain dynamics in DOC patients based on neuroimaging methods, which have provided a profound analysis of brain activation and mechanism in terms of cerebral metabolic levels, brain activation, connectivity and dynamics.

One of the main alterations reported in the brain activity of DOC patients is a decrease in the cerebral metabolic rate. Indeed, impairments of consciousness have been associated with a decrease in the global cerebral metabolic levels of 40-60 % in UWS and MCS patients measured using PET diagnosis (Laureys et al., 2004; Stender et al., 2015). Furthermore, the hemispheric preservation of brain glucose metabolism predicts the presence and recovery of consciousness, which allows diagnosing and extracting prognostic markers in DOC patients (Stender et al., 2016). In particular, in UWS patients, large effects of hypo-metabolism were found in the left and right lateral parietal and lateral prefrontal cortices, corresponding to the external network, and in the midline precuneus/ posterior cingulate cortex and mesiofrontal/anterior cingulate cortices, corresponding to the internal network (Stender et al., 2015; Thibaut et al., 2012). Interestingly, in MCS patients, the external/lateral network is less important than the intrinsic/medial network, consistent with the clinical findings and suggesting that awareness is supported by two distinct mesocircuits.

In terms of EEG fluctuations and brain connectivity, alterations at global and local levels have been reported in DOC patients in particular frequency bands. EEG studies show that the connectivity depends on the frequency of the signals, finding a positive link between connectivity in the alpha band and conscious states indexed by behaviour and a maladaptive link between the delta band connectivity and outcomes (Chennu et al., 2017). Furthermore, the structural hubs in frontal and parietal cortices have been suggested to be essential for the recovery of consciousness (Chennu et al., 2017; Stender et al., 2016). Moreover, the EEG signals' spectral entropy shows an increase in the power in the theta and alpha bands and lower

delta power in MCS patients than in UWS (Piarulli et al., 2016). Further EEG studies show a decrease in the brain network integration and an increase in segregation in DOC patients compared to healthy controls (Rizkallah et al., 2019), significantly larger in the left precuneus and left orbitofrontal cortex.

Further studies applied this perturbation in unconscious states where it was shown that during this state, the brain shows a breakdown of functional connectivity indicated by the rapid extinction and poor propagation of the perturbation input (Massimini et al., 2005; Ferrarelli et al., 2010; Casali et al., 2013). These studies use the Perturbational Complexity Index (PCI) described above, as a measure of the global response to the TMS perturbation. The authors showed that the PCI can discriminate between different levels of consciousness, such as during wakefulness, dreaming, sleep, under different levels of anesthesia and in DOC patients. This suggests that the complexity and the functional communication is impaired in low-level states of consciousness (Massimini et al., 2005; Casali et al., 2013; Ferrarelli et al., 2010; Rosanova et al., 2018).

On the other hand, fMRI recordings have allowed the study of functional networks and their alterations in global and local dynamics in DOC patients. Interestingly, the functional networks commonly captured in the brain dynamics of the healthy wakefulness (DMF, frontoparietal, salience, auditory, sensorimotor and visual networks) were found in DOC patients and the functional connectivity of those networks correlated with the conscious behavioural scores, highlighting their contribution to the level of consciousness (Demertzi et al., 2015). The auditory network has the most highly discriminative capacity when comparing MCS and UWS, significantly larger effects in bilateral auditory and visual cortices. Analysis restricted to the connectivity of the DMN pointed out that the connectivity in all default network regions is negatively correlated with the degree of clinical consciousness impairment, with a larger effect in the precuneus when MCS and UWS are compared (Vanhaudenhuyse et al., 2010).

Recently, Demertzi et al., (Demertzi et al., 2019) studied the fMRI spatiotemporal patterns in DOC patients and healthy controls and found dif-

ferent connectivity patterns that were more or less present according to the level of consciousness, see Figure 1.8. In particular, a connectivity pattern of positive and negative long-distance coordination, high modularity and low similarity to the anatomical connectivity was prominently observed in the healthy controls and MCS patients, but not in UWS patients (pattern 1 in Figure 1.8). In contrast, a pattern with low interregional dynamic coordination, low efficiency, with high similarity to anatomical connectivity appeared more frequently in UWS patients (pattern 4 in Figure 1.8). The results presented in that article suggest that the brain dynamics in low-level states of consciousness are characterized by a loss of complexity and more rigid (i.e. constrained by the SC) spatiotemporal patterns.

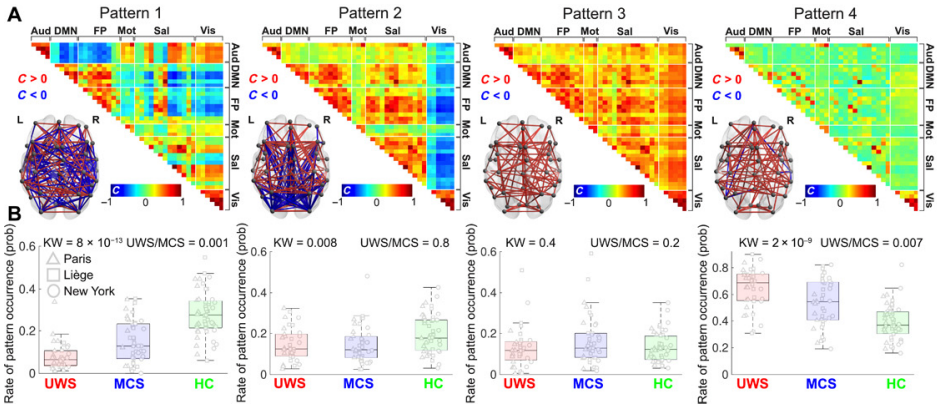

Figure 1.8: **The pattern occurrence probability of the temporary brain states show changes in DOC patients compared with healthy controls. A)** Four patterns of coordination captured from the fMRI BOLD signals. **B)** Patient groups differed with respect to the likelihood of each coordination pattern occurrence. Figure edited from (Demertzi et al., 2019).

These results suggest that brain damage causing disorder of consciousness has profound effects on both local and global brain functions. However, the relation between the altered brain dynamics and the brain mechanism (e.g. modifications in the global and local dynamics or alterations in specific subnetworks) has still to be elucidated. So far, the studies done in this line have indicated a reduced metabolic rate in these states, accom-

panied by alterations in the power of frequency bands and alterations in the spatiotemporal properties of the functional networks and activation patterns.

1.4.2. Anesthesia

Loss of consciousness is also temporarily achieved by means of pharmacological drugs, such as anesthesia. Anesthesia induces a process in the brain characterized by different stages. At low doses of anaesthetics, the experienced brain states are similar to drunkenness, suppress thinking, focused attention, analgesia, amnesia, distorted time perception, depersonalizing and increased sleepiness (Alkire et al., 2008; Hudetz, 2012). With higher doses, the patients show serious difficulties moving in response to a command and consciousness begins to fade (Alkire et al., 2008; Hudetz, 2012). Upon further increases in anaesthetic dose, nociceptive and autonomic reflexes are suppressed (Hudetz, 2012). High doses of anesthesia can lead to brain death in which brain activity is wholly suppressed (Wijdicks, 2001). Even if the anesthesia is applied commonly in medicine and its behavioural changes are well-known, the brain mechanism underlying sedated dynamics is a subject of intense research.

Several PET studies have shown a substantial reduction in the global metabolic rate under general anesthesia at the cortical level. The pioneer studies performed by Alkire et al. showed that the global metabolic rate is reduced in the range of 30-70 % during deep anesthesia and present also in other common anaesthetics (Alkire et al., 1995). The most considerable reductions of the metabolic rates were shown in the medial thalamus, certain medial posterior parietal (precuneus and posterior cingulate), occipitotemporal and orbitofrontal regions (Fiset, 1999; Fiset et al., 2005; Campagna et al., 2003). Furthermore, previous EEG studies also showed uncoupling of coherent anterio-posterior and inter-hemispherical electrical activity during anesthesia induced unconsciousness (John et al., 2001).

Evidence suggests that anesthesia also modulates the strength of the functional connectivity (Martuzzi et al., 2010; Barttfeld et al., 2015; Boveroux et al., 2010; Monti et al., 2013; Schrouff et al., 2011). During anesthe-

sia, there is an impairment of thalamo-cortical and cortico-cortical connections, found by a disruption in the FC when analyzed within fronto-parietal and between fronto-parietal and thalamus connections (White and Alkire, 2003; Alkire and Miller, 2005). Further studies pointed out that anesthesia reduces the posterior cingulum cortex's functional connectivity significantly (Greicius, 2008; Stamatakis et al., 2010; Uhrig et al., 2018) and that the precuneus and lateral temporo-parietal components of DMN persisted under anesthesia (Vincent et al., 2007). Other studies focused on the appearance of the functional network that commonly can be observed on the awake resting-state activity. Studies highlighted the presence of the RSNs that characterize the spatiotemporal fluctuations of the awake rest brain activity (especially, the oculomotor, somatomotor, visual and default Mode networks) during anesthesia in monkeys (Vincent et al., 2007). Following studies investigated the alterations in the DMN, especially showing a reduction in the connectivity with hubs in this network, such as the posterior cingulate (Greicius, 2008) and alterations in the global connectivity of this network (Deshpande et al., 2010). Furthermore, changes within and between different networks have been shown as differences in connectivity between primary and higher-order networks (Martuzzi et al., 2010); propofol anesthesia suppresses the higher-order networks, such as default, controls executive network and salience networks and primary networks (such as auditory and visual) did not show significant reductions (Boveroux et al., 2010). The functional interactions' effects have been shown to affect the integration within and between the RSNs by decreasing the mutual information (Schrouff et al., 2011). Furthermore, they found that the integration between parietal and frontal regions and between the parietal and temporal regions was substantially reduced (Schrouff et al., 2011).

A seminal work performed by Bartffeld and colleagues (Barttfeld et al., 2015) measured the dynamical functional connectivity of resting-state fMRI activity in awake and anaesthetized monkeys, see Figure 1.9. This study showed that the spatiotemporal patterns changed in both states. The patterns that appeared under anesthesia were more frequent, inherited the structure of anatomical connectivity, and exhibited fewer small-world properties and a lack of negative correlations. Similar results have been reported elsewhere (Vincent et al., 2007; Uhrig et al., 2018), showing

that the FC patterns show analogy to the structural organization and a restricted repertoire of states during anesthesia.

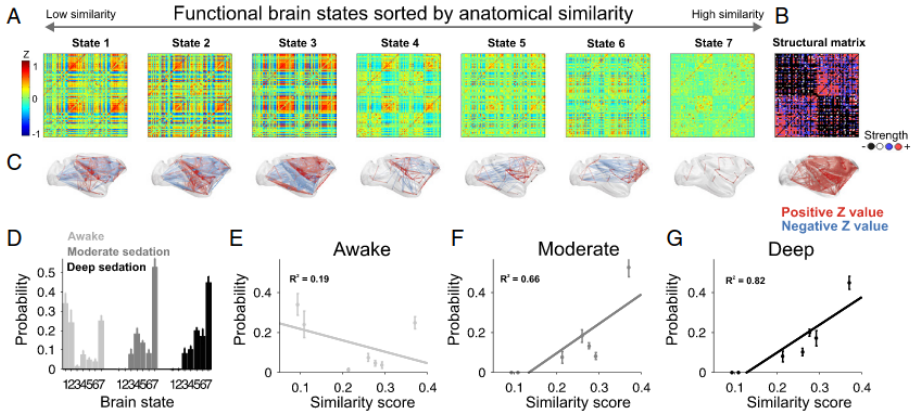

Figure 1.9: **Dynamical connectivity and brain states for all vigilance conditions. A)** Seven brain states obtained by clustering.Brain states are sorted according to their similarity to the structural connectivity matrix. **B)** Structural matrix derived from the anatomical macaque cortical connectivity. **C)** Brain renders displaying the 400 strongest links for each brain state. Red lines represent positive connections between ROIs; blue lines represent negative connections. **D)** Probability distributions of brain states for all vigilance condition. **E-G)** Probability of occurrence of each brain state as a function of the similarity between functional and structural connectivity for awake **E)**, moderate **F)**, and deep **G)** conditions. Each point in the figure corresponds to a brain state, characterized both by a similarity score and a probability of occurrence within each vigilance condition. Figure extracted from (Barttfeld et al., 2015)

Altogether, it appears that both pathological (DOC) and physiological (anesthesia) low-level states of consciousness share similar characteristics, such as reduction in the cerebral metabolic rate, alteration in the global FC, loss of connectivity and complexity of the FC, imbalance in the integration-segregation organization, and alterations in the temporal properties of the coordinated patterns. Despite recent achievements in finding signatures of loss of consciousness, the neural mechanisms underlying these processes remain unclear. In Chapters 2 and 3, we will focus on the human brain during low-level states of consciousness to find a mechanistic explanation of the discussed characteristic changes in brain

activation and connectivity.

1.5. Motivation for using computational brain models

The studies investigating whole-brain dynamics have been mainly focused on measuring brain activation patterns and extracting collective signals' properties, but the study of the mechanism and its underlying principles remain an open question. In particular, it is unknown how the brain generates the observed coordinated patterns, which continuously rearrange in time and space; how these collective patterns *emerge*; which are the *mathematical principles* underlying these dynamics, among others.

The idea of better understanding macroscopic brain dynamics using computational models has emerged as a powerful tool for investigating the collective properties of the brain (Deco and Kringelbach, 2014; Gilson et al., 2019b; Kringelbach and Deco, 2020). In a broad sense, modelling refers to idealizing (or simplifying while keeping the essential ingredients) the processes that generate the observed phenomena in a real system. Theoretical models are often applied to study complex non-linear systems, such as the brain, in order to investigate the interplay between known dynamical and structural features, e.g. combining SC with local dynamics to generate resting-state FC. For this, it is required to explain the relevant observable features and to ensure a robust interpretation of the models' parameters to link them back to biological variables. Thus, theoretical models need to achieve a trade-off between simplicity and richness to explain the mechanisms underlying complex biological systems.

Current theoretical models describe the resting-state brain dynamics at different scales, see Figure 1.10. At the microscopic cellular scale, several models simulate neural activity at the level of neurons, i.e. describing the dynamics of membrane voltages and synapses (Hodgkin and Huxley, 1952; FitzHugh, 1961; Izhikevich and Edelman, 2008). At the microcircuit level, models simulate the dynamics of neural populations of different cell types, i.e. excitatory and inhibitory, and the interaction between them (Pot-

jans and Diesmann, 2014; Markram et al., 2015). At a mesoscopic scale, more abstract models are typically used to describe the dynamics of populations of neurons in a simplified manner, for example using mean-field approximations to describe the input-output mapping of firing activity (Wilson and Cowan, 1972; Ghosh et al., 2008; Deco et al., 2009). Finally, large-scale or whole-brain models generally study networks of brain regions (often described as neural populations at the microcircuit or mesoscopic scale). Whole-brain models have successfully simulated the activity of large neuronal populations using fMRI (Ghosh et al., 2008; Deco et al., 2009; Honey et al., 2009; Deco and Jirsa, 2012), MEG (Cabral et al., 2014; Nakagawa et al., 2014) and EEG signals (Hindriks et al., 2014).

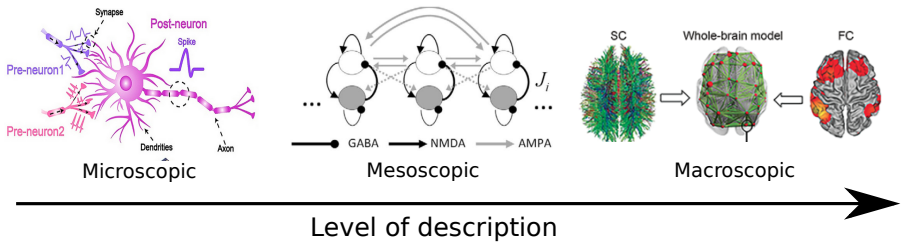

Figure 1.10: **Different levels of description of the computational brain models.** Depending on the level of description, the computational models can describe the neural dynamics of the cells (microscopic level), the dynamics of whole populations of neurons (mesoscopic level) and the connectivity of brain regions (macroscopic level). Figures extracted from (Yang et al., 2020; Deco and Kringelbach, 2014; Padilla et al., 2019).

The whole-brain computational models are used depending on the question addressed, its complexity, the available data, and the level of description needed. Indeed, the models are classified into types depending on different factors that describe the nature and the approach of the model. For example, depending on the complexity of the model (e.g. the number of the free parameters), one can find different models that range from very simple, homogeneous models (Cabral et al., 2011; Deco et al., 2017a) to models of high complexity and heterogeneity with many free parameters (Gilson et al., 2016; Demirtaş et al., 2019). The whole-brain models can be also classified depending on the level of determinism. A model is *deter-*

ministic when biologically plausible brain dynamics are assumed (tipically given by differential equations) and the model is built on them. On the contrary, it can be *statistical* if the model targets the probability of some empirical statistics. Furthermore, depending on their composition, models can have a bottom-up or top-down approach. The bottom-up approach builds models by combining units or subsystems with known dynamics to simulate the entire systems, whereas the top-down approach estimates the behavior of units and subsystems based on the observed system's behavior.

Many models have been developed to describe or simulate brain dynamics in different ways depending on the approach, the nature of the model or the level of description needed. For example, **Statistical** models can successfully describe in a top-down approach the collective neural dynamics (Munoz, 2017; Schneidman et al., 2006; Tkacik et al., 2009; Ponce-Alvarez et al., 2018). These models were originally developed in the field of statistical mechanics, but their interest in describing the brain dynamics lies in understanding how complex patterns can collectively emerge from large populations of neurons, which is assumed to be largely independent of the microscopic details of the neuronal system (Schneidman et al., 2006; Tkacik et al., 2009). In this context, Bialek and coworkers developed data-driven models of biological systems that are consistent with certain measured observables, but otherwise have as little structure as possible (i.e. maximum entropy principle) (Schneidman et al., 2006; Tkacik et al., 2009; Bialek et al., 2012). Recently, this family of inverse models has been successfully applied to whole-brain dynamics (Watanabe et al., 2013; Ezaki et al., 2017; Ponce-Alvarez et al., 2021).

On the other hand, several **deterministic** models with a bottom-up approach have been used to describe the brain's network activity, based on experimental data and known biophysical mechanisms. An usual assumptions is that the brain's resting-state activity emerges from the interaction between brain regions in an interconnected neuroanatomical network (Deco et al., 2011; Jirsa et al., 1998; Nakagawa et al., 2014; Cabral et al., 2011; Deco et al., 2009; Deco and Jirsa, 2012; Ghosh et al., 2008; Honey et al., 2007; Jobst et al., 2017; Saenger et al., 2017). One can find different models depending on the choice for nodal dynamics, i.e. the intrinsic behaviour of a brain region in the spontaneous state, such as conductance-

based dynamics (Breakspear et al., 2003; Honey et al., 2007), spiking networks (Deco and Jirsa, 2012; Deco et al., 2013b), phase oscillators (Cabral et al., 2011; Ponce-Alvarez et al., 2015), and Hopf (or Stuart Landau) oscillators (Deco et al., 2017a). Of particular interest for the present thesis, the Stuart Landau oscillators allow us to study the phase and amplitude interactions in large-scale models. This deterministic model has been successfully applied to simulate the network non-linear dynamics occurring at the ultra-slow scale of resting-state BOLD signals (Deco et al., 2017a; Saenger et al., 2018). Furthermore, the model global and regional parameters obtained from a heuristic optimization of the model can discriminate between brain states, thereby improving our understanding of brain network and local alterations in different brain states (Saenger et al., 2017; Jobst et al., 2017; Senden et al., 2017).

Linear dynamics have been also used to describe large-scale brain activity (e.g. (Deco et al., 2013b)). These models have proven to be useful to estimate effective connectivity. With this objective, multivariate Ornstein-Uhlenbeck (MOU) dynamics have been used to reproduce the statistics corresponding to the propagation of the empirical signals. The MOU model can be constrained by enforcing a specific topology on EC using the empirical structural (anatomical) connectivity. In this way, the model explains the spatiotemporal brain activity by modulating of the efficacies of the (putatively) existing anatomical connections. The model parameters are learned at the link level, which provides a refined description that is especially interesting for finding biomarkers between brain states (Gilson et al., 2019a).

1.6. Objectives

As previously reported, many studies have shed light on the functional and architectural features of the conscious resting-state brain activation and how they are altered in low-level states of consciousness. Although of great importance for understanding brain processing during resting-state and altered brain states, these observations still lack generative explanations. The main goal of the present thesis is to use computational modelling to simulate and extract information about the brain mechanism with simple models that allow providing a physical explanation of the system in different contexts.

In chapters 2 and 3, the main goal is to compare the brain dynamics and mechanism of the healthy resting-state participants with the dynamics captured in low-level states of consciousness, i.e. DOC patients and propofol-induced sedation. Chapter 2 studies the brain dynamics characterizing each state by using phase-synchronization analyses that capture the relationships between the phases of BOLD signals at high temporal resolution. We further investigate the mechanism using a whole brain model based on Stuart-Landau nonlinear oscillators that simulate the activation of each brain region. This model combines single-node local oscillatory dynamics and network interactions. It can generate different collective dynamics depending on the anatomical connectivity structure, the global strength of connections, and the local state of the network's nodes. We also use standard graph theory tools to study the alterations in the structural connectivities of the patients' physical anatomical substrate.

Chapter 3 aims to characterize the brain propagation after a perturbation in the cerebral network in healthy controls and how this is altered in patients who lose consciousness due to severe brain damage. We used a multivariate Ornstein-Uhlenbeck (MOU) process as a generative model that can reproduce the covariance patterns captured from the BOLD time series by generating the effective connectivity (EC). We further apply the dynamic communicability framework to characterize the impulse response of the network to a unit perturbation in a source node given its EC.

Finally, in chapter 4, we study the collective behaviours of the resting-state brain activation in healthy participants by describing how the brain's dynamical properties change across temporal scales. Since our study's goal requires a high temporal resolution, this analysis was performed using EEG signals, where the time series have a millisecond temporal resolution. We use a maximum entropy model (MEM) to study the statistics of the activation of the patterns extracted from the EEG signals. This approach approximates the probability distribution of the activation patterns captured in the signals and describes the system properties based on measures inspired by statistical mechanics, such as entropy and heat capacity.

CHAPTER 2

The underlying brain dynamics of low-level states of consciousness

Low-level states of consciousness are characterised by disruptions of brain activity that sustain arousal and awareness. Yet, how structural, dynamical, local and network brain properties interplay in the different levels of consciousness is unknown. Here[1], we study fMRI brain dynamics from patients that suffered brain injuries leading to a disorder of consciousness and from healthy subjects undergoing propofol-induced sedation. We show that pathological and pharmacological low-level states of consciousness display less recurrent, less connected and more segregated synchronization patterns than conscious state. We use whole-brain models built upon healthy and injured structural connectivity to interpret these dynamical effects. We found that low-level states of consciousness were associated with reduced network interactions, together with more homogeneous and

[1]Work in this Chapter can be found in: *Loss of consciousness reduces the stability of brain hubs and the heterogeneity of brain dynamics.* Accepted in *Nature Communications Biology.*

more structurally constrained local dynamics. Notably, these changes lead the structural hub regions to lose their stability during low-level states of consciousness, thus attenuating the differences between hubs and non-hubs brain dynamics.

2.1. Introduction

It is widely accepted that consciousness is decreased during sleep, under anesthesia, or as a consequence of major brain lesions producing disorders of consciousness (DOC). In clinical settings, different states of consciousness have been defined depending on the level of wakefulness (i.e. arousal) and awareness (i.e. the content of consciousness) (Laureys, 2005). Wakefulness is usually evaluated by eye opening, and awareness by the responsiveness of the patients and their ability to interact with the environment, as a proxy for subjective experience. The study of these different levels of consciousness has proven to be essential to understand the neural correlates of consciousness, yet, the underlying mechanisms remain largely unknown. Elucidating these mechanisms is challenging since they seemingly rely on a non-trivial combination of alterations in local dynamics and network interactions.

During the last decades, the study of the organization of the brain and its dynamics has provided increased understanding of the healthy brain structure and function (Sporns et al., 2005; van den Heuvel and Sporns, 2019; Biswal et al., 1995; Greicius et al., 2003; Damoiseaux et al., 2006; Zamora-López et al., 2011). On the one hand, analyses of electroencephalography (EEG), functional MRI (fMRI), and magnetoencephalography (MEG) have shown that a hallmark of healthy awake brain dynamics is the balance between integration and segregation (Deco et al., 2015a; Deco and Kringelbach, 2017; Dehaene and Changeux, 2011; Tononi and Koch, 2008). On the other hand, graph theory studies have shown that the modular and hierarchical organization of the human connectome facilitates the efficiency and robustness of information transmission (van den Heuvel and Sporns, 2019; Zamora-López and Brasselet, 2019). For these reasons, consciousness has been considered to result from the interplay between dynamics and connectivity allowing the coordination of brain-wide activity to ensure

the conscious functioning of the brain (Demertzi et al., 2019; Luppi et al., 2019; Panda et al., 2016; Escrichs et al., 2019). In contrast, unconscious states are characterized by a loss of integration (Rizkallah et al., 2019; Luppi et al., 2019; Monti et al., 2013), a loss of functional complexity (Rosanova et al., 2018; Casali et al., 2013), and a loss of communication at the whole-brain level (Bodart et al., 2018; Boly et al., 2011; Deco and Kringelbach, 2017; Monti et al., 2013). Interestingly, it has been shown that functional connectivity deviates from structural connectivity during conscious wakefulness but it follows closer the organization of the anatomical connections during unconscious states (Greicius, 2008; Barttfeld et al., 2015; Tagliazucchi et al., 2016b; Demertzi et al., 2019). Along with these global network effects, it has been proposed that some brain regions play an important role in maintaining consciousness, e.g. fronto-parietal regions, the posterior cingulate, precuneus, thalamus and parahippocampus (Laureys, 2005; Dehaene and Naccache, 2001; Crone et al., 2014). To study how structural, dynamical, local and network brain properties interplay in the different levels of consciousness, theoretical models are needed that incorporate all these levels of description.

In this study, we built whole-brain models with global and local parameters to investigate the possible mechanisms underlying the reduction of consciousness as a consequence of severe brain injury and transient physiological modifications due to propofol anesthesia. For this, we studied the fMRI dynamics of patients who have suffered brain injuries from various etiologies (i.e. traumatic brain injury (TBI), anoxia, haemorrhage) affecting different brain regions implicated in DOC. Specifically, we analysed data from patients with Unresponsiveness Wakefulness Syndrome (UWS; preserved arousal but no behavioural signs of awareness)(Laureys et al., 2010) and in Minimally Conscious State (MCS, fluctuating but reproducible signs of consciousness) (Giacino et al., 2002), and compared them with healthy control subjects (CNT) during conscious wakefulness i.e. resting-state. We also considered fMRI recordings of healthy controls scanned during conscious wakefulness (W), propofol-induced sedation (loss of responsiveness, S) and during the recovery from it (responsiveness regained, R). To study the brain dynamics, we performed phase-synchronization analyses that capture the relationships between the phases of BOLD signals at high

temporal resolution – a method that has proven to effectively describe the spatiotemporal dynamics of fMRI signals (Ponce-Alvarez et al., 2015).

To interpret these observations, we used a whole-brain model based on Hopf bifurcations (Deco et al., 2017a). This model combines single-node local oscillatory dynamics and network interactions. It is able to generate different collective dynamics depending on the shape of anatomical connectivity, the global strength of connections and the local state of the network's nodes. Importantly, the model allows investigating the interplay between the network structure and the dynamics at the local and global level. In particular, it allows us to study how network dynamics depend on the local activity of brain regions that have an important place in the structural network, such as highly connected nodes, usually referred to as "hubs".

2.2. Methods

2.2.1. Participants

This study includes a cohort of healthy controls and patients suffering from disorder of consciousness (DOC), and a cohort of healthy subjects undergoing anesthesia-induced loss of consciousness. The study was approved by the Ethics Committee of the Faculty of Medicine of the University of Liège. Written informed consent to participate in the study was obtained directly from healthy control participants and the legal surrogates of the patients.

We selected 48 DOC patients, 33 in MCS (9 females, age range 24-83 years; mean age ± SD, 45 ± 16 years) and 15 with UWS (6 females, age range 20-74 years; mean age ± SD, 47 ± 16 years) and 35 age and gender-matched healthy controls (14 females, age range 19-72 years; mean age ± SD, 40 ± 14 years). The DOC patients data was recorded 880 ± 35 days after injury. The healthy controls data was collected while awake and aware. The diagnosis of the DOC patients was confirmed through repeated behavioural assessment with the Coma Recovery Scale-Revised (CRS-R) that evaluates auditory, visual, motor, sensorimotor function, communication and arousal (Giacino, 2005). The DOC patients were included in the

study, if MRI exam was recorded without anesthetized condition and the behavioural diagnosis was carried out at least five times for each patient using CRS-R examination (Wannez et al., 2017). 5 CRS-R assessments were performed within a period of 14 days, usually within one week. The best CRS-R diagnosis was used for clinical diagnosis. One CRS-R assessment was performed before the MRI acquisition on the same day, yet the clinical diagnosis was made based on the best out of 5 CRS-R's. The exclusion criteria of patients were as follows: (i) having any significant neurological, neurosurgical or psychiatric disorders prior to the brain insult that lead to DOC, (ii) having any contraindication to MRI such as electronic implanted devices, external ventricular drain, and (iii) being not medically stable or large focal brain damage, i.e. $> 2/3$ of one hemisphere. Details on patients' demographics and clinical characteristics are summarized in the Appendix.

For the propofol anesthesia, 16 healthy control subjects (14 females, age range, 18-31 years; mean age $\pm$ SD, 22 $\pm$ 3.3 years) were selected in three clinical states including normal wakefulness with eyes closed (W), propofol anesthesia-induced sedation (S) and recovery from propofol anesthesia (R). Propofol was infused through an intravenous catheter placed into a vein of the right hand or forearm and an arterial catheter was placed into the left radial artery. During the study ECG, blood pressure, SpO2 and breathing parameters were monitored continuously. The level of consciousness was evaluated clinically throughout the Ramsay scale, representing the verbal commands; for details on the procedure, see (Boveroux et al., 2010). It should be noted that during the recovery of consciousness, R, subjects showed clinical recovery of consciousness (i.e. same score on Ramsay sedation scale as during wakefulness) but they showed residual plasma propofol levels and lower reaction times scores. The healthy subjects did not have MRI contraindication, any history of neurological or psychiatric disorders or drug consumption, which have significant effects in brain function. It shall be noted that the anesthesia dataset has a gender imbalance of $70\% - 30\%$ female to male.

2.2.2. MRI acquisition and data analysis

For the DOC dataset, structural and fMRI data were acquired on a Siemens 3T Trio scanner (Siemens Inc, Munich, Germany); propofol dataset was acquired on a 3T Siemens Allegra scanner (Siemens AG, Munich, Germany). The acquisition parameters are described in the Appendix.

The preprocessing of MRI data and the extraction of BOLD time series are described in Appendix. Briefly, independent component analysis was used for motion correction, spatial smoothing and non-brain removal. After preprocessing, FIX (FMRIB's ICA-based X-noiseifier) (Griffanti et al., 2014) was applied to remove the noise components and the lesion-driven artefacts, independently and manually, for each subject. Finally, FSL tools were used to obtain the BOLD time series of 214 cortical and subcortical brain regions in each individual's native EPI space, defined according to a resting-state Shen atlas (Shen et al., 2013) and removing the cerebellar parcels.

2.2.3. Structural connectivity

A whole-brain structural connectivity (SC) matrix was computed for each subject from the DOC dataset, using diffusion imaging and probabilistic tractography (see Appendix for details). The procedure resulted in a symmetric SC matrix summarizing the density of anatomical links among the 214 ROIs, for each healthy control and participant.

2.2.4. Phase-interaction matrices

To evaluate the level of synchrony in brain activity, the phase interaction between BOLD signals was evaluated. Therefore, a band-pass filter within the narrowband of $0.04 - 0.07$ Hz was applied in order to extract the instantaneous phases $\phi_j(t)$ for each region j. This frequency band captures more relevant information than other frequency bands in terms of brain function (Glerean et al., 2012). The instantaneous phases, $\phi_j(t)$, were then estimated applying the Hilbert transform to the filtered BOLD signals individually. The Hilbert transform derives the analytic representation of a real-valued signal given by the BOLD time series. The analytical signal, $s(t)$, represents the narrowband BOLD signal in the time

domain. This analytical signal can be also described as a rotating vector with an instantaneous phase, $\phi(t)$, and an instantaneous amplitude, $A(t)$, such that $s(t) = A(t)cos(\phi(t))$. The phase and the amplitude are given by the argument and the modulus, respectively, of the complex signal $z(t) = s(t) + i \cdot H[s(t)]$, where i is the imaginary unit and $H[s(t)]$ is the Hilbert transform of $s(t)$.

The synchronization between pairs of brain regions was characterised as the difference between their instantaneous phases. At each time point, the phase difference $P_{jk}(t)$ between two regions j and k was calculated as:

$$P_{jk}(t) = \cos\left(|\phi_j(t) - \phi_k(t)|\right). \tag{2.1}$$

Here, $P_{jk} = 1$ when the two regions are in phase ($\phi_j = \phi_k$), $P_{jk} = 0$ when they are orthogonal and $P_{jk} = -1$ when they are in anti-phase. At any time t, the phase-interaction matrix $P(t)$ represents the instantaneous phase synchrony among the different ROIs. The time averaged phase-interaction matrix, $\langle P \rangle = \sum_{t=1}^{T} P(t)/T$, was bias-corrected by subtracting the expected phase-interactions phase-randomized surrogates, designed to decorrelate the phases while preserving the power spectrum of the original signals.

The instantaneous global level of synchrony of the whole network $r(t)$ was calculated as the average of the phase differences at each time point. Since $P(t)$ is a symmetric matrix, then:

$$r(t) = \frac{1}{N(N-1)} \sum_{j=1}^{N} \sum_{k=j+1}^{N} P_{jk}(t). \tag{2.2}$$

Finally, the fluctuations of $r(t)$ over time indicate the diversity of the observed network phase interactions. The *phase-interaction fluctuations* m were thus calculated as the standard deviation of r. When all the nodes of a network are synchronised then $r(t) = 1$ for all t and thus $m = 0$. However, if the network switches among synchronization states over time leading to fluctuations of r, then $m > 0$, reflecting those fluctuations.

2.2.5. Integration

Integration refers to the capacity of the brain to maintain communication between different parts and subnetworks. Here, we employed a metric of integration that assesses the connectivity out of the functional connectivity matrix, scanning across different scales (Deco et al., 2015a; Deco and Kringelbach, 2017; Deco et al., 2018a; Adhikari et al., 2017). More precisely, the time averaged phase-interaction matrix, $\langle P \rangle$, is scanned through all possible thresholds ranging from 0 to 1. At each threshold, the matrix is binarised and the size of its largest connected component is identified. Integration is then estimated as the integral of the size of the largest connected component as a function of the threshold.

2.2.6. Segregation

Segregation refers to the breakdown of a system into functional subcomponents. Quantitatively, segregation was estimated by the modularity index Q (Newman, 2006) of the time-averaged functional connectivity matrix $\langle P \rangle$, which is the metric evaluating how good a community detection method in networks could separate the network into modules. Therefore, we first binarized the matrix $\langle P \rangle$ by detecting the pairs of regions with average phase interaction significantly ($p < 0.01$) larger than expected in phase-randomized surrogates. Second, the Louvain algorithm was employed to subdivide this matrix into modules. The Newman modularity Q of the optimal partition was then considered as the measure of segregation (Rubinov and Sporns, 2011). Modularity is a cost function that evaluates the quality of subdivisions of networks into modules by targeting the maximization of the number edges within the modules and thus the minimization of edges across them (Rubinov and Sporns, 2011). Thus, the modularity index on the functional connectivity is a reasonable representation of the subdivision of the brain's activity into functional subdivisions.

2.2.7. Functional connectivity dynamics (FCD)

We evaluated the presence of repeating patterns of network states by calculating the recurrence of the phase-interaction patterns. For this, we used the functional connectivity dynamics (FCD). This measure is based on previous studies that defined the FCD for FC matrices calculated in

different time windows (Hansen et al., 2015). In our study, the duration of scans (10 min) was divided into sliding windows of 30 time points, shifted in 2 s steps. For each time window, centred at time t, the average phase-interaction matrix, $\langle P(t)\rangle$, was calculated as:

$$\langle P\rangle(t) = \frac{1}{T}\sum_{|t-t'|<15} P(t'), \tag{2.3}$$

where T is the total number of TRs. We then constructed the $M \times M$ symmetric matrix whose (t_1, t_2) entry was defined by the cosine similarity, S_{cos}, between the upper diagonal elements of two matrices $\langle P\rangle(t_1)$ and $\langle P\rangle(t_2)$, given as:

$$S_{cos}(t_1, t_2) = \frac{\vec{p}(t_1).\vec{p}(t_2)}{|\vec{p}(t_1)||\vec{p}(t_2)|} = cos(\theta), \tag{2.4}$$

where $\vec{p}(t_1)$ and $\vec{p}(t_2)$ are the vectorized representations of matrices $\langle P\rangle(t_1)$ and $\langle P\rangle(t_2)$, respectively, and θ corresponds to the angle formed between the two vectors, $\vec{p}(t_1)$ and $\vec{p}(t_2)$. Finally, the FCD measures was given by the distribution of these cosine similarities for all pairs of time windows.

2.2.8. Surrogate Analysis

For the phase surrogate analysis, first, the Fourier transform (FT) of the signals was computed. The phase of the Fourier transform was substituted with uniformly distributed random numbers while preserving their modulus. Then, the inverse FT was applied to return to the time domain with the new Fourier coefficients. This procedure effectively randomizes the phases of the signals while preserving the same power spectra as the original time-courses. Specifically, let $x_i(t)$ be the original BOLD time-course from the brain area i. The discrete Fourier transform of x_i is given by:

$$\tilde{x}_i(k) = \sum_{t=1}^{T} x_i(t) e^{-j\frac{2\pi kt}{T}} \tag{2.5}$$

where j is the imaginary unit and k goes from 1 to T (k=1,...,T). The phase shuffled surrogate is given by:

$$x_i^{surr}(t) = \frac{1}{T}\sum_{k=1}^{T} |\tilde{x}_i(k)| e^{-j(\frac{2\pi kt}{T}+\varphi_r)} \tag{2.6}$$

where φ_r is random variable uniformly distributed between $-\pi$ and π. These surrogates were used to rerun the analysis and extract a phase interaction matrix used to correct the empirical matrices.

2.2.9. Whole-Brain Network Model

The brain network model consists of $N = 214$ coupled brain regions derived from the Shen parcellation (Shen et al., 2013). The global dynamics of the brain network model used here results from the mutual interactions of local node dynamics coupled through the underlying empirical anatomical structural connectivity matrix C_{ij}. Local dynamics are simulated by the normal form of a supercritical Hopf bifurcation, i.e. Stuart-Landau oscillator (LANDAU and D., 1944; Stuart, 1960), describing the transition from noisy oscillations to sustained oscillations (Kuznetsov, 2004), and is given, in the complex plane, as:

$$\frac{d\mathbf{z}}{dt} = (\mathbf{a} + i\boldsymbol{\omega}) \odot \mathbf{z} - (\mathbf{z} \odot \bar{\mathbf{z}})\mathbf{z} + \beta\boldsymbol{\mu}(t), \tag{2.7}$$

where $\odot$ is the Hadamard element-wise product, $\boldsymbol{z} = [z_1, ..., z_N]$ are the complex-valued state variables of each node, $\bar{\boldsymbol{z}}$ is the complex conjugate of $\boldsymbol{z}$, $\mathbf{a} = [a_1, ..., a_N]$ and $\boldsymbol{\omega} = [\omega_1, ..., \omega_N]$ are the vectors containing the bifurcation parameters and intrinsic frequencies of each node in the range of 0.04-0.07 Hz band, respectively, and $\boldsymbol{\mu} = [\mu_1, ..., \mu_N]$ is a Gaussian noise vector with standard deviation $\beta = 0.02$ based on previous studies (Deco et al., 2017a; Saenger et al., 2017; Jobst et al., 2017). The intrinsic frequencies were estimated from the averaged peak frequency of the narrowband empirical BOLD signals of each brain region. For $a_j < 0$, the local dynamics present a stable spiral point, producing damped or noisy oscillations in absence or presence of noise, respectively. For $a_j > 0$, the spiral becomes unstable and a stable limit cycle oscillation appears, producing autonomous oscillations with frequency $2\pi f_j = w_j$. The BOLD

fluctuations were modelled by the real part of the state variables, i.e. Real(z_j).

The whole-brain dynamics were obtained by coupling the local dynamics through the C_{ij} matrix:

$$\frac{dz_j}{dt} = z_j[(a_j + i\omega_j) - |z_j|^2] + g\sum_{k=1}^{N} C_{jk}(z_k - z_j) + \beta\mu_j(t), \qquad (2.8)$$

where g represents a global coupling scaling the structural connectivity C_{ij}.The matrix C_{ij} is scaled to a maximum value of 0.2 to prevent full synchronization of the model. Interactions were modelled using the common difference coupling, which approximates the simplest (linear) part of a general coupling function (Pikovsky et al., 2002).

Homogeneous model: Fitting the global coupling g

To create a representative model of BOLD activity in each brain state, we adjusted the model parameters (g and a_j) to fit the spatiotemporal BOLD dynamics for each brain state and each dataset. Our first aim was to describe the global properties of the spatiotemporal dynamics of each subject in each state, independently of the variations in the dynamics of local nodes. For that reason, in this first approach to the model, all nodes were set to $a_j = 0$, called the homogeneous model. The global coupling parameter g was obtained by fitting the simulated and empirical data. Specifically, for each value of g, the model FCD was computed and compared with the empirical FCD using the Kolmogorov-Smirnov (KS) distance between the simulated and empirical distribution of the FCD elements. The KS-distance quantifies the maximal difference between the cumulative distribution functions of the two samples. Thus, the optimal value of g was the one that minimized the KS distance.

Heterogeneous model: Local optimization of the bifurcation parameters

To evaluate the heterogeneous local dynamics on the network's dynamics, we extended the model to allow differences in bifurcation parameters a_j for different ROIs. The g parameter was the one estimated with the homogeneous model. The bifurcation parameters were optimized based on the empirical power spectral density of the BOLD signals in each node. Specifically, we fitted the proportion of power in the 0.04-0.07 Hz band with respect to the 0.04-0.25 Hz band (i.e. we removed the smallest frequencies below 0.04 Hz and considered the whole spectrum up to the Nyquist frequency which is 0.25Hz) (Saenger et al., 2017). For this, the BOLD signals were filtered in the 0.04-0.25 Hz band and the power spectrum $PS_j(f)$ was calculated for each node j. We then defined the proportion of power in the 0.04-0.07 Hz band as:

$$p_j = \frac{\int_{0.04}^{0.07} PS_j(f)df}{\int_{0.04}^{0.25} PS_j(f)df} \tag{2.9}$$

We updated the local bifurcation parameters by an iterative gradient descendent strategy, i.e.:

$$a_j^{new} = a_j^{old} + \eta(p_j^{emp} - p_j^{sim}), \tag{2.10}$$

until convergence. η was set to 0.1 and the updates of the a_j values were done in each optimization step in parallel.

Relation between the strength of a node and its dynamics

Finally, the relation between local and network dynamics was studied. An effective bifurcation parameter a_j^{eff} was defined which contains information of the local dynamics and local structure given by its strength. This parameter permits to extract the relation between the dynamics and structure of each node. Note that the effective bifurcation parameter refers to the perturbed local dynamics including network effects (not to

be confused with *effective* connectivity). More specifically, in equation 2.6, we separated the part that relates to the effective local dynamics and the part that relates to the interaction between nodes. Noting that $\sum_{k=1}^{N} C_{jk}(z_k - z_j) = \sum_{k=1}^{N} C_{jk} z_k - z_j \sum_{k=1}^{N} C_{jk}$, equation 2.6 can be written as:

$$\frac{dz_j}{dt} = (a_j - g\sum_{k=1}^{N} C_{jk} + i\omega_j)z_j - z_j|z_j|^2 + g\sum_{k=1}^{N} C_{jk} z_k + \beta\mu_j(t). \quad (2.11)$$

Taking $a_j^{eff} = a_j - g\sum_{k=1}^{N} C_{jk}$, we get:

$$\frac{dz_j}{dt} = (a_j^{eff} + i\omega_j)z_j - z_j|z_j|^2 + g\sum_{k=1}^{N} C_{jk} z_k + \beta\mu_j(t). \quad (2.12)$$

Note that, if a_j is homogeneous across the network ($a_j = a$ for all j), a_j^{eff} is linearly related to the nodal strength $S_j = \sum_{k=1}^{N} C_{jk}$.

2.2.10. Linear stability analysis

In this section we studied the linear stability of the whole-brain network. The model consists of 214 coupled brain regions, with local Hopf dynamics, coupled through the connectivity matrix $\mathbf{C}$. The dynamical system presented in equation 2.5 and considering the coupling to the structural connectivity can be written in vector form as:

$$\frac{d\mathbf{z}}{dt} = (\mathbf{a} - g\mathbf{S} + i\boldsymbol{\omega}) \odot \mathbf{z} - (\mathbf{z} \odot \bar{\mathbf{z}})\mathbf{z} + g\mathbf{C}\mathbf{z} + \beta\boldsymbol{\mu}(t), \quad (2.13)$$

where $\boldsymbol{S} = [S_1, ..., S_N]$ is the vector containing the strength of each node, i.e. $S_j = \sum_{k=1}^{N} C_{jk}$. The model parameters $\mathbf{a}$ and $\boldsymbol{\omega}$ were estimated from the data, using the heterogeneous model, and g, using the homogeneous model, for each experimental condition.

We studied the linear stability of the fixed point $\boldsymbol{z} = \mathbf{0}$, which is solution of $\frac{d\boldsymbol{z}}{dt} = 0$. In the linearized system the quadratic terms (i.e. $\boldsymbol{z} \odot \bar{\boldsymbol{z}}$) are

not taken into account and the evolution of fluctuations $\delta \boldsymbol{z}$ around $\boldsymbol{z} = \mathbf{0}$ can be approximated as:

$$\frac{d}{dt}\delta \mathbf{z} = \mathbf{A}\delta \mathbf{z} + \beta \boldsymbol{\mu}(t), \tag{2.14}$$

where $\mathbf{A}$ is the Jacobi matrix, given as: $\mathbf{A} = \mathrm{diag}(\mathbf{a} - g\mathbf{S} + i\boldsymbol{\omega}) + g\mathbf{C}$, and $\mathrm{diag}(\boldsymbol{x})$ is the diagonal matrix whose entries are the elements of the vector $\boldsymbol{x}$.

2.2.11. Graph analysis of the structural connectivity

The network organization of the SC matrices was investigated using measures of graph theory (GAlib: Graph Analysis library in Python / Numpy, `www.github.com/gorkazl/pyGAlib`). We focused only on the potential presence of hub regions and a rich-club to relate these structural features to the observed dynamical properties of the brain regions. Given a connectivity matrix C with entries C_{jk} indicating the weight of the link between nodes j and k, the strength of a node (S_j) is defined as the sum of the connections it makes: $S_j = \sum_1^N C_j k$. A rich club is a supra-structure of a network happening when (i) a network contains hubs and (ii) those hubs are densely interconnected with each other, forming a cluster (Zhou and Mondragón, 2004). Identifying the presence of a rich-club typically implies the evaluation of k-density, $\rho(k)$, an iterative process which evaluates the density $\rho(k')$ of the remaining part of network after all nodes with degree $k < k'$ have been removed (Zhou and Mondragón, 2004). Here, we employed the version of the metric adapted for weighted networks, iterating from node strength $S' = 0$ to $S' = S_{max} = 10$ in steps of $\Delta S = 0.2$. At each iteration step, the average link weight $\rho(S')$ between the nodes with strength $S > S'$ was computed.

2.2.12. Statistical analysis

Statistical differences between levels of consciousness were assessed using one-way repeated measures (rm) ANOVA followed by multiple comparisons using False Discovery Rate (FDR) correction (Benjamini and Hochberg, 1995). The threshold for statistical significance was set to p-values$<$0.05. Wilcoxon rank-sum test (equivalent to a Mann-Whitney U

test) was applied in order to find region-wise differences between CNT and DOC patients in the strength of the SC. We corrected for multiple comparisons by using the FDR correction, considering $P<0.05$ as statistically significant.

2.3. Results

We performed both data- and model-driven analyses to compare different levels of consciousness in two neuroimaging datasets comprising DOC and healthy subjects under propofol sedation. The first dataset consisted of fMRI signals and diffusion-MRI based structural connectivities (SC) from healthy subjects during conscious wakefulness (n =35), and MCS and UWS patients (n = 33 and n = 15, respectively). The analysis was complemented with an additional fMRI dataset from 16 healthy controls scanned during conscious wakefulness (W), sedation (S) and recovery from it (R).

2.3.1. Decreased brain phase dynamics complexity in low-level states of consciousness

The first step in our analysis consisted of searching for spatiotemporal signatures of loss of consciousness from the whole-brain dynamics, as measured by the blood-oxygen-level-dependent (BOLD) signals, Figure 2.1A. For this, we calculated the time-evolving functional connectivity based on the degree of synchrony between the signals. The instantaneous phases of the BOLD were extracted in the 0.04-0.07 Hz frequency band (Glerean et al., 2012; Damoiseaux et al., 2006; Ponce-Alvarez et al., 2015) using the Hilbert transform, Figure 2.1B-C. The phase-interaction matrix $P(t)$ was then defined as the pairwise phase differences between all regions of interest (ROIs), Figure 2.1D. A $P(t)$ matrix is defined at every time point t, thus allowing us to define functional connectivity at the same temporal resolution as the BOLD. A variety of spatiotemporal properties were then quantified from the phase-interaction matrices.

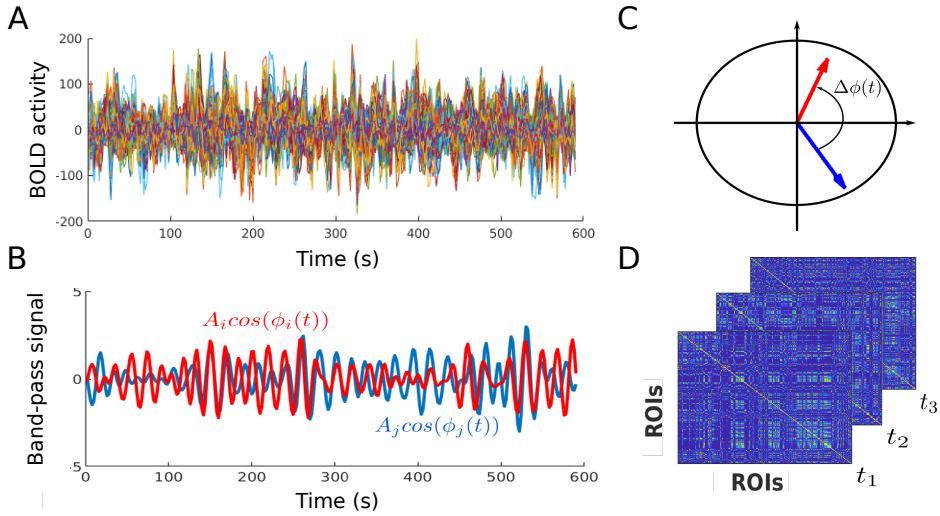

Figure 2.1: **Extraction of the instantaneous phases as the basis for the phase-synchronization analysis. A)** BOLD timeseries of all the regions . **B)** BOLD band-pass signals (0.04-0.07 Hz) for two samples ROIs. The instantaneous phases, $\phi_j(t)$ and $\phi_k(t)$, of each signal were computed using the Hilbert transform. **C)** At each time frame, the interaction between ROIs was given by the instantaneous phase difference, $\Delta\phi_{jk}(t) = |\phi_j(t) - \phi_k(t)|$, which can be represented as vectors in the unit circle of the complex plane. **D)** Phase-interaction matrices $P_{jk}(t)$ were calculated as the cosine of the phase difference, $\cos(\Delta\phi_{jk}(t))$, at time t. All global measures used afterwards were based on the phase-interaction matrices.

We first examined the spatial properties of the phase-interaction matrices. To estimate the level of specialization and coordination in the network, we used measures of integration and segregation. The level of integration – cohesiveness in the network – was calculated by hierarchically scanning through the formation of connected components in the time-averaged phase-interaction matrix $\langle P \rangle$ (Deco et al., 2015a; Deco and Kringelbach, 2017; Deco et al., 2018a; Adhikari et al., 2017) (see Methods). To quantify segregation, we applied community detection methods on the matrix $\langle P \rangle$ to detect functional clusters of ROIs (Rubinov and Sporns, 2011). The quality of a partition of ROIs into clusters is evaluated by the modularity function (see Methods). A large modularity implies that ROIs are divided into well-defined clusters, indicating strong segregation. On one hand, we found that the average integration across time was significantly lower for

MCS and UWS, compared to CNT, for S and R compared to W, and for S compared to R (Figure 2.2A, see table 2.1 for statistics). On the other hand, we found that the average segregation was significantly stronger for UWS compared to CNT, and for S compared to W (Figure 2.2B, see table 2.1 for statistics). Thus, low-level states of consciousness were characterised by a decrease of integration and an increase of segregation.

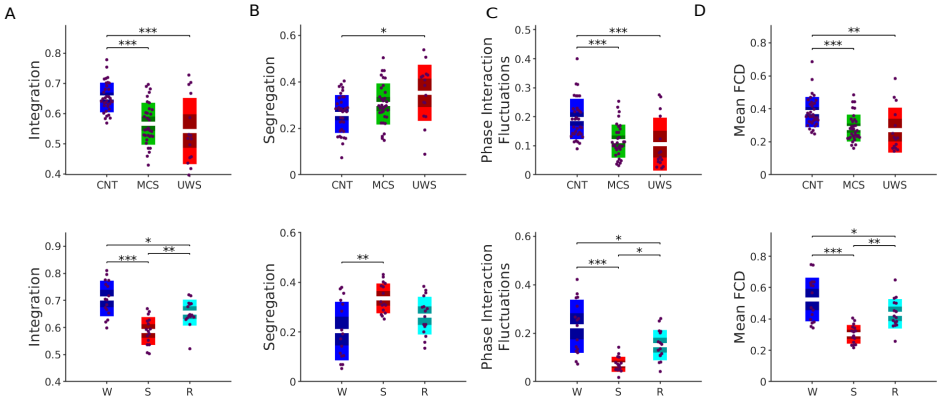

Figure 2.2: **Changes in global properties of phase-dynamics induced by loss of consciousness. A-B)** The structure of phase interactions was described in terms of the integration and the segregation of the time-averaged phase interaction matrix (see Methods). **C)** We quantified the temporal fluctuations of the mean phase synchrony (i.e. the average over ROIs of matrix $P(t)$) through its temporal standard deviation. **D)** To detect the existence of recurrent synchronization patterns, we computed the FCD comparing phase-interaction matrices at different time (see Methods). Briefly, the FCD represents the (cosine) similarities between phase-interaction matrices at times t and t' for all possible pairs (t, t'). The panel shows the average similarity for each experimental condition. In panels d-g, each dot represents a participant and the boxes represent the measure's distribution. Boxplots represent the mean of the measures' values with a 95% confidence interval (dark) and 1 SD (light). Differences between groups were assessed using one-way ANOVA followed by FDR p-value correction. *: $p < 0.05$; **: $p < 0.01$; ***: $p < 0.001$ (see Table 2.1 for details).

Second, we evaluated the temporal fluctuations of the mean phase-interaction. For this, at each time t, we computed the phase interaction averaged over ROIs, i.e. $r(t)$, see Methods. The standard deviation of $r(t)$ provides an estimate of how much the average synchronization fluctuates in time. We found a significant reduction of phase-interaction fluctuations in low-level

states of consciousness compared to conscious states (Figure 2.2C; see also Table 2.1 for statistics), i.e. indicating that synchronization patterns in low-level states of consciousness fluctuate less than in conscious states.

DOC Datasets	Integration	Segregation	Phase Interaction Fluctuations	Mean FCD
CNT	0.65± 0.01	0.26 ± 0.01	0.19 ± 0.01	0.38 ± 0.02
MCS	0.56 ±0.01	0.31 ± 0.01	0.12 ± 0.01	0.28± 0.02
UWS	0.54 ± 0.03	0.35 ± 0.03	0.11± 0.02	0.27 ± 0.03
ANOVA	$p < 0.001$ $F_{2,80} = 18.51$	p=0.006 $F_{2,80} = 5.21$	$p < 0.001$ $F_{2,80} = 13.39$	$p < 0.001$ $F_{2,80} = 10.90$
Multiple Comparisons				
$p_{CNT-MCS}$	< 0.001	0.207	< 0.001	0.014
$p_{CNT-UWS}$	< 0.001	0.016	< 0.001	0.023
$p_{MCS-UWS}$	0.241	0.223	0.882	0.594
Propofol Anesthesia Datasets	Integration	Segregation	Phase Interaction Fluctuations	Mean FCD
W	0.71 ±0.02	0.20 ± 0.03	0.23 ± 0.03	0.52 ± 0.04
S	0.59 ±0.01	0.34 ± 0.02	0.07 ± 0.01	0.30 ± 0.01
R	0.65 ±0.01	0.27 ± 0.02	0.15 ± 0.02	0.43 ± 0.02
ANOVA	$p < 0.001$ $F_{2,45} = 18.80$	$p < 0.001$ $F_{2,45} = 8.93$	$p < 0.001$ $F_{2,45} = 17.46$	$p < 0.001$ $F_{2,45} = 18.80$
Multiple Comparisons				
p_{W-S}	< 0.001	0.001	< 0.001	< 0.001
p_{W-R}	0.029	0.126	0.014	0.041
p_{S-R}	0.006	0.115	0.014	0.004

Table 2.1: **Results of the mean values of the global measurements for each group and statistics.** The table shows the mean values and standard error of the empirical measures of integration, segregation, phase interaction fluctuations and mean FCD. Group comparison statistics were computed with a one-way ANOVA, followed by FDR correction (adjusted p-values are shown).

Temporal fluctuations of the average phase-interaction matrix indicate excursions of the total level of synchrony over time but, alone, they do not capture the presence of connectivity patterns which re-occur over time. Therefore, we next evaluated the temporal recurrence of the phase-interaction matrices, referred as functional connectivity dynamics (FCD, see Methods), that describes how recurrent in time the synchronization patterns were. Briefly, this method computes the phase-interaction matrices averaged over sliding time windows and measures the similarity across all pairs of time windows, which is summarized in the FCD matrix. We found that low-level states of consciousness presented a significantly lower

average FCD than in normal wakefulness (Figure 2.2D; see also table 2.1 for statistics). This suggests that the phase synchronization patterns were less recurrent in time for low-level states of consciousness.

Altogether, the above results show that, in both pathological and pharmacological low-level states of consciousness, the patterns of phase-synchronization were less connected, more segregated and less recurrent in time than in healthy conscious states.

2.3.2. Decreased global coupling in low-level states of consciousness

To gain insights into the possible mechanisms underlying the changes in functional connectivity reported in the previous sections, we used a computational model to describe the whole-brain dynamics. In this model, brain regions were modeled as oscillators, allowing the study of phase-synchronization patterns. Specifically, the local dynamics of individual brain regions were modeled by noisy Stuart-Landau oscillators, see Eqs. (2.5) and (2.6) in Methods. This model captures the so-called Hopf bifurcation, a transition from noisy to oscillatory signals by the variation of a single parameter, and it has shown to fit the resting-state BOLD dynamics quite accurately (Deco et al., 2017a). In this case, the bifurcation parameter is the parameter a_j, representing the decay or growth rate of the system and thus controlling its stability. When $a_j < 0$, ROIs produce noisy signals, see Figure 2.3A, and when $a_j > 0$ their signals become sustained oscillations, see Figure 2.3B.

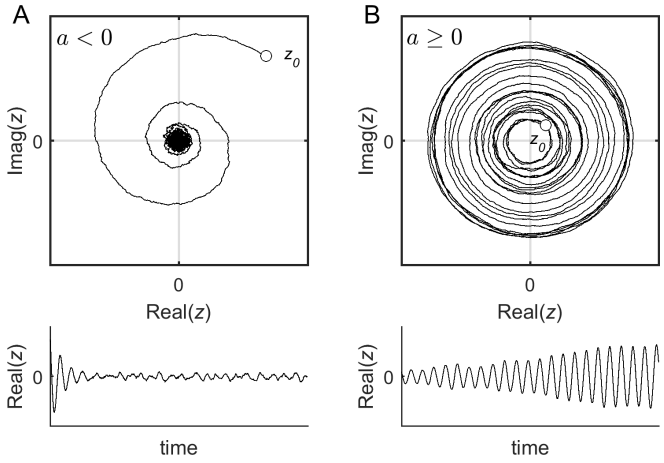

Figure 2.3: **Phase space for an example of a single Hopf oscillator. A)** Subcritical Hopf oscillator ($a < 0$). Top: In this regime, a stable spiral, or focus, exists at $\boldsymbol{z} = 0$. The system relaxes towards the focus with damped oscillations. In the presence of noise, however, the system fluctuates around the focus, thus producing noise-induced oscillations. $\boldsymbol{z_0} = \boldsymbol{z}(t = 0)$ indicates the initial condition. Bottom: temporal evolution of $Real(z)$. **B)** Supercritical Hopf bifurcation ($a \geq 0$). Top: In this regime, the focus at $\boldsymbol{z} = 0$ becomes unstable and a stable limit-cycle appears, thus producing autonomous or self-sustained oscillations. Bottom: temporal evolution of $Real(z)$.

At the transition, when $a_j \sim 0$, ROIs display flexible noisy oscillations of low amplitude, a regime in which ROIs are most susceptible to the inputs from other ROIs. The natural frequency of oscillations for each ROI was estimated from the peak of the power spectra estimated from their BOLD in the frequency band 0.04-0.07 Hz. Then, the $N = 214$ brain regions were coupled through the connectivity matrix C_{jk}, which is given by the structural connectivity of healthy subjects. The brain regions were defined according to the Shen atlas, ignoring the cerebellum (Shen et al., 2013). The matrix C_{jk} was scaled by a global coupling g. Thus, the large-scale network was weakly or strongly connected for small or large values of g, respectively (Figure 2.4a). In summary, at this level of description the network dynamics depended on three ingredients: the local parameters for each node (a_j), the global strength of connections (g) and the network's structure (C_{jk}).

First, we studied the network dynamics for the homogeneous case, in which we set $a_j = 0$ for all nodes. This choice was based on previous studies which suggest that the best fit to the empirical data arises at the brink of the Hopf bifurcation where $a \sim 0$ (Deco et al., 2017a). In this case, the network dynamics were determined by a single free parameter: the global coupling strength g. This parameter was estimated by fitting the FCDs from the empirical data with the FCDs calculated from the simulated signals at various values of g (Deco et al., 2017a; Saenger et al., 2017). Specifically, empirical and simulated FCDs were compared using the Kolmogorov-Smirnov distance of their values (KS-distance, Figure 2.4b).

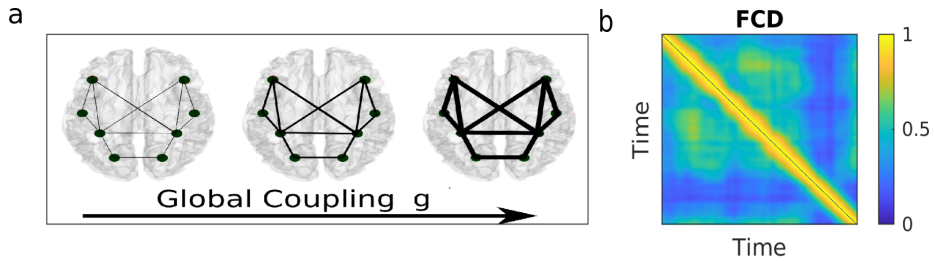

Figure 2.4: **Fitting of global coupling parameter in the whole-brain network model. a)** The global coupling model parameter g scales the weights of the SC matrix. Low and high values of g represent weakly and strongly coupled networks, respectively. **b)** To estimate this global parameter, we sought for the model that best reproduced the distribution of FCD values (fixing all other model parameters).

For low and high values of g, large KS distance indicates differences between the mean values of the FCD distributions. In the intermediate range of g shorter KS distance evidenced a closer similarity between the empirical and the simulated FCDs. We considered the g where KS distance is minimised as the optimal working point of the model (Deco et al., 2017a; Saenger et al., 2017; Padilla et al., 2019). Notably, although the fit of the model was based on the FCD, the models also maximized the fit of other data statistics including Pearson correlation matrix (Figure 2.5).

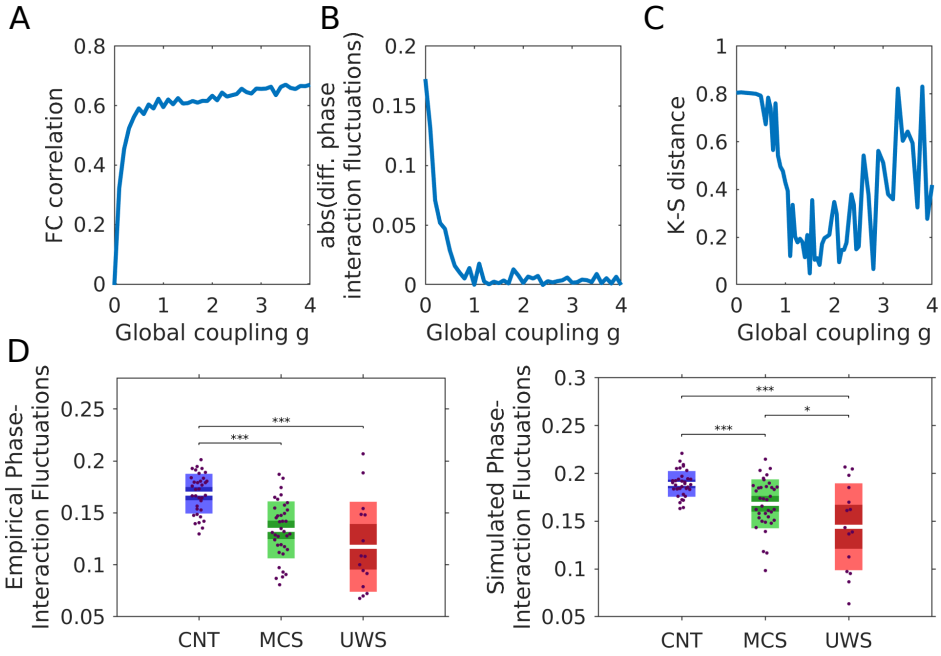

Figure 2.5: **Goodness of fit of the whole-brain computational model computed by using different measures. A)**Pearson correlation between the empirical and simulated functional connectivity (FC) matrices as a function of parameter g. **B)** Absolute difference between the empirical and simulated phase-interaction fluctuations as a function of g. **C)** Kolmogorov-Smirnov distance between the empirical and simulated FCD distributions. **D)** The optimal value of g was obtained using the KS-distance between the empirical and simulated FCD distributions. We verified that, for the obtained values of g in each condition, the differences in the phase interaction fluctuations observed in the data were preserved in the model. For this we used the SC matrix of individual subjects and the parameter g was fixed for each group. Boxplots represent the mean of the measures' values with a 95% confidence interval (dark) and 1 SD (light). Differences between groups were assessed using one-way ANOVA followed by FDR p-value correction. *: $p < 0.05$; **: $p < 0.01$; ***: $p < 0.001$.

We found that the optimal value of g was smaller for states of low-level states of consciousness than for conscious wakefulness (Figure 2.6, see also table 2.2).

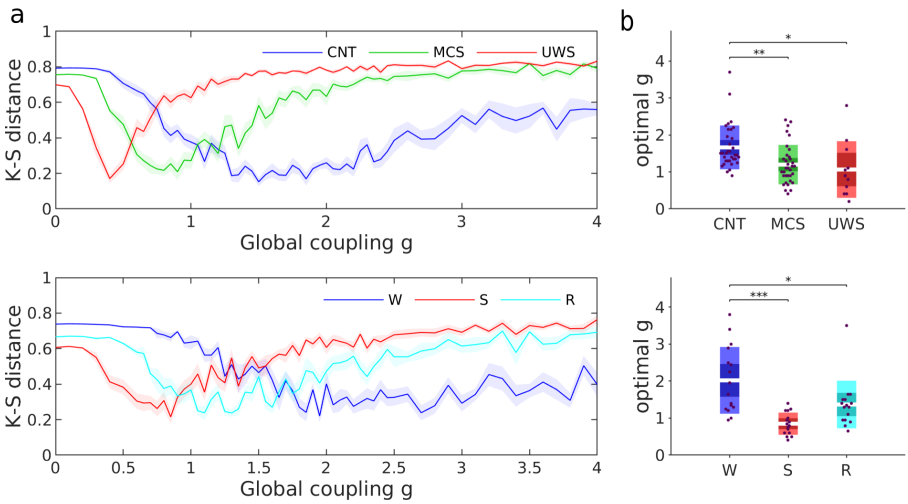

Figure 2.6: **Fitting of global coupling parameter in the whole-brain network model. a)** KS-distance between the empirical and the model FCD distributions, as a function of g, for one participant of each subject group (top: healthy controls and DOC patients; bottom: awake and sedated subjects). Solid lines and shaded areas represent the mean and the standard error of the fitting curves over simulation trials. **b)** Optimal global coupling g for all participants. In each panel, each dot represents a participant and the boxes represent the distribution of g. Boxplots represent the mean of the measures' values with a 95% confidence interval (dark) and 1 SD (light). Differences between groups were assessed using one-way ANOVA followed by FDR p-value correction. *: $p < 0.05$; **: $p < 0.01$; ***: $p < 0.001$. In panels c and d, we used the healthy structural connectome as the underlying connectivity of all models.

Conditions	**CNT**	**MCS**	**UWS**	**W**	**S**	**R**
Global coupling g	1.7 ± 0.1	1.2 ± 0.1	0.8 ± 0.2	2.0 ± 0.2	0.9 ± 0.1	1.4 ± 0.2

Table 2.2: Estimated global couplings for all experimental conditions. p-values: $p_{CNT-MCS} = 0.015$, $p_{CNT-UWS} = 0.019$, $p_{MCS-UWS} = 0.7984$; $p_{W-S} < 0.001$, $p_{W-R} = 0.031$, $p_{R-S} = 0.080$.

This is consistent with the observation reported in the previous section that the correlation between structural and Pearson functional connectivity increases in states of low-level states of consciousness (Figure 2.7). The global coupling g is a scaling parameter that controls for the conductivity of the fibers given by the SC. At low g the network interactions are

mainly restricted to ROIs directly connected by high strength links. Thus, increasing the global coupling favours the propagation of recurrent activity within the network allowing for correlations to emerge between nodes that are not directly connected with each other via structural connections. These results showed that in low-level states of consciousness, the brain dynamics were more constrained by the pairwise structural connections while in conscious awake – characterised by stronger levels of g – brain dynamics decouple from the purely direct anatomical constraints.

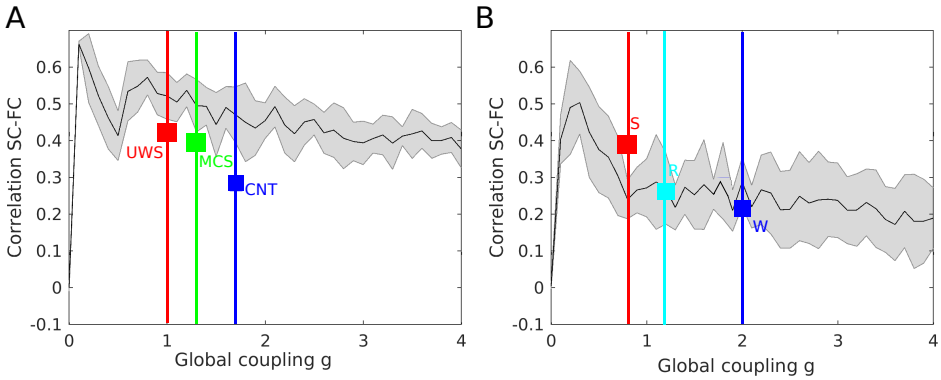

Figure 2.7: **Empirical and model correlations between the SC and FC matrices for each group.** In **A)** and **B)** the black line corresponds to the correlation between the empirical SC and the FC simulated with the whole-brain model learned from the different experimental groups, as a function of g. The shaded area corresponds to the standard error of the values obtained for different simulations. The curve shows a peak for small g and then it decreases slowly as g increases. In **A)** the lines are located in the corresponding optimal global coupling g for each brain state. In **B)** the lines correspond to the states for the propofol anesthesia dataset. For all cases, the values correspond to the optimal g extracted from the homogeneous model (depicted in Figure 2.4). In **A)** and **B)** the squares correspond to the empirical values of the empirical SC and FC correlation. Both empirically and using the model, we observed a shift to smaller values in the SC-FC correlation while the level of consciousness decreases.

2.3.3. Loss of regional heterogeneity in low-level states of consciousness

We next asked whether we can obtain additional information by relaxing the homogeneity constraint on the local bifurcation parameters. In this

case, the global coupling parameters g were fixed to the ones estimated in the previous section – the homogeneous model in which all $a_j = 0$ – but the local parameters a_j were allowed to vary, thus introducing heterogeneity in the working point of the ROIs. The individual a_j were estimated from the data using a gradient descent method (see Methods).

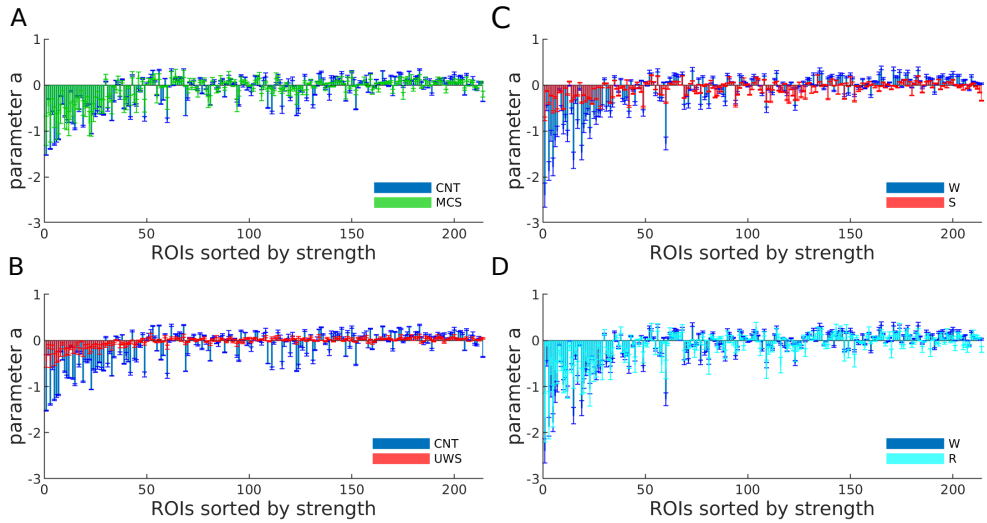

Figure 2.8: **Local bifurcation parameters of the whole-brain model. a-d** Estimated bifurcation model parameters a for each of the 214 nodes (sorted by node strength). Bars indicate the mean ± standard deviations across simulation trials. Results for low-level states of consciousness (MCS and UWS) are compared against the healthy controls in a and b. Results for anesthesia and recovery (S and R states) are compared to the initial awake state (W) in c and d respectively.

We compared the resulting bifurcation parameters across nodes within and across groups. We found that bifurcation parameters in normal wakefulness (CNT and W groups) tended to be more negative as compared to those in low-level states of consciousness, Figure 2.8a-d. This implies that the behaviour of ROIs in normal wakefulness are characterised by noisy oscillations – that are more stable – than their corresponding behaviour in low-level states of consciousness. This was especially the case for the dynamics of the structural hub ROIs, i.e. the nodes with the highest val-

ues of SC strength, which showed strong negative values of a_j in normal wakefulness, Figure 2.8A-D. Notice that in Figure 2.8 ROIs are sorted by their SC strength in descending order. Comparing normal wakefulness (W) before and after sedation (recovery, R), both cases showed a similar distribution of a_j. In particular, the negativity of a_j was reestablished for hubs in the recovery stage (Figure 2.8C-D). We note that the resulting distribution of a_j contributed to network collective dynamics, since shuffling the values of a across brain regions lead to worse fits of the network statistics, Figure 2.9.

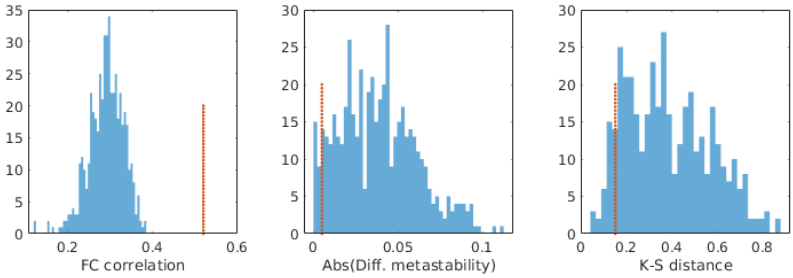

Figure 2.9: **Goodness of fit of the heterogeneous model compared to models shuffling the order of the a's.** Goodness of fit for the Pearson correlation of the FC matrices, the absolute difference in phase-interaction fluctuations and the Kolmogorv-Smirnov distance between the FCD matrices. The blue histograms correspond to the fitting after shuffling the labels of the a_i values and the red line corresponds to the mean fitting of the heterogeneous model.

To identify the regions with the largest alterations in the local dynamical properties, we computed the absolute difference in local parameters, i.e. Δa, between patients and controls and between sedation/recovery and wakefulness (Figure 2.10a). The largest differences in local parameters between controls and MCS/UWS patients were found in subcortical regions (thalamus, caudate, hippocampus and amygdala) and in some cortical regions (calcarine, insula, fusiform, frontal superior orbital, precuneus, cingulum, and temporal areas), see Figure 2.10b top left. When comparing the local parameters between wakefulness and sedation, the regions with largest differences included subcortical regions (thalamus, caudate, hippocampus, parahippocampal and putamen), and cortical regions (cingulum, insula, some frontal regions, paracentral and precentral), Figure

2.10b top right. The main differences between wakefulness and recovery were found in the hippocampus, the cingulum and the precuneus, Figure 2.10b bottom right. Interesting, Δa and the connectivity strength of the brain regions significantly correlated (correlation: $0.40 - 0.94, p < 0.001$, Figure 2.10c), indicating that the regions with the largest difference in the local bifurcation parameters were mostly the hubs.

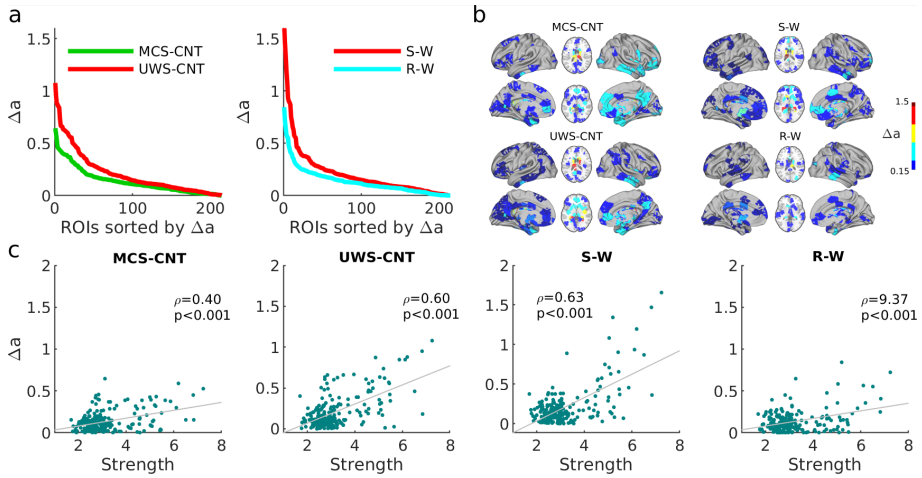

Figure 2.10: **Differences between groups in the optimized bifurcation parameters. a** Ranked absolute parameter difference, Δa, for all the comparisons. **b** Spatial distribution of $\Delta a > 0.15$ in the brain for each of the group comparisons. **c** Relationship between the absolute difference Δa and the strength of each node. The absolute difference of the parameter a values between different groups in function of the strength of the nodes extracted from the SC of the healthy controls. ρ corresponds to the Pearson correlation.

Furthermore, we investigated the role of the regional dynamics in the stability of the system. For this, we studied the linear stability of the system by decomposing the Jacobi matrix $\mathbf{A}$ into eigenvectors (see Methods). Figure 2.11 shows the eigenvectors of $\mathbf{A}$ as a function of the node structural strengths and the real part of the eigenvalues associated to the eigenvectors, Real(λ). Since the system is stable, Real(λ) < 0 for all eigenvalues. Clearly, the network hubs contribute the most to the most

stable eigenvectors, i.e. those with lowest Real(λ). This indicates that the hubs are key nodes to stabilize the system. Moreover, the stability of these dominant eigenvectors was reduced for models estimated from data corresponding to low-level states of consciousness, see Figure 2.11. Thus, these results showed that the hubs lost their stabilizing role in low-level states of consciousness.

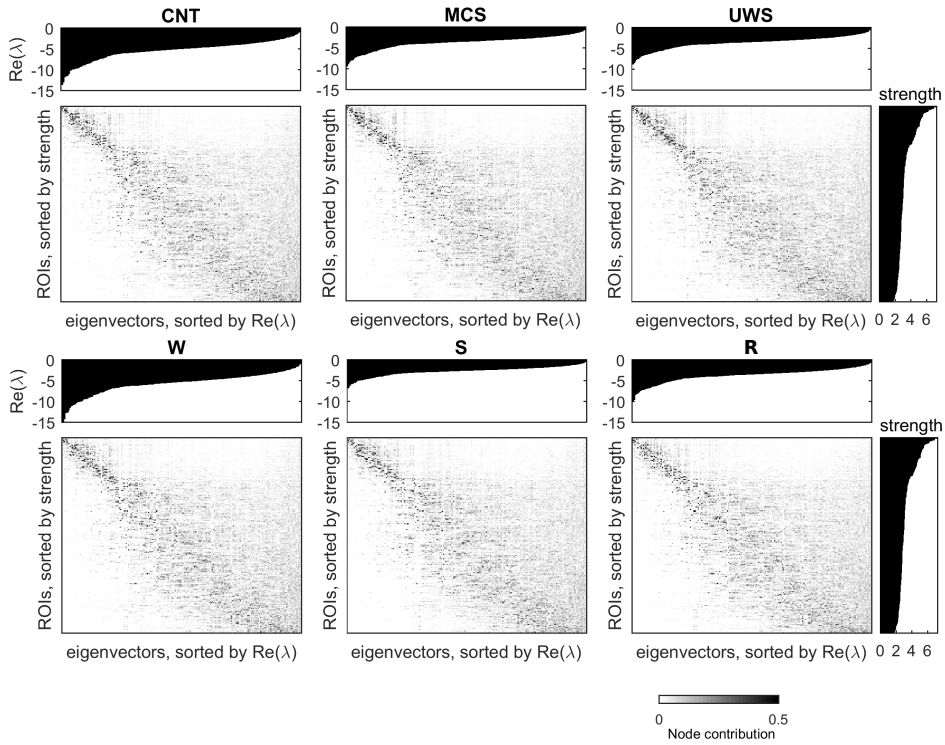

Figure 2.11: **Eigendecomposition of the Jacobi matrix.** The eigenvectors of the Jacobi matrix (N-dimensional vectors) were sorted according to the real part of the associated eigenvalues (top insets), Real(λ), and the strength of the nodes (right insets).

2.3.4. Disentangling regional and network effects

When observing the temporal activity of a brain region, as we do here via their BOLD signals, this activity is representative of the behaviour of the ROI embedded in the whole-brain network. In other words, we do not

have access to the intrinsic activity of brain regions in isolation, as if they were separated from the rest of the network. Therefore, all ROI-specific parameters we estimated are necessarily affected by the network interactions. For example, the local bifurcation parameters presented in Figure 2.8 incorporate effects coming both from the local dynamics and originated from the network interactions. In the following, we used a strategy to disentangle the changes in local parameters due to network effects from those due to local modifications. This analysis provides information about the origin (local or network-related) of the different dynamics of the ROIs for the different states of consciousness.

We defined an *effective* local parameter that is composed of the bifurcation parameter (a_j) and the connectivity strength of each node ($S_j = \sum_k C_{jk}$), given as: $a_j^{eff} = a_j - gS_j$, (see Methods). For the family of homogeneous models ($a_j = const.$), the effective parameter is linearly related to the connectivity strength, while in the heterogeneous case deviations from this linear relation are to be expected. In other words, in the homogeneous case differences in effective local dynamics are fully explained by the network connections. In contrast, the heterogeneous model can produce additional diversity of local dynamics.

To disentangle the network effects from changes in local dynamics, we evaluated the deviations from the expected linear relation between effective local parameters and node strength in the different levels of consciousness. First, we estimated a_j^{eff} from the data in each brain state using gradient descent with fixed g for each condition (the values of g were those of Figure 2.6d). Note that, in this case, instead of estimating a_j, the method estimates directly a_j^{eff} (see Methods, Eq. 2.10). Next, we evaluated the linear regression deviation between a_j^{eff} and the strength of the nodes (Figure 2.12a-b). We found that the residuals of a linear regression were larger for control subjects and during healthy wakefulness than for DOC patients and sedation (Figure 2.12c, $p < 0.002$ for all comparisons in both datasets computed with a one-way-ANOVA, followed by FDR correction).

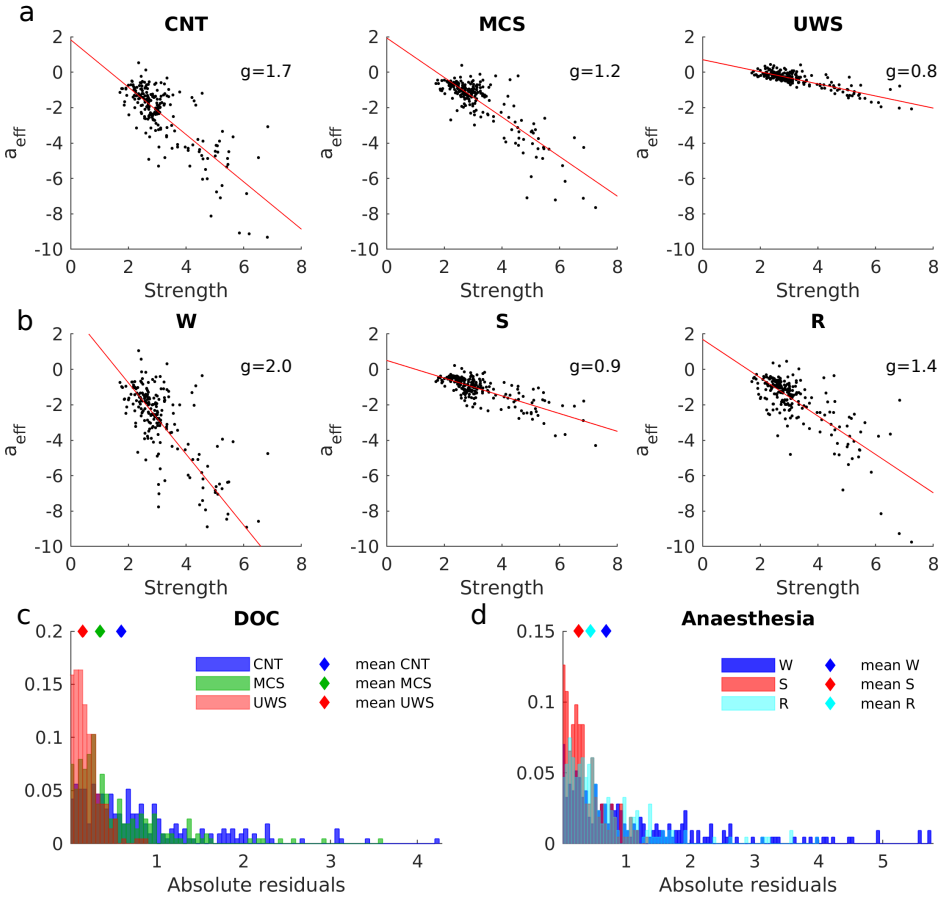

Figure 2.12: **Disentangling structurally- and dynamically-driven heterogeneity of local nodes. a-b)** The effective local bifurcation parameters, a_j^{eff}, were estimated using the heterogeneous model. In this model, the parameters a_j^{eff} were optimized, after fixing g to that obtained for the homogeneous model (see Methods). The obtained parameters were compared to the strengths of the nodes S_j, for healthy controls and DOC patients (a) and for awake and anesthetized conditions (b). In each panel, each dot represents one node. The red lines indicate the linear fits. **c)** Distribution of the absolute residuals of each node given by the squared difference between the value of a_j^{eff} and the estimated linear relationship between a_j^{eff} and S_j, for each group. **d)** Same as c) but for W, S and R states.

These results indicated that conscious states are associated with collective dynamics emerging from regional heterogeneity – variance in the working point of the ROIs. In contrast, low-level states of consciousness are associated with dynamics generated by a network of ROIs with homogeneous working points. In this case, the observed dynamical differences across ROIs are predominantly explained by differences in connectivity strength. These results provided additional evidence that dynamics in low-level states of consciousness are strongly constrained by structural connections.

2.3.5. Alteration of the structural core in DOC patients

In the previous section, we have shown that under conditions of loss of consciousness the dynamical heterogeneity of the ROIs is reduced and that these changes affect specially the ROIs with largest node strength (Figure 2.8a-d). In order to close the loop, our goal is now to investigate possible alterations in the structural connectivity of patients due to brain injuries that could cause the changes observed at the dynamic level. Therefore, we took a closer look at the hierarchical organization of the ROIs and their structural interconnections. We compare the strength of the ROIs – the sum of connection weights per node – to search for highly connected ROIs (hubs). Notice that the models performed in the previous sections were constrained using the structural connectivity of the healthy subjects. Using only the SCs of controls allowed comparing the optimal parameters of the model between groups and interpreting the alterations in the system.

The node strength across ROIs is heterogeneous in the control subjects with the strength of some ROIs notably standing out from the rest (Figure 2.13b, blue line). However, the strength of ROIs in DOC patients (Figure 2.13b, green and red lines) is rather homogeneous and no ROI stands out; implying that the presence of hubs is suppressed in DOC patients due to brain lesions. Regions with significantly decrease strength compared to controls ($p < 0.05$, Wilcoxon rank-sum test with FDR correction) in MCS patients include the thalamus, the posterior and the anterior cingulum, hippocampus, the frontal medial, motor areas, caudate, precuneus, insula and precentral, for MCS patients (Figure 2.13c left). In UWS patients, it

included the aforementioned regions plus the fusiform, the parahippocampal, the cuneus, the lingual and the temporal areas (Figure 2.13c right). Figure 2.13d shows the distribution of node strengths in the population average SCs for the three cases: control subjects (blue), MCS patients (green) and UWS patients (red). As seen, the presence of hub regions in the controls is characterised by a slow decay of the distribution at the higher end while the distributions for MCS and UWS patients rapidly decay. Hub regions with strength $S > 4.5$ in the controls are depicted in Figure 2.13e. They comprise the insula, thalamus, caudate, hippocampus, parahippocampal, calcarine, precuneus and cingulum mid.

Next, we examined the interconnections between the hub ROIs. A network is said to contain a rich-club if (i) it contains hubs and (ii) those hubs are densely interconnected among themselves forming a cluster. The presence of a rich-club is often regarded as the structural core that helps maintain the integration of cross-modular information, thus potentially facilitating consciousness (Tagliazucchi et al., 2016b; Demertzi et al., 2015; Amico et al., 2014). As already shown, the presence of hubs is disrupted in the DOC patients and thus according to the first condition, without hubs no rich-club can be formed. We confirmed the disruption of the rich-club in DOC patients in two manners. First, we computed the weighted k-density on the population average SCs. This metric evaluates the average link weight between the regions with node strength S larger than a given strength S', scanning for all values of strength from zero to S_{max}. For healthy controls, the weighted k-density growed monotonically evidencing that the larger the strength of the nodes, the stronger were the links between them (Figure 2.13f, blue curve). However, the lack of hubs in MCS and UWS patients led to an early cut-off of the k-density (green and red curves) evidencing the absence of a rich-club in these cases. Second, we compared the average link weight between the hub regions (previously selected from the SC of healthy controls as ROIs with $S > 4.5$) and non-hub regions, Figure 2.13g. Clearly, the SC hubs were connected by stronger links than non-hubs in the three cases, and those links were strongest in the SCs of healthy controls.

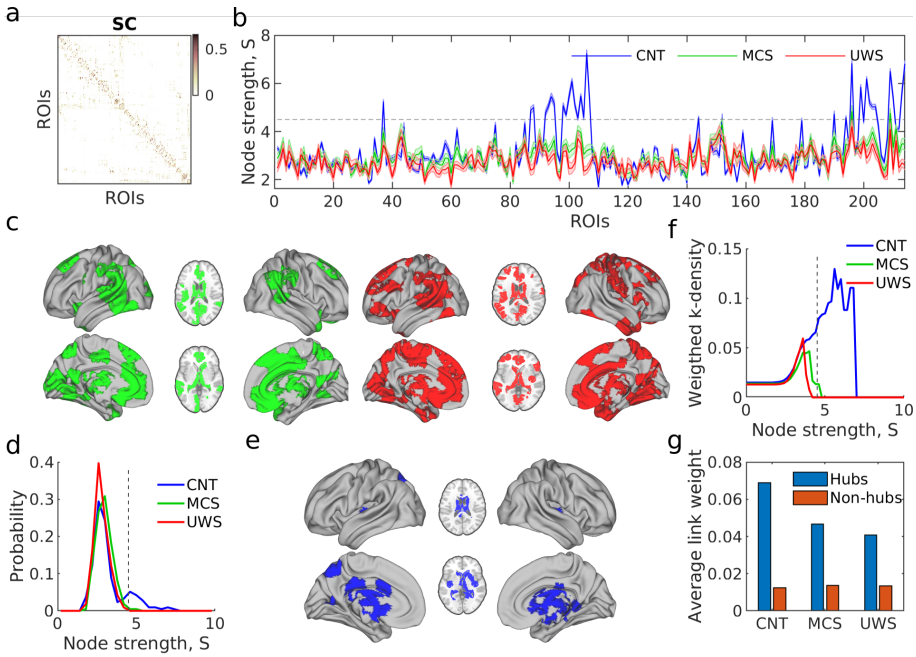

Figure 2.13: **Disruption of the structural connectivity in DOC patients.** **a** SC matrices were averaged over subjects for each clinical group (CNT, MCS, and UWS). **b** Average node strength of each node for each group. Shaded areas represent the standard error across subjects. The grey dashed line corresponds to the threshold, $S = 4.5$, which determines the hub regions. **c** ROIs with significant decrease of strength in patients as compared to controls (Wilcoxon rank-sum test, followed by FDR correction). Left (green): CNT-MCS comparison; Right (red): CNT-UWS comparison. **d** Distribution of the node strength in the population average SCs. The distribution in controls displays a longer tail corresponding to hub regions, depicted in **e**. **f** k-density curves – average weight of links between regions with strength $S > S_0$ – show the loss of a rich-club structure in MCS and UWS patients. **g** Average link weight between hubs (i.e. regions with $S > 4.5$) in yellow and the average link weight between non-hubs regions (i.e. $S < 4.5$) in violet.

Last, we remind that the whole-brain modelling performed in the previous sections were performed using the structural connectivity of the healthy subjects to constrain the model. We repeated the simulations for the cases of MCS and UWS patients using the injured connectomes from the patients. In these simulations, we did not find significant differences in the global coupling parameter g in comparison with the values identified before

(see Figure 2.14). This was due to the high inter-individual variability of the structural connectivities.

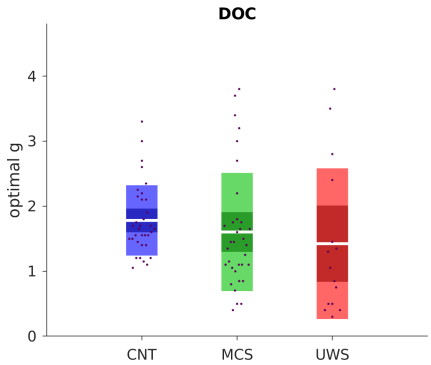

Figure 2.14: **Whole-brain model global coupling parameter fitting for the individual SC.** Optimal global coupling g for each of the subjects of the DOC dataset using the individual SC to set the interactions between model nodes. One-way-ANOVA p-value: $p_{CNT-MCS} = 0.665$, $p_{CNT-UWS} = 0.446$ and $p_{UWS-MCS} = 0.878$. Boxplots represent the mean of the measures' values with a 95% confidence interval (dark) and 1 SD (light).

Also, consistent with the results above, we found that the heterogeneity of local bifurcation parameters was reduced for the models corresponding to DOC patients (Figure 2.15). Moreover, the dynamically-based heterogeneity was significantly reduced as compared to the control case (Figure 2.15c), indicating that local parameters were strongly determined by structural connections. These effects were stronger using injured SCs than using the healthy SC for all conditions, implying that structural damage in patients causes a rather homogeneous dynamical behaviour across ROIs.

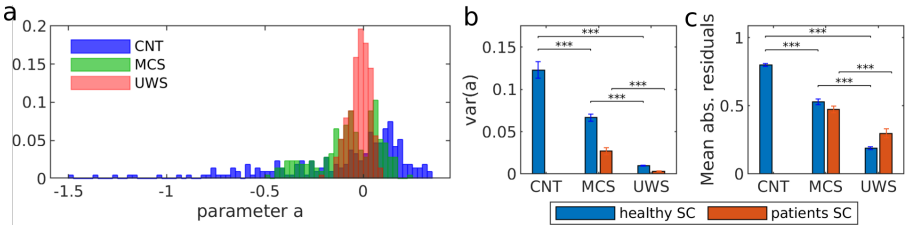

Figure 2.15: **Alteration in the model parameters when using the injured structural connectivities.** **a** Distribution of the estimated bifurcation parameters a_j using the average SC for each clinical group (healthy, MCS, and UWS). **b** The variance of the distribution of parameters a_j for each clinical group. **c** Median of the absolute residuals of the linear relationship between the a_{eff} vs strength. ***: p <0.001, Wilcoxon rank-sum test, followed by FDR correction.

2.4. Discussion

In the present study, we have analysed and modelled brain dynamics from patients with reduced consciousness due to brain damage (MCS and UWS), and from healthy participants under propofol-induced sedation. We have shown that reduction of consciousness is characterized by brain dynamics with less recurrent, less connected and more segregated patterns of phase-synchronization than for conscious states. Using whole-brain network models constrained upon healthy and injured structural connectivities, we could show that both pathological and pharmacological low-level states of consciousness present altered network interactions characterized by closer global resemblance between the phase synchronization patterns and the structural connectivity than in conscious wakefulness. Furthermore, low-level states of consciousness also manifest more homogeneous dynamical behaviour across regions. This effect was especially prominent in the structural hub regions – the most structurally connected ROIs – whose local dynamics shift towards unstable oscillatory regimes with a loss of their stability and disentangling from the constraints to the anatomy in low-level states of consciousness.

The whole-brain network model used here allows us to understand how structural, dynamical, local and network properties interplay in the different levels of consciousness. Within this model, the network dynamics

depend on three ingredients: (i) the global strength of connections, (ii) the regional bifurcation parameters and (iii) the organization of the structural connectivity. We allowed these features to vary in the different model versions we used here. First, assuming homogeneous local dynamics across brain regions, we found that low-level states of consciousness had lower global coupling strength than conscious states. This finding is consistent with the observation that functional connectivity decreases in states of low-level states of consciousness (Demertzi et al., 2015; Barttfeld et al., 2015) and it explains why in this case functional connectivity follows closer to structural connectivity. Indeed, the global coupling is a scaling parameter that controls for the conductivity of the structural connections in the model. At low coupling, the propagation of activity is mainly restricted to ROIs connected by links with large strength. Increasing the global coupling favours the propagation of activity through direct and indirect connections within the network, thus allowing for correlations to emerge also between nodes that are not directly connected with each other.

Second, we used a model where the local bifurcation parameters (a) were allowed to vary individually for each region. These parameters were estimated from the data, resulting in a more heterogeneous distribution of their values in conscious wakefulness than in low-level states of consciousness. In particular, we found that during conscious wakefulness the behaviour of structural hubs is characterised by noisy oscillations ($a < 0$) that are more stable than for the rest of the regions. In contrast, in low-level states of consciousness, all regions display oscillations close to the transition ($a \sim 0$) without differentiation between hubs and non-hubs. Interestingly, linear stability analysis showed that the stable noisy oscillations of the hubs primarily determine the network stability. These results suggest that in order to release the structural constraints on local dynamics, while ensuring the global stability of the system, hubs play an important role by diminishing their variability. In contrast, unstable hubs would propagate noise to the rest of the network, thus degrading the communication among brain regions. Furthermore, we showed that differences in local parameters could arise by different local dynamics or by different connectivity to the rest of the network. We disentangled these two possible origins of variability by estimating the effective local parameters. Our

analysis showed that, for low-level states of consciousness, the estimated local dynamics were strongly determined by the structural connections, impeding any additional heterogeneity arising from dynamics, which is consistent with the weaker coupling previously discussed.

The relevance of the results presented here shall be framed under various aspects. Theories of consciousness such as Integrated Information Theory (Tononi and Koch, 2008) or the Global-Workspace Theory (Dehaene and Naccache, 2001; Dehaene and Changeux, 2011) propose that higher-level associations and consciousness require the dynamic integration of sensory information processed previously by specialised brain regions (segregation). Thus, an imbalance of this coexistence between integration and segregation could lead to different pathologies. Consistent with this view, we found an alteration of integration-segregation of functional phase interactions during low-level states of consciousness caused by brain damage, propofol anesthesia, and anesthesia's long-lasting effects during recovery (Figure 2.2). Here, we showed that the diversity of phase synchronization patterns and their recurrence in time were also reduced in low-level states of consciousness, presumably leading to a failure to dynamically balance integration and segregation. These results are in line with previous studies showing differences in the synchronized states both in space and time during altered states of consciousness (Tagliazucchi et al., 2016a; Demertzi et al., 2015; Amico et al., 2014; Barttfeld et al., 2015; Chennu et al., 2017; Rizkallah et al., 2019; Luppi et al., 2019; Monti et al., 2013).

From an anatomical point of view, the study of brain connectivity in the recent decades has shown that large-scale structural connectivity is modular and hierarchically organised, with the multiple communication pathways centralised by a set of highly connected brain regions (the hubs) that are densely interconnected forming a rich-club (Zamora-López et al., 2010; van den Heuvel and Sporns, 2011). This architecture, also known as core-periphery networks, is expected to facilitate the coexistence of integration and segregation of information in the brain. It has been proposed that the imbalance between integration and segregation can lead to loss of consciousness (Demertzi et al., 2013; Rizkallah et al., 2019), impairing the

neural communication across specialized brain modules or subnetworks (Tononi and Koch, 2008; Deco and Kringelbach, 2016; Deco et al., 2015b) or impeding the integration of that information by the core hubs. Here, we showed that structural breakdown of core-periphery architecture, as observed in injured structural connectivity, leads to a reduction of dynamical heterogeneity (Figure 2.15). Including the damaged structural connectivities due to brain injuries in the DOC patients into the model showed a further limitation of the diversity of local dynamics in pathological low-level states of consciousness.

From a dynamical point of view, our results show that the breakdown of an additional dynamic-based heterogeneity observed in conscious states leads to an attenuation of the stability properties of the hubs during low-level states of consciousness. We believe that the dynamical stability of the hubs is a signature of consciousness and has functional implications. Indeed, the stability of hubs is required to maintain a functional core-periphery architecture. Such core-periphery architecture is essential to achieve a trade-off between stability and flexibility (Kitano, 2004), with the network periphery supporting more responsivity and plasticity while the network core aids in maintaining the robustness of the system (Gómez-Gardeñes et al., 2010; Gollo et al., 2015; Van Den Heuvel et al., 2012; van den Heuvel and Sporns, 2013). Consistent with this view, previous works on whole-brain fMRI have observed core-periphery organization during resting-state (Gu et al., 2017) and a stable core together with a variable periphery during learning (Bassett et al., 2013). In conclusion, we find that functional disruption in low-level states of consciousness might partly be caused by an attenuation of core-periphery structure induced by (i) the structural damage of the hubs or (ii) the loss of stability of the hubs.

Overall, our results suggest that, during healthy wakefulness, in order to allow a dynamically-based heterogeneity of local dynamics across the brain, resulting in diverse collective activity patterns, while preserving stability and a core-periphery architecture, the hubs are required to "anchor" the dynamics by increasing their stability.

It is well known in clinical literature that loss or reduction of consciousness is related to the impairment of certain key brain regions that are dynamically and/or structurally altered during low-level states of consciousness. These regions have been proposed previously to be involved in the thalamo-cortical loop and are thought to down-regulate the activity of the cortical network which is impaired in loss of consciousness (Schiff, 2010; Laureys, 2005; Dehaene and Naccache, 2001; Crone et al., 2014). The results presented here evidence that the regions characterized by altered dynamical and structural properties coincide with the structural hubs. Among these regions , we found stronger effects in subcortical regions , such as the thalamus and hippocampus, and the precuneus and the posterior cingulate areas, for both pathological and physiological low-level states of consciousness. Our results not only indicate the regions affected by the loss or reduction of consciousness but also give a mechanistic explanation, such as loss of heterogeneity, loss of stability and higher constraint to the anatomy, of the underlying brain dynamics in low-level states of consciousness.

Indeed, the methodology and results presented here provide new insights into the understanding of the brain network behaviour after applications of interventions. The observed decrease in global connectivity is consistent with previous studies of EEG signals after a transcranial magnetic stimulation (TMS)-mediated perturbation, showing that the brain was less responsive in low-level states of consciousness than in conscious states (Massimini et al., 2005; Rosanova et al., 2018; Casali et al., 2013). A prediction of our study is thus that, under localized external stimulation, hub regions should be less responsive during conscious states compared to low-level states of consciousness. A current hypothesis in the field is that the enhancement of neural excitability in the affected regions through therapeutic procedures may improve the conscious recovery process (Thibaut et al., 2019). However, current stimulation protocols using TMS to investigate the network response during different states of consciousness in humans (Massimini et al., 2005; Rosanova et al., 2018; Casali et al., 2013) cannot achieve the required localization of the perturbation propagation to test our predictions. TMS is a strong external perturbation that indirectly activates several cortical and subcortical areas, producing a global

perturbation of ongoing activity. Furthermore, the measurement of the response using EEG is not described with enough spatial resolution to measure the effect on hubs directly. Nevertheless, at the moment, in-silico perturbation of diverse computational models (Deco et al., 2018a) might be useful to test this prediction.

Our study is restricted to the comparison between conscious wakefulness and low-level states of consciousness, i.e. DOC patients and propofol-induced anesthesia state, which are distinguished by the levels of awareness and wakefulness. Interestingly, although the underlying physiology for loss of consciousness differs between DOC patients and propofol sedation, the dynamics at the whole-brain level and the alterations in local dynamics seem to be similar. Future work should study in more detail the differences in the local mechanism altering the global state of consciousness. Indeed, the relatively similar phenomenology (Brown et al., 2010) of the two different states may have a shared cellular basis, at the level of pyramidal neurons, underlying the observed alterations in the global dynamics (Aru et al., 2020; Suzuki and Larkum, 2020).

Given the patient inclusion criteria of the present study, generalization of our results to a broader spectrum of DOC patients, such as those presenting larger brain structural damage, remains to be corroborated. Future studies should consider the confirmation of the results to other anaesthetics agents besides propofol, such as ketamine and sevoflurane, whose effect takes place through different molecular pathways. Also, other theories have proposed a multi-dimensional definition of consciousness which include additional factors such as visual perception, cognition or/and experience of unity (Bayne and Carter, 2018). Those dimensions show different levels in states of altered consciousness, such as under psychedelic drugs or meditation. In the light of our results, we would expect that under a drug-induced psychedelic state, where the conscious content seems to increase and the brain shows higher entropy in the local firing rates (Herzog et al., 2020), the whole-brain models will show an increase of heterogeneity and a larger decoupling from the structural connectivity, while the hubs should lose the stability present during resting-state and the entropy associated

with the repertoire of states would increase.

In this study, we intended to study a whole-brain model that is able to produce oscillations, as needed to represent the synchronization statistics of the data. Thus, we chose the Stuart-Landau model to characterise the local, regional dynamics. This model represents the normal form of a Hopf bifurcation, i.e. the universal behavior around a bifurcation producing oscillation through a limit-cycle. Despite its simplicity and non-biological origin, the model has shown to generate a rather accurate fit to the BOLD dynamics, beyond the success of other models in the past (Deco et al., 2017a; Saenger et al., 2017; Jobst et al., 2017). However, many alternative mean-field or population models exist that could be chosen for the regional dynamics. Therefore, the generalization of the results here presented shall be confirmed in future studies, which employ different local models.

Using global synchronization measures, we found significant differences for different levels of consciousness (CNT and DOC patients and W, S, and R), but these measures mostly failed to identify a significant difference between patients groups (MCS vs. UWS) (Figure 2.2). However, our model-based analysis of local dynamics was able to distinguish between patients groups (Figs. 2.10, 2.12, 2.15). This highlights the clinical translation potential of multi-parameter whole-brain models and the need for further studies that consider region-specific measures for clinical predictions.

Electrophysiological, fMRI and MEG studies have shown that heterogeneous local dynamics, differing between sensory and association brain regions, contribute to the hierarchical specialization across areas at the functional level (Honey et al., 2012; Murray et al., 2014; Deco et al., 2018b; Demirtaş et al., 2019; Margulies et al., 2016). Recently, it has been shown that extending models to include heterogeneous information of local dynamics, e.g. as given by positron-emission tomography (PET) maps of neurotransmitter receptor density (Deco et al., 2018b) or by $Tw1/Tw2$ maps as proxies of microcircuit properties (Demirtaş et al., 2019), in-

creases model performance to fit empirical data. Our model could be extended to include these and other axes of hierarchy to explore the brain mechanism of consciousness.

In conclusion, our results show that pathological and pharmacological low-level states of consciousness presented altered network interactions, more homogeneous, structurally constrained local dynamics, and less stability of the network's core compared to conscious states. These results provide relevant information about the mechanisms of consciousness both from the theoretical and clinical point of view.

CHAPTER 3

Brain ignition and propagation flow characterize pathological state of consciousness

Theories of consciousness agree that the loss of consciousness is related to a breakdown of propagation of inputs in the brain that results in a reduction of information integration. Still, the brain mechanism that ensures the input propagation in conscious wakefulness and how it is impaired in low-level states of consciousness is not well understood. In this chapter, we studied the propagation of perturbations in fully aware conscious controls and patients who suffered from a brain injury that leads to a disorder of consciousness (DOC). We first showed that the brain in low-level states of consciousness propagates less the spontaneous activity, reflecting a reduction of the brain's intrinsic ignition capabilities, along with a decrease of the timescale of specific regions. We further interpreted these effects using a whole-brain model that explains the spatiotemporal properties of the BOLD-fMRI time series by the description of the effective connectivity (EC). We found a global reduction of the effective connections and propagation of inputs in DOC patients, with a hyper-connectivity in par-

ticular links. Furthermore, using dynamic communicability measures, i.e. time-dependent graph-like descriptors, our results suggest a reduction of receiving and broadcasting information flow in two distinct microcircuits: posterior regions fail to receive the information and we observed a reduction of information broadcasting in subcortical, temporal, parietal and frontal regions.

3.1. Introduction

The functional properties captured in the resting-state activity of different levels of consciousness have been widely studied to investigate the alterations of the brain's local and collective dynamics that lead to disorders of consciousness. Several studies indicated that states of pathologically reduced consciousness are characterized by reduced neural activity, metabolism and network connectivity in cortical areas (Laureys et al., 2004; Stender et al., 2014; Demertzi et al., 2015; Chennu et al., 2017). In particular, functional network connectivity metrics, which allow the quantification of how brain regions show correlated activity, pointed out that brain dynamics should have sufficient synchronization to sustain effective communication or propagation of neuronal activation and, in this way, ensure conscious processing (Tononi et al., 2016; Deco and Kringelbach, 2017; Demertzi et al., 2015; Luppi et al., 2019). In normal conditions, this neural synchronicity displays distinct spatial patterns of coordinated activation organized in modules with specific functions (i.e. segregation), that have certain connections that ensure the integration (i.e. integration) (Zamora-López et al., 2010; Sporns, 2013; Deco et al., 2015a; Mohr et al., 2016). Brain integration and segregation have been reported to reach a balance in healthy conscious subjects, whilst such balance is disrupted in pharmacological and pathological states of reduced consciousness (Monti et al., 2013; Rizkallah et al., 2019; Demertzi et al., 2019). The patterns of coordinated activity have different spatiotemporal characteristics (e.g. changes in the occurrence and duration of the patterns) in altered states of consciousness (Barttfeld et al., 2015; Panda et al., 2016; Demertzi et al., 2019; Luppi et al., 2019), which indicate that the spatial and temporal dynamics of the collective patterns characterize the states of consciousness. However, they do not explain the brain mechanism that ensures the

propagation of neural activity in the network during healthy wakefulness and that is impaired in low-level states of consciousness.

Beyond the insights obtained from the resting-state signals, direct external perturbations can be used to explore how the brain's network reorganizes to propagate and integrate such perturbations. The seminal study of Massimini et al. (Massimini et al., 2005) uses a transcranial magnetic stimulation (TMS) pulse to apply an external high-voltage perturbation directly to the cortex. The whole-brain cerebral response to this perturbation is measured with high temporal resolution using electroencephalography (EEG). The compressibility of the cortical response to perturbation, using an index referred to as the Perturbational Complexity Index (PCI), is used to proxy for integrated information and complexity. This procedure showed that unconscious states are characterized by a breakdown of cortical complexity and a fast extinction of the perturbation with limited propagating through the network. Moreover, this measure can discriminate the level of consciousness at the single-subject level during wakefulness, sleep, anesthesia and pathological states of consciousness (Ferrarelli et al., 2010; Rosanova et al., 2018; Casali et al., 2013). However, it is important to note that this index comes from the average of an evoked potential, ignoring local dynamical properties and the network directional interactions in propagating the perturbation.

Inspired by this approach, additional empirical measures have successfully studied the propagation of natural events in spontaneous brain activity and quantify connections/interactions within the brain. In line with this direction, intrinsic events could be used to quantify the alteration of whole-brain integration by the neural propagation of both feedforward and recurrent activity as quantified in the Intrinsic Ignition framework (Deco and Kringelbach, 2017). This framework has successfully explored resting-state dynamics (Deco and Kringelbach, 2017; Deco et al., 2017b; Escrichs et al., 2019), and shows decreased intrinsic ignition during sleep and anesthesia-related loss of consciousness (Deco et al., 2017b; Signorelli et al., 2021) and during a subjective state of dissociation during meditation (Escrichs et al., 2019). Different approaches have also investigated

the temporal properties of the local dynamics to react to a given perturbation by studying the autocorrelations of the activity time courses, i.e. its intrinsic timescale fluctuations (Murray et al., 2014; Chaudhuri et al., 2015; Watanabe et al., 2019). The heterogeneity of the timescales suggests a functionally relevant role of a hierarchical organization of local dynamics that ensures conscious brain processing – short timescales in the sensory areas that can detect and faithfully track dynamic inputs and longer timescales in areas responsible for the integration of information– (Murray et al., 2014; Watanabe et al., 2019). Hence, brain regions' neural propagation and intrinsic dynamical properties seem to be key biomarkers for (un)conscious processes.

A boost to the field of traditional perturbational studies came from advances in computational neuroscience by using whole-brain models that can be perturbed *in-silico* (Perl et al., 2020). Whole-brain models allow for an exhaustive exploration of the neuronal mechanism underlying spatiotemporal brain dynamics. Studies using computational models have indicated alterations in responsiveness and stability of brain networks in states of reduced consciousness captured at whole-brain level, which is originated from alterations in global, network and local dynamics (Perl et al., 2020; Luppi et al., 2021; Jobst et al., 2017). Recently, the combination of whole-brain models and perturbed dynamics has been proposed as a promising tool for understanding the propagation of brain activity (Deco et al., 2018a; Gilson et al., 2019b; Deco et al., 2019a). These models account for the underlying mechanism originating these dynamics and can also be used to extract biomarkers of neuropsychiatric diseases or conscious levels (Deco et al., 2018a; Gilson et al., 2019b).

In particular, the whole-brain model based on a multivariate Ornstein-Uhlenbeck (MOU) process can extract the spatiotemporal information about the BOLD dynamics given the effective relationships between brain regions (Gilson et al., 2016). This model decomposes the empirical covariance matrices in estimated parameters, which describe the local variability and network connectivity as the whole-brain effective connectivity matrix (i.e. MOU-EC). The estimated MOU-EC captures the propagation of the

fluctuating activity across brain regions, and it has been previously proposed as a robust signature of subject identity (Pallarés et al., 2018) and of task vs resting-state (Gilson et al., 2019a). Furthermore, the MOU model has also been used in dynamic communicability, a computational approach to parallel the empirical perturbation studies using TMS or auditory stimulation. Specifically, this analysis links the network structure to the pairwise functional associations of brain regions and characterizes the impulse response of the network to a unit perturbation in a source node given its effective connectivity (EC) (Gilson et al., 2017; Estrada and Hatano, 2008). This method allows for the definition of graph measures that quantify the spatiotemporal organization of network interactions, from short to longer latencies after the perturbation, and can identify the directionality of the propagation in local nodes to describe nodes as 'broadcasters' or 'listeners'.

In this study, we propose to study neural spatiotemporal interactions using data-driven and model-based approaches, both at the whole brain network and at the regional level, in patients with prolonged disorders of consciousness (DOC). For this, we studied the fMRI dynamics of 36 healthy controls (CNT) and patients suffering from a disorder of consciousness (i.e. 33 MCS patients and 16 UWS patients). We hypothesize that the healthy brain has a specific propagation pattern that arises from the effective network interactions that support the integration of spontaneous and in-silico generated events. The effective connectivity patterns can be quantified via directional connections estimated from fMRI data to quantify the propagation capability of the specific brain areas. We expect to find global alterations of the propagation capabilities of the network caused by loss of consciousness, as well as local changes in the receiving and broadcasting patterns.

3.2. Methods

3.2.1. Participants

In this study, we selected a cohort including healthy controls and patients suffering from disorder of consciousness (DOC). The study was approved by the Ethics Committee of the Faculty of Medicine of the University of

Liège. Written informed consent to participate in the study was obtained directly from healthy control participants and the legal surrogates of the patients.

We selected 48 DOC patients, 33 in MCS (9 females, age range 24-83 years; mean age ± SD, 45 ± 16 years) and 15 with UWS (6 females, age range 20-74 years; mean age ± SD, 47 ± 16 years) and 35 age and gender-matched healthy controls (14 females, age range 19-72 years; mean age ± SD, 40 ± 14 years). Detailed information about the participants can be found in section 2.2.1 and Appendix.

3.2.2. MRI Data Acquisition

Structural and functional MRI (fMRI) data were acquired on a Siemens 3T Trio scanner (Siemens Inc, Munich, Germany). The BOLD fMRI resting-state (i.e. task free) was acquired using EPI, with the parameters presented in section 2.2.2 and Appendix.

3.2.3. MRI data preprocessing

For the DOC dataset, structural and fMRI data were acquired on a Siemens 3T Trio scanner (Siemens Inc, Munich, Germany); propofol dataset was acquired on a 3T Siemens Allegra scanner (Siemens AG, Munich, Germany). The detailed procedure is described in the Appendix.

3.2.4. Structural Connectivity Matrix

A whole-brain structural connectivity (SC) matrix was computed for each subject from the DOC dataset, using diffusion imaging and probabilistic tractography (see the Appendix for details). The procedure resulted in a symmetric SC matrix summarizing the density of anatomical links among the 214 ROIs, for each healthy control and participant. Finally, a group structural connectivity (SC) mask was obtained by averaging the all CNT subjects' SC matrix and applying a threshold of 80% to maintain the top 20% of strongest connections. This SC was then binarized. This SC mask was used to constrain the effective connectivity matrix during the model tuning.

3.2.5. Intrinsic Ignition

We quantified the capability of a given local node to propagate neural activity to other regions using the *intrinsic ignition* framework (Deco et al., 2017b; Escrichs et al., 2019; Padilla et al., 2019), see Figure 3.1 A. Intrinsic ignition (II) describes the influence of spontaneously occurring events across the network. Events are defined region-wise when the BOLD signal reaches a given threshold. To this end, first, the BOLD signals were transformed into z-scores, $z_i(t)$, and then binarized by imposing a threshold θ given by the sum of the mean and 1 standard deviation. This process results in binary time-series per region for which events are indicated with 1, i.e. $\sigma_i(t) = 1$, if $z_i(t) > \theta$ and $\sigma_i(t) = 0$, otherwise (Tagliazucchi et al., 2012). Next, for each node i, we calculated the global effect in the network synchronization caused by each of the events captured in that node (see Figure 3.1 A).

The network synchronization was measured using the global integration previously described in (Deco and Kringelbach, 2017) and in section 2.2.5, which determines the whole network's capacity to become interconnected and exchange information. Briefly, the global integration is quantified using the largest subcomponent of the phase-locking matrices, see section 2.2.4 and Figure 3.1 B-C. We quantified the global effect of each node by measuring the global integration in a window of 4 TR after each triggering event. The average and standard deviation of the integration was calculated over all triggering events in each node to define the global Intrinsic ignition (i.e. mean integration) and the Hierarchy (i.e. temporal variability of integration) associated with the node (Deco and Kringelbach, 2017), respectively. Intrinsic ignition (II) and Hierarchy estimate the influence of a given node on the rest of the network and the diversity of network configurations displayed after the activation of that node.

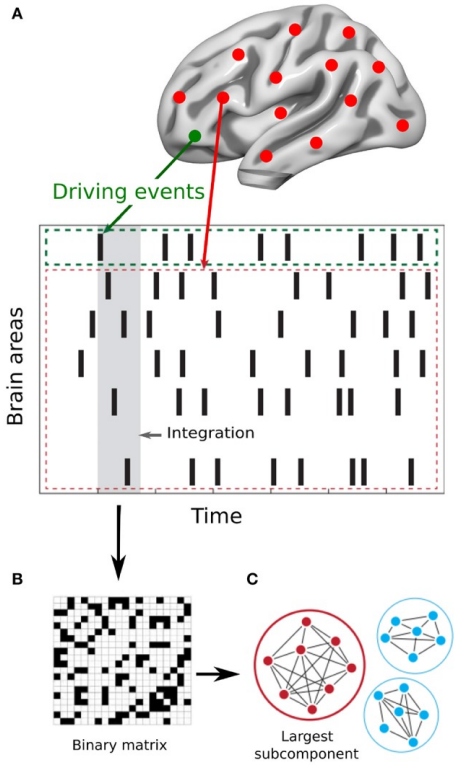

Figure 3.1: **Measuring the intrinsic ignition. A)** The intrinsic ignition is measured by defining the driving events in each brain area from the BOLD time series. When a driving event is captured in a given brain area, the network alterations in a window of 4 TR (in grey) is measured. **B)** The effects of each event are quantified by measuring the changes in the global integration after the event occurs. The global integration is measured as the synchronization in the connectivity matrix, i.e. in the phase-locking matrices calculated for each time point. **C)** In particular, the global integration is measured as the size of the largest subcomponent captured in the connectivity matrix. This figure has been extracted from (Escrichs et al., 2019).

3.2.6. Whole-Brain computational modelling

Perturbations can also be explored using a whole-brain computational model that permits to study how the perturbations are propagated in the network. In this study, we adopted a whole-brain computational modeling approach to implement a dynamic network-oriented analysis and to

study the effects of local perturbations in the network. Specifically, we tune a multivariate Ornstein-Uhlenbeck (MOU) process to reproduce the statistics of the whole-brain resting-state fMRI signals captured in the covariance matrices (without and with time lag). This procedure provides estimates for MOU effective connectivity (MOU-EC) which describes the local variability and network connectivity, by capturing the dynamical interactions between brain regions and the influence that one region exerts over another (Gilson et al., 2016). Moreover, the motivation behind the use of this model is the analytical formulation of its Green function, which allows to describe the interactions between nodes across time for the estimated dynamics after a perturbation in a source node (Gilson et al., 2018). This model-based approach provides a time-dependent graph-like descriptor, named dynamic communicability, that characterizes the roles that either nodes or connections play in the propagation of activity within the network at both global and local level (Gilson et al., 2019;2019b).

3.2.7. Spatiotemporal properties extracted from empirical fMRI data

The empirical variables for fitting and estimating the model's parameters were extracted from the resting-state BOLD time series of each subject, see Figure 3.2. In particular, the covariance matrices of the BOLD time-series for different time shifts were used to determine the estimation of the weights of the MOU-EC (Gilson et al., 2016). We extract the BOLD covariance between node i and node j without, $\hat{Q}^0_{ij}$, and with the time shift of 1 TR, $\hat{Q}^1_{ij}$, as:

$$\hat{Q}^0_{ij} = \frac{1}{T+2} \sum_{1<t<T-1} (s^t_i - \bar{s}_i)(s^t_j - \bar{s}_j) \tag{3.1}$$

$$\hat{Q}^1_{ij} = \frac{1}{T+2} \sum_{1<t<T-1} (s^t_i - \bar{s}_i)(s^{t+1}_j - \bar{s}_j) \tag{3.2}$$

where the BOLD time series for each brain area is denoted by s_i, the mean signal of each brain area, $\bar{s}_i$, is computed as $s_i \frac{1}{T} \sum_t s^t_i$ and T is the total number of time points of the recordings. For each subject, Pearson correlation is calculated from the covariances as $FC0 = Q^0_{ij}/Q^0_{ii}Q^0_{jj}$ in the

case of time lag 0 and $FC1 = Q^1_{ij}/Q^1_{ii}Q^1_{jj}$ otherwise.

Furthermore, the local time constant τ was also extracted from the empirical signals. The time constant τ is associated with the exponential decay, and it can be interpreted as an abstraction of the hemodynamic response decay, see Figure 3.2. The τ_i was computed using the autocovariance corresponding to the node i using time shifts from 0 to 1 TRs.

$$\tau_i = \frac{1}{a(v_i|u)} \tag{3.3}$$

Where $a(vi|u)$ corresponds to the slope of the linear regression of $v_i = [log(Q^0_{ij}, log(Q^1_{ij})]$ by $u = [0, 1]$.

3.2.8. MOU-EC Process

We applied a MOU process which can be interpreted as a non-conservative propagation of fluctuating activity in a network with linear feedback (Gilson et al., 2016,0). The network model consists of heterogeneous interconnected neural populations, whose activity is characterized by an intrinsic noise and shaped by the excitation caused by other brain regions ' activity. The main aim is to generate the spatiotemporal patterns that appeared in the empirical data, captured in the covariance matrices of the BOLD signals, i.e. Q^0 and Q^1, by tuning the effective connectivity (EC).

The MOU process has three basic properties which determine the generated activity of each node (Gilson et al., 2016;2019); (i) the activity of each area is associated with a local leakage related to a decay τ, (ii) the interactions between nodes is given by a weighted matrix $\mathbf{A}$ associated with linear coupling (MOU-EC) and, finally, (iii) each node is affected by fluctuating inputs with zero mean and a given covariance matrix Σ. Thus, the node activity is governed by the following coupled ordinary differential stochastic equations:

$$dx^t_i = [-\frac{x^t_i}{\tau_x} + \sum_{k \neq i} A_{ik}x_k]dt + dB^t_i \tag{3.4}$$

where x_i corresponds to the node activity of node i and τ is the time constant characterizing the exponential decay. For the model, we have considered the average τ for all the nodes in each subject, considering the variability across subjects, following a previously published approach (Gilson et al., 2016,0). The node's activity evolves depending on the activity of other populations given by the recurrent connections in **A**. The SC mask is also imposed here considering that **A** elements are non zero only if they exhibit anatomic connection in the SC mask. Finally, dB is colored noise given by a covariance matrix Σ. This covariance matrix comprises random fluctuations in the diagonal and cross-correlated inputs corresponding to anti-diagonal elements for each node. In the MOU process, the Jacobian is determined by a decay of a time constant τ and the matrix **A**:

$$J_{ij} = -\frac{\delta_i}{\tau} + A_{ij} \tag{3.5}$$

where δ_i corresponds to the Kronecker delta, i.e. $\delta = 1$ when $i = j$ and 0 otherwise. The matrix **A** determines the Jacobian of the dynamic system, reflecting the interactions in the propagation of brain activation in the network.

In the model, all variables x have zero mean, and the model's covariances can be calculated by solving the consistency equation (Gilson et al., 2016). Specifically, for extracting the simulated covariance, i.e. Q^0 and Q^1 from the model, the following equation is solved:

$$JQ^0 + Q^0 J^\dagger + \Sigma = 0 \tag{3.6}$$

The covariances including time lags are extracted with the following equation:

$$Q^t = Q^0 expm[J^\dagger t] \tag{3.7}$$

where $expm$ corresponds to the exponential matrix and t the time lag.

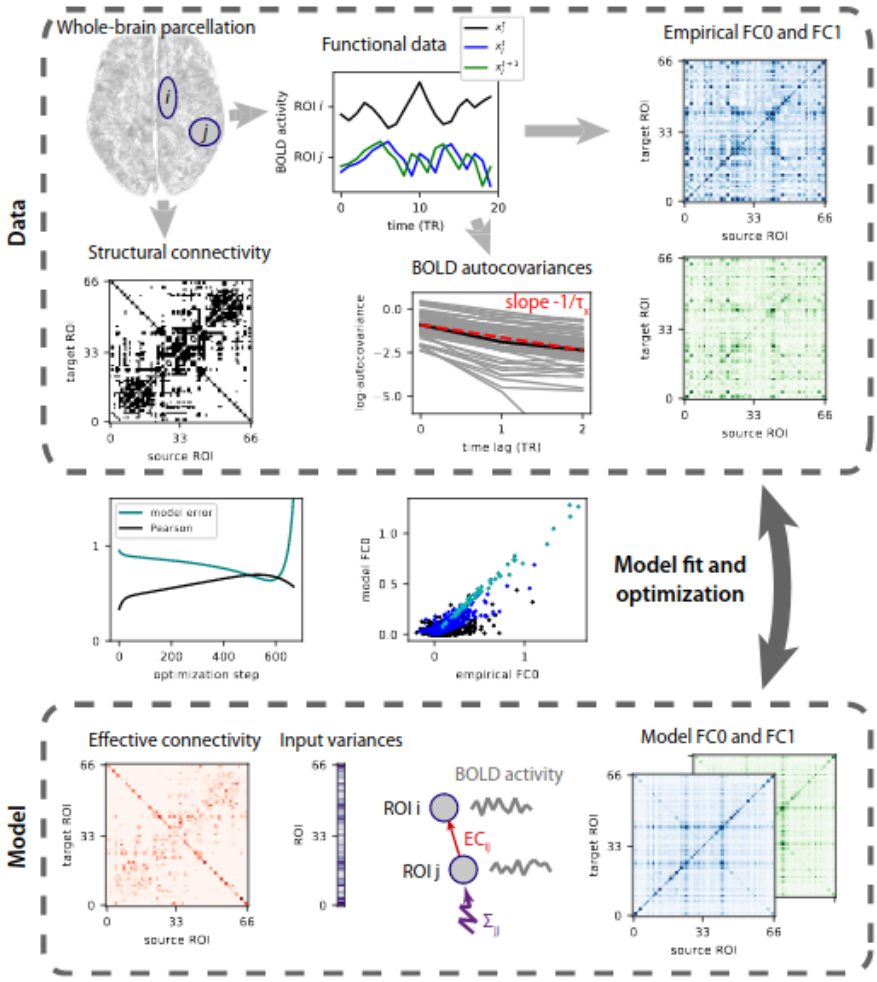

Figure 3.2: **Dynamic model and optimization procedure to capture BOLD dynamics.** This model uses the empirical data to tune the model's variables based on the empirical covariances (blue and green matrices) extracted from the BOLD timeseries (top left in top box), both without and with time lag, as depicted by the blue and green curve. From the empirical data, the BOLD autocovariances are also extracted, which describes the decay of the time series and serves to calibrate the nodal dynamics in the model. Furthermore, The topology of existing connections is determined by the structural connectivity (black matrix in top box). The dynamic network model (bottom box) describes the fluctuating activity of the ROIs and comprises a parameter for the spontaneous activity of each ROI and each directed connection between ROIs (effective connectivity, MOU-EC). The optimization of the model (central panel between the boxes) is similar to a gradient descent during which the model covariance matrices are evaluated at each step and compared to the empirical ones. From the differences between the corresponding matrices, an update of the MOU-EC and model parameters are calculated, and the procedure is repeated until reaching a minimum for the model error (light grey-blue curves in the left). The step where the model error is minimal also corresponds to the highest value for the Pearson correlation between the matrix elements of the model and empirical FCs (black curve). Figure extracted from (Gilson et al., 2019b).

3.2.9. Tuning the model to the empirical data

The optimization is based on the idea of best reproducing the covariance matrices, $\hat{Q}^0$ and $\hat{Q}^1$, which represent the spatiotemporal structure of the BOLD signals. The tuning process optimizes the model's parameters until the covariance matrices Q^0 and Q^t of the model reproduce the empirical covariances, $\hat{Q}$, see Figure 3.2. The best fit of the model parameters corresponds to the values obtained when the error function E, i.e. the function that quantifies the difference between the empirical and simulated covariances, is minimal. Here, we followed the steps presented in previous works where the model parameters (Σ, τ and $\mathbf{C}$) are tuned using a 'natural' gradient descent algorithm (Gilson et al., 2016;2018).

The model is initialized with the following parameters; τ corresponds to the one extracted from the empirical autocovariance averaged across all ROIs, no connectivity, i.e. $\mathbf{A} = 0$, and the noise matrix Σ corresponds to the unit variances and without covariances. At each step, the Jacobian is computed straightforward using the $\mathbf{A}$ matrix and the values of τ, for the diagonal. Using the current Σ and the Jacobian, the simulated $\mathbf{Q}$ matrices are computed from the consistency equations (eq. 3.6 and 3.7), using the Bartels-Stewart algorithm to solve the Lyapunov equation.

To determine the model error, the simulated and empirical covariance matrices are compared by computing their difference, $\Delta Q^0 = \hat{Q}^0 - Q^0$ and $\Delta Q_t = \hat{Q}_t - Q_t$, reflected in the error function, E, which is computed as follows:

$$E = \frac{\sum_{i,j}(\Delta Q^0_{ij})^2}{2\sum_{i,j}(\Delta \hat{Q}^0_{ij})^2} + \frac{\sum_{i,j}(\Delta Q^1_{ij})^2}{2\sum_{i,j}(\Delta \hat{Q}^1_{ij})^2} \tag{3.8}$$

In each optimization step, the model's error is minimized by optimizing the rest of the parameters. Thus, the differences in the empirical and simulated covariances, ΔQ^0 and ΔQ^t are also used to update the rest of the model's parameters.

The Jacobian update is given by the matrix:

$$\Delta J = \frac{1}{Q^0}(-\Delta Q^0 + \Delta Q^1 expm[J]) \tag{3.9}$$

Using the update of the Jacobian matrix, the connectivity update is performed as followed:

$$\Delta A_{ij} = \eta \mathbf{A} \Delta J_{ij} \tag{3.10}$$

This update is applied only for existing connections; other weights are forced to 0 using the SC mask which is given by the anatomical connection averaged across CNT. We also impose non-negativity for the EC values during the optimization. To compensate for the increase of the recurrent connections in the $\mathbf{A}$ matrix, the τ is also updated as:

$$\Delta \tau = \eta_\tau (\tau_{ac} + \frac{1}{\lambda_{max}}) \tag{3.11}$$

This step is made to avoid explosion of the network dynamics (when $\lambda_{max} > 0$) while letting the model connectivity $\mathbf{A}$ develop a non-trivial structure to reproduce the empirical $\hat{Q}$.

Finally, the values of the noise matrix Σ are also updated to take properly the effect of the cross-correlated inputs into account:

$$\Delta \Sigma = -\eta_\Sigma (J^\dagger \Delta Q^0 - \Delta Q^0 J) \tag{3.12}$$

For non-existing connections, elements distinct from the diagonal and cross-correlated inputs are kept equal to 0 at all times. In numerical simulations, we use $\eta_C = 0.0005$, $\eta_\Sigma = 0.05$ and $\eta_\tau = 0.0001$.

The optimization steps are repeated until reaching a minimum in the model error, which is given by the distance matrix between the simulated and empirical covariances, see Figure 3.2. The estimated $\mathbf{A}$ is considered the MOU-EC, which is, in general, a directed and weighted matrix (Gilson et al., 2016).

3.2.10. Dynamic Communicability

The output of the MOU process can also be used as the basis to describe the *dynamic communicability* of the system, which measures the network response when applying a perturbation in a given source node. The dynamic communicability characterizes the impulse response of the network due to its connectivity given by the EC and ignoring the input properties of the noise matrix Σ (Gilson et al., 2018). Intuitively, it can be understood as a network impulse when fluctuating activity (akin to noise) is generated at each ROI and propagates via the recurrent EC.

The concept used here is adapted from associated stable dynamics to our dynamics characterized by a Jacobian that combines the connectivity $\mathbf{A}$ and a leakage time constant τ. Based on previous studies (Estrada and Hatano, 2008; Gilson et al., 2018), we applied a Green function (or network response) to obtain the dynamic communicability for every node, focusing on the temporal evolution of node interactions, see Figure 3.3. *Communicability* is defined as the matrix exponential of the adjacency matrix, e^A. Since the matrix exponential has an exact series expansion, i.e. $e^A = \sum_{n\geq 0} \frac{A^n}{n!}$, communicability can be understood as a summation of influence over all possible paths with a factorial decay for the influence of path length. The computing of communicability relies on two simple and realistic assumptions; (i) the interaction between nodes accumulates along all possible paths of various lengths, and (ii) shorter paths are more influential than longer paths.

For the MOU process, communicability is the 'deformation' of its Green function due to the presence of $\mathbf{A}$, as compared to the Green function corresponding to the initial Jacobian, with leakage only and no connectivity, $J^0_{ij} = -\delta_{ij}/\tau$, and is given by:

$$C(t) = ||J^0||(e^{Jt} - e^{J^0 t}) \tag{3.13}$$

where t corresponds to the time for the propagation of activity within the network, referred to as 'integration time'. The scaling factor $||J^0||^-1 =$

$|| \int_{t>0} e^{J^0 t} dt||$ where $|| \cdot ||$ is the L1 norm for matrices is used for normalization purposes (Gilson et al., 2018). The element C_{ij} of e^{Jt} describes the effect of the impulse response from j onto i after time t when taking network effects into account, see Figure 3.3.

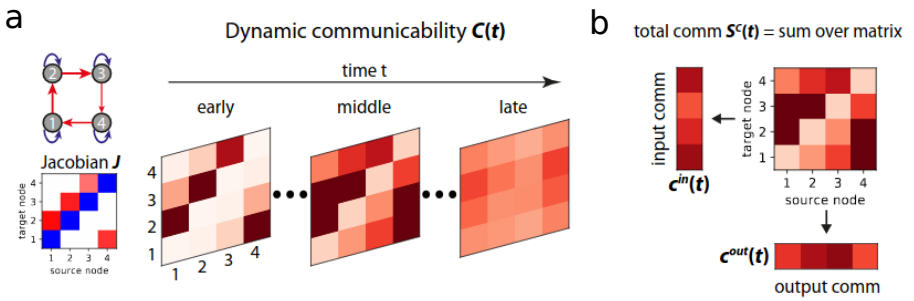

Figure 3.3: **Total communicability extraction to characterize the propagation of perturbation through the effective connections across time. a)** The dynamics for the network (top left) is determined by the Jacobian matrix J (bottom left) characterize by the decay $-1/\tau$ on the matrix diagonal in blue and the recurrent connectivity A (off-diagonal elements). Dynamic communicability is calculated as the Green function of a system with the jacobian J and is described by the family of matrices $C(t)$. **b** The matrix $C(t)$ for each time point provides the directional propagation and describes the input and output communicability of each node. The sums of matrix elements in $C(t)$ along rows and columns give the input and output communicability for each node, respectively. Figure edited from (Gilson et al., 2018).

For each matrix $\mathbf{C}(t)$, we defined the total communicability as the sum of the interactions:

$$C^{tot}(t) = \sum_{\{i,j\}} C_{ij}(t) \tag{3.14}$$

Total communicability measures the effect, after the integration time t, of a simultaneous perturbation applied to all nodes at time $t = 0$. The function $C_{tot}(t)$ reflects the global network feedback determined by the matrix $\mathbf{A}$ and more precisely relates to the eigencentrality as it is mainly determined by the largest eigenvalue of $\mathbf{A}$ (Gilson et al., 2019;2019b).

Due to the asymmetry in input and output connections, some nodes seem to play the role of 'broadcasting' information while others are clearly more likely to act as 'receivers'. We evaluated the properties of individual nodes by defining the input and output communicability as the row and column sums (Gilson et al., 2018;2019) (see Figure 3.3 b).

$$C_i^{in}(t) = \sum_i C_{ij}(t) \tag{3.15}$$

$$C_i^{out}(t) = \sum_j C_{ij}(t) \tag{3.16}$$

3.3. Results

Our main goal is to characterize the neural propagation after perturbation in the cerebral network of awake healthy control (CNT) subjects and to measure how this is altered in patients with severe brain damage leading to a disorder of consciousness (DOC). The study includes 33 CNT subjects, 14 patients in the Unresponsive Wakefulness Syndrome (UWS) and 30 patients in the Minimally Conscious State (MCS). Our approach includes data-driven and model-driven frameworks in which both local and global properties are evaluated. First, we study how internal naturally occurring events in the regional BOLD signal propagate and integrate at the whole-brain level, employing the Intrinsic Ignition methodology (Deco and Kringelbach, 2017). We furthermore explore the autocorrelation of the signal, τ, to quantify the similarity between observations as a function of the time lag between them (Murray et al., 2014; Chaudhuri et al., 2015).

Second, we used a whole-brain modeling approach that simulates the ongoing dynamics, accounting for the structural and functional connectivity. This model allows to study the effect of in-silico perturbation of the BOLD signal, after which the whole-brain effective connectivity (EC) is extracted. This approach captures neural activity propagation and integration that one local node exerts over all individual other cerebral nodes (Gilson et al., 2016). Furthermore, we use the dynamical communicability framework to study the propagation of perturbation in each node through the ensemble of feedforward and recurrent pathways, given the EC, across time (Gilson

et al., 2018;2019a:2019b). The dynamical interactions from every node to the rest of the brain permits defining the local nodes as 'receiver' (i.e. in-communicability) or 'broadcaster' (i.e. out-communicability).

3.3.1. Global integration after a local intrinsic event is hampered in reduced conscious states

We studied if spontaneous regional activation propagates through the whole brain differently depending on the state of consciousness by adopting the *Intrinsic Ignition* framework, which allows measuring the effect of the propagation of spontaneous and local occurring activation on global integration captured at whole-brain level. The intrinsic ignition framework generates two measures: Intrinsic Ignition and hierarchy (Deco and Kringelbach, 2017). The Intrinsic Ignition captures the mean global integration after an internal perturbation, or event, occurred in the time series of a given ROI. We found that the mean Intrinsic Ignition across nodes was significantly lower in MCS and UWS patients than CNT ($CNT = 0.81 \pm 0.01, MCS = 0.79 \pm 0.01, UWS = 0.78 \pm 0.01$, CNT vs MCS p-value=1.3e-05, CNT vs UWS p-value=1.8e-08, MCS vs UWS p-value=0.012, see Figure 3.4 a).

To understand how the local perturbation affects the temporal dimension of network integration and the alterations in different consciousness levels, we assessed the network hierarchical disruptions. We measured hierarchy from the temporal variability of the global integration after an event (Deco and Kringelbach, 2017). We found that the mean hierarchy was significantly lower in UWS patient than in MCS patients and, which both showed lower hierarchy than CNT ($CNT = 0.03 \pm 0.005, MCS = 0.023 \pm 0.003, UWS = 0.019 \pm 0.003$, CNT vs MCS p-value=1.8e-07, CNT vs UWS p-value=2.9e-0.8, MCS vs UWS p-value=0.007), see Figure 3.4 b.

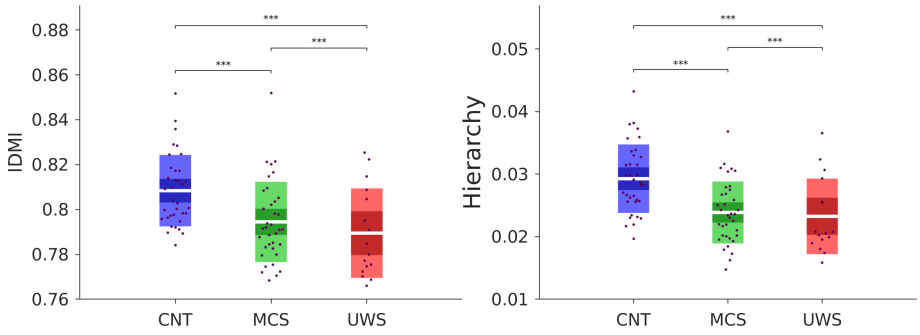

Figure 3.4: **Results of the intrinsic ignition framework. a)** Mean intrinsic ignition, which denotes the mean global integration right after a natural event within a brain region, decreases with the lower level state of consciousness. **b)** Mean hierarchy, which denotes spatiotemporal diversity intrinsic ignition, is lower for lower level states of consciousness. Boxplots represent the mean of the measures' values with a 95% confidence interval (dark) and 1 SD (light).

3.3.2. Altered temporal structure of the BOLD signal

Measuring timescales from experimental data can uncover the underlying mechanisms controlling the local dynamics and determine their operating regime. We evaluated the autocovariance of the BOLD signal for every ROI, τ, to measure the 'memory depth' of the BOLD. This describes the duration for which the signal is altered before going back to pre-event/baseline activity and gives an indication how the signals are structured. For estimating τ, the autocovariance of the BOLD signal for every ROI was fitted with an exponential decay function (Murray et al., 2014; Wilting and Priesemann, 2018; Cavanagh et al., 2016; Chaudhuri et al., 2015; Watanabe et al., 2019). A high value of τ reflects a longer lingering effect in the signal suggesting that it might stay available for processing longer. τ at the whole brain level was lower in UWS patients (1.96 ± 0.38) compared to CNT (2.72 ± 0.35; p-value = 4.5e-08) and MCS patients (2.70 ± 0.58; p-value=0.0001), see Figure 3.5a and Figure 3.6.

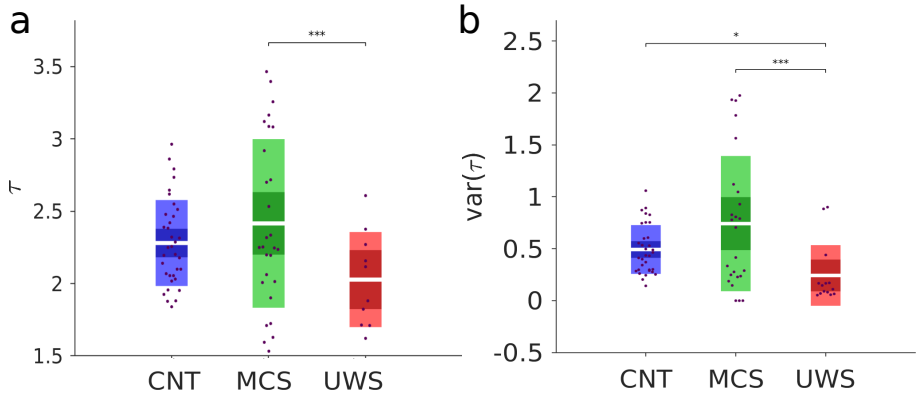

Figure 3.5: **Mean intrinsic timescales, τ, characterizing the BOLD-fMRI timeseries of each group.** a) Whole brain mean τ, the time constant of the BOLD time series, is lower for UWS patients than MCS patients and CNT subjects. b) Results show similar pattern for the variance of τ, which is lower for UWS patients than MCS patients and CNT subjects. Boxplots represent the mean of the measures' values with a 95% confidence interval (dark) and 1 SD (light). The * in the bar graph represent the significant level, *: $p < 0.05$; **: $p < 0.01$; ***: $p < 0.001$.

Investigating regional estimations, we found that the patterns of the τ in healthy controls show a gradient distribution with shorter timescales in subcortical regions and longer timescales in the frontal and parietal areas, see Figure 3.6a. This pattern was not observed in DOC patients, where τ values distribution was more homogeneous in the brain, see Figure 3.5b and 3.6 b-c. Compared to CNT, τ was lower in MCS patients in the bilateral thalamus and left medial prefrontal cortex, see Figure 3.7 a. A widespread decrease in τ was found in UWS patients with the most predominant alterations in the bilateral thalamus, right caudate, left hippocampus, parahippocampus, bilateral posterior, middle and anterior cingulate, insula, inferior, middle, superior and dorsolateral frontal regions, see Figure 3.7 b. UWS patients presented widespread lower compared to MCS patients in the precuneus, left inferior frontal, inferior parietal, angular and middle cingulate regions, see Figure 3.7 c. Overall, the Intrinsic Ignition and analysis suggests a breakdown in the signals' spatiotemporal structure that involves a reduced propagation and integration capabilities in loss of consciousness.

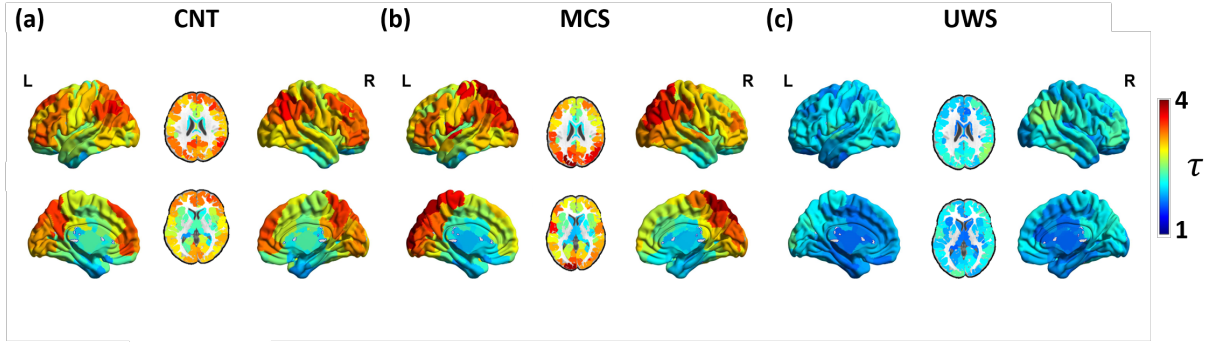

Figure 3.6: **Distribution of the τ values across brain regions for each of the states.** The τ values are given by the mean average of the values of all the subjects for each brain region in (a) controls, (b) MCS and (c) UWS.

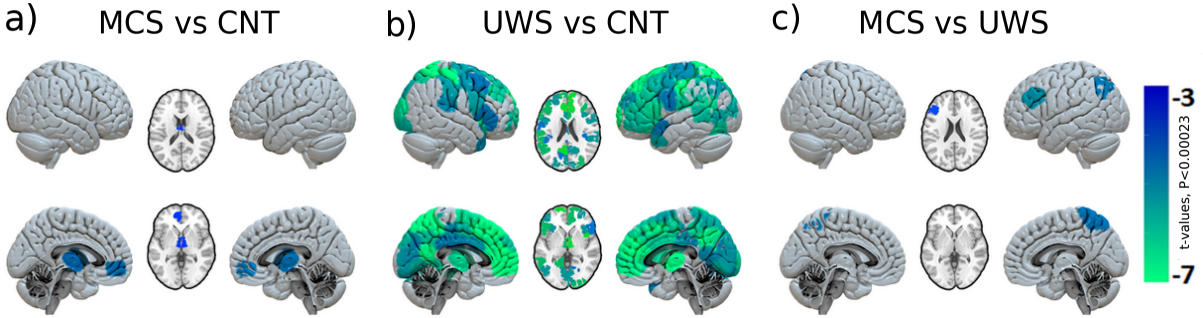

Figure 3.7: **Regional comparison between the τ of the corresponding groups. a-c)** Regional significant differences of for (a) MCS lower than CNT (b) UWS lower than CNT (c) UWS lower than MCS. Color bar in the glass brain represents the t-values of between-group significant differences (Bonferroni corrected for 214 tests, $p = 0.05$).

3.3.3. Whole-brain effective connectivity shows altered interactions in DOC patients

We employed a whole-brain dynamical model of effective interactions that introduces stimuli into the system to unravel the mechanism underlying the propagation of perturbations. The multivariate Ornstein-Uhlenbeck (MOU) process was used as a generative model of the spatiotemporal properties of the fMRI BOLD time series, given by the estimated effective connectivity (EC). The tuning of the model is based on the covariance matrices' reproducibility, $\hat{Q}^0$and $\hat{Q}^1$, and it iteratively adjusts the model parameters until the covariance matrices Q^0 and Q^t of the model reproduce the empirical covariances, $\hat{Q}$, Figure 3.8.

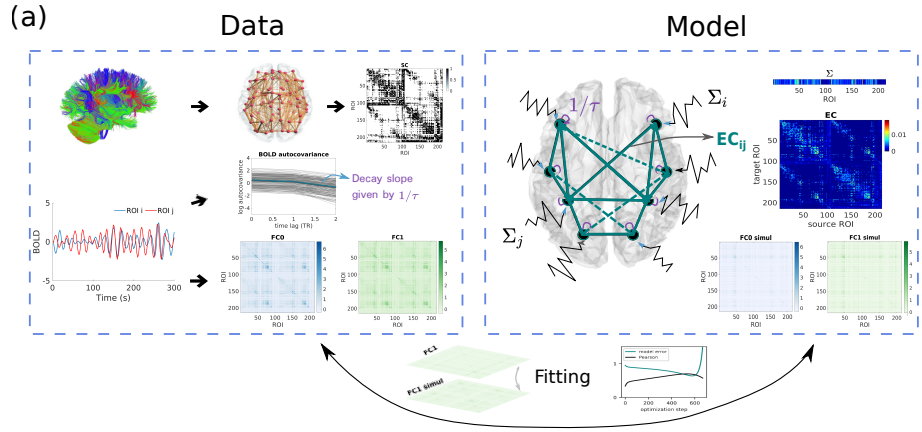

Figure 3.8: **Building of the dynamical model. a)** The model is initialized based on the empirical measures obtained from the data, i.e. the covariance matrices, the decay slope τ, both extracted from the fMRI-BOLD timeseries, and the structural connectivity, SC, extracted from the DTI. Once it is initialized, the model undergoes a tuning process where the Σ, EC matrix and simulated covariance matrices are calculated. The MOU can be interpreted as a non-conservative propagation of fluctuating activity in a network with linear feedback. The network model consists of heterogeneous interconnected neural populations, whose activity is characterized by an intrinsic noise (Σ) and shaped by the excitation caused by the activity of other brain regions (EC). Finally, the fitting of the model is performed by comparing the empirical and simulated covariance matrices for each step. The fitting is optimal when the distance between the two matrices is minimal.

Figure 3.9 indicates the details about the tuning process for all subjects in each group. Figure 3.9 a shows the number of steps needed to obtain the best fitting calculated with the distance between the covariance matrices, Figure 3.9 b. In the step with the best fitting, we also found high Pearson correlation values between the tuned and empirical matrices, see Figure 3.9 c. These results suggest that the fitting of the UWS patients is slightly lower than in the other groups because it requires more steps, and the distance and correlation show impoverished tuning of the model. Even though the correlation is > 0.6 in all the cases, suggesting that the model's tuning process captures the spatiotemporal properties appearing in the empirical matrices.

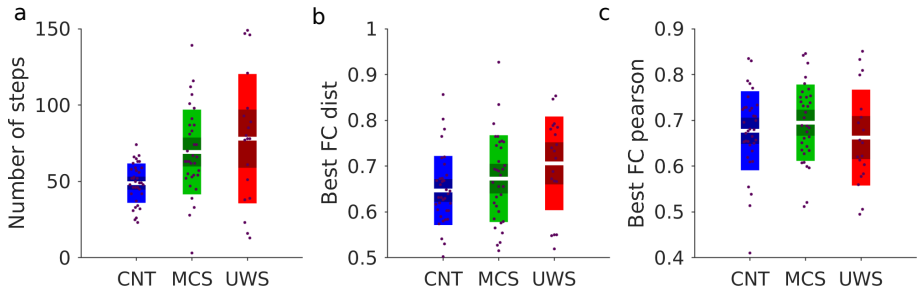

Figure 3.9: **Fitting of the dynamical model. a)** Number of steps in the optimization process to obtain the best fitting of the empirical covariance matrices. **b** The tuning process is performed until the error function E, i.e. the function that quantifies the distance between the empirical and simulated covariances, is minimal. **c)** The Pearson correlation between the simulated and empirical covariance matrices in the step where the distance between them is minimal. Boxplots represent the mean of the measures' values with a 95% confidence interval (dark) and 1 SD (light).

The estimate MOU-EC quantifies the propagation of fluctuating BOLD activity across ROIs in terms of spatiotemporal interaction. For the following analysis, we used the average EC for each group extracted by tuning the MOU process for each of the subjects in each group, see Figure 3.10. The mean EC connections across all node was similar for MCS patients and CNT subjects, and significantly higher in UWS patients than CNT subjects and MCS patients ($CNT = 0.015 \pm 0.002$, $UWS = 0.019 \pm 0.004$, $MCS = 0.014 \pm 0.003$, CNT vs UWS $p - value = 2.1e-05$, MCS vs UWS $p - value = 2.6e-04$).

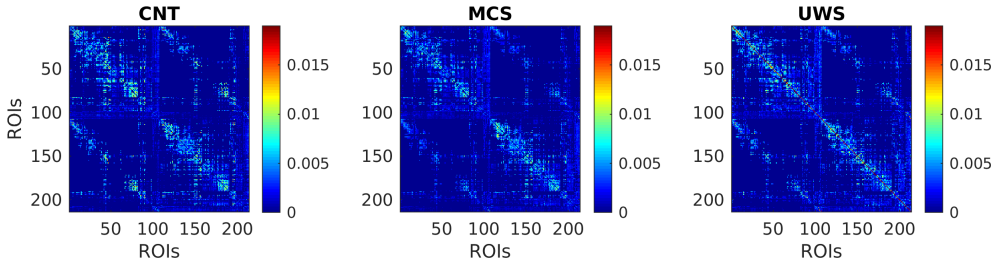

Figure 3.10: **MOU-EC estimation from the whole-brain model.** Average MOU-EC matrices for each subject calculated by tuning the model with a gradient descent that optimizes the model parameters to simulate the covariance matrices obtained empirically. The EC quantifies the propagation of fluctuating BOLD activity across ROIs in terms of spatiotemporal interaction. The average matrix has been calculated by averaging the MOU-EC matrices across subjects.

Interestingly, when comparing MCS patients and CNT subjects we noted that MCS patients have especially lower EC in connections from posterior to frontal and temporal regions and midline regions encompassing the middle prefrontal and posterior cortex and the thalamus, see Figure 3.11 a. In UWS patients, in contrast, both increased and decreased EC can be observed. The UWS patients showed increased EC specifically for connections with subcortical regions (thalamus, caudate and putamen). Contrary, UWS patients had decreased EC in connections spanning posterior (i.e. parietal, occipital) to frontal (i.e. temporal and frontal) regions as well as between midline posterior regions (parietal, occipital) and middle frontal regions, see Figure 3.11 b.

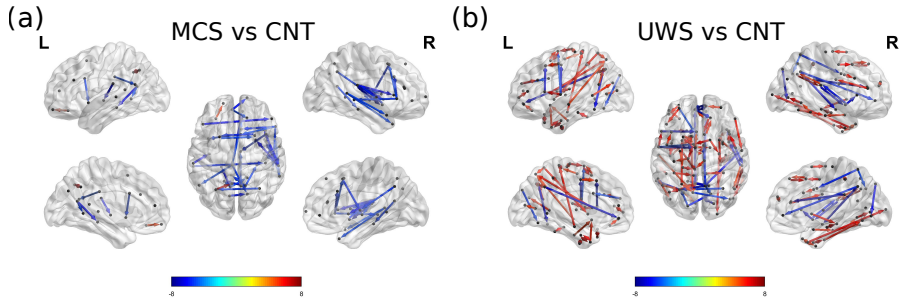

Figure 3.11: **MOU-EC link comparisons across brain states. a)** MCS patients versus CNT (top is within hemisphere and bottom between hemisphere EC) show decrease EC in MCS specifically fronto temporal and midline between hemisphere regions. **b)** UWS patients versus CNT (top is within hemisphere and bottom between hemisphere EC) show both decrease and increase EC in UWS (decreased in fronto-temporal and frontal-parietal of midline between hemisphere regions, increased in locally within hemisphere and subcortical regions between hemispheres). Thickness of link represents significant levels and color of link represents connectivity differences, red color is increased connectivity and blue color is decreased connectivity.

3.3.4. Dynamic communicability reveals altered spatiotemporal structure of information in- an outflow

After observing that the EC is decreased in certain regions and increased in others (in UWS patients), we assessed the effects of external (in-silico) perturbation for every node over time. The framework of dynamical communicability (DC) quantifies how a stimulus propagates and integrates through the network in time, accounting for direct and indirect connections, initially aligned with MOU-EC (Gilson et al., 2019a). Briefly, the time-varying region-to-region communicability matrices, $\mathbf{C}$, describe the interaction between pairs of ROIs. In particular, $C_{ij}(t)$, represents the influence that a simulated perturbation (at $t = 0$) on node i exert over node j at the so-called 'integration time' $t > 0$.

We present the early (i.e. $t = 2$ TR), middle (i.e. $t = 10$ TR), late ($t = 30$ TR) and very late ($t = 200$ TR) communicability matrices to illustrate how the patterns of communicability progressively reshape for the different groups, see Figure 3.12. The progression of the interaction matrices

(Figure 3.12a-c) is reflected in the total dynamic communicability curve (Figure 3.12d). The DC curves show increasing nodal interaction patterns that stabilize as the reaction to the perturbation decays and the system relaxes back to its stationary state, indicated by the homogenization of the matrices and decreased DC for longer latencies. For healthy controls, the total communicability reaches the peak around 22 sec computational time and then decays very slowly. The curve of the UWS patients arrives sooner to the maximum, which is higher than in CNT and MCS, and then it decays faster than in the other groups. For the MCS, the pattern is similar to the CNT yet it reaches a lower maximum than CNT. The decay observed in MCS patients is slow and reaches lower values of total communicability than in CNT subjects.

To quantify total communicability, we compute the area under the curve (AUC) of the communicability curve for time periods that are significantly different between all three groups (60-200 sec modeled time). This total DC represents the total responsiveness of the network, accumulated over time. We found evidence for a significant decrease in total communicability in UWS (0.65 ± 0.33) and MCS (0.91 ± 0.22) patients as compared to CNT (1.25 ± 0.18) 20 integration time after perturbation (CNT vs MCS p-value=2.4e-08, CNT vs UWS p-value=4.9e-10, MCS vs UWS p-value=0.0059). In UWS patients, a sudden increase of total communicability can be observed immediately after the perturbation (0.017 ± 0.004), as compared to MCS (0.011 ± 0.004) patients and CNT (0.013 ± 0.002; CNT vs UWS p-value=0.00016, MCS vs UWS p-value=0.00013), see Figure 3.12.

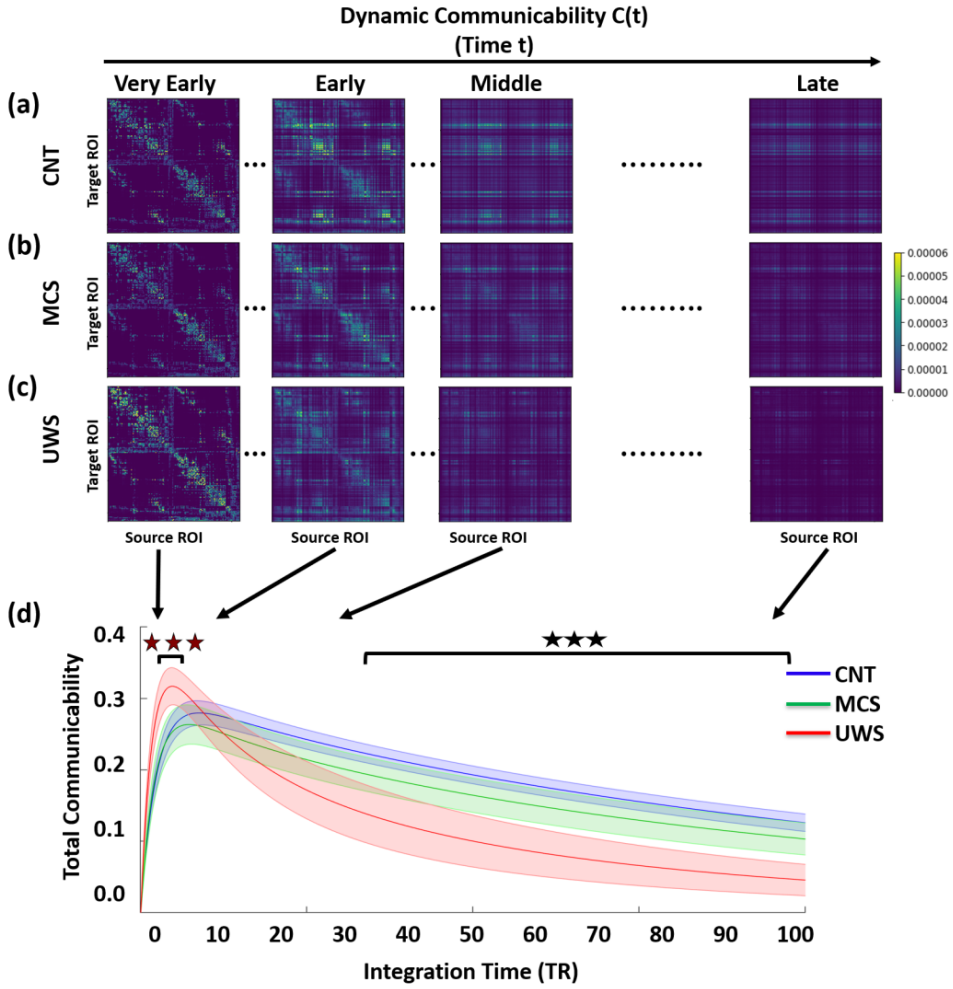

Figure 3.12: **Evolution of the whole-brain dynamic communicability in different levels of consciousness. a-c)** Examples of communicability matrices averaged across subjects for each level of consciousness and different time scales after perturbation (early (i.e. t=2 TR), middle (i.e. t= 10 TR), late (t= 30 TR) and very late (t= 200 TR)). Color bars of the connectivity matrix represent strength of the connectivity between brain regions. **d)** Whole brain total communicability for CNT subjects and DOC patients (MCS and UWS). Total communicability reflects the global network interactions after a unit perturbation in t=0. Error bars represent the 95 % confidence intervals. The black color *** indicates all the three groups have differences of $p < 0.05$, Bonferroni corrected and red color *** indicates UWS differences in CNT vs MCS of $p < 0.05$, Bonferroni corrected. Time of the x-axis of whole brain communicability is the model integration time, which is unit free.

3.3.5. Regions with high potential for in- and out communicability in different states of consciousness

After studying the global communicability properties, we studied the local alterations of individual nodes. Due to the asymmetry in the communicability matrices (i.e. the sum of row reflects in-communicability and the sum of column reflects out-communicability), this approach allows to explore the regional capacity to receive (i.e. integration, how much the regional activity is altered after stimulation) and broadcast (i.e. propagation, how much the region influences the activity of other ROIs in the network) stimuli respectively. All levels of consciousness are characterized by 'broadcaster' and 'receiver' nodes that show distinct spatial distributions, see Figure 3.13.

For CNT subjects high broadcasting and receiving properties were present in the bilateral occipital, calcarine, lingual, cuneus, precuneus, superior and inferior parietal, right superior temporal regions as compared to the rest of the brain. Furthermore, receiver properties (i.e. information integration) were high in the bilateral posterior cingulate cortex (PCC), precuneus, supramarginal gyrus, thalamus, middle cingulate, left anterior cingulate and right inferior frontal cortex (Figure3.13a top). On the other hand, the bilateral inferior, middle and superior temporal, right parahippocampal, putamen, bilateral insula, inferior parietal, SupraMarginal, precuneus, middle cingulum and right inferior frontal areas tend to broadcast more information (i.e. higher out-communicability) (Figure 3.13a bottom).

Unlike for CNT subjects, the MCS patient group was characterized by globally reduced receiving and broadcasting properties as compared to CNT subjects, however showed relatively preserved receiving and broadcasting of information within bilateral occipital, cuneus, left calcarine, bilateral superior and inferior parietal, supramarginal, precuneus and the right PCC. Additionally, MCS patients have preserved receiving properties in the bilateral thalamus and preserved broadcasting properties in the bilateral middle temporal, postcentral, right calcarine and left inferior frontal cortices, see Figure 3.13b. UWS patients do not show a set of nodes with high receiving or broadcasting properties, actually only the thalamus shows relatively preserved receiving properties, see Figure 3.13c.

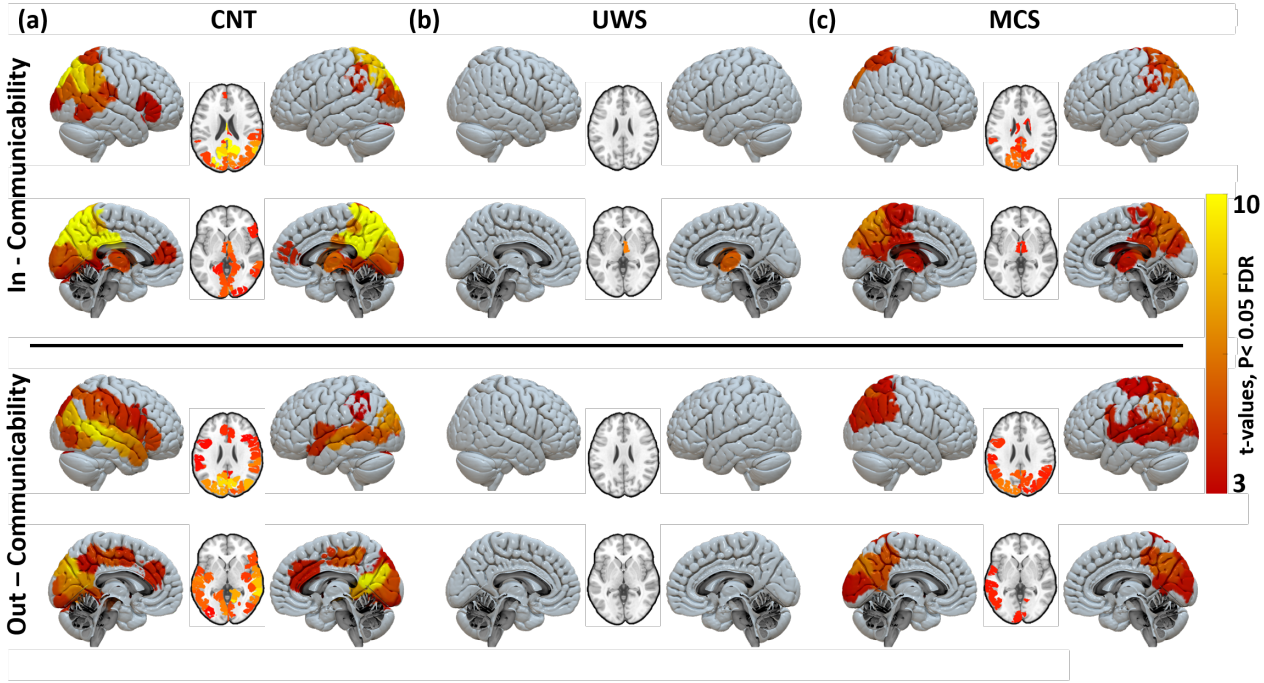

Figure 3.13: **Regions with high receiving (in-communicability) and broadcasting (out-communicability) of information.** Regions with high receiving (in-communicability) and broadcasting (out-communicability) of information, rendered on a glass brain for (a) healthy control (b) MCS vs UWS patients. The color code represents the T values, only regions with significantly high information flow (FDR corrected for multiple comparisons) are presented.

3.3.6. Marked reduction of information in- and outflow in states of reduced consciousness

After assessing the groupwise in- and out-communicability profiles, we next quantified group differences in node-wise receiving and broadcasting properties (i.e 60-200 and 2-12 computational time after perturbation) for the different consciousness states. These contrasts identify regions with more important alterations and are a first step towards developing a biomarker for consciousness.

As compared to CNT subjects, MCS patients show a significant reduction in the ability to receive information in the bilateral precuneus, PCC, cuneus, right lingual, calcarine, bilateral middle cingulum, and right middle temporal cortices. The ability to broadcast information in MCS patients as compared to CNT subjects was lower in bilateral thalamus, parahippocampus, left hippocampus, bilateral insula, inferior and middle temporal, right superior temporal and bilateral fusiform and lingual (Figure 3.14a). Most affected receiving regions comprise important hub regions, and the most affected broadcasting regions comprise areas involved in memory and self-consciousness.

The regions with impaired information in- and outflow UWS patients show a similar pattern as MCS patients, albeit more profound. UWS patients contrasted against CNT subjects show a profound reduction of the capacity to receive information at the bilateral precuneus, PCC, lingual, calcarine, fusiform, middle occipital, middle and anterior cingulum, inferior and superior parietal, supramarginal, middle temporal, inferior frontal cortices and the VMPFC. These regions encompass primary visual and auditory areas, but also higher integration areas in the PCC that have an important hub function within the whole-brain network. The reduction of information inflow in the parahippocampal cortex might be related to a loss of memory function. Reduced information broadcasting in UWS patients is present at bilateral hippocampus, parahippocampus, thalamus, caudate, amygdala, putamen, insula, inferior and middle temporal, temporal pole, right superior temporal, fusiform, lingual, calcarine, occipital, right inferior frontal cortices and the right VMPFC (Figure 3.14b). The lack of broadcasting of the subcortical regions might reduce the activity

of the whole network. The (para)hippocampal, temporal areas and insula might highlight dysfunction of processes related to memory and bodily self consciousness. UWS patients as compared to MCS patients show a significant reduction in receiving and in broadcasting of information at the left precuneus, occipital cortex, temporal and right superior parietal (Figure 3.14c). Information flow in these regions might be the most important to sustain conscious information processing.

Within the UWS patient group, in addition to decreased communicability, we observe the interesting phenomenon of hyper-communicability (i.e. greater and faster growth and decay after perturbation, Figure 3.15). Hyper-communicability is unique to the UWS patients group, and has a very similar spatial distribution as the late (i.e. 60-200 sec computational time) in- and out communicability decreases as compared to CNT subjects. The semi-instant excessive neural response after perturbation suggests that information flow in those brain regions is not only affected by reduced integration and propagation capacity, but that the whole network architecture to process information is unbalanced and dysfunctional.

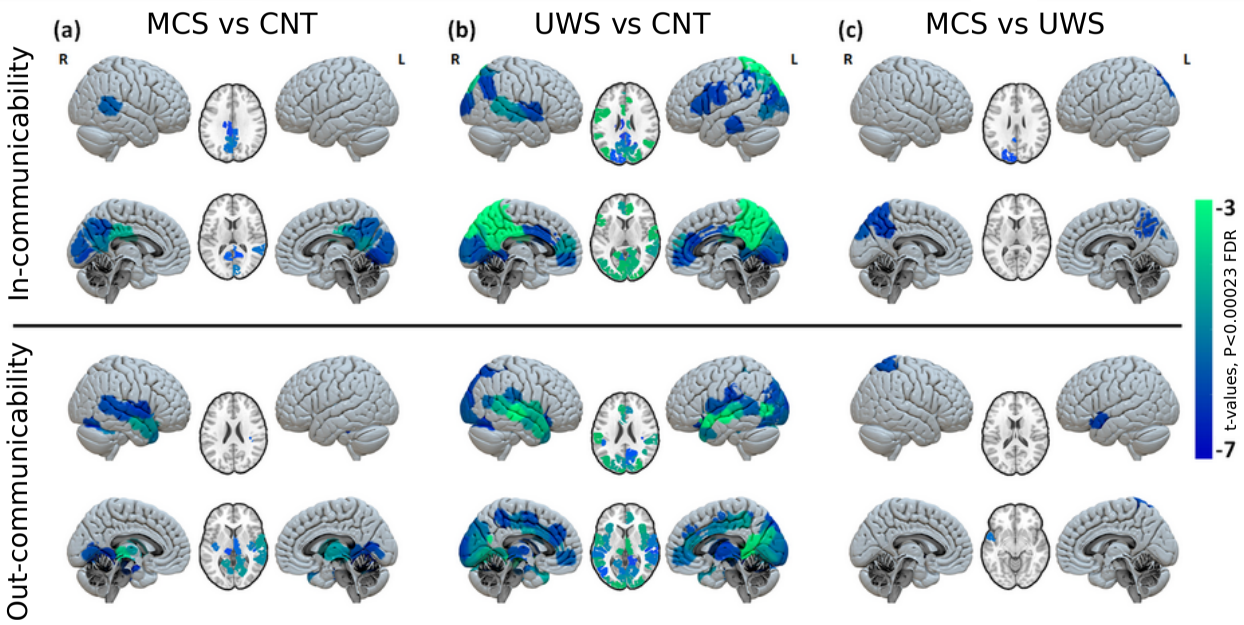

Figure 3.14: **In and out Communicability comparison between groups.** Brain regions differ in (a) MCS patients as compared to CNT and (b) UWS patients compared to CNT (c) (b) UWS compared to MCS patients for receiving (in-communicability, top) and broadcasting (out-communicability, bottom) of information. The between group effect sizes were rendered on a glass brain which showed significantly ($p < 0.05$ FDR corrected) reduced information transfer properties in MCS and UWS patients as compared to CNT subjects. There were no regions with increased communicability in MCS and UWS patients as compared to CNT subjects. Color bar represents the t-values for regions with significant between-group differences (Bonferroni corrected for 214 tests).

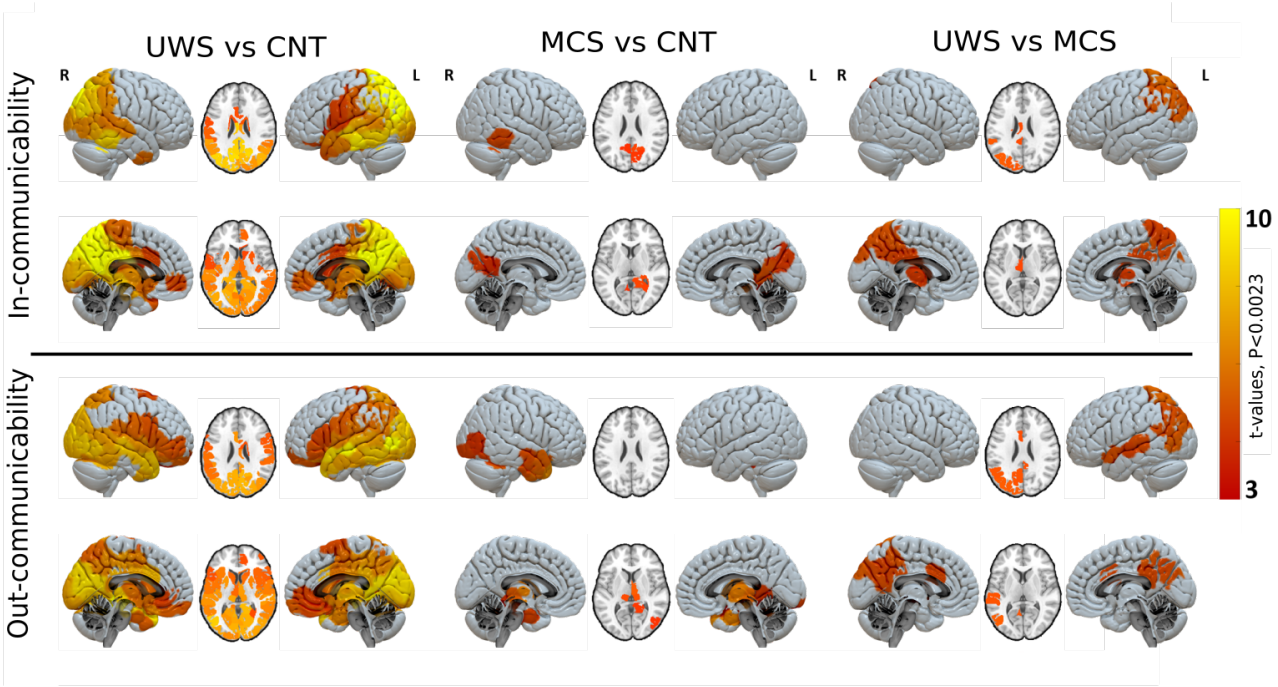

Figure 3.15: **Brain regions hyper communicability.** The hyper communicability (higher growth with sudden decay) differ in (a) UWS patients compared to HC (b) MCS patients compared to HC (c) UWS compared to MCS patients for receive information (i.e. in-communicability or information inflow, top) and broadcast (i.e. out-communicability or information outflow, bottom). Color bar represents the t-values for regions with significant between-group differences (Bonferroni corrected for 214 tests).

3.4. Discussion

In this study, we investigated the brain's ability to process incoming events in normal wakefulness and pathological altered states of consciousness. Our approach includes the assessment of the propagation of neural events by adopting both empirical and computational modeling measures. We characterize cerebral capacity in terms of integrity at the global (i.e. whole brain) level and the local (i.e. region and link) level. First, we showed that the brain propagates less spontaneous activity in reduced states of consciousness, resulting in a reduction of the brain's intrinsic ignition. Additionally, unconscious states are characterized by a fast attenuation of intrinsic BOLD fluctuations, i.e. τ, most pronounced in midline and frontal-parietal areas. We next quantified the capacity for neural propagation and integration of external, synthetic stimuli introduced in a computational model. We measured the spatiotemporal evolution of these network interactions after perturbation, so called 'communicability', at the global and regional level in terms of receiving (i.e. integration, inflow or in-communicability) and broadcasting flow (i.e. propagation, outflow or out communicability). Whole-brain communicability was reduced in DOC patients, with specific temporal dynamics for UWS and MCS patients. The reduction of receiving and broadcasting information flow was most pronounced in two distinct microcircuits. That is, the posterior regions failed to receive information in conjunction with reduced broadcasting of information in subcortical, temporal, parietal and frontal regions.

Cerebral integration and responsiveness of spontaneous events is reduced in loss of consciousness

To measure the propagation of spontaneous activity within the brain's network, we employed the Intrinsic Ignition framework. During spontaneous brain activity, brain regions can self-ignite and propagate brain activity across the rest of the network, creating transient global changes to the integration of information (Deco and Kringelbach, 2017). We found that in DOC patients, and even more pronounced in UWS patients, the ignition driven integration is significantly lower than during normal wakefulness. Previous studies in sleep and anesthesia have also shown reduced propagation of neuronal activity (Deco et al., 2017b; Signorelli et al., 2021). The

empirical results suggest that patients with altered states of consciousness have a reduced capacity for the integration of events that would lead to conscious perception.

Potentially contributing to the low intrinsic ignition is the alterations in the spatial patterns of τ values across the states. τ indicates the temporal structure of the signal and it can be seen as the time that the signal needs to come back to the basal level after suffering from a perturbation. Global decrease of the decay component decreases with decreased levels of consciousness, and is lowest for UWS patients, suggesting that the signal might stay available for processing for a shorter time. For CNT, we found that the τ values show a gradient distribution in the brain, with longer timescales in the frontal and parietal areas than the values in the subcortical and posterior areas. This gradient distribution of the timescales has been previously reported in numerous studies (Chaudhuri et al., 2015; Gollo et al., 2015; Honey et al., 2012; Murray et al., 2014; Watanabe et al., 2019). Indeed, our results are in line with previous studies suggesting that frontal and parietal areas, higher-order cortices which ensure sensory information processing, need long timescales to integrate diverse information (Hasson et al., 2008; Lerner et al., 2011; Stephens et al., 2013; Yeshurun et al., 2017; Gauthier et al., 2012). UWS patients show more homogeneous τ values across the brain compared with wakefulness, which is considered to be related to loss of the hierarchy in the brain, see Figure 3.5b. Furthermore, we notice that the regions showing the strongest decreases in τ within the UWS patient group show striking overlap with the key regions of the Global Neuronal Workspace (GNW) theory (Dehaene and Changeux, 2011; van Vugt et al., 2018). We thus believe that the reduced τ might not allow the establishment of recurrent activity between the higher order cortices and primary sensory areas, prerequisite for conscious awareness according to the GNW.

Interestingly, the temporal BOLD structure is not altered for the engagement of tasks involving different content of consciousness (Gilson et al., 2018; He, 2013), but it shows a clear change in pathological brain states (Watanabe et al., 2019). A reduction in the the τ values has been associated with a loss in the robustness of the brain network response to

fluctuations (Honey et al., 2012; Murray et al., 2014) and with a loss in grey matter volume (Watanabe et al., 2019), which, in our DOC population, could arise from a reduction in the structural anatomy (Annen et al., 2018), (see also section 2.3.5). Thus, an alteration of hemodynamics, as measured with τ can help explain the altered spontaneous neuronal dynamics observed in patients with DOC. If neuronal dynamics become more noisy, it may be weakening slow rhythms in its temporal structure, which would result in shorter τ and lower Intrinsic Ignition.

Spatiotemporal dynamics after model-based perturbation

We further studied the propagation properties of the brain. For this, we study effective connectivity (EC) after in-silico perturbation using a whole-brain model based on a MOU process. Our results showed that UWS is characterized by higher EC compared to CNT and MCS. Interestingly, when examining the local EC, MCS patients present only decreased EC, while UWS patients show regions with either decreased or increased EC. Indeed, previous studies in UWS patients, anaesthetised healthy subjects and patients with generalised epilepsy at loss of consciousness showed hyperconnectivity and increased hemodynamic response specifically in the thalamus and limbic areas (Di Perri et al., 2013; Wu et al., 2019; Cavanna and Trimble, 2006; Wang et al., 2019). The increased (re)activity of these areas might lead residual neural activity to form self-reinforcing neural loops, resulting in abnormal connectivity. This suggests that hyperconnectivity is linked with pathological loss of consciousness and that even if the unconscious brain attempts to propagate activity throughout the network, it fails to integrate the input.

The spatiotemporal structure of EC was further explored to gain understanding about how the contrasting hypo and hyper EC influence nodal temporal dynamics and global integration after in-silico perturbation. The temporal structure of EC indicates the total integration of information within the network over time after in-silico perturbation, resulting in a communicability curve (Gilson et al., 2019a). For the CNT, the response function shows an initial pattern of high communicability, in the early communicability (2-60 sec after perturbation), where the effect of the per-

turbation is propagated and integrated in the network. The limited decay in the range of late response (60 - 200 sec after perturbation) suggests a sustained propagation of the network response which might be supported by the recurrent connections and heterogeneity in brain dynamics, consistent with previous studies (Gilson et al., 2019a; Demertzi et al., 2019; Luppi et al., 2019). The communicability curve observed in UWS patients is characterized by a high early peak with short latency and steep rise and decay. The early peak in the UWS goes in line with the hyperconnectivity observed for the EC, and could indicate rapid propagation of information. However, rapid extinction of the input reflected by the low late communicability is also observed. This is likely related to the breakdown in the EC that sustains cerebral propagation. Indeed, also empirical perturbation studies by Massimini and colleagues (Massimini et al., 2005; Casali et al., 2013), show that the recruitment of global neural activity after perturbation, both in space and time is reduced during deep sleep, anesthesia and disorder of consciousness (Massimini et al., 2005; Casali et al., 2013; Colombo et al., 2019; Casarotto et al., 2016). After TMS induced brain stimulation, the temporal intensity and spatial complexity of local to global neural propagation get reduced in loss of consciousness (Casali et al., 2013; Sarasso et al., 2014), which we also observed in our in-silico perturbation by delivering into the BOLD signal. In MCS patients, the propagation of the perturbation is relatively preserved as compared to UWS patients, and although the global levels of dynamical communicability are reduced in comparison with the CNT subjects, they are closer to the healthy than unconscious range. Our findings, in line with TMS induced perturbational approaches, indicate that the unconscious brain has a weaker capacity for neural propagation and information integration, resulting in loss of awareness and cognitive processes.

Distinct pattern of receiving and broadcasting of information after in-silico perturbation characterize conscious states

Complementary to the assessment of global loss of information integration, we investigated nodal dynamical characteristics in terms of in-communicability (i.e. regional influence of a perturbation applied to the network, simplified as 'receiving information flow') and out-communicability (i.e. regional

capacity to influence the network after perturbation, simplified as 'broadcasting information flow').

Conscious healthy subjects present two different flow patterns of receiving and broadcasting information, which helps to explain the neurobiological mechanisms underlying impaired stimulus processing in terms of cause-effect structure. In CNT subjects, we noted that in-communicability (i.e. receiving information flow) is relatively higher in the posterior (precuneus, PCC, occipital and parietal cortices) and the thalamic regions, consistent with the results presented in a study using the same communicability framework (Gilson et al., 2019a). MCS patients present an incommunicability pattern similar to CNT subjects, even if the regional differences are less pronounced. UWS patients show very different incommunicability, specially the capacity to receive and integrate information is reduced in UWS patients in the posterior regions, supporting the postulates of IIT and the posterior hot zone theory. These model-based measures of information flow might indicate that the posterior regions respond to incoming information, aligning with their functional specialization as the first entry point of sensory information. Furthermore, the reduction of responses to perturbation in higher-order integration cortices (PCC and precuneus) and breakdown of broadcasting in subcortical, temporoparietal, frontal might be linked to the alternation of internal and external awareness. The PCC and precuneus are primary hub regions of the Default Mode Network that sustains consciousness and internal awareness (Laureys et al., 2004). In UWS patients, the PCC and precuneus show decreased structural connectivity (Annen et al., 2016), glucose metabolism (Annen et al., 2016; Thibaut et al., 2012), BOLD functional connectivity (Vanhaudenhuyse et al., 2010), topological properties such as integration (Rizkallah et al., 2019; Luppi et al., 2019), homogeneity and stability (see previous chapter and (Perl et al., 2020)). The functional network properties of the PCC and precuneus have also found to be involved in other pathological unconscious state such as during epileptic seizures (Wang et al., 2019), anesthesia (Luppi et al., 2019), sleep (Tagliazucchi et al., 2016a) and subjective state of dissociation induced by meditation (Panda et al., 2016). Our results provide a mechanistic explanation for the established network alterations that characterize the unconscious brain, namely

that it is caused by the reduced ability to receive information in hub regions of the DMN. The lack of receiving of information in the perceptual areas and the DMN, hamper that a stimulus or event reaches awareness, as external input is a prerequisite for external consciousness (Herbet et al., 2014). In turn, the loss of information integration in the posterior region may affect functional connectivity and recurrent processing as postulated to be crucial for consciousness by the mesocircuit hypothesis and the Global Neuronal Workspace theory.

In CNT subjects broadcasting of information flow is predominant in a broad range of cognitive modules, including the hippocampus, parahippocampal, temporal, posterior and inferior frontal regions. This subcortical-cortical loop is proposed to mediate the sensory information to be globally 'accessible' to other cognitive functions through feedforward and feedback loops in the GNW theory, and only when access to all cognitive modules occurs, sensory content is elevated to conscious perception (Dehaene and Changeux, 2011; Mashour et al., 2020). As expected, the broadcasting of information from the primary cortical to the rest of the brain is relatively preserved in MCS patients. However, information integration is importantly reduced in the unconscious UWS state. Specifically, UWS patients in comparison with CNT show reduced broadcasting of information in cortical regions involved in higher cognitive functions (i.e. precuneus, parahippocampus, mid-temporal, inferior parietal, supra marginal, anterior cingulate and inferior frontal areas). The reduction of information broadcasting in the subcortical regions (i.e. thalamus, caudate, putamen) in UWS patients aligns with the meso-circuit hypothesis (Schiff, 2010). Thus, our findings unravel that reduction of broadcasting from the thalamus, caudate and putamen leads to a breakdown of activity transmission, functional integration and lack of recurrent activity between subcortical and cortical neurons, potentially causing loss of cognitive ability, conscious perception and awareness in UWS patients.

We believe our approach could serve as a potentially useful marker of quantifying conscious level and identifying where (i.e. in low-level perceptual areas or high-level integration areas) information processing fails, in the future even at the single subject level. This might help to address more challenging aspects of the assessment of consciousness, namely the

internal awareness or subjective feeling.

Whole-brain models have emerged as a powerful tool for investigating the brain mechanism underlying pathological brain states and have proposed potential clinical applications such as the simulations of perturbations to transient from one brain state to another (i.e. from sleep to resting state) (Deco et al., 2019a; Deco and Kringelbach, 2014; Kringelbach and Deco, 2020; Gilson et al., 2019b; Perl et al., 2020; Ipiña et al., 2020). The presented approach, by addressing receiving and broadcasting of information, could help to unravel the loops that are impaired and could guide the identification of novel stimulation protocols (i.e. the type and location of stimulation).

In this study, we used a MOU generative process with linear relationships that allow extracting the spatiotemporal properties of the BOLD time series at the whole-brain level. Crucially this model is based on the estimation of the EC, which captures the BOLD dynamics and represent the asymmetric relationships among nodes. It is important to highlight also that the model explains the spatiotemporal brain activity through the modulation of the efficacies of the putative existing connections, in contrast to other models that assume that the neural activity emerges from the interaction between brain areas in an interconnected neuroanatomical network (Deco et al., 2013b; Ponce-Alvarez et al., 2015; Deco et al., 2017a). Furthermore, the optimization process tunes all the EC weights at link level –while it takes into account the network effect–, which allows describing a multivariate estimate rather than other models that fit the spatiotemporal dynamics with a few parameters only (Messé et al., 2014). The link level estimators have been shown to be a robust biomarker of task (Gilson et al., 2018) and participants (Pallarés et al., 2018). A limitation of the MOU-EC is the interpretation of the neuronal coupling, considering that this model lacks hemodynamic functions in contrast to previous models estimating ECs (Friston et al., 2003). This choice comes from the priority of the estimation robustness with simpler dynamics over the biological interpretability (Gilson et al., 2019b). Finally, the application of the Green function to derive the dynamic communicability framework can be easily adapted to distinct local dynamics for which the Green function is known, so its interpretability is not restricted to the MOU model

(Gilson et al., 2018).

The work presented in this study can be seen as a first step to understand how the states of loss of consciousness altered brain capacity for neural activation propagation and information flow in resting state. Our results suggest that the brain capabilities of propagating neural events and the temporal structure of the signals reduces in loss of consciousness. Furthermore, this is reflected in the effective connectivity of the network, which shows altered regional dynamics in two microcircuits: posterior regions fail to receive the information in conjunction with reduced broadcasting of information flow at subcortical, temporal, parietal and frontal regions. Apart from the obtained results, the main novelty of this study comes from the methods applied to explain the alteration in the brain mechanism and propagation of activity flow in loss of consciousness which are suggested to promise a great help to support diagnosis and therapeutic interventions in disease.

CHAPTER 4

Characterization of the collective activity patterns of brain dynamics across temporal scales

The brain's collective activity continuously displays complex spatiotemporal patterns at multiple scales. However, the relevant temporal scale to study these dynamics at the whole-brain level is unknown. Here, we explored how the collective features of brain dynamics change at different temporal scales. For this, we evaluated the complexity of resting-state EEG signals in terms of the diversity of activated patterns as a function of temporal coarse-graining. Specifically, we used a dimensionality-reduction technique to represent the brain's activity as a reduced number of spatiotemporal motifs, which were then used to analyse temporal activation. Next, we used the maximum entropy principle to estimate the distribution of all pattern configurations within this reduced activity space. This analysis was done by employing maximum entropy models that provided relevant information about the collective dynamics. Overall, we found that the maximal complexity of the EEG signals was observed in the 50-300 ms range. In this range, order and disorder coexist; a balance suggestive

of critical dynamics. Interestingly, this temporal scale has previously been used to detect EEG microstates. Thus, our analysis provides a theoretical justification for using this temporal scale in the characterisation of EEG patterns.

4.1. Introduction

The brain comprises individual non-linear elements (i.e. neurons) interconnected anatomically, creating large conglomerates of single cells (i.e. neural populations). A system consisting of many microscopic units, like the brain, may exhibit diverse macroscopic behaviours, which emerge from the collective activity of the units at multiple spatiotemporal scales. Indeed, coordinated patterns of activity have been observed at multiple spatiotemporal scales, as revealed by multi-electrode arrays (Beggs and Plenz, 2003; Friedman et al., 2012), optical imaging (Scott et al., 2014), fMRI (Biswal et al., 1995; Damoiseaux et al., 2006), EEG (Lehmann et al., 1987; Michel and Koenig, 2018) and MEG (de Pasquale et al., 2010; Baker et al., 2014). However, it remains unknown which are the relevant temporal and spatial scales for understanding brain resting-state activation at the whole-brain level.

EEG/MEG recordings are especially suitable for the study of brain dynamics at different temporal scales due to their refined temporal resolution at the millisecond scale. EEG dynamics have been characterised by structured patterns of activation captured in the broadband signals. These structured patterns are defined by the location of the maximal and minimal values of the EEG signals, which remain stable in specific areas of the scalp topography for a certain period. After a fast transition, their organisation changes and remains stable, creating a different scalp topography (Lehmann et al., 1987). These regular topological scalp maps of collective neural activation are called EEG 'microstates' (Lehmann et al., 1998). Since their discovery, many studies have focused on shedding light on their spatial description, duration and temporal structure (Michel and Koenig, 2018). Nowadays, it is widely accepted that the number of distinguishable EEG microstates is limited, usually in the range from two to six (Wackermann et al., 1993). Furthermore, the spatial distributions of microstate activation reflect specific brain functions such as visual, attention,

salience and auditory functions (Britz et al., 2010).

The temporal time courses of the EEG microstates are crucial for the explanation of the collective features of resting-state dynamics. It is well known that brain processing must undergo reorganisation into different patterns at a sub-second scale to rapidly respond to changing inputs and meditate complex mental activity (Bressler, 1995). Indeed, the characteristic duration of EEG microstates is 60-150 ms, in the range of the lifetime of the spatiotemporal patterns obtained using MEG and fMRI, using a whole-brain model that allows simulation of BOLD fluctuations at the millisecond scale (Baker et al., 2014; Deco et al., 2019b; Kobeleva, 2020). This range of temporal scales has been proposed to be decisive for maintaining correct brain processing. Indeed, alterations in the duration of specific microstates have been found in neuropsychiatric diseases such as schizophrenia (Lehmann et al., 2005; Koenig et al., 1999) and dementia (Nishida et al., 2013).

An intense debate has surrounded how and why the transition between microstates occurs. The transition probabilities have been considered non-random during the healthy resting-state (Lehmann et al., 2005; Wackermann et al., 1993), and randomness increases during disease (Lehmann et al., 2005). Researchers have proposed the concept of metastability as a possible mechanism underlying these fast transitions, which states that the brain shows a rich, dynamical repertoire during the resting-state and that it flexibly switches from one pattern to another (Deco et al., 2017a; Haldeman and Beggs, 2005; Hellyer et al., 2014). The flexible transitions between patterns is a property of systems working in a specific, dynamical regime, in a critical phase transition, i.e. in the phase transition between stability and instability. The study of the dynamical regime of this spontaneous activity has led to a vast amount of studies investigating critical behaviour in terms of measures of complexity and neural avalanches (Van de Ville et al., 2010; Plenz and Thiagarajan, 2007; Ponce-Alvarez et al., 2018). Nevertheless, these measures heavily rely upon the spatiotemporal scale of the recordings.

Here, we investigated how the functionally-relevant collective features of EEG resting-state signals change at different temporal scales. In order to do this, we first extracted the spatiotemporal motifs of the EEG signals

using an independent component analysis (ICA) algorithm. From the temporal and spatial properties of those spatiotemporal motifs, we calculated the capacity of ROIs to broadcast neural activation or the brain 'hierarchy' (Deco et al., 2019b). After describing the activation time-courses of the spatiotemporal motifs, we used the maximum entropy principle to estimate the probability distribution of all activation patterns. Based on a maximal entropy model (MEM), we studied the switching of the patterns in terms of entropy and their accessibility, by measuring the heat capacity. MEMs have been mainly used in micro-scale data, where the patterns are defined by binarising the activity of the electrodes. Here, our aim is to investigate how the patterns evolve from one into another, based on their activation statistics. Using these three measures (hierarchy, entropy and accessible patterns), we provided insights into the temporal scale's functional relevance for detecting and studying spatiotemporal dynamics.

4.2. Methods

4.2.1. EEG Data and source projection

Data were recorded from 18 healthy controls (27 ± 13 years, 6 female) as part of an epilepsy study at the EEG and Epilepsy Unit, University Hospital of Geneva. The local ethics committee approved this study. Each participant gave informed consent to the study. Participants were seated comfortably and were instructed to relax for about ten minutes, with eyes closed while avoiding any facial or body movements. Two participants were excluded from further analyses because of major artefacts being apparently visible in the raw data. We proceeded to analyse the remaining 16 available participants.

A full description of the imaging parameters and preprocessing pipeline can be found in (Glomb et al., 2019). In summary, resting-state EEG was collected with the Geodesic Sensor Net with 256 electrodes. Inverse solutions were computed using LAURA with LSMAC as implemented in CARTOOL (Brunet et al., 2011). Segmentation and ROI extraction was performed using the Connectome mapper (Tourbier et al., 2020). We applied the Lausanne 2008 parcellation (Hagmann et al., 2008), which

contains $N = 82$ ROIs. ROI time-courses were obtained by performing SVD on the time-courses of all solution points (~ 5000) within an ROI and projecting onto the main direction of variance (Rubega et al., 2019).

4.2.2. Filtering and binning

A band-pass filter (1-40 Hz) was applied to the ROI time courses for the first analyses. For band-limited studies, narrowband filters of 2 Hz width were used to obtain ten frequency bands (1-3 Hz, 3-5 Hz,...,38-40 Hz). We also extracted time-courses in the following brain oscillation frequency bands: delta (1-4 Hz), theta (4-8 Hz), alpha (8-12 Hz), beta (12-30 Hz) and gamma (30-40 Hz). Within each band, Hilbert transformation was applied to extract the envelope of each signal.

Time was discretized in non-overlapping bins of different sizes to study the temporal scale of the EEG dynamics. The binning was performed by averaging the envelope of each signal within each bin size (i.e. downsampling) (Deco et al., 2019b), Figure 4.1. The bin size of the downsampling fixes the temporal scale. The number of time points for each downsampled envelope, B, is given by the actual time points recorded in the original time series divided by the bin size. We completed the following analysis for each of the downsampled envelopes.

4.2.3. Extraction of spatiotemporal patterns

For the extraction of the spatiotemporal motifs that characterize the dynamical repertoire of the signals, we based our analysis on the framework previously used to detect neuronal assemblies from spiking data (Lopes-dos Santos et al., 2013), which was recently generalized to the whole-brain level by (Deco et al., 2019b).

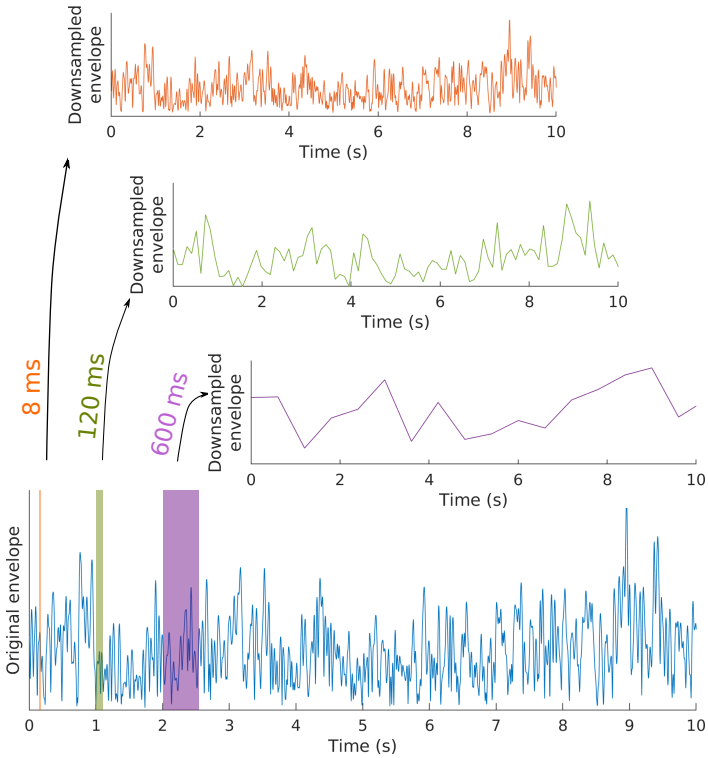

Figure 4.1: **Binning of the original envelope to extract the downsample envelopes binned with different temporal scales.**Examples of the binning of the original envelope (in blue) using three different bin sizes that define the temporal scales (8 ms -in orange-, 120 ms -in green- and 600 ms-in purple-). The downsampling of the signals is performed by averaging the original envelope of each signal within each bin size. The resulting downsampled envelopes show different levels of description of the original envelope.

Construction of the events matrix

First, the downsampled envelope of each ROI was thresholded with the sum of the mean and 1 SD of the signal. If the envelope exceeds the threshold for consecutive time points, only the first point will be considered active or marked as an event. This procedure results in an event matrix E, of $N \times B$ dimensions, where N is the number of ROIS and B is the number of time points of the downsampled envelope. This method

is a well-established point process binarization algorithm used for BOLD, MEG and EEG signals (Deco and Kringelbach, 2017; Tagliazucchi et al., 2012; Fagerholm et al., 2015). Indeed, the analysis of cortical cascades of EEG recordings, which relies on the time series binarization, shows consistent results with thresholds in the range of 1.0 to 2.5 SD (Fagerholm et al., 2015).

Extracting the patterns from the events matrix

The binarised data's spatiotemporal motifs were extracted using a dimensionality reduction technique, i.e. Independent Component Analysis (ICA). We used ICA based on previous studies where the best estimation of the motifs was obtained using ICA compared with other dimensionality reduction algorithms (Lopes-dos Santos et al., 2013). In particular, we used the fast ICA algorithm (Peyrache et al., 2010) (as implemented in the FastICA toolbox for MATLAB, `http://research.ics.aalto.fi/ica/fastica/`). The number of motifs was set to 6, based on existing literature on EEG microstates (Michel and Koenig, 2018). Each of the 6 motifs was noted as $\vec{w_c}$, with $c = 1, ..., 6$. This vector contains N values corresponding to each ROI's weights or participation in that spatiotemporal motif.

Extracting the activity time-courses of the patterns

Next, we computed the activity time course of the motifs, $\vec{A_c}$, to investigate the temporal properties of the functional dynamical repertoire. We calculated the activity time-courses by projecting the columns of the event matrices onto the space given by $\vec{A_c}$, as following:

$$\vec{A_c} = \mathbf{E}(\vec{w_c} \otimes \vec{w_c})\mathbf{E} \tag{4.1}$$

where the multiplication $\vec{w_c} \otimes \vec{w_c}$ corresponds to the projection provided by the spatiotemporal motif c and $\mathbf{E}$ corresponds to the event matrix. Briefly, the activity time-courses are given by the similarity between the spatiotemporal motif vector, , and the event matrix, $\mathbf{E}$, for each time point.

4.2.4. Measures of hierarchical organization

We investigated the roles of the ROIs in the broadcasting of neural activation by using the novel measure referred to as cohesiveness (Deco et al., 2019b; Kobeleva, 2020). It has been previously proposed that the brain cortex shows a graded distribution of functional and structural features, essential for sustaining conscious brain processing (Deco and Kringelbach, 2017; Deco et al., 2017b; Escrichs et al., 2019; Murray et al., 2014; Sporns et al., 2005). Indeed, this hierarchical distribution also has a functional role in transmitting and integrating information across the brain (Dehaene and Changeux, 2011; Mashour et al., 2020). The concept of cohesiveness comprises the influence of the ROIs in the rest of the network by considering three different aspects of the propagation of neural activation. First, the weight of the ROI i in spatiotemporal motif c, $\vec{w}_{ic}$, which reflects the participation of that ROI for that motif. Then, the probability of that motif to be activated across time, $P(c)$, given by $P(c) = \frac{\sum_t A_{tc}}{\sum_{c,t} A_{tc}}$. Finally, the 'broadness' of the component defined as its size, i.e. the correlation with the rest of the ROIs $\sum_j w_{j,c}$. Thus, the cohesiveness is calculated for each ROI i as follows:

$$Coh(i) = \sum_c (w_{ic} P(c) \sum_j w_{j,c}) \tag{4.2}$$

The variability in the cohesiveness values across ROIs is described using the hierarchy as:

$$Hierarchy = \frac{std(coh)}{mean(coh)} \tag{4.3}$$

The hierarchy is a global measure that reflects the degree of diversity of the ROIs in the spreading brain activation across the whole brain.

4.2.5. Maximum Entropy Model (MEM)

We applied a MEM to study the collective features that emerge from the statistics of the activation patterns given by the activity time courses of the spatiotemporal motifs. This model, originally proposed to study the

joint spiking activity of neurons (Schneidman et al., 2006), requires a description of the system as a binary pattern. The underlying idea of this model is to obtain the probability distribution over 2^C possible binary patterns. As we are interested in the activation of the spatiotemporal motifs and not in the synchronization of the electrodes' activity, C corresponds to the number of motifs, i.e. 6. The activation time-course of each spatiotemporal motif, $\vec{A_c}$, was binarized using a threshold given by the mean plus 1SD of the activation time-courses. If the binary activation exceeds the threshold for consecutive time bins, only the first bin will be considered active. The resulting vector for each motif c shows $\sigma_c = 1$ if this motif is activated and -1 otherwise. The activation pattern at time b is given by a vector$\vec{\sigma}$, where $\vec{\sigma}^b = [\sigma_1^b, \sigma_2^b, ..., \sigma_6^b]$.

To estimate the probability distribution of the activation patterns, $P(\vec{\sigma})$, we used a maximum entropy principle which maximizes the entropy of the activation patterns to find the most unstructured distribution. The only constraint imposed was the preservation of the activation rates $< \sigma_c >$ and the pairwise correlations $< \sigma_c \sigma_d >$ captured on the empirical data. It is well known that the maximum entropy distribution consistent with these expectation values is given by (Schneidman et al., 2006; Tkačik et al., 2015):

$$P(\vec{\sigma}) = \frac{e^{-E(\vec{\sigma})}}{Z} \tag{4.4}$$

where the normalization factor $Z = \sum_{s=1}^{2^C} e^{E(\vec{\sigma}_s)}$ corresponds to the partition function and $E(\vec{\sigma})$ to the energy of the patterns given by the following equation:

$$E(\vec{\sigma}) = -\sum_{c=1}^{6} h_c \sigma_c - \frac{1}{2} \sum_{c=1}^{6} \sum_{d=1}^{6} J_{cd} \sigma_c \sigma_d \tag{4.5}$$

where h_c represents the tendency of spatiotemporal motif c to be activated or deactivated, and J_{cd} represents the interaction between the motifs c and d.

4.2.6. Estimation of h and J parameters

The estimations of the parameters **h** and **J** were obtained using a gradient descent algorithm. Specifically, we iteratively minimized the absolute difference between the empirical activation rates ($< \sigma_c >$) and pairwise correlations ($< \sigma_c \sigma_d >$) and the predicted ones using the model and Monte Carlo simulations (Tkacik et al., 2009). In each iteration, the difference was minimized using the following equations:

$$h_c^{new} = h_c^{old} - \alpha(< \sigma_c >_{model} - < \sigma_c >) \tag{4.6}$$

$$J_c^{new} = J_c^{old} - \alpha(< \sigma_c \sigma_d >_{model} - < \sigma_c \sigma_d >) \tag{4.7}$$

where α is the learning rate ($\alpha = 0.1$). Our study stopped the simulations once the difference between the model and empirical values is less than 0.005 or if its tolerance was not reached within a maximum number of iterations defined as 100.

4.2.7. Goodness of fit

The fitting of the model was evaluated using the symmetric version of the Kullback-Leibler divergence (D_{KL}) defined as the Jensen Shannon divergence (D_{JS}). This measure evaluates the difference between the probability distribution of the empirical and model binary patterns (Marre et al., 2009) and is given by:

$$\begin{aligned} D_{JS}(P_{emp}|P_{model}) = \frac{1}{2} D_{KL}(P_{emp}|(P_{model} + P_{emp})/2) + \\ \frac{1}{2} D_{KL}(P_{model}|(P_{model} + P_{emp})/2) \end{aligned} \tag{4.8}$$

To evaluate the importance of correlations, we used the accuracy index, r_D, which is given by (Watanabe et al., 2013):

$$r_D = \frac{D_{JS}(P_{emp}|P_{modelMEM}) - D_{JS}(P_{emp}|P_{modelIND})}{D_{JS}(P_{emp}|P_{modelMEM})} \tag{4.9}$$

where $D_{JS}(P_{emp}|P_{modelMEM})$ is the Jensen Shannon divergence between the probability distribution of the empirical and the pairwise MEMs. $D_{JS}(P_{emp}|P_{modelIND})$ corresponds to the divergence between the probability distribution of the empirical and the independent MEMs. The accuracy index, r_D, estimates the pairwise model's accuracy compared to the independent model (Watanabe et al., 2013).

4.2.8. Entropy, heat capacity and critical point

Once the parameters **h** and **J** are obtained, the probability distribution of the energies $E(\vec{\sigma})$ is calculated from the model. The distribution of the energies permits obtaining relevant features of the collective dynamics.

The entropy measure describes the switching between different activation patterns, i.e. it quantifies the fluctuations across patterns, and it is given by:

$$H(\vec{\sigma}) = -\sum_{b=1}^{B} p(\vec{\sigma}_b) \log p(\vec{\sigma}_b) \tag{4.10}$$

where $p(b)$ corresponds to the probability of the activity pattern b and the *log* is the logarithmic function.

Another important quantity is the *heat capacity*, HC, which explains the dependency of the energies' distribution as a function of T. This parameter T is an analogy to the temperature in statistical physics. It is introduced in the model as a scaling factor for the model parameters as $\mathbf{h} \rightarrow \mathbf{h}/T$ and $\mathbf{J} \rightarrow \mathbf{J}/T$. Specifically, the heat capacity, HC, is given by:

$$HC([\mathbf{h},\mathbf{J}], T) = \frac{var[E^2]}{T^2} \tag{4.11}$$

The energies (E) were calculated using a large number of Monte Carlo simulations ($L = 100000$ simulations) for different values of T, see next section. The curve of the heat capacity is computed using the variance of the energies. The temperature corresponding to the peak of the curve, T_{max}, describes the collective behaviour that emerges from the statistics

of the activation patterns. The re-scaling parameter T controls the level of disorder, and it can be understood by examining the energy levels E that are accessible to the system. At low temperatures, the system is predominantly silent. It accesses few and separated excited energy levels, is relatively ordered (its entropy is low), and, since interactions dominate, the system scarcely fluctuates, leading to weak correlations. At high temperatures, the system has a high probability of occupying the excited patterns, which are barely separated, making it easy to fluctuate among them, thus increasing the disorder and decreasing the correlations (fluctuations dominate over interactions, effectively decorrelating the system). As for low temperatures, high temperatures lead to a low HC. However, for a particular temperature, $T_{critical}$, a large range of energies is accessible to the system, leading to a maximal HC, and the balance of fluctuations and interactions leads to a maximal mean correlation. This range is the expected behaviour close to a critical point where both order and disorder coexist. In conclusion, a maximal heat capacity close to the operating point (i.e. $T_{max} = 1$ in this model) corresponding to the model of the real data) suggests that the system is likely to be close to a critical state.

4.2.9. Metropolis Monte Carlo:

The Monte Carlo method is usually used in complex systems that contain a high number of random variables to obtain the probability distribution of different outcomes. The idea of the Metropolis Monte Carlo method is to generate samples of the activity patterns for given values of the model parameters, $\mathbf{h}$ and $\mathbf{J}$. Transitions between patterns are determined by the energy difference associated with those patterns. For this, we first generate a random vector of size C whose energy level is given by equation 4.5. Once that the actual energy state is known, we use the following steps:

1. Pick a random element j of the activity pattern.
2. Flip the value of the activation of that element j, i.e. from $\sigma_j = 1$ to $\sigma_j = -1$ or, otherwise, from $\sigma_j = -1$ to $\sigma_j = 1$.
3. Compute the change in the energy associated with the flipping, i.e. $\Delta E = E_2 - E_1 = -2\sigma_j h_j - 2\sigma_j \mathbf{J}\sigma_j + 2J_{jj}$.

4. The system transits to the new pattern with probability equal to $exp(\Delta E)$ (or, equivalently, remains in the current pattern with probability $1 - exp(\Delta E)$).

5. Repeat steps 1-4 iteratively for L times.

4.2.10. Phase shuffled surrogates

For the phase surrogate analysis, first, the Fourier transform (FT) of the signals was computed. The phase of the Fourier transform was substituted with uniformly distributed random numbers while preserving their modulus. Then, the inverse FT was applied to return to the time domain with the new Fourier coefficients. This procedure effectively randomizes the phases of the signals while preserving the same power spectra as the original time courses. Specifically, let $x_i(b)$ be the original BOLD time-course from the brain area i. The discrete Fourier transform of $\tilde{x}_i$ is given by:

$$\tilde{x}_i(k) = \sum_{b=1}^{B} x_i(b) e^{-j\frac{2\pi kb}{B}} \tag{4.12}$$

where j is the imaginary unit and k goes from 1 to B. The phase shuffled surrogate is given by:

$$x_i^{surr}(b) = \frac{1}{B} \sum_{k=1}^{B} |\tilde{x}_i(k)| e^{-j(\frac{2\pi kb}{B} + \varphi_r)} \tag{4.13}$$

where φ_r is random variable uniformly distributed between $-\pi$ and π. These surrogates were used to rerun the analysis and compare the results with the empirical ones.

4.3. Results

This study investigates how the EEG resting-state collective brain dynamics of 16 healthy participants change at different temporal scales. For that, we used the inverse solution of the EEG recordings extracted with

the LAURA algorithm (see Methods). In the first step, the ROI time courses were filtered using a broadband pass filter (1-40 Hz), and their envelopes were extracted using the Hilbert transform. Envelopes were down-sampled using bins of different sizes, ranging from milliseconds to seconds, i.e. the envelope was averaged within time windows of various sizes. The bin size fixes the temporal scale (Deco et al., 2019b). We binarized each of the downsampled envelopes using the mean and 1 standard deviation (SD) as a threshold. This procedure results in an event matrix **E**, of the dimensions of $N \times B$, where N is the number of ROIs and B is the number of time points, Figure 4.2 A. An ICA algorithm was applied in these event matrices to extract 6 spatiotemporal motifs, a standard number of patterns used in EEG microstates studies (Michel and Koenig, 2018). The spatiotemporal motifs were described by the vector $\vec{w_c}$, which contains the weights or participation of the ROIs in spatiotemporal motif c, Figure 4.2 B. We further explored the activation time-courses, $\vec{A_c}$, by projecting them into the original space given by the event matrices, Figure 4.2 C (see Methods). This projection reflects the similarity between the spatiotemporal motifs and the event matrices. Thus, the activation time-courses indicate when a spatiotemporal motif is activated in the EEG recordings.

4.3.1. Hierarchical organization of the brain

After having the spatial and temporal description of the motifs obtained from the downsampled envelopes in different temporal scales, we wanted to study how the role of the ROIs in propagating brain activation changes across bin sizes. For that, we used the concept of cohesiveness which was previously proposed in (Deco et al., 2019b). The cohesiveness is computed for each ROI as the multiplication of three factors; the participation of the ROI i in spatiotemporal motif c, the probability of that motif c to be activated and the correlation with the rest of the ROIs.

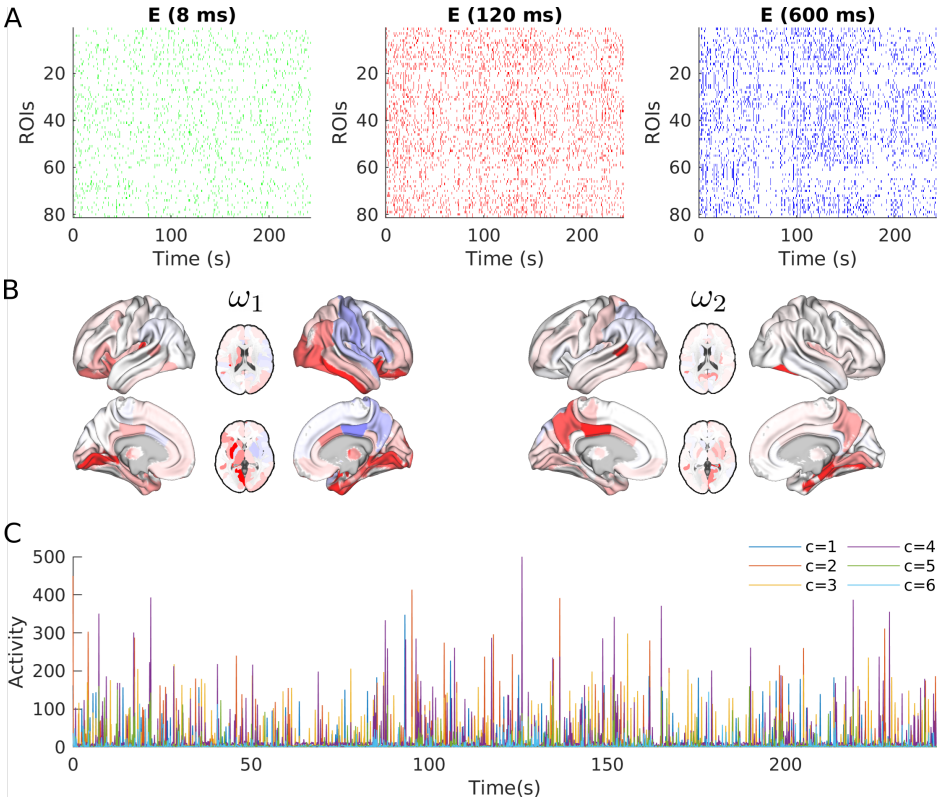

Figure 4.2: **Binning of the EEG inverse signal using binning of different sizes and extraction of the patterns. A)** Examples of the raster plots of binned envelopes using three different binning sizes (8 ms, 120 ms and 600 ms, respectively). The binning was performed averaging the signal within a window of the binning size, which fixed the signal's temporal scale. A binarization was performed in each signal using the threshold given by the sum of the mean and 1 SD. The event matrix $\mathbf{E}$ of size $N \times B$ gathers the recreated envelopes. **B)** Example of the spatial distribution of the components, $\vec{w}_c$, extracted using ICA from the event matrix $\mathbf{E}$ in A. The $\vec{w}_c$ vectors display the weight of each ROI in the component c. These examples correspond to the components extracted for the signal corresponding to the temporal scale of 120 ms. **C)** Activity courses, A_c, for each component. The activity courses were computed by projecting the vectors $\vec{w}_c$ in B) into the event matrix in A).

Our results showed that the distribution of the cohesiveness across ROIs changes depending on the bin size, Figure 4.3 A. The profiles of cohesiveness across ROIs show a non-uniform gradation for temporal scales in the

range of 100-300 ms. We found sparser distributions of the cohesiveness for this range of bin sizes compared with temporal scales of > 300 ms. The sparsity of the distribution is coming mostly from the 20 ROIs with the highest cohesiveness values. To describe those distributions qualitatively, we measured the hierarchy given by the diversity in the cohesiveness values (i.e. the standard deviation of the cohesiveness values across ROIs). We found that the hierarchy was lower for short and long temporal scales (from 0 to 100 ms and from 400 to 1000 ms) and that it reached its maximum at ~ 250 ms, Figure 4.3 B.

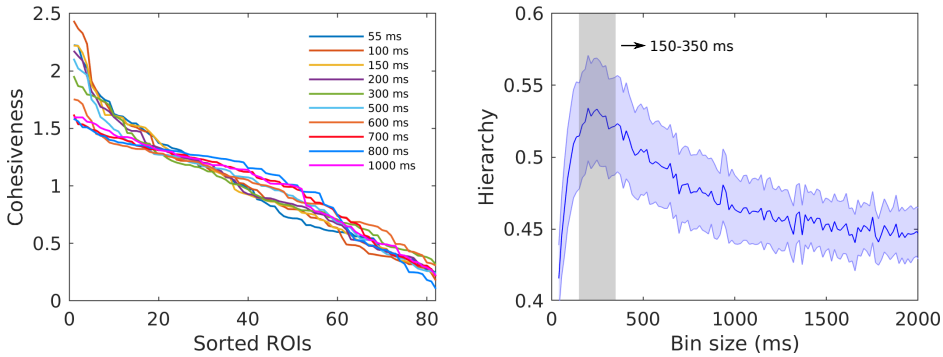

Figure 4.3: **Distribution of the local cohesiveness and global hierarchy at different temporal scales. A)** Distribution of the cohesiveness values for all the ROIs for different temporal scales (example for one subject). For each temporal scale, the distribution was sorted independently in a descending manner. The cohesiveness values show differences across bin sizes, especially in the graded values of the first 20 ROIs. Temporal scales in the range of 100-200 ms show the sparsest distribution of the cohesiveness values. **B)** The hierarchy computed as the standard deviation of the cohesiveness and as a function of all the bin sizes used for the analysis. The hierarchy changes across bin sizes, with a peak in the range of temporal scales of 150 to 350 ms. The shaded curve corresponds to the standard error across subjects. The window in grey indicates the temporal scales with the highest hierarchy.

We explored the spatial distribution of the cohesiveness values in the brain for the bin size where the hierarchy is maximal. For this specific bin size, we found that the ROIs with the highest cohesiveness values were mostly in the thalamus, cingulate and precuneus, Figure 4.4. Crucially, the PCC and precuneus were previously investigated due to their role in maintaining consciousness in different states of consciousness (Cavanna and Trimble,

2006; Wang et al., 2019; Luppi et al., 2019; Panda et al., 2016) and the thalamus is known because of its role in the feedforward excitability that is a prerequisite to support conscious processes (Schiff, 2010; Wang et al., 2019).

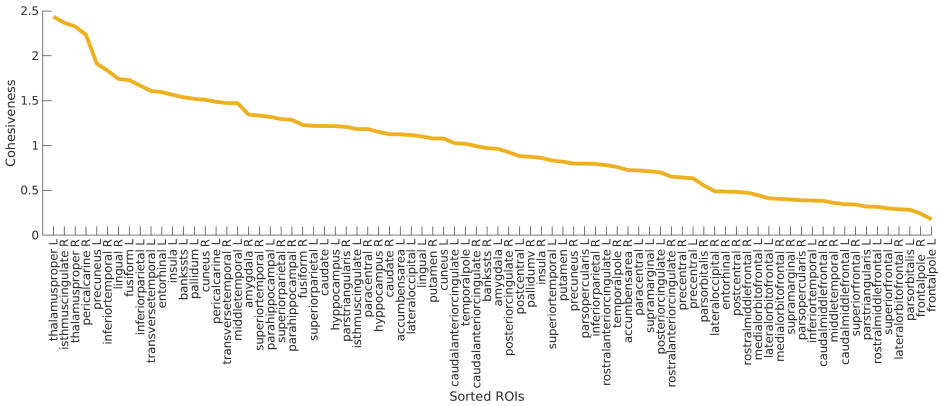

Figure 4.4: **Spatial distribution of the cohesiveness values.** Spatial distribution of the cohesiveness values for the bin size with the maximal value of the hierarchy in Figure 4.3 A. The values with the highest cohesiveness values are located in the thalamus, cingulate, thalamus and precuneus.

4.3.2. Statistics of the activation patterns

Intending to study how the activation patterns evolve from one into another and the emergent collective properties given by their activation and interactions, we investigate the activation time-courses of the spatiotemporal motifs, focusing on their statistics. We used the maximum entropy principle to build a MEM, which allows us to estimate the distribution of activation patterns and to obtain relevant information about the collective dynamics (see Methods). This model was originally proposed for studying the spiking binarized activity of single neurons (Schneidman et al., 2006). Here we aim to analyse the statistics of the motifs' activation, so activity time-courses $\vec{A_c}$, see Figure 4.5. These time-courses were discretized as $A_c = +1$ if the spatiotemporal motif c in the time point b shows an activity, A_c, that exceeds the sum given by its mean and 1 SD (activation) and $A_c = -1$ otherwise (quiescence).

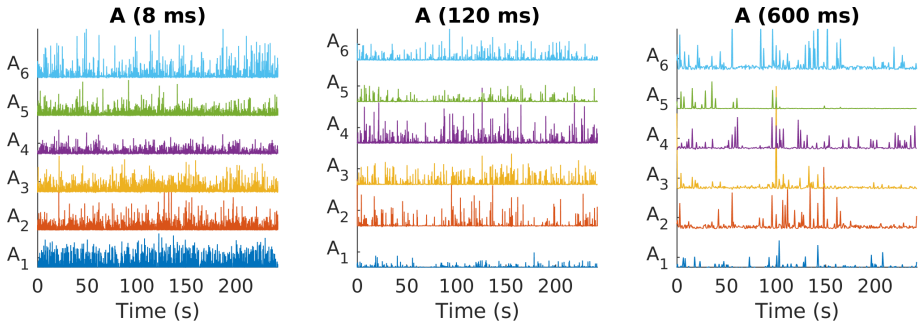

Figure 4.5: **The activity time courses of all the spatiotemporal motifs for the 8, 120 and 600 ms bin sizes.** The activity time courses were binarized using the sum of the mean and 1 SD.

For each time point b, the activity pattern, given by the binarization of the activity time-courses of the 6 motifs, is described by a binary vector $\vec{\sigma^b}$(see Methods). We used a maximum entropy principle to find the probability distribution of the activity patterns using the most unconstrained distribution. For that, the entropy is maximized by imposing the constraint of the preservation of the mean activation rate ($< \sigma_c >$) and the mean pairwise correlations ($< \sigma_c \sigma_d >$) (see Methods). The resulting distribution is $P(\vec{\sigma}) \sim \exp(-E(\vec{\sigma}))$, where $E(\vec{\sigma}) = -\sum_{c=1}^{6} h_c \sigma_c - \frac{1}{2} \sum_{c=1}^{6} \sum_{d=1}^{6} J_{cd} \sigma_c \sigma_d$ is the energy of each activation pattern. In this equation, h_c represents the intrinsic tendency of spatiotemporal motif c towards activation and J_{cd} represents the effective interaction between the spatiotemporal motifs c and d. The model parameters, $\omega = \{\mathbf{h}; \mathbf{J}\}$, were estimated from the data using a gradient descent algorithm (see Methods). We built a model for each bin size.

First, the model's goodness of fit, which provides a relative quantification of how well the model explains the empirical activity patterns, was evaluated by studying the role of the correlations in the model. The performance of the pairwise-MEMs was compared to the performance of independent-MEMs for which the Jcd are cancelled. The Jensen-Shannon divergence was used to evaluate the agreement with the data (Hahn et al.,

2017). We computed the accuracy of fit to normalize the value between 0 and 1 (Watanabe et al., 2013). Figure 4.6 shows the model's accuracy decreases for longer bin sizes, but in all cases, the accuracy $r_D > 0.8$, even for the bin size of 1 s. An accuracy of 0.8 indicates that the application of the pairwise MEM reduces the distance between the estimated and empirical distributions of patterns by 80% compared with the independent MEM.

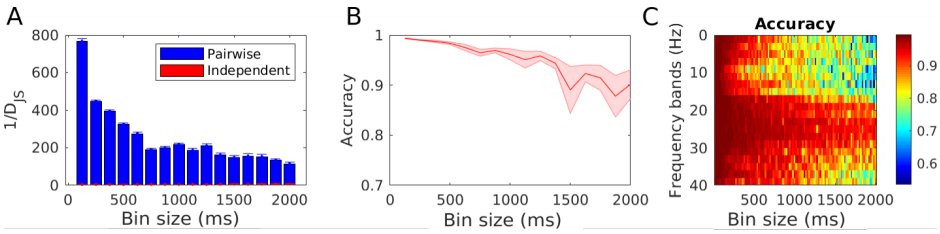

Figure 4.6: **Goodness-of-fit of the maximum entropy model MEM for different bin sizes. A)** The inverse of the Jensen Shannon divergence measures the difference between the probability distribution of the empirical and model binary patterns. A higher value in the Jensen-Shannon divergence's inverse means a smaller difference between the probability of the empirical and the model. Comparison between the empirical and pairwise distributions in blue and comparison between the empirical and independent model in red. **B)** Accuracy index for the pairwise MEM computed for each downsampled envelope using different bin sizes. The curve corresponds to the accuracy index extracted using the signal filtered in broad-band. The accuracy, r_D, is higher than 0.8 for all the bin sizes. **C)** Accuracy index for each bin size and frequency band filtered using 2Hz bands. The accuracy of the MEM pairwise model is superior to 0.8 for almost all frequency bands and bin sizes, with few exceptions in the low-frequency bands for the bin sizes around 2 s.

After checking that the model reproduces sufficiently the dynamical properties of the empirical data, we further studied the temporal entropy, H, given by the switching between the activity patterns, σ, across time (see Methods). We found that the entropy varies as a function of the bin size, Figure 4.7. We found a peak with maximal values of entropy for the temporal scales in the range 50-120 ms, suggesting that the brain dynamics described by these temporal scales show more switching between patterns.

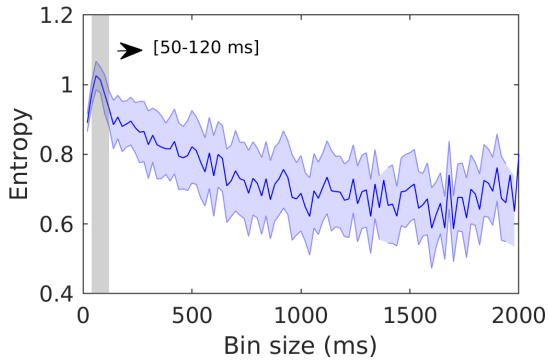

Figure 4.7: **The mean entropy shows maximal entropy for the temporal scales in the range of 50 to 120 ms.** We show the results of the temporal entropy in different bin sizes. As can be seen, very clearly, the entropy shows a peak in the range of 50 to 120 ms. The shaded curve corresponds to the standard error across subjects. The window in grey indicates the bin sizes with the highest entropy.

4.3.3. Accessible patterns

To further explore the emergent collective features captured from the activity patterns statistics, the working point of the models was studied in terms of criticality. For that, the heat capacity, HC, was calculated as a function of T. The temperature, T, is a scaling parameter of the model parameters $\mathbf{h}$ and $\mathbf{J}$ introduced, dividing the model parameter by T, i.e. $\mathbf{h} \rightarrow \frac{\mathbf{h}}{T}$ and $\mathbf{J} \rightarrow \frac{\mathbf{J}}{T}$. The temperature T controls the level of disorder. Its effect can be understood by examining the energy levels E that are accessible to the system by calculating the heat capacity, i.e. $HC = var[E]/T^2$ (Figure 4.8 A, see Methods for details). At low temperatures, the system accesses few and separated patterns of low energies, i.e. the system scarcely fluctuates (Figure 4.8 A, $T < T_c$). At high temperatures, the system has numerous accessible energy levels which are very close to each other, so that the system can fluctuate from one to another easily but in a small range of energies (Figure 4.8 A, $T > t_c$). Finally, at the critical point, the system can access a large range of separated energy levels, yielding a maximal dispersion of energies (Figure 4.8 A, $T \sim T_c$).

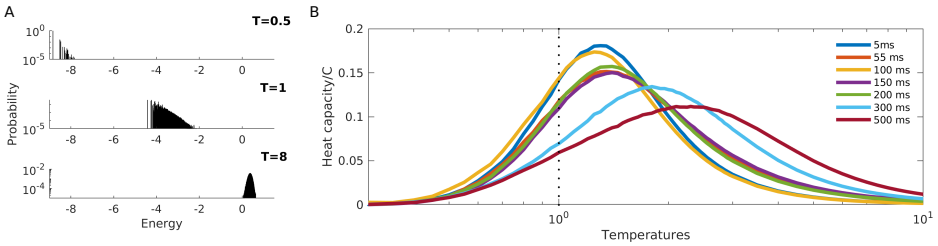

Figure 4.8: **Description of the accessible patterns given by the heat capacity and the results for the temperature corresponding to the peak of the heat capacity, T_{max}. A)** Description of the accessible patterns when considering different values of the temperature parameter T. For $T < T_c$, the system can only access a few distinguished, accessible patterns characterized by low energy values. For $T > T_c$, the system can easily access a larger number of energy levels, which are barely separated. Finally, for $T \sim T_c$, the system accesses a larger repertoire characterized by a larger range of energies. The data presented in this example corresponds to a model that shows the $T_{max} \sim 1$. B) Examples of the Heat Capacity curves in function of the scaling parameter T for different temporal scales. For all the cases, the HC shows low values for low and high values of T, and the peak of the HC curve varies in location and value across temporal scales.

We calculated the heat capacity curves for temperatures ranging from 0 to 10 and for all the temporal scales. The heat capacity curves showed a maximum value at different temperatures (noted T_{max}) for the different temporal scales, Figure 4.8 B. As shown in Methods, the heat capacity peak can be used as a diagnostic tool to assess criticality: the heat capacity is expected to peak at $T < 1$, $T = 1$ and $T > 1$ for supercritical, critical and subcritical dynamics, respectively. We found that T_{max} was close to 1 only for the temporal scales range of 50-120 ms, suggesting critical dynamics, Figure 4.9. Outside this range, a departure towards the subcritical regime was observed. These results indicate that a specific temporal scale range, 50-120 ms, exists for which critical-like dynamics were observed, indicating that the system visits a more diverse set of activation patterns in terms of associated energies.

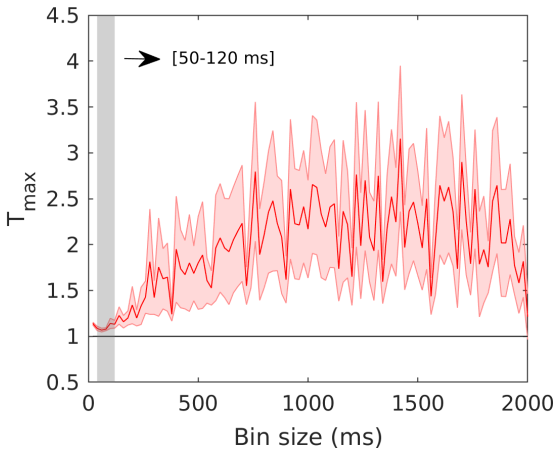

Figure 4.9: **The results of the temperature corresponding to the peak of the heat capacity in function of the bin size.** The T_{max}, reflects the physical regime of the EEG dynamics, changes with the bin sizes, showing values close to 1 for the range of bin sizes of 50-120 ms, and a monotonically increasing for larger temporal scales. The grey window indicates the temporal scales with the $T_{max} \sim 1$, i.e. critical-like dynamics. The black line corresponds to the system describing critical dynamics by definition, i.e. $T_{max} = 1$. The shaded curve corresponds to the standard error across subjects.

4.3.4. Frequency bands

We next studied how collective dynamics changes both as a function of the bin size and frequency. For this, we examined the dynamics of the EEG signals filtered in narrow frequency bands of 2 Hz width. The original signals' envelopes were obtained for each frequency band, and then, the binning was applied to each of them. As for broadband signals, the hierarchy, entropy and heat capacity were calculated for each bin size, 4.10 A. In this case, the hierarchy showed a peak for the whole spectrum of frequency bands in the range of 200-600 ms, clearer for high-frequency bands (beta and gamma) than for the lower ones. Similar results were found for the entropy, but in this case, the range is broader, and it extends from 200-800 ms, and a clear peak was found in frequency bands around 18 Hz. Finally, the maximum value of the heat capacity was located at $T_{max} \sim 1$ only for short bin sizes, in the range of 50-700 ms, except in the frequency bands of 20-30 Hz, wherein in all the cases, the T_{max} is very close to 1

suggesting critical-like dynamics.

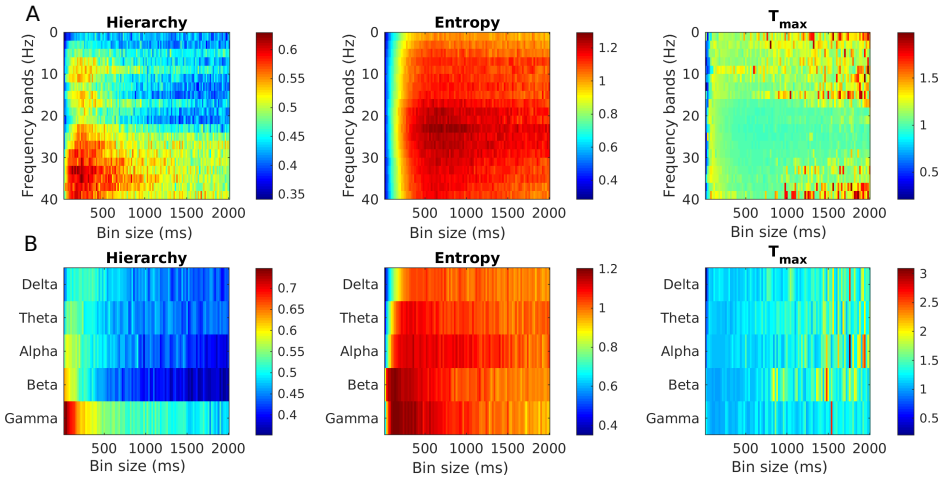

Figure 4.10: **Results for frequency bands for different temporal scales. A)** We show the results of using three different measures (hierarchy, entropy and location of the peak of the heat capacity) for frequency bands of 2 Hz wide in different bin sizes. As it can be seen clearly, the hierarchy peaks for the high frequency bands for small bin sizes ($< 500ms$) , while for the entropy the peak is clearer for lower frequency bands in the range 20-30 Hz. The T_{max} of the HC shows values close to 1 for all the frequency and bin sizes. **B)** The results of the mean hierarchy, entropy and location of the heat capacity peak across subjects for the normal frequency bands (delta, theta, alpha, beta, gamma) show similar results to the one presented in the narrow frequency bands, with a clear peak in frequency bands in the range of 100 ms for the gamma band and a peak in beta and gamma for the entropy for the same range of temporal scales. For the T_{max}, the results indicate that for bin sizes $< 500ms$, the collective behavior of the brain dynamics showed critical like dynamics, i.e. $T_{max} \sim 1$ for all the frequency bands.

Similar results were obtained for the typical frequency bands, Figure 4.10 B. The hierarchy showed a clear peak in the gamma band, and for the entropy, the results showed a more prominent rise for the high-frequency bands (beta and gamma). Finally, for the bands from delta to beta, for short bin sizes, the T_{max} remains close to 1 and then varies to higher values. For the gamma band, it remains close to 1 for all the bin sizes.

4.3.5. Scalp level

To study the reproducibility of the results at different levels, we investigated the dynamics of the EEG data obtained directly from the scalp channels without applying the algorithm to extract the inverse solution of the ROIs time courses. In contrast with the results obtained from the inverse solution signals, the scalp signals showed more varied results. The hierarchy for the broadband signals shows a decay with the bin sizes, and for the frequency bands from 1-20 Hz, it shows a decay for the small bin sizes and the contrary tendency for the higher bands in the range of 20-40 Hz, see Figure 4.11.

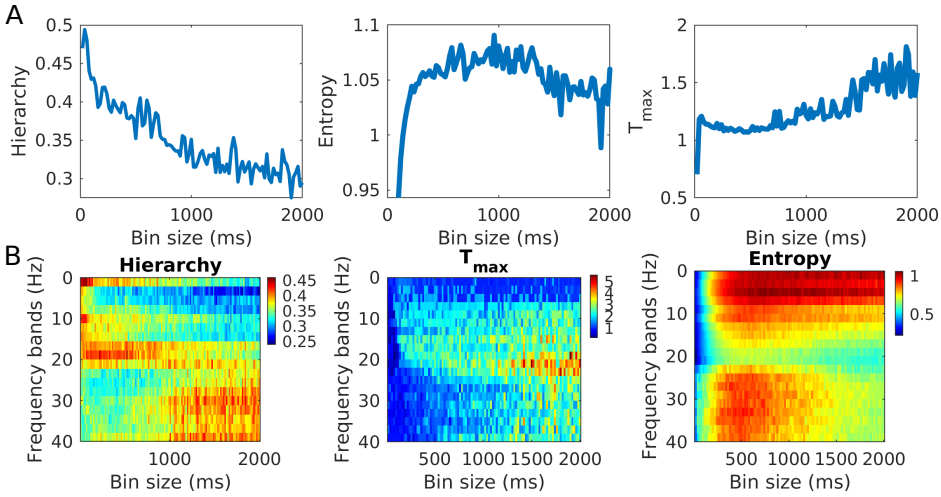

Figure 4.11: **Main results using recordings in the scalp space obtained from 204 channels. A)** Results of the hierarchy, entropy and temperature corresponding peak of the heat capacity for different temporal scales at scalp level showed that the hierarchy shows a decay with the bin size, the entropy shows an increase that stays constant for the bin sizes $>$ 500 ms and T_{max} of the HC shows critical-like dynamics from 50 ms to 1s. B) The results using narrowband filters in the range of 2Hz showed that the hierarchy shows variability across frequency bands, the entropy shows a clear peak for the high frequency bands only, which was not shown in the low frequency bands and the T_{max} show critical like dynamics for the bin sizes $<$ 500 ms for the frequency bands in the range 20-40 Hz, and $T_{max} > 1$ in the frequency bands $<$ 20 Hz for all the bin sizes.

We also found that the entropy in the broadband signals increases and then remains stable for the temporal scales $>$ 200ms, similar to the frequency bands' results, where we also found differences across bands. Finally, the results of T_{max} of the heat capacity are the only ones that showed comparable results to the ones obtained in the inversed signals, especially in the higher frequency bands. The mismatch of results across measures points that the three measurements are describing different aspects of the dynamics. Furthermore, these results indicate that the inverse signals give a more consistent description to extract spatiotemporal motifs and collective features.

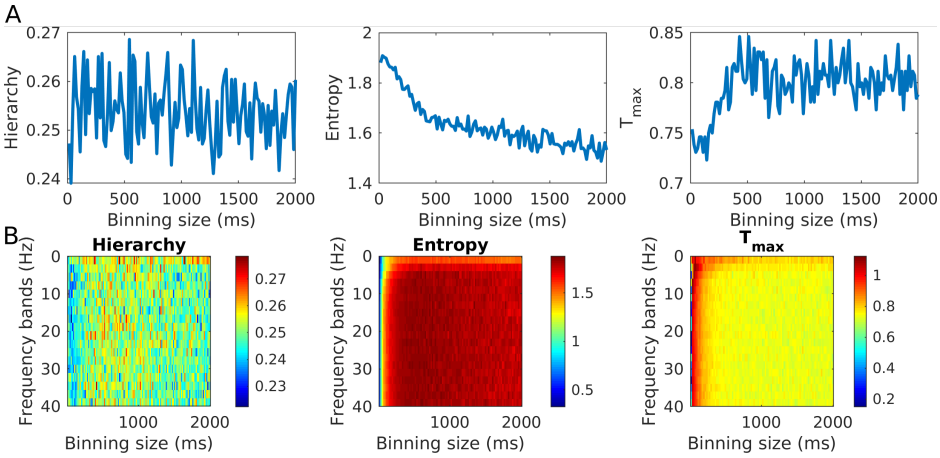

Figure 4.12: **Results for surrogate data using the three measures (hierarchy, entropy and T_{max}). A)** Broadband results for the hierarchy, entropy and maximum heat capacity in the shuffled recordings showed that the hierarchy shows very fluctuating results for the bin sizes, the entropy reduces with the bin sizes and the T_{max} show values < 1 for all the bin sizes. **B)** Results for the three measures obtained using the shuffled signals filtered in narrow bands of 2Hz width show high heterogeneity in the hierarchy, homogeneous values of entropy and subcritical dynamics in the HC.

4.3.6. Surrogates

Finally, we performed a phase-shuffled surrogates analysis to validate the obtained results. All the calculations were rerun with the shuffled data that preserves the power spectral density of the signals but destroys the

correlations. Results suggested an absence of a peak in the hierarchy curve, neither in the broadband nor in the narrow band (see Figure 4.12). Similar results were obtained for the entropy, which shows an increase for tiny bin sizes and then remains stable for both filters. Lastly, the heat capacity peaks increase at short bin sizes and then decay to supercritical dynamics, $T_{max} < 1$. These results validate our framework and clarify that results are reflecting the dynamics captured from the signals.

4.4. Discussion

In this study, we analysed how the collective features of brain activation extracted from EEG resting-state signals change as a function of the temporal scales. We showed that the collective features change in terms of diversity of broadcast pathways, quantified by the hierarchy, which is maximal for the temporal scales around 200 ms. We also built MEMs based on the statistics describing the synchronisation of the activation patterns. We found that the entropy of the switching of the activation patterns is maximal at temporal scales between 50 and 150 ms. In the same range of temporal scales, our results suggested that the collective dynamics depict a shift to the critical regime. When testing other temporal scales, the collective features of brain dynamics were characterised by low hierarchy and entropy, and subcritical dynamics. Overall, our results demonstrate the relevance of the temporal scale when observing and describing the EEG spatiotemporal patterns and dynamics. Furthermore, they provide a theoretical justification for using this temporal scale in the characterisation of EEG patterns.

Description of the macroscopic collective behaviour across temporal scales

Our results indicate that the global description of brain dynamics changes with the time scaling of the signals and, crucially, in a very narrow range, from 50-300 ms, this description coincides with the properties that maximize the hierarchical distribution of broadcast pathways across ROIs and the dynamical repertoire of the brain. Previous works have suggested

a hierarchical organisation of functional and structural features at the whole-brain level (Mesulam, 1998; Deco and Kringelbach, 2017; Sporns, 2013). Functionally, the intrinsic regional neural time scales have suggested a hierarchical organisation that distinguishes between the transmodal and unimodal sensory regions (Murray et al., 2014; Watanabe et al., 2019; Golesorkhi et al., 2021). This functional hierarchy is also been observed in the propagation pathways of internal perturbations (Deco and Kringelbach, 2017; Escrichs et al., 2019), which are impaired in low-level states of consciousness (Deco et al., 2017b; Signorelli et al., 2021). Furthermore, converging evidence shows hierarchical organisation in spatial terms, that is, in its topographical architecture (Sporns, 2013; van den Heuvel and Sporns, 2011; Zamora-López et al., 2011). Overall, previous research agrees that a hierarchical organisation is important for ensuring correct brain processing, and that imbalances of this hierarchy can lead to diseases (Watanabe et al., 2019; Gollo, 2019). Our results suggested that the maximal distribution in the broadcasting pathways, i.e. maximal hierarchy, is obtained for the range of 50-250 ms. Furthermore, brain areas with large cohesiveness values play a central role in broadcasting information, such as the thalamus, parahippocampal, hippocampus and fusiform, some parts of the cortex, most regions of the cingulate, the precuneus and superior parietal, which have been previously identified as key regions to maintain conscious processing (Dehaene et al., 1998; Tononi and Koch, 2008; Schiff, 2010; Haber and Calzavara, 2009; Sanchez-Vives et al., 2021; Annen et al., 2016).

Using the MEMs, we identified interesting collective emergent features of brain activation patterns, captured from the activity time courses using different temporal scales. A system showing high entropy values is a favourable functional scenario, since it permits the flexible exploration of the dynamic repertoire, facilitating a dynamic response to a stimulus (Tononi and Koch, 2008; Deco and Kringelbach, 2014; Garrett et al., 2013; He, 2013). This switching among activation patterns has been previously suggested to be a fundamental dynamical property of resting-state activity, in line with the hypothesis of the brain behaving as a metastable system that can flexibly switch from one pattern to another (Tognoli and Kelso, 2014; Werner, 2007; Beggs, 2008; Kitzbichler et al., 2009; Deco and Jirsa,

2012). Moreover, the MEMs also allow the estimation of the system's heat capacity for each temporal scale, a measure that quantifies the extent of the accessible dynamical repertoire. Indeed, a high heat capacity indicates that the system can display many energy patterns and that these patterns are distinguishable (Figure 4.8). Thus, maximal heat capacity indicates a large capacity to represent information in numerous separable energy levels. The resulting heat capacity curves suggested that brain dynamics are critical in the range of 50-150 ms, while other temporal scales suggest subcritical dynamics. Working in the critical regime is especially beneficial for the brain, since it optimises several brain functions, such as information transmission, input sensitivity and an optimal balance between robustness and flexibility (Shew and Plenz, 2013; Beggs and Plenz, 2003; Haldeman and Beggs, 2005; Munoz, 2017).

Our results also show that the collective features show different descriptions across bin sizes for the frequency bands, both in narrow and established bands. For the inversed signals, the gamma band showed maximal hierarchy and switching between more accessible activation patterns for short bin sizes. This frequency band has been strongly associated with the ventromedial-prefrontal cortex (Mantini et al., 2007). On the other hand, alpha and beta frequency bands showed maximal entropy and critical dynamics for all temporal scales. These bands have a strong positive correlation with the default and self-referential network (Mantini et al., 2007; Laufs et al., 2003). Thus, the EEG dynamics described by different frequency bands might explain different brain processes characterized by different temporal scales, but in order to explain the collective network features, the broadband signals show more robust results consistent across the three measures.

Characteristic temporal scale in the range of 50-300 ms and its cognitive implications

The study of spatiotemporal network activation in the last years has shown that the whole-brain activation patterns have a temporal scale of hundred milliseconds (Deco et al., 2019b; Baker et al., 2014; Lehmann et al., 1987; Dehaene et al., 1998). Indeed, research using different neuroimaging meth-

ods coincide in the same range of temporal scales for explaining resting-state dynamics. It has been shown that the lifetime of EEG microstates is in the range of 60-120 ms (Lehmann et al., 1987; Koenig et al., 2002; Michel and Koenig, 2018). Furthermore, using a whole-brain model that allows the simulation of fMRI dynamics at the millisecond scale, it was found that the time scale of 200 ms is optimal to describe the spatiotemporal structure of the collective patterns (Deco et al., 2019b; Kobeleva, 2020). Using MEG, coordinated patterns have been extracted using hidden Markov models, with a mean lifetime of around 200 ms (Baker et al., 2014). Consistently, our results highlighted that, in the range of 50-300 ms, the collective behaviour of brain activation shows crucial properties that might be responsible for ensuring conscious processing, i.e. large values of hierarchy and entropy, and critical-like dynamics. Similarly, it has been proposed that the duration of microstates is crucial to explain specific properties of brain dynamics, such as the mono-fractal behaviour based on the Hurst exponent, which is a characteristic of critical systems (Van de Ville et al., 2010).

This range of temporal scales has been related to conscious cognitive processing. This temporal scale coincides with the mean duration of EEG microstates, which constitute the 'basic building blocks of cognition', underlying conscious cognitive activity (Lehmann et al., 1987). Furthermore, according to the global workspace theory of consciousness (Baars, 2002; Dehaene et al., 1998), the brain's processing of conscious experience occurs at the critical temporal scale range of 200-250 ms (Dehaene and Changeux, 2011; van Vugt et al., 2018). In line with this theory, studies showed that sequentially presented stimuli are not perceived as separate when they follow each other within less than 80 ms (Efron, 1970), and masking a stimulus is efficient when presented with a latency of less than 100 ms (Libet, 1993). Interestingly, a similar temporal range was found for episodes of synchronous thalamocortical activity (Llinás and Ribary, 1998), sequence of alpha bursts (Williamson et al., 1996), visuomotor pattern discrimination task in monkeys (Ding et al., 2000) and face-recognition tasks in humans (Rodriguez et al., 1999).

Limitations and future work

One potential limitation of this study is the number of subjects and unique parcellation applied to extract the spatiotemporal motifs. Previous studies have suggested that the properties of spatiotemporal patterns depend on the number of regions of the parcellation in the fMRI time series (Kobeleva, 2020), and it could be interesting to apply this analysis to EEG data and determine the optimal number of brain regions for extracting the collective features of brain dynamics. Another interesting extension of this work could be to study the alterations in collective brain properties across temporal scales in multiple brain states, such as in patients that suffer from neuropsychiatric disorders, low-level states of consciousness or participants engaged in tasks.Alterations in the organisation of temporal brain dynamics have been shown during diseased brain dynamics, such as changes in the duration of specific microstates, and an increase in the randomness of the transition between microstates (Rieger et al., 2016; Lehmann et al., 2005; Tomescu et al., 2015; Nishida et al., 2013). The extraction of the temporal scales with maximal hierarchical organization and critical dynamics could be a biomarker to characterize brain states (Ponce-Alvarez et al., 2021).

The algorithm presented here for extracting the spatiotemporal patterns in EEG signals differs from the previous algorithm for extracting the EEG microstates. Instead of studying the signals' extrema and their evolution across time, we performed a dimensionality reduction using ICA to extract the spatiotemporal motifs that explain the binarised signals' maximal variance. We used binarization to avoid using noisy signals and consider extreme values, following the logic of the microstate extraction algorithm. The algorithm applied here has been previously used successfully to extract spatiotemporal motifs that agree with the well-established resting-state networks (RSNs) of fMRI and MEG data (Deco et al., 2019b). Further studies should consider the relationship between the patterns extracted here and typical microstates, considering the spatial distribution and their temporal structure.

Our results suggest a key range of temporal scales, from 50-300 ms, where

the brain's signals show a maximal hierarchy, maximal switching between activity patterns and maximal diversity in the patterns' accessibility, suggesting critical-like dynamics. These results provide a possible theoretical justification for using this temporal scale in the characterisation of EEG patterns, increasing the understanding of the spatiotemporal structure of resting-state activity, which in turn can be used to understand the alterations in different brain states.

CHAPTER 5

General discussion

The present work explored the mechanisms of the collective neural dynamics during normal wakefulness and low-level states of consciousness. For the latter, I studied the loss of consciousness induced by two different origins: a pathological case that was studied using data from patients who suffered brain injuries that lead to disorder of consciousness (DOC) and a physiological case that was studied using data from healthy participants that underwent propofol anesthesia and recovered from it. I used different whole-brain models that focus on different properties of neuronal dynamics in the previous chapters. This section aims to summarize the findings and to put them in context with the literature, while bridging the results across the different models to provide an overarching viewpoint of consciousness-related modulations of brain activity patterns.

In chapter 2, we compared the phase synchronization properties in pathological and pharmacological low-level states of consciousness and found that brain phase-synchronization patterns were less connected, less recur-

rent and more segregated in time than in healthy conscious states, consistent with previous studies (Tagliazucchi et al., 2016a; Demertzi et al., 2015; Amico et al., 2014; Barttfeld et al., 2015; Chennu et al., 2017; Rizkallah et al., 2019; Luppi et al., 2019; Monti et al., 2013). To gain insights into the possible mechanisms, we studied a whole-brain computational model based on a Hopf bifurcation (Deco et al., 2017a; Jobst et al., 2017; Saenger et al., 2017; Deco et al., 2018a). The results indicated that the brain dynamics in low-level states of consciousness were more constrained by the structural connectivity due to lower coupling values on a global level, consistent with previous research (Alkire et al., 2008; Tagliazucchi et al., 2013; Jobst et al., 2017; Demertzi et al., 2019). We further showed that bifurcation parameters in normal wakefulness tended to display more stable noisy oscillations than low-level states of consciousness. Crucially, our results suggest that the heterogeneity in local dynamics was reduced in low-level states of consciousness. Notably, this effect was mostly observed for the structural hub ROIs, which showed strong negative values of the local bifurcation parameter during normal wakefulness and a dominant contribution to system's stability. The results suggest that the differentiation between hubs and non-hubs is a crucial marker of consciousness, promoting the core-periphery organization of the brain networks.

Chapter 3 continued elaborating on the state of pathologically altered states of consciousness by investigating the changes in effective connectivity. This was done using a model that allows for the quantification of propagation of brain activity after a perturbation. Using the intrinsic ignition framework, we showed that loss of consciousness reduces the propagation of brain activity through the brain's network. The observed reduction of the brain's intrinsic ignition capabilities is consistent with previous studies (Deco and Kringelbach, 2017; Signorelli et al., 2021). A major contribution of intrinsic ignition properties was given by the τ parameter, which describes the time constant of each network node and, thus, determines the time that dynamics need to come back to the baseline value after a perturbation. DOC patients showed more homogeneous τ values, with reductions for the whole DMN and frontoparietal network in UWS patients, while MCS patients showed reduced τ only in the ACC and PCC, and recovery in the frontoparietal cortices. Diving

deeper into the mechanism that explains the propagation of perturbations through the networks, we used a whole-brain model based on a multivariate Ornstein-Uhlenbeck (MOU) process as a generative model (Gilson et al., 2016) that was interpreted within the dynamic communicability framework (Gilson et al., 2017; Estrada and Hatano, 2008). Interestingly, each group's response function to unit perturbations in all nodes showed different dynamics that suggest that the perturbations in the CNT were propagated through the recurrent connections in the network and that this integration was impaired in DOC patients. The reduction of receiving and broadcasting information flow was most pronounced in two distinct microcircuits. Posterior regions failed to receive the information conjugate with reduced broadcasting of information flow of subcortical, temporal, parietal and frontal regions, in line with previous studies (Boly et al., 2017; Koch et al., 2016). DOC patients compared to CNT showed reduced broadcasting of information in the subcortical regions and those regions involved in higher cognitive functions, specifically the thalamus, caudate, precuneus, parahippocampus, mid-temporal, inferior parietal, supramarginal, anterior cingulate and inferior frontal cortical areas (Dehaene and Changeux, 2011; Mashour et al., 2020).

In Chapter 4, I studied the collective dynamics of EEG signals at different temporal resolutions. To characterize the statistics of collective activity, I used maximum entropy models to described the binarized EEG data with varying bin sizes. The results showed a maximal hierarchy in the states, maximal switching and critical-like dynamics in the temporal scale in the range of 50-300 ms. Notably, this temporal scale coincides with the lifetimes of the EEG 'microstates', i.e. 50-150 ms, which are considered the 'basic building blocks of cognition', underlying conscious cognitive activity (Lehmann et al., 1987) and with the patterns observed in the brain dynamics captured by different neuroimaging methods (Deco et al., 2019b; Baker et al., 2014). Thus, the results suggest that the temporal scale for observing the brain dynamics is influential for describing the brain networks' collective features, consistent with previous works (Deco et al., 2019b; Kobeleva, 2020; Dehaene et al., 2003; Lehmann et al., 1998; Michel and Koenig, 2018).

In the following, I will discuss how the results of the different sections relate between each other, in light of the current scientific literature.

5.1. Heterogeneous and hierarchical organization of the brain networks is fundamental for maintaining consciousness

The heterogeneous and hierarchical distribution of nodal brain properties, i.e. the variability in parameters such as the structural degree or the excitability across the brain regions, has been widely investigated (Zamora-López et al., 2010; Deco and Kringelbach, 2017; Dehaene and Changeux, 2011; Chaudhuri et al., 2015; Gollo et al., 2015; Chen et al., 2015; Cocchi et al., 2016; Honey et al., 2012; Murray et al., 2014; Watanabe et al., 2019; Hilgetag and Goulas, 2020). Indeed, patterns of coordinated activation derived from fMRI-BOLD signals exhibit a hierarchical structure of modules-within-modules (Bullmore and Sporns, 2009; Sporns, 2011). Furthermore, physiological analyses showed that brain regions follow a hierarchical ordering in the timescale of their intrinsic fluctuations, as given by activity autocorrelations (i.e. shorter timescales in unimodal sensory regions and larger in DMN and frontoparietal networks) (Ito et al., 2020; Watanabe et al., 2019; Murray et al., 2014). In addition, the Global Workspace Theory states that multiple functional modules work together to support the conscious perception by forming a hierarchical transmission of the activation that carries information for conscious content (Baars, 1997; Dehaene and Changeux, 2011; Mashour et al., 2020). Altogether, this evidence suggests a hierarchical organization of brain regions that ensures the transmission and integration of inputs during resting-state. This hierarchical organization may confer important evolutionary and adaptive advantages, particularly the ability to create modules that can respond to the environment without affecting the entire system's function (Simon, 1962).

Consistent with this view, the studies presented in this thesis showed a hierarchical spatial distribution of functional parameters across brain regions during conscious wakefulness in healthy subjects. The results showed a breakdown of this hierarchical organization in low-level states

of consciousness. In chapter 3, two empirical analyses were performed that also account for the distribution of the propagating properties of the network nodes. On one hand, the intrinsic ignition method showed that the perturbation-induced global integration presents higher hierarchy for healthy awake subjects than for DOC patients (see Figure 3.4), in line with previous findings (Deco and Kringelbach, 2017; Deco et al., 2017b; Escrichs et al., 2019). On the other hand, the intrinsic time scale of fluctuations in the fMRI-BOLD time series, i.e. τ, was reduced for DOC patients, which showed more homogeneous values, thus indicating an attenuation of hierarchy of time scales in low-level states of consciousness (see Figure 3.5 and 3.6). These results are consistent with the hierarchical distribution of the intrinsic fluctuations observed in previous work (Murray et al., 2014) and its homogenization during disease (Watanabe et al., 2019). The hierarchical distribution of the intrinsic timescales might have a functionally relevant role for brain processing by ensuring that short time scales in the sensory areas can detect and faithfully track dynamic inputs. In contrast, longer time scales can be responsible for the integration of information (Murray et al., 2014).

Chapter 4 showed that the temporal scale where EEG dynamics have maximal entropy and critical-like behavior coincides with the scale of maximal hierarchical distribution across brain regions (see Figure 4.2B, 4.6 and 4.8). Thus, this functional hierarchy, given by the standard deviation of the distribution of the cohesiveness values across the brain regions, was reduced for the temporal scales yielding small fluctuations and subcritical dynamics. We found that the temporal scales that account for the spatiotemporal patterns that describe maximal hierarchy and critical dynamics, i.e. 50-300 ms, coincide with the previous lifetimes of brain processing patterns (Lehmann et al., 1998; Michel and Koenig, 2018). Notably, our results indicated that the maximal hierarchical organization is achieved for critical-like dynamics. This is consistent with previous studies showing that hierarchy is an emergent property of critical systems (Muñoz et al., 2010; Moretti and Muñoz, 2013; Ódor, 2016).

Furthermore, early studies on structural connectivity have shown that the brain network shows a hierarchical/modular topology with a central rich-

club, in which brain regions with a high number of connections are also highly connected among themselves (Zamora-López et al., 2010; van den Heuvel and Sporns, 2011). The analysis performed in chapter 2 described this hierarchical distribution of the brain anatomy and its functional role by studying the topological alterations in connectomes of DOC patients. The results presented in section 2.3.5 indicated that the connections of the hubs in the healthy subjects are reduced or missing in the DOC patients (see Figure 2.13). This alteration suggests that the connectome of DOC patients lacks structural connections mostly for the hub regions, which, in turn, induces an attenuation of the core-periphery organization of the network. In this line, lesion-based data from both animals and humans shows that localized injuries have specific functional consequences affecting the core-periphery architecture (Langlois et al., 2006; Alstott et al., 2009). Evidence from studies in other brain states supports the idea of a breakdown of the human anatomical connectome underlying neurophysiological and neuropsychiatric disorders (van den Heuvel and Sporns, 2019; Rudie et al., 2012; Lord et al., 2017; Vaessen et al., 2013; Alexander-Bloch et al., 2010; Zhang et al., 2018). This core-periphery architecture, i.e. the presence of a highly connected rich-club, has been suggested to be one of the main mechanisms of neural networks to sustain robustness, a network property that allows a system to maintain its functions despite external and internal perturbations (Csermely, 2018; Kitano, 2004; Ponce-Alvarez et al., 2020), to develop fast and efficient responses (May, 1972), and to facilitate the learning process (Bassett et al., 2013).

Beyond studying the empirical functional and structural connectivities, the studies presented here also examined the dynamical properties of whole-brain models. The heterogeneous model used in chapter 2 allows the characterization of the dynamical regime of each nodal dynamics and showed that, during conscious wakefulness, the heterogeneity of the regional dynamics is reduced in low-level states of consciousness. Notably, the largest alterations of regional dynamics were found for the hubs which, as shown by linear stability analysis, ensure the network stability. These results are consistent with previous computational studies demonstrating that hierarchical organization increases the stability of self-sustained network activity (Kaiser and Hilgetag, 2010). The observed homogenization

of bifurcation parameters, mostly affecting the hubs, yield an attenuation of the core-periphery architecture. Moreover, by using the injured structural connectivity of the DOC patients in the whole-brain model, the loss of heterogeneity in the local dynamics was more pronounced than using the healthy structural connectivities. These results suggest that the loss of the hierarchical organization of the human connectome implies the homogenization of the dynamical properties of the brain regions and leads to a loss or reduction of consciousness at a behavioural level.

Altogether, our results confirmed the previous pieces of evidence suggesting that (i) hierarchical distribution of the intrinsic functional properties is essential to ensure the maximal switching between global activity patterns and the emergence of criticality in the brain; (ii) the maximal hierarchy in the broadcasting of activity flow is needed for maintaining consciousness; (iii) low-level states of consciousness show a breakdown or reduction of hierarchical structural and functional properties, mostly in the hub regions; and (iv) a breakdown in the hierarchical organization of the structural connectome has important effects in the reduction of heterogeneity of the dynamical parameters.

5.2. The role of hubs' local dynamical properties in the propagation of activity and their functional properties

One of the main conclusions of Chapters 2 and 3 is that the brain's dynamics, structural properties, and effective connectivity are altered in low-level states of consciousness compared to conscious wakefulness. On the one hand, results in Chapter 2 indicated the nodal dynamics, given by the local bifurcation parameters, showed strong alterations in specific brain regions (i.e. structural hubs) in low-level states of consciousness in comparison to healthy wakefulness. On the other hand, as shown in chapter 3, specific subnetworks showed changes in their ability to propagate activity through the network. These alterations are reflected in the statistical properties of the BOLD time series (i.e. τ) and their response to perturbations through the effective connection (i.e. Σ, the role in broadcasting and receiving information flow). In the following, to relate the local dy-

namics to network propagation, I will compare the properties of the nodal dynamics obtained with the Hopf model and the properties of the connections given by the MOU model.

Figure 5.1 shows that the local bifurcation parameters and the decay exponent, τ, measured in the data, highly correlate for healthy controls (Spearman test, $\rho = 0.88, p < 0.001$). Indeed, the brain regions displaying strongly stable noise oscillations (i.e. those with strongly negative bifurcation parameters) show the shortest values of τ. As mentioned in Chapter 3, the time-constant τ relates to the time that a brain area needs to recover after a perturbation. Moreover, brain regions with strongly negative bifurcation parameters coincide with the structural hubs (Figure 2.8) and contribute the most to the network's stability (Figure 2.11). Thus, the results indicate that hubs are less responsive to perturbations, enforcing their key role in maintaining the stability of the network (Ipiña et al., 2020; Perl et al., 2020).

On the other hand, to relate the two models, one way is to compare the model parameters such as the local bifurcation parameters of the Hopf model and Σ, which is a model parameter of the MOU that quantifies the input noise to each node. Figure 5.1. shows a significant correlation between the bifurcation parameters and Σ (Spearman test, $\rho = 0.69, p < 0.001$). This correlation indicates that the brain regions with negative bifurcation parameters have the lowest values of Σ, suggesting that the dynamics of those regions, i.e. the structural hubs, are characterized by smaller variances in their signal see Figure 5.1.

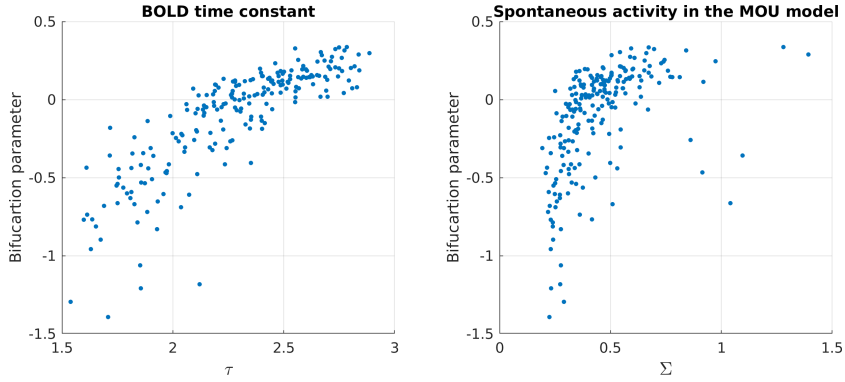

Figure 5.1: **Exploration of the relationship between the regional dynamical regimes and their dynamical properties. A** Scatter plot showing the relationship between the mean local bifurcation parameters obtained in Chapter 2 and the values of τ calculated from the average across subjects in chapter 3, in both cases considering the healthy control participants. **B** Relation between the bifurcation parameters and Σ which quantifies the variance of the signals.

Finally, the relationship between the bifurcation parameters and the in/out communicabilities can also shed light on the properties related with the information flow. Figure 5.2 shows that the relation between the bifurcation parameters and in/out communicability depicts a distinction between the regions with negative bifurcation parameters and the regions with bifurcation parameters close to 0 (Spearman test, $\rho = 0.46, p < 0.001$); the regions with the more negative bifurcation parameters show low values of in and out communicability while the rest of the nodes, i.e. the regions that show their bifurcation parameter is close to 0, show larger values of communicability (Spearman test, $\rho = 0.49, p < 0.001$). We found that strongly negative bifurcation parameters were associated with low communicability. Altogether these results suggest that the hubs' functional role might be to stabilize the network rather than the common assumption that the main role of hubs is to transmit information across the brain network. Indeed, the stability analysis, the relation between bifurcation parameters, communicability, τ, and Σ, suggest that hubs have a key role in maintaining the stability of the network and being resilient to perturbation.

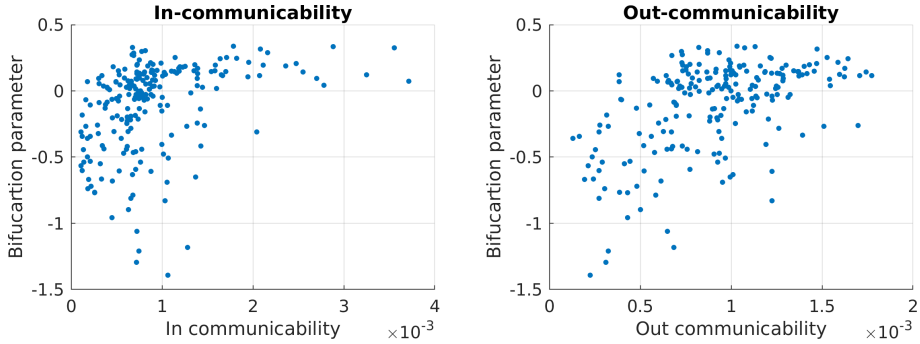

Figure 5.2: **Relationship between the bifurcation parameters and in/out communicability.** Scatter plot showing the relationship between the mean local bifurcation parameters obtained in Chapter 2 and the values of in/out communicability calculated from the average across subjects in chapter 3 for the healthy control participants.

One can find several literature attempts that investigate the hubs' key cognitive role in sustaining brain dynamics. Indeed, simulations studies employing a steady-state attractor model have suggested that the hubs may allow the brain to sustain a large functional repertoire of states characterized by diverse configurations of peripheral regions around a stable high degree core (Deco and Jirsa, 2012; Senden et al., 2014). Concerning the role of the oscillatory behaviour of the hubs, several studies have investigated the cognitive role of these dynamics under the hypothesis that these key regions can facilitate the synchronization among groups of cortical regions, suggesting that the hubs can support functional coupling among peripheral brain regions (Gollo et al., 2015; Senden et al., 2017; Schmidt et al., 2015; Senden et al., 2014). These studies have focused on investigating the changes of the oscillatory dynamics when the brain is involved in specific cognitive tasks. According to them, hub regions may utilize oscillations as a local control mechanism to organize brain regions into functional networks as they dynamically adjust their oscillatory behaviour in response to changing task demands. At the same time, these studies suggested that hubs were not oscillatory during rest, but they show noisy dynamics and could, thus, not improve a specific rhythm on the cortex; this behaviour might be more conducive to flexible re-coupling among peripheral regions. Indeed, the hubs' negative values during rest allow larger groups of peripheral regions to engage in oscillatory behaviour

and, hence, engage in functional coupling without producing a fully coupled state (Senden et al., 2017). Recent studies have also shown a division in the oscillatory regimes along with the level of consciousness (Ipiña et al., 2020; Perl et al., 2020). These studies showed that during healthy wakefulness the brain dynamics are characterized by stable dynamics in the frontoparietal areas, while in low-level states of consciousness, the brain dynamics show a reduction of oscillations in sensory areas and a loss of stability in the DMN.

It should be noted that, in the present thesis, the brain regions associated with hubs were given by the DTI structural connectivity matrices and were mostly located in subcortical regions. Opposite to this, many of the previous studies that have discussed the role of the hubs in brain dynamics used brain atlases that only include the brain cortex without considering the subcortical areas. In these cases, the brain regions with the highest structural connectivity values are different from those obtained here, and the interpretation of the results is also different.

5.3. Possible mechanisms underlying alterations of consciousness

The present studies have investigated the resting-state activity mechanism in healthy subjects and states of altered consciousness at the whole-brain level, based on the signals recorded with neuroimaging methods. In all the studies presented here, the physiological mechanism underlying those alterations was not investigated. One of the most relevant points for understanding consciousness is the quest to find the neurobiological mechanism of consciousness that not only takes into account the mechanistic role of the brain regions at the whole-brain level but also considers the microscopic aspects of the reduction or loss of consciousness (Crick and Koch, 1990; Llinás and Paré, 1991; Koch et al., 2016). In the following section, I will discuss the possible neural mechanisms, from a microscopic to a macroscopic level, which may also offer valuable insights into the field of consciousness and explain the neural bases of loss and recovery of con-

sciousness.

A candidate framework has been be inspired by intracortical single-pulse electrical stimuli and mesoscopic LFP recordings. Cortical bistability has been proposed as a simple mechanism responsible for the emergence of sustained interaction among cortical areas (Compte et al., 2003; Sanchez-Vives et al., 2017). According to this framework, the neuronal activation is characterized by two regimes; first, there is an initial activation where the signals show an increase in the amplitude (UP state), and then, the neurons' signal depicts deactivation that reflects a silent hyperpolarized state (DOWN state) (Pigorini et al., 2015). Down states, mainly generated by activity-dependent potassium (K+) currents, may be critical for consciousness (Timofeev, 2001). Indeed, disruptions in this mechanism have been reported during sleep (Pigorini et al., 2015), caused by alterations of inhibition/excitation balance (Murase et al., 2004) or due to white matter injury (Timofeev, 2001). Furthermore, cortical bistability has been proposed to account for the complexity observed in resting-state activity and altered in low-level states of consciousness (Sanchez-Vives et al., 2017). This mechanism could be responsible for the alterations in the local oscillatory regimes that have been observed in Chapter 2, where alterations in the local neuronal dynamics of specific brain regions yield a shift in the bifurcation parameter and alter the stability of the network. Furthermore, given that, in Chapter 3 we showed that the EC is altered when changing local neuronal variables, e.g. the excitability and synaptic efficacy, one expects to have alterations in the effective connections when the microscopic UP/DOWN dynamics are altered. Indeed, a recent microscale study using electrical stimulation and recordings in isolated cortical slices showed that complex causal interactions, measured by a PCI-like measurement, could be restored by pharmacological manipulations that reduce neuronal bistability (D'andola et al., 2018) .

Other perspectives have been proposed to account for the cellular mechanisms supporting consciousness (Aru et al., 2020). From the point of view of information flow, studies have shown that the cortical layer 5 pyramidal (L5p) cells have a central role in the neurobiological mechanisms of

consciousness (Crick and Koch, 1990; Bachmann and Hudetz, 2014; Aru et al., 2019). The cell bodies of L5p cells lie in layer 5 of the cortex, but their dendrites span across all layers reaching the surface of the cortex in layer 1. Layer 5 pyramidal neurons consist of three compartments, an apical compartment that integrates information from higher-order processes, the basal compartment receiving information from lower compartments, and the coupling compartment that integrates activity from both pyramidal compartments and the thalamus. In a recent study (Suzuki and Larkum, 2020), the apical compartment's behaviour in awake and anaesthetized animals was evaluated by optogenetically stimulating the apical compartment of L5p cells. According to the results, the awake states' stimulation leads to large effects that promote the high-frequency firing of neurons. On the other hand, during the anaesthetized states, the same stimulation do not propagate the soma, suggesting that the basal and the apical compartments are decoupled under anesthesia. Indeed, according to the 'Dendritic Integration Theory' (DIT), if the pyramidal cells are in the coupled state, activity can freely propagate, activate the thalamus, spread through corticocortical loops, and give rise to global dynamics of consciousness (Aru et al., 2020). This hypothesis can be associated with DOC patients, where the circuit might be predominantly affected by the thalamus and/or the basal and coupling compartments, while, in anesthesia, the apical compartment seems most affected. Interestingly, we found that the thalamus' structural connections are impaired in DOC patients, which, according to this hypothesis, could be associated with decoupling in the apical compartments. Comparing the local dynamics in the thalamus in DOC patients and sedation with conscious wakefulness, our results suggest that the local bifurcation shows a strong deviation from the conscious wakefulness, which might reflect the decoupling of these compartments. Furthermore, this theory claims that the decoupling is associated with the propagation of the inputs through the cortico-cortical loops. This claim is consistent with our results in chapter 3, indicating that the nodal properties of the thalamus show a breakdown in the capacity of broadcast activation flow across the network.

Another potential neurobiological mechanism underlying loss of consciousness is an alteration, at the mesoscopic level, of the excitatory-inhibitory

balance in favour of inhibition. Indeed, it is well known that propofol is an agonist of inhibitory GABA-A receptors (Yip et al., 2013; Jurd et al., 2003). Recent evidence using the whole-brain computational Dynamic Mean Field model (Deco et al., 2018b) that incorporates the information of the density of GABA-A receptors across the brain regions, quantified using PET, has been shown that the GABA-mediated inhibition is crucial to explain the characteristic brain dynamics captures during propofol-sedation. Furthermore, when considering the distribution of GABA-mediated inhibition, the fitting of the model of the DOC patients improved, suggesting that human consciousness arises from a delicate balance of local excitation and inhibition (Luppi et al., 2021). So, according to this view, the imbalance of excitation and inhibition could be the common neurobiological mechanism underlying loss of consciousness during propofol sedation and in DOC patients, even if the cause of the loss consciousness is different (Luppi et al., 2021). This hypothesis goes in line with our results that show similar global and nodal alterations in low-level states of consciousness induced by anesthesia or DOC.

Finally, at the macroscopic level, physicians have long attempted to adapt concepts and methods from statistical mechanics to shed light on the organization of biological systems (Bialek et al., 2012; Kelso, 1984; Haken et al., 1985; Hopfield, 1982). In this view, non-trivial system's behaviors emerge from the interactions of its units (i.e. neurons or brain regions) leading to qualitatively different states. Recent evidence has demonstrated that this framework could also give a plausible explanation to the alterations captured in the brain dynamics of different brain states (Tagliazucchi et al., 2016b; Fekete et al., 2018; Ponce-Alvarez et al., 2021). These studies have shown that the alterations in the macroscopic brain dynamics during states of anesthesia-induced sedation are associated with shifts in the dynamical regime of the brain that move the brain dynamics away from the critical point, supporting the reduction of complexity captured under those states, as shown in chapter 2 and 3 and in previous studies (Casali et al., 2013; Hudetz et al., 2015; Schartner et al., 2015). Furthermore, according to our results, during healthy wakefulness, the regional dynamics are characterized by a high level of heterogeneous dynamics which is also a signature of criticality. Finally, the reduction in the global coupling that

is shown in chapter 2 during low-level states of consciousness is a sign of reduced connectivity in the brain network which might indicate supercritical dynamics, as has been suggested in the case of different anaesthetics (Ponce-Alvarez et al., 2021).

In summary, several potential mechanisms could be responsible for consciousness at the microscopic (imbalance in the UP/DOWNs, alterations in the layers of specific neurons in the thalamus), mesoscopic (alteration in the excitatory-inhibitory balance in favour of inhibition), and macroscopic (shift from criticality) levels. Future models will need to consider all these levels of description to explain consciousness and its alterations.

5.4. Limitations

While the usefulness and limitations of the whole-brain models have been discussed in the previous chapters, some limitations of the studies presented here require further discussion. On one hand, some caveats relate to technical limitations of data acquisition that will hopefully be solved in the forthcoming years. Many others concern the field of computational modelling, a field that is in continuous growth and that still needs improvements (Kringelbach and Deco, 2020; Kobeleva et al., 2021).

5.4.1. Technical limitations

Some of these limitations arise from the empirical neuroimaging data used on the studies, i.e. EEG and fMRI recordings. In chapter 4, EEG signals were used to extract the collective activity patterns of the resting-state dynamics and how they change across temporal scales. The EEG signals offer the opportunity to study brain dynamics at a very high temporal resolution, in the order of milliseconds, but it lacks spatial resolution, restricted to the number of scalp electrodes. In addition, the volume conduction limits the interpretation of the data because one local electrode not only detects neuronal activity from that area but may also record the activity of other sources remotely located, which results in an intrinsic correlation among signals, leading to the estimation of sham links affecting the connectivity metrics (De Munck, 1988; Van de Steen et al., 2019;

Haufe et al., 2013; Brunner et al., 2016). Thus, to overcome this limitation and obtain physiologically plausible results, brain source activity reconstruction is strictly required before computing connectivity. However, the underlying brain source activity cannot be estimated uniquely from the scalp data without invoking priors or constraints on the inverse solution. Still, there is a big debate in the field of source reconstruction models, so further research should be done to determine the optimal procedure to obtain the reconstructed EEG data (Rubega et al., 2019; Marinazzo et al., 2019).

One also faces limitations in the case of fMRI recordings, their acquisition, analysis and interpretation. Firstly, the BOLD signal origin is not well understood up to date. The BOLD signal reflects the brain's hemodynamic response which is an indirect measure of neural activity (Buxton et al., 2004). Furthermore, the fMRI BOLD recordings are contaminated by the low-frequency noise from scanners and participants' breathing and heartbeat (Constable, 2006; Power et al., 2012). Due to all those different noise sources causing distortions in the recorded data, it is important to preprocess the recorded data. It has been shown that the preprocessing of the data plays a very important role in data-analysis and modelling studies due to the variability found in the results concerning the steps given in this process (Botvinik-Nezer et al., 2020). For these reasons, in the last years, the neuroscience community is moving towards making robust, structured and common pipelines for the preprocessing of the data, avoiding variability in the results, and making reliable interpretations of the obtained results.

A deep understanding of the mechanism of loss of consciousness requires creating individualized models that portray subjects' specific information. Here, there was an effort to build models of individualizing time series and connectomes, but the results were not conclusive due to the noise and high variability across subjects. One key limitation for performing single-subject analyses is the variability and noise in the single subject structural matrices. Indeed, this a common limitation is given by the complexity of fibre tracking, which involves many steps inherently sub-

ject to potential errors from and decision regarding local fibre orientation modelling, integration/ propagation, interpolation, seeding, masking and stopping criteria (Jeurissen et al., 2019; Donahue et al., 2016). Given the effort that is being made to improve these acquisitions and preprocessing (Schilling et al., 2020), we hope to benefit soon from the individualized models, especially in the diseased brain, in the search for better treatments.

5.4.2. Models usefulness, differences and limitations

The field of whole-brain modelling is a recent and emergent discipline that has been rapidly growing during the last years. However, due to the high variability in the models' assumptions, approximations and interpretations, this field still requires many improvements that ensure robustness, reproducibility and less ambiguous analysis (Kringelbach and Deco, 2020; Gilson et al., 2019b; Munoz, 2017). In this section, we will discuss the limitations of the models presented in these studies.

In chapter 2, intending to describe the phase dynamics of each brain state, we chose a whole-brain model based on oscillators. In particular, we chose the Stuart Landau oscillators, representing the normal form of a Hopf bifurcation. Despite its simplicity and non-biological origin, the model has shown to generate a rather accurate fit to the BOLD dynamics and distinguish between brain states, beyond the success of other models in the past (Deco and Kringelbach, 2017; Saenger et al., 2017; Jobst et al., 2017). This model introduces different dynamical regimes in a simple way by only containing two types of parameter models; a global parameter and local bifurcation parameters. However, due to this simplicity, some features of the data could be missing in the description. For example, the model has a strong dependency on SC, which determines the interaction between nodes. As we stated above, it is inherently associated with noise and inter-subject variability sources, along with the lack of directionality in describing the interactions between nodes. Furthermore, the model fits the data by optimizing the global coupling parameter, which scales the underlying SC, which assumes uniform conductivity across the

brain without exploring local conductance. Further studies should work in this direction which might create a more robust model sensitive to local changes, both dynamic and structural, giving further information about the heterogeneity of the brain dynamics. Another potential limitation of this model is the fitting; in contrast to the other two models where the fitting was performed in a top-down fashion, this fitting is calculated in a bottom-up fashion considering the similarity of the simulated and empirical global connectivity measures. Other approaches could investigate fittings that combine the top-down and bottom-up descriptions.

Chapter 3 uses a MOU process to estimate the MOU-EC that reproduces the empirical covariance matrices. The choice for using the MOU dynamics is motivated by the simplicity of the tractable analytical calculation and the richness of the generated activity when modulating the parameters (Gilson et al., 2019b), which allows interpreting the generated activity using graph theory. One of the main advantages of this model is the extraction of the Green function as the basis for information processing based on the cause of activity propagation rather than on the observed activity. Furthermore, the MOU allows modelling the potential heterogeneity in conductivity by adapting the effective connectivity to the empirical data (Gilson et al., 2016). Indeed, in this model, instead of relying on the SC, we use model-based estimates of the effective connectivity where measures of FC can enhance and supplement the SC.

Finally, we used a probabilistic computational model, which uses the statistics captured from the experimental data and the maximum entropy principle to build a model for the distribution over the system state. This procedure automatically generates a Boltzmann-like distribution describing the probability of the states of the system through an energy function (Tkačik et al., 2013). It should be noted that this model is not an analogy to the system described in the ferromagnetic models at thermal equilibrium, but it is a mathematical equivalence: the Boltzmann distribution arises by assuming that i) the relevant observables are the mean activations and the interactions limited to the second order (only pairwise correlations, not triplets or higher-order correlations), and ii) that the

distribution has maximum entropy (i.e. less structure). Given these assumptions, the model model parameters (biases and couplings) are given by the Lagrange multipliers when seeking to maximize functions (i.e. the entropy) subject to some constraints (i.e. on the means and pairwise correlations). However, when interpreting the argument of the Boltzmann distribution as a physical energy, we do make analogies. Rigorously, the energies of the maximum entropy model, are equal to the patterns' minus log probabilities, or "surprise", minus the lnZ (a constant, analogous to the free energy), i.e. $E(\sigma) = lnP(\sigma) + lnZ$. Thus, the variance of the energy (heat capacity) measures the range of surprises of the different collective states. A large heat capacity allows the system to represent sensory events that occur with a wide range of likelihoods (energy states that are distributed, numerous, and separable).

The MEM has provided interesting insights into the understanding of the physical properties in the context of statistical mechanics (Schneidman et al., 2006; Tkacik et al., 2009; Ponce-Alvarez et al., 2021; Munoz, 2017; Ponce-Alvarez et al., 2018). However, even if this model benefits from the few assumptions to build the model, it faces several limitations. First, the model's inference relies heavily on the amount of data used to extract the empirical data's spatiotemporal properties. This dependency on long recordings is a strong limitation when the activity time series is recorded at the whole-brain model. Recently, a new algorithm has been proposed to describe the collective activity patterns of a system composed of up to 200 elements (Ezaki et al., 2017), which improves the algorithm applied in chapter 4 that has a limit of 10 elements (Tkacik et al., 2009). In both cases, the temporal acquisition must be very long to ensure a good fitting of the model, which is hard when considering neuroimaging recordings, such as EEG and even more in fMRI. On the other hand, this model assumes independence in the temporal sequence of the energy patterns, i.e. it presumes that there is no sequential correlation in the energy patterns. The time-independency can be a serious limitation considering the temporal correlations of the activation time courses. Algorithms using a Markov approximation have been proposed to overcome this limitations but at the cost of increasing the model's complexity and the need for large datasets (Marre et al., 2009). All these limitations suggest that more accurate

measurements and detailed analysis would be needed to explore further the collective features and description of the existence of an underlying dynamical critical process (Munoz, 2017).

Another general criticism is that these computational models rely on the existence of a theoretical point where the best possible fit to empirical observations (Munoz, 2017). The criticism is coming from the fact that if the empirical data that we are considering has very rich functional features, i.e. is very complex; then, it seems almost a tautology to conclude that the best fitting of the model is captured in the dynamical regime where the model shows critical-like dynamics or the transition between phases. Indeed, this regime is the only regime where the parameter space generates complex patterns and dynamics. In this view, interesting observations are deviations from criticality, more than criticality per se. For instance, MEM analysis of fMRI data has shown that, while dynamics during wakefulness were found to be critical, anesthetized dynamics were supercritical (Ponce-Alvarez et al., 2021).

Altogether, even if computational models have allowed investigating and increasing our knowledge about the brain mechanism, as shown in this thesis, the field of brain computational modelling still needs further improvements. These improvements should follow the line of combining different approaches, develop common pipelines of preprocessing, acquire more accurate recordings, analyses that allow for individualized modelling and a formalization of the field (Kobeleva et al., 2021).

5.5. Future outlook: perspectives of the whole-brain models

In the quest for clinical applications, future models should include the influence of other biological factors, such as neurotransmitters, proteins or genes. One point that should be further explored is the inclusion and combination of different techniques such as neurophysiological and neuroimaging methods to enrich and explore a more detailed description of the resting-state activity (Bettinardi et al., 2015). In this way, var-

ious spatiotemporal scales could be included in the models, allowing a more complete description of brain dynamics. Recently, the inclusion of the PET-based spatial distribution (density maps) of neuromodulators in whole-brain models has been investigated (Deco et al., 2018b; Luppi et al., 2021). The inclusion of neuromodulator maps significantly increases the fitting of the model (Deco et al., 2018b; Luppi et al., 2021). Similarly, studying the levels of consciousness, the inclusion of GABA receptors has helped to understand a potential neurobiological mechanism underlying loss of consciousness (Luppi et al., 2021). Other studies that account for the density of myelin, estimated through T1/T2 maps, have reported improved fitting of the model (Demirtaş et al., 2019). These initial efforts in combining different methods, scales and mechanisms in the computational models could help understand the brain mechanism and, ultimately, consciousness in the brain.

Further work should also translate the knowledge and valuable understanding of brain dynamics obtained in theoretical studies, such as the ones presented in this dissertation thesis, into potential applications that can improve the well-being of humanity. The study of neuroimaging data of low-level states of consciousness during the last decades, particularly DOC patients, has been very important in understanding brain dynamics in these states. The advancements in the neuroimaging methods have allowed the development of new biomarkers that have facilitated the work of the clinicians (Owen et al., 2006; Owen, 2019). Further evidence from experimental clinical studies shows that stimulation in certain brain areas can alleviate neuropsychiatric and motor disordered disease symptoms such as Parkinson (Williams and Okun, 2013). Restricting to low-level states of consciousness presented here, one can find attempts in the literature of potential protocols to provide non-invasive therapeutic procedures based on stimulation such as transcranial direct current stimulation(tDCS) and transcranial magnetic stimulation (rTMS). Indeed, tDCS and rTMS attempted to provide therapeutic treatments in DOC patients targeting the posterior regions (Lin et al., 2018; Huang et al., 2017; Lin et al., 2019), and preliminary results shows posterior region stimulation by tDCS and rTMS helps in functional recovery in DOC patients (Lin et al., 2019). On the other hand, from animal research, it is known that the thalamic stim-

ulation improves the level of consciousness after seizures (Chudy et al., 2018; Gummadavelli et al., 2015). In DOC patients, deep brain stimulation is also attempted targeting thalamus and subcortical regions to excite the neural activity in subcortical-cortical loop, which could help for functional recovery/behavioural improvements in unconscious patients (Schiff, 2010). Although several treatments have been developed, there is no one-size-fits all solution for the treatment of DOC patients (Briand et al., 2020). The results presented in this thesis could help to unravel the loops that are impaired and might provide a tool to identify novel stimulation protocols. The model-based approach presented here might eventually allow quantifying the effect of a specific stimulation protocol (e.g. tDCS, tTMS and DBS), targeting the activity of a specific area, on the whole brain dynamics that subsurve consciousness at the single subject level. Based on computational models, the studies presented here have promised a great help to support diagnosis and therapeutic interventions in disease (Deco and Kringelbach, 2014; Gilson et al., 2019b; Kringelbach and Deco, 2020). In this line, recent efforts have been made to investigate how manipulating the brain can solve the fundamental problem of how force transitions between different states (Deco et al., 2019a; Ipiña et al., 2020; Perl et al., 2020). Based on the results obtained in this work, where we can give a robust definition of each DOC patient, one strategy could be to find the potential precise perturbations in key areas or specific links that can force a transition between patients' state to normal wakefulness. Further work in this line can potentially shed light on the possibility of promoting transitions in the scales of awareness and wakefulness.

5.6. Final remarks

In the collection of studies presented in this thesis work, we investigated the collective emergent features and brain mechanism underlying brain dynamics in resting-state healthy participants. We compared them with patients showing pathological disorder of consciousness and participants who undergo pharmacological propofol-sedation. During this dissertation thesis, our studies suggested that the functional and structural alterations of the low-level states of consciousness are reflected in a loss of heterogeneity, stability, and a higher constraint to the anatomy and reduced capacity

to propagate perturbations within the network. This breakdown of propagation is particularly affected in two microcircuits; posterior regions failed to receive the information in conjunction with reduced broadcasting of information flow of subcortical, temporal, parietal and frontal regions. In the subsequent study, we have shown that collective emergent properties of the resting-state dynamics change with the temporal scale, with a key optimal temporal range of 50-300 ms. In this range, brain dynamics were characterized by maximal hierarchy, entropy and critical-like dynamics, which indicate that this temporal scale is crucial for sustaining conscious processing. These results, along with the methodology, determine directions towards understanding the mechanism of consciousness in the brain. The studies presented here also highlight how the theory (model-based approaches) is essential to understand how interesting functions can emerge collectively and simulate brain dynamics, which opens new avenues to new research and potential clinical applications.

Overall, the presented methods and results contribute significantly to the ongoing investigation of the dynamical brain mechanisms underlying resting-state and low-level states of consciousness and pave the way for the possible application of computational models in future clinical contexts.

APPENDIX A

Data details

A.1. MRI acquisition and data analysis

For the healthy controls and DOC patients, structural and functional MRI (fMRI) data were acquired on a Siemens 3T Trio scanner (Siemens Inc, Munich, Germany). The BOLD fMRI resting-state (i.e. task free) was acquired using EPI, gradient echo with following parameters: volumes = 300, TR = 2000 ms, TE = 30 ms, flip angle = 78°, voxel size = $3 \times 3 \times 3$ mm^3, FOV = 192×192 mm^2, 32 transversal slices, with a duration of 10 minutes. Subsequently, structural 3D T1-weighted MP-RAGE images with were acquired with following parameters: 120 transversal slices, TR = 2300 ms, voxel size = $1.0 \times 1.0 \times 1.2$ mm^3, flip angle = 9°, FOV = 256×256 mm^2. Last, diffusion weighted MRI (DWI) was acquired in 64 directions (b-value =1,000 s/mm^2, voxel size = $1.8 \times 1.8 \times 3.3$ mm^3, FOV = 230×230 mm^2, TR= 5,700 ms, TE= 87 ms, 45 transverse slices, 128×128 voxel matrix) preceded by a single unweighted image (b0). The DWI was acquired twice.

The propofol dataset was acquired on a 3T Siemens Allegra scanner (Siemens AG, Munich, Germany). The fMRI resting-state were acquired using the following parameters: EPI, gradient echo, volumes = 200; TR = 2460ms, TE = 40 ms, voxel size = $3.45 \times 3.45 \times 3$ mm^3, FOV = 220×220 mm, 32 transverse slices, $64 \times 64 \times 32$ matrix size. The structural images were acquired using 3D T1-weighted MP-RAGE with following parameters: 120 transversal slices, TR = 2250 ms, TE=2.99ms, voxel size = 1 mm3, flip angle = 9°, FOV = $256 \times 240 \times 160$mm.

Preprocessing of MRI data was performed using MELODIC (Multivariate Exploratory Linear Optimized Decomposition into Independent Components) version 3.14 (Beckmann and Smith, 2004), which is part of the FMRIB's Software Library (FSL, `http://fsl.fmrib.ox.ac.uk/fsl`). Preprocessing steps included: discarding the first 5 volumes, motion correction using MCFLIRT (Jenkinson et al., 2002), non-brain removal using BET (Brain Extraction Tool) (Smith, 2002), spatial smoothing with 5 mm FWHM Gaussian Kernel, rigid-body registration, high pass filter cutoff = 100.0 s, and single-session ICA with automatic dimensionality estimation. After preprocessing, FIX (FMRIB's ICA-based X-noiseifier) (Griffanti et al., 2014) was applied to remove the noise components and the lesion-driven artefacts, independently, for each subject. Specifically, FSLeyes package in Melodic mode was used to manually classify the single-subject Independent Components (ICs) into "good" for signal, "bad" for noise or lesion-driven artefacts and "unknown" for ambiguous components. Each component was classified by looking at the spatial map, the time series, and the temporal power spectrum (Salimi-Khorshidi et al., 2014; Griffanti et al., 2017). Finally, FIX was applied by using the default parameters to obtain a cleaned version of the functional data.

FSL tools were used to obtain the blood-oxygen-level-dependent (BOLD) time series of the 214 cortical and subcortical brain regions (without the cerebellum) in each individual's native EPI space, defined according to a resting-state atlas (Shen et al., 2013). Specifically, the cleaned functional data previously obtained were co-registered to the T1-weighted structural image by using FLIRT (Jenkinson and Smith, 2001). Then, the T1-weighted image was co-registered to the standard MNI space by

using FLIRT (12 DOF) and FNIRT (Jenkinson and Smith, 2001; Andersson et al., 2007). The resulting transformations were concatenated and inverted and applied to warp the resting-state atlas from MNI space to the cleaned functional data. To ensure the preservation of the labels, a nearest-neighbour interpolation method was used. Then, the BOLD time series for each of the 214 brain regions were extracted for each subject in their native space by using *fslmaths* to obtain a binary mask of each brain region, and *fslmeants* to obtain the time series of each binary mask.

The grand average of the functional connectivity matrix, FC, was constructed using Matlab 2017 (The MathWorks Inc.) to compute the pairwise Pearson correlation between all 214 brain regions, applying Fisher's transform to the r-values to get the z-values for the final 214×214 functional connectivity matrices.

A.2. Structural connectivity

A whole-brain structural connectivity (SC) matrix was computed for each subject from the DOC dataset, using two-step process as described in previous studies (Gong et al., 2009; Cao et al., 2013; Muthuraman et al., 2016). Similar to the procedure used for analysing the resting-state fMRI data, we used the resting-state atlas to create a structural connectivity in each individual's diffusion native space. First, DICOM images were converted to Neuroimaging Informatics Technology Initiative (NIfTI) format using dcm2nii (`www.nitrc.org/projects/dcm2nii`). The b0 image in DTI native space was co-registered to the T1-weighted structural image by using FLIRT (Jenkinson and Smith, 2001). The T1-weighted structural image was co-register to the standard space by using FLIRT and FNIRT (Jenkinson and Smith, 2001; Andersson et al., 2007). The resulting transformations were inverted and applied to warp the resting-state atlas from MNI space to the native MRI diffusion space by applying a nearest-neighbour interpolation algorithm. Second, analysis of diffusion images was performed using the processing pipeline of the FMRIB's Diffusion Toolbox (FDT) in FMRIB's Software Library (`www.fmrib.ox.ac.uk/fsl`). The non-brain tissues were extracted by applying the Brain Extraction Tool (BET) (Smith, 2002), the eddy current distortions and head motion were corrected using eddy correct tool (Andersson et al., 2016), and

the gradient matrix was reoriented to correct for subject motion (Leemans and Jones, 2009). Then, Crossing Fibres were modelled using the default BEDPOSTX parameters and the probability of multi-fibre orientations were calculated to improve the sensitivity of non-dominant fibre populations (Behrens et al., 2003,0). Then, Probabilistic Tractography was performed in native MRI diffusion space using the default settings of PROBTRACKX (Behrens et al., 2003,0). For each brain region, the connectivity probability to each of the other 213 brain regions was computed. The resulting matrix was then symmetrized by computing their transpose matrix and averaging both matrices, therefore $C_{ij} = C_{ji}$. Finally, to obtain the structural probability matrix, the value of the probability pairs of brain regions was divided by its corresponding number of generated tracts. To summarize, for each participant, a 214x214 symmetric weighted network was constructed and normalised by the total number of fibres in the whole network; thus, the structural connectivity matrix (SC) represents the density of links of the anatomical organization of the brain.

A.3. Patients' demographic and clinical characteristics

Condition	Etiology	TSI	Age	Gender	Auditory	Visual	Motor	Verbal	Communication	Arousal	Total CRS-R
MCS 1	TBI	3034	34	F	3	3	2	2	0	2	12
MCS 2	TBI	1294	40	F	2	3	2	2	0	2	11
MCS 3	CVA	13	62	M	0	3	2	1	0	1	7
MCS 4	TBI	589	30	M	3	2	2	2	0	1	10
MCS 5	TBI	28	65	M	3	4	3	1	0	2	13
MCS 6	Haemorrhage	17	83	M	3	0	2	1	0	0	6
MCS 7	TBI	521	28	M	1	3	2	2	0	2	10
MCS 8	Epilepsy	20	52	M	3	3	2	2	1	2	13
MCS 9	Haemorrhage	43	67	M	2	3	5	2	0	2	14
MCS 10	TBI	533	47	M	3	5	2	1	0	2	13
MCS 11	CVA	2639	38	M	1	3	2	2	0	1	9
MCS 12	TBI	2690	24	M	3	3	5	1	0	2	14
MCS 13	TBI+anoxia	401	29	M	1	3	2	1	0	2	9
MCS 14	Anoxia	9900	39	M	3	3	5	2	0	2	15
MCS 15	Anoxia	396	57	M	3	0	2	2	0	2	9
MCS 16	TBI+Anoxia	314	26	F	3	1	2	1	0	2	9
MCS 17	TBI	407	31	M	0	1	2	2	0	1	6
MCS 18	Anoxia	64	29	M	1	3	2	2	0	2	10
MCS 19	Haemorrhage	242	46	F	2	3	2	1	0	2	10
MCS 20	Anoxia	639	43	M	2	3	1	2	0	2	10
MCS 21	TBI	1241	53	M	0	3	2	2	0	2	9
MCS 22	TBI	135	51	M	3	4	2	1	0	2	12
MCS 23	TBI	30	67	F	0	3	2	0	0	2	7
MCS 24	Haemorrhage	1383	68	F	3	1	3	2	0	2	11
MCS 25	TBI	1331	35	M	3	0	2	1	0	2	8
MCS 26	TBI - Haemorrhage	35	73	M	0	2	0	1	0	1	4
MCS 27	CVA	104	43	F	3	1	3	1	0	0	8
MCS 28	TBI	319	41	M	1	0	2	1	0	1	5
MCS 29	TBI - Haemorrhage	255	39	M	4	5	4	2	1	2	18
MCS 30	Anoxia	1482	32	M	3	4	2	2	1	2	14
MCS 31	TBI	641	23	M	3	3	0	1	0	2	9
MCS 32	TBI	37	26	F	2	3	3	0	1	1	10
MCS 33	Haemorrhage	389	59	F	2	1	2	1	0	2	8

Table A.1: **MCS patients' demographic and clinical characteristics.** The table includes condition, etiology (traumatic brain injury (TBI) and cerebral vascular accident (CVA)), time science injury (TSI), age, gender (F=female, M=male), Coma Recovery Scale-Revised (CSR-R) auditory, visual, motor, verbal, communication and arousal subscores and total.

Condition	Etiology	TSI	Age	Gender	Auditory	Visual	Motor	Verbal	Communication	Arousal	Total CRS-R
UWS 1	Anoxia	2890	49	M	1	1	1	2	0	2	7
UWS 2	TBI	283	52	F	1	0	2	2	0	1	6
UWS 3	Anoxia	743	30	M	1	0	2	1	0	2	6
UWS 4	Anoxia	92	74	M	1	0	1	1	0	1	4
UWS 5	Haemorrhage	43	64	M	1	0	2	1	0	1	5
UWS 6	Anoxia	18	20	M	1	0	0	1	0	1	3
UWS 7	Anoxia	1683	39	F	1	0	2	1	0	2	6
UWS 8	Anoxia	38	50	F	0	0	0	2	0	1	3
UWS 9	Anoxia	50	69	F	0	1	2	1	0	1	5
UWS 10	Anoxia	129	49	F	1	0	0	1	0	2	4
UWS 11	TBI	24	58	M	0	1	2	0	0	1	4
UWS 12	Anoxia	335	40	F	1	0	2	1	0	2	6
UWS 13	Anoxia	7814	34	M	1	0	1	1	0	2	5
UWS 14	Anoxic Asphyxia	304	60	M	1	1	1	1	0	2	6
UWS 15	Anoxia	30	44	M	1	1	1	1	0	1	5

Table A.2: **UWS patients' demographic and clinical characteristics.** The table includes condition, etiology (traumatic brain injury (TBI)), time science injury (TSI), age, gender (F=female, M=male), Coma Recovery Scale-Revised (CSR-R) auditory, visual, motor, verbal, communication and arousal subscores and total.

Bibliography

Achard, S., Salvador, R., Whitcher, B., Suckling, J., and Bullmore, E. (2006). A resilient, low-frequency, small-world human brain functional network with highly connected association cortical hubs. *Journal of Neuroscience* 26, 63–72. 10.1523/JNEUROSCI.3874-05.2006

Adhikari, M. H., Hacker, C. D., Siegel, J. S., Griffa, A., Hagmann, P., Deco, G., et al. (2017). Decreased integration and information capacity in stroke measured by whole brain models of resting state activity. *Brain* 140, 1068–1085. 10.1093/brain/awx021

Aertsen, A. M., Gerstein, G. L., Habib, M. K., and Palm, G. (1989). Dynamics of neuronal firing correlation: Modulation of 'effective connectivity'. *Journal of Neurophysiology* 61. 10.1152/jn.1989.61.5.900

Alexander-Bloch, A. F., Gogtay, N., Meunier, D., Birn, R., Clasen, L., Lalonde, F., et al. (2010). Disrupted modularity and local connectivity of brain functional networks in childhood-onset schizophrenia. *Frontiers in systems neuroscience* 4, 147. 10.3389/fnsys.2010.00147

Alkire, M. T., Haier, R. J., Barker, S. J., Shah, N. K., Wu, J. C., and Kao, Y. J. (1995). Cerebral metabolism during propofol anesthesia in

humans studied with positron emission tomography. *Anesthesiology* 82, 393–403. 10.1097/00000542-199502000-00010

Alkire, M. T., Hudetz, A. G., and Tononi, G. (2008). Consciousness and Anesthesia. *Science* 322, 876–880. 10.1126/science.1149213

Alkire, M. T. and Miller, J. (2005). General anesthesia and the neural correlates of consciousness. 10.1016/S0079-6123(05)50017-7

Allen, E. A., Damaraju, E., Plis, S. M., Erhardt, E. B., Eichele, T., and Calhoun, V. D. (2014). Tracking whole-brain connectivity dynamics in the resting state. *Cerebral cortex (New York, N.Y. : 1991)* 24, 663–76. 10.1093/cercor/bhs352

Alstott, J., Breakspear, M., Hagmann, P., Cammoun, L., and Sporns, O. (2009). Modeling the impact of lesions in the human brain. *PLoS Computational Biology* 5. 10.1371/journal.pcbi.1000408

Amico, E., Gomez, F., Di Perri, C., Vanhaudenhuyse, A., Lesenfants, D., Boveroux, P., et al. (2014). Posterior Cingulate Cortex-Related Co-Activation Patterns: A Resting State fMRI Study in Propofol-Induced Loss of Consciousness. *PLoS ONE* 9, e100012. 10.1371/journal.pone.0100012

Andersson, J. L. R., Graham, M. S., Zsoldos, E., and Sotiropoulos, S. N. (2016). Incorporating outlier detection and replacement into a non-parametric framework for movement and distortion correction of diffusion MR images. *NeuroImage* 141, 556–572. 10.1016/j.neuroimage.2016.06.058

Andersson, J. L. R., Jenkinson, M., Smith, S., Jenkinson, M., SMITH, S., Andersson, J., et al. (2007). Non-Linear Registration aka Spatial Normalisation FMRIB Technial Report TR07JA2.

Annen, J., Frasso, G., Crone, J. S., Heine, L., Di Perri, C., Martial, C., et al. (2018). Regional brain volumetry and brain function in severely brain-injured patients. *Annals of Neurology* 83, 842–853. 10.1002/ana.25214

Annen, J., Heine, L., Ziegler, E., Frasso, G., Bahri, M., Di Perri, C., et al. (2016). Function-structure connectivity in patients with severe brain injury as measured by MRI-DWI and FDG-PET. *Human Brain Mapping* 37, 3707–3720. 10.1002/hbm.23269

Aru, J., Suzuki, M., and Larkum, M. E. (2020). Cellular Mechanisms of Conscious Processing. 10.1016/j.tics.2020.07.006

Aru, J., Suzuki, M., Rutiku, R., Larkum, M. E., and Bachmann, T. (2019). Coupling the State and Contents of Consciousness. *Frontiers in Systems Neuroscience* 13, 30. 10.3389/fnsys.2019.00043

Baars, B. J. (1997). Some Essential Differences between Consciousness and Attention, Perception, and Working Memory. *Consciousness and Cognition* 6, 363–371. 10.1006/ccog.1997.0307

Baars, B. J. (2002). The conscious access hypothesis: origins and recent evidence. *Trends in Cognitive Sciences* 6, 47–52. 10.1016/S1364-6613(00)01819-2

Bachmann, T. and Hudetz, A. G. (2014). It is time to combine the two main traditions in the research on the neural correlates of consciousness: C=LxD. *Frontiers in Psychology* 5, 940. 10.3389/fpsyg.2014.00940

Baker, A. P., Brookes, M. J., Rezek, I. A., Smith, S. M., Behrens, T., Probert Smith, P. J., et al. (2014). Fast transient networks in spontaneous human brain activity. *eLife* 3, e01867. 10.7554/eLife.01867

Barttfeld, P., Uhrig, L., Sitt, J. D., Sigman, M., Jarraya, B., and Dehaene, S. (2015). Signature of consciousness in the dynamics of resting-state brain activity. *Proceedings of the National Academy of Sciences of the United States of America* 112, 887–92. 10.1073/pnas.1418031112

Bassett, D. S., Wymbs, N. F., Rombach, M. P., Porter, M. A., Mucha, P. J., and Grafton, S. T. (2013). Task-Based Core-Periphery Organization of Human Brain Dynamics. *PLoS Computational Biology* 9. 10.1371/journal.pcbi.1003171

Bayne, T. and Carter, O. (2018). Dimensions of consciousness and the psychedelic state. *Neuroscience of Consciousness* 2018. 10.1093/nc/niy008

Bayne, T., Hohwy, J., and Owen, A. M. (2016). Are There Levels of Consciousness? 10.1016/j.tics.2016.03.009

Beckmann, C. and Smith, S. (2004). Probabilistic Independent Component Analysis for Functional Magnetic Resonance Imaging. *IEEE Transactions on Medical Imaging* 23, 137–152. 10.1109/TMI.2003.822821

Beggs, J. M. (2008). The criticality hypothesis: How local cortical networks might optimize information processing. *Philosophical Transactions of the Royal Society A: Mathematical, Physical and Engineering Sciences* 366, 329–343. 10.1098/rsta.2007.2092

Beggs, J. M. and Plenz, D. (2003). Neuronal avalanches in neocortical circuits. *The Journal of neuroscience : the official journal of the Society for Neuroscience* 23, 11167–77

Behrens, T., Berg, H. J., Jbabdi, S., Rushworth, M., and Woolrich, M. (2007). Probabilistic diffusion tractography with multiple fibre orientations: What can we gain? *NeuroImage* 34, 144–155. 10.1016/j.neuroimage.2006.09.018

Behrens, T., Rohr, K., and Stiehl, H. (2003). Robust segmentation of tubular structures in 3-D medical images by parametric object detection and tracking. *IEEE Transactions on Systems, Man and Cybernetics, Part B (Cybernetics)* 33, 554–561. 10.1109/TSMCB.2003.814305

Bellay, T., Klaus, A., Seshadri, S., and Plenz, D. (2015). Irregular spiking of pyramidal neurons organizes as scale-invariant neuronal avalanches in the awake state. *eLife* 4, e07224. 10.7554/eLife.07224

Benjamini, Y. and Hochberg, Y. (1995). Controlling the False Discovery Rate: A Practical and Powerful Approach to Multiple Testing. *Journal of the Royal Statistical Society: Series B (Methodological)* 57, 289–300. 10.1111/j.2517-6161.1995.tb02031.x

Bettinardi, R. G., Tort-Colet, N., Ruiz-Mejias, M., Sanchez-Vives, M. V., and Deco, G. (2015). Gradual emergence of spontaneous correlated brain activity during fading of general anesthesia in rats: Evidences from fMRI and local field potentials. *NeuroImage* 114, 185–98. 10.1016/j.neuroimage.2015.03.037

Bialek, W., Cavagna, A., Giardina, I., Mora, T., Silvestri, E., Viale, M., et al. (2012). Statistical mechanics for natural flocks of birds. *Proceedings of the National Academy of Sciences of the United States of America* 109, 4786–4791. 10.1073/pnas.1118633109

Biswal, B., Hudetz, A. G., Yetkin, F. Z., Haughton, V. M., and Hyde, J. S. (1997). Hypercapnia reversibly suppresses low-frequency fluctuations in the human motor cortex during rest using echo-planar MRI. *Journal of Cerebral Blood Flow and Metabolism* 17, 301–308. 10.1097/00004647-199703000-00007

Biswal, B., Yetkin, F. Z., Haughton, V. M., and Hyde, J. S. (1995). Functional connectivity in the motor cortex of resting human brain using echo-planar MRI. *Magnetic resonance in medicine* 34, 537–41

Bodart, O., Amico, E., Gómez, F., Casali, A. G., Wannez, S., Heine, L., et al. (2018). Global structural integrity and effective connectivity in patients with disorders of consciousness. *Brain Stimulation* 11, 358–365. 10.1016/J.BRS.2017.11.006

Boly, M., Garrido, M. I., Gosseries, O., Bruno, M.-A., Boveroux, P., Schnakers, C., et al. (2011). Preserved Feedforward But Impaired Top-Down Processes in the Vegetative State. *Science* 332, 858–862. 10.1126/science.1202043

Boly, M., Massimini, M., Tsuchiya, N., Postle, B. R., Koch, C., and Tononi, G. (2017). Are the neural correlates of consciousness in the front or in the back of the cerebral cortex? Clinical and neuroimaging evidence. *Journal of Neuroscience* 37, 9603–9613. 10.1523/JNEUROSCI.3218-16.2017

Botvinik-Nezer, R., Holzmeister, F., Camerer, C. F., Dreber, A., Huber, J., Johannesson, M., et al. (2020). Variability in the analysis of a single neuroimaging dataset by many teams. *Nature* 582, 84–88. 10.1038/s41586-020-2314-9

Boveroux, P., Vanhaudenhuyse, A., Bruno, M. A., Noirhomme, Q., Lauwick, S., Luxen, A., et al. (2010). Breakdown of within- and between-network resting state functional magnetic resonance imaging

connectivity during propofol-induced loss of consciousness. *Anesthesiology* 113, 1038–1053. 10.1097/ALN.0b013e3181f697f5

Breakspear, M., Terry, J. R., and Friston, K. J. (2003). Modulation of excitatory synaptic coupling facilitates synchronization and complex dynamics in a biophysical model of neuronal dynamics. *Network: Computation in Neural Systems* 14, 703–732. 10.1088/0954-898X_14_4_305

Bressler, S. L. (1995). Large-scale cortical networks and cognition. 10.1016/0165-0173(94)00016-I

Briand, M. M., Gosseries, O., Staumont, B., Laureys, S., and Thibaut, A. (2020). Transcutaneous Auricular Vagal Nerve Stimulation and Disorders of Consciousness: A Hypothesis for Mechanisms of Action. *Frontiers in Neurology* 11, 933. 10.3389/fneur.2020.00933

Britz, J., Van De Ville, D., and Michel, C. M. (2010). BOLD correlates of EEG topography reveal rapid resting-state network dynamics. *NeuroImage* 52, 1162–70. 10.1016/j.neuroimage.2010.02.052

Brookes, M. J., Woolrich, M., Luckhoo, H., Price, D., Hale, J. R., Stephenson, M. C., et al. (2011). Investigating the electrophysiological basis of resting state networks using magnetoencephalography. *Proceedings of the National Academy of Sciences of the United States of America* 108, 16783–8. 10.1073/pnas.1112685108

Brown, E. N., Lydic, R., and Schiff, N. D. (2010). General Anesthesia, Sleep, and Coma. *New England Journal of Medicine* 363, 2638–2650. 10.1056/nejmra0808281

Brunet, D., Murray, M. M., and Michel, C. M. (2011). Spatiotemporal Analysis of Multichannel EEG: CARTOOL. *Computational Intelligence and Neuroscience* 2011, 1–15. 10.1155/2011/813870

Brunner, C., Billinger, M., Seeber, M., Mullen, T. R., and Makeig, S. (2016). Volume Conduction Influences Scalp-Based Connectivity Estimates. *Frontiers in Computational Neuroscience* 10, 121. 10.3389/fncom.2016.00121

Bullmore, E. and Sporns, O. (2009). Complex brain networks: graph theoretical analysis of structural and functional systems. *Nature Reviews Neuroscience* 10, 186–198. 10.1038/nrn2575

Bullmore, E. and Sporns, O. (2012). The economy of brain network organization. 10.1038/nrn3214

Buxton, R. B., UludaÇ§, K., Dubowitz, D. J., and Liu, T. T. (2004). Modeling the hemodynamic response to brain activation. In *NeuroImage* (Neuroimage), vol. 23. 10.1016/j.neuroimage.2004.07.013

Cabeza, R. and Nyberg, L. (2000). Imaging cognition II: An empirical review of 275 PET and fMRI studies. 10.1162/08989290051137585

Cabral, J., Hugues, E., Sporns, O., and Deco, G. (2011). Role of local network oscillations in resting-state functional connectivity. *NeuroImage* 57, 130–139. 10.1016/j.neuroimage.2011.04.010

Cabral, J., Kringelbach, M. L., and Deco, G. (2014). Exploring the network dynamics underlying brain activity during rest. *Progress in Neurobiology* 114, 102–131. 10.1016/j.pneurobio.2013.12.005

Campagna, J. A., Miller, K. W., and Forman, S. A. (2003). Mechanisms of Actions of Inhaled Anesthetics. *New England Journal of Medicine* 348, 2110–2124. 10.1056/nejmra021261

Cao, Q., Shu, N., An, L., Wang, P., Sun, L., Xia, M.-R., et al. (2013). Probabilistic Diffusion Tractography and Graph Theory Analysis Reveal Abnormal White Matter Structural Connectivity Networks in Drug-Naive Boys with Attention Deficit/Hyperactivity Disorder. *Journal of Neuroscience* 33, 10676–10687. 10.1523/JNEUROSCI.4793-12.2013

Carhart-Harris, R. L., Leech, R., Hellyer, P. J., Shanahan, M., Feilding, A., Tagliazucchi, E., et al. (2014). The entropic brain: A theory of conscious states informed by neuroimaging research with psychedelic drugs. *Frontiers in Human Neuroscience* 8. 10.3389/fnhum.2014.00020

Casali, A. G., Gosseries, O., Rosanova, M., Boly, M., Sarasso, S., Casali, K. R., et al. (2013). A Theoretically Based Index of Consciousness

Independent of Sensory Processing and Behavior. *Science Translational Medicine* 5, 105–198. 10.1126/scitranslmed.3006294

Casarotto, S., Comanducci, A., Rosanova, M., Sarasso, S., Fecchio, M., Napolitani, M., et al. (2016). Stratification of unresponsive patients by an independently validated index of brain complexity. *Annals of Neurology* 80, 718–729. 10.1002/ana.24779

Cavanagh, S. E., Wallis, J. D., Kennerley, S. W., and Hunt, L. T. (2016). Autocorrelation structure at rest predicts value correlates of single neurons during reward-guided choice. *eLife* 5. 10.7554/eLife.18937

Cavanna, A. E. and Trimble, M. R. (2006). The precuneus: A review of its functional anatomy and behavioural correlates. 10.1093/brain/awl004

Chang, C. and Glover, G. H. (2010). Timeâfrequency dynamics of resting-state brain connectivity measured with fMRI. *NeuroImage* 50, 81–98. 10.1016/j.neuroimage.2009.12.011

Chaudhuri, R., Knoblauch, K., Gariel, M. A., Kennedy, H., and Wang, X. J. (2015). A Large-Scale Circuit Mechanism for Hierarchical Dynamical Processing in the Primate Cortex. *Neuron* 88, 419–431. 10.1016/j.neuron.2015.09.008

Chen, J., Hasson, U., and Honey, C. J. (2015). Processing Timescales as an Organizing Principle for Primate Cortex. 10.1016/j.neuron.2015.10.010

Chennu, S., Annen, J., Wannez, S., Thibaut, A., Chatelle, C., Cassol, H., et al. (2017). Brain networks predict metabolism, diagnosis and prognosis at the bedside in disorders of consciousness. *Brain* 140, 2120–2132. 10.1093/brain/awx163

Chudy, D., Deletis, V., Almahariq, F., Marčinković, P., Škrlin, J., Paradžik, V., et al. (2018). Deep brain stimulation for the early treatment of the minimally conscious state and vegetative state: Experience in 14 patients. *Journal of Neurosurgery* 128, 1189–1198. 10.3171/2016.10.JNS161071

Cocchi, L., Sale, M. V., Gollo, L. L., Bell, P. T., Nguyen, V. T., Zalesky, A., et al. (2016). A hierarchy of timescales explains distinct effects of

local inhibition of primary visual cortex and frontal eye fields. *eLife* 5. 10.7554/eLife.15252

Colombo, M. A., Napolitani, M., Boly, M., Gosseries, O., Casarotto, S., Rosanova, M., et al. (2019). The spectral exponent of the resting EEG indexes the presence of consciousness during unresponsiveness induced by propofol, xenon, and ketamine. *NeuroImage* 189, 631–644. 10.1016/j.neuroimage.2019.01.024

Compte, A., Sanchez-Vives, M. V., McCormick, D. A., and Wang, X. J. (2003). Cellular and network mechanisms of slow oscillatory activity (¡1 Hz) and wave propagations in a cortical network model. *Journal of Neurophysiology* 89, 2707–2725. 10.1152/jn.00845.2002

Constable, R. T. (2006). Challenges in fMRI and its limitations. In *Functional MRI: Basic Principles and Clinical Applications* (Springer New York). 75–98. 10.1007/0-387-34665-1_4

Cordes, D., Haughton, V. M., Arfanakis, K., Wendt, G. J., Turski, P. A., Moritz, C. H., et al. (2000). Mapping functionally related regions of brain with functional connectivity MR imaging. *American Journal of Neuroradiology* 21, 1636–1644

Crick, F. and Koch, C. (1990). Towards a neurobiological theory of consciousness. *undefined*

Crone, J. S., Soddu, A., Höller, Y., Vanhaudenhuyse, A., Schurz, M., Bergmann, J., et al. (2014). Altered network properties of the fronto-parietal network and the thalamus in impaired consciousness. *NeuroImage: Clinical* 4, 240–248. 10.1016/j.nicl.2013.12.005

Csermely, P. (2018). The Wisdom of Networks: A General Adaptation and Learning Mechanism of Complex Systems. *BioEssays* 40, 1700150. 10.1002/bies.201700150

Damoiseaux, J. S., Rombouts, S. A. R. B., Barkhof, F., Scheltens, P., Stam, C. J., Smith, S. M., et al. (2006). Consistent resting-state networks across healthy subjects. *Proceedings of the National Academy of Sciences of the United States of America* 103, 13848–53. 10.1073/pnas.0601417103

D'andola, M., Rebollo, B., Casali, A. G., Weinert, J. F., Pigorini, A., Villa, R., et al. (2018). Bistability, Causality, and Complexity in Cortical Networks: An In Vitro Perturbational Study. *Cerebral Cortex* 28, 2233–2242. 10.1093/cercor/bhx122

De Luca, M., Beckmann, C. F., De Stefano, N., Matthews, P. M., and Smith, S. M. (2006). fMRI resting state networks define distinct modes of long-distance interactions in the human brain. *NeuroImage* 29, 1359–1367. 10.1016/j.neuroimage.2005.08.035

De Munck, J. C. (1988). The potential distribution in a layered anisotropic spheroidal volume conductor. *Journal of Applied Physics* 64, 464–470. 10.1063/1.341983

de Pasquale, F., Della Penna, S., Snyder, A. Z., Lewis, C., Mantini, D., Marzetti, L., et al. (2010). Temporal dynamics of spontaneous MEG activity in brain networks. *Proceedings of the National Academy of Sciences of the United States of America* 107, 6040–5. 10.1073/pnas.0913863107

Deco, G., Cabral, J., Saenger, V. M., Boly, M., Tagliazucchi, E., Laufs, H., et al. (2018a). Perturbation of whole-brain dynamics in silico reveals mechanistic differences between brain states. *NeuroImage* 169, 46–56. 10.1016/j.neuroimage.2017.12.009

Deco, G., Cruzat, J., Cabral, J., Knudsen, G. M., Carhart-Harris, R. L., Whybrow, P. C., et al. (2018b). Whole-Brain Multimodal Neuroimaging Model Using Serotonin Receptor Maps Explains Nonlinear Functional Effects of LSD. *Current biology : CB* 28, 3065–3074. 10.1016/j.cub.2018.07.083

Deco, G., Cruzat, J., Cabral, J., Tagliazucchi, E., Laufs, H., Logothetis, N. K., et al. (2019a). Awakening: Predicting external stimulation to force transitions between different brain states. *Proceedings of the National Academy of Sciences of the United States of America* 116, 18088–18097. 10.1073/pnas.1905534116

Deco, G., Cruzat, J., and Kringelbach, M. L. (2019b). Brain songs framework used for discovering the relevant timescale of the human brain. *Nature Communications* 10, 583. 10.1038/s41467-018-08186-7

Deco, G., Jirs, V., McIntosh, A. R., Sporns, O., and Kötter, R. (2009). Key role of coupling, delay, and noise in resting brain fluctuations. *Proceedings of the National Academy of Sciences of the United States of America* 106, 10302–10307. 10.1073/pnas.0901831106

Deco, G. and Jirsa, V. K. (2012). Ongoing cortical activity at rest: criticality, multistability, and ghost attractors. *The Journal of neuroscience : the official journal of the Society for Neuroscience* 32, 3366–75. 10.1523/JNEUROSCI.2523-11.2012

Deco, G., Jirsa, V. K., and McIntosh, A. R. (2011). Emerging concepts for the dynamical organization of resting-state activity in the brain. *Nature Reviews Neuroscience* 12, 43–56. 10.1038/nrn2961

Deco, G., Jirsa, V. K., and McIntosh, A. R. (2013a). Resting brains never rest: Computational insights into potential cognitive architectures. 10.1016/j.tins.2013.03.001

Deco, G. and Kringelbach, M. L. (2014). Great expectations: using whole-brain computational connectomics for understanding neuropsychiatric disorders. *Neuron* 84, 892–905. 10.1016/j.neuron.2014.08.034

Deco, G. and Kringelbach, M. L. (2016). Metastability and Coherence: Extending the Communication through Coherence Hypothesis Using A Whole-Brain Computational Perspective. *Trends in Neurosciences* 39, 125–135. 10.1016/j.tins.2016.01.001

Deco, G. and Kringelbach, M. L. (2017). Hierarchy of Information Processing in the Brain: A Novel âIntrinsic Ignitionâ Framework. *Neuron* 94, 961–968. 10.1016/j.neuron.2017.03.028

Deco, G., Kringelbach, M. L., Jirsa, V. K., and Ritter, P. (2017a). The dynamics of resting fluctuations in the brain: Metastability and its dynamical cortical core. *Scientific Reports* 7, 1–14. 10.1038/s41598-017-03073-5

Deco, G., Ponce-Alvarez, A., Mantini, D., Romani, G. L., Hagmann, P., and Corbetta, M. (2013b). Resting-state functional connectivity

emerges from structurally and dynamically shaped slow linear fluctuations. *The Journal of neuroscience : the official journal of the Society for Neuroscience* 33, 11239–52. 10.1523/JNEUROSCI.1091-13.2013

Deco, G., Tagliazucchi, E., Laufs, H., Sanjuán, A., and Kringelbach, M. L. (2017b). Novel Intrinsic Ignition Method Measuring Local-Global Integration Characterizes Wakefulness and Deep Sleep. *eneuro* 4, 0106–17. 10.1523/ENEURO.0106-17.2017

Deco, G., Tononi, G., Boly, M., and Kringelbach, M. L. (2015a). Rethinking segregation and integration: contributions of whole-brain modelling. *Nature Reviews Neuroscience* 16, 430–439. 10.1038/nrn3963

Deco, G., Tononi, G., Boly, M., and Kringelbach, M. L. (2015b). Rethinking segregation and integration: contributions of whole-brain modelling. *Nature Reviews Neuroscience* 16, 430–439. 10.1038/nrn3963

Dehaene, S. and Changeux, J.-P. (2011). Experimental and Theoretical Approaches to Conscious Processing. *Neuron* 70, 200–227. 10.1016/j.neuron.2011.03.018

Dehaene, S., Charles, L., King, J. R., and Marti, S. (2014). Toward a computational theory of conscious processing. 10.1016/j.conb.2013.12.005

Dehaene, S., Kerszberg, M., and Changeux, J. P. (1998). A neuronal model of a global workspace in effortful cognitive tasks. *Proceedings of the National Academy of Sciences of the United States of America* 95, 14529–34. 10.1073/pnas.95.24.14529

Dehaene, S. and Naccache, L. (2001). Towards a cognitive neuroscience of consciousness: basic evidence and a workspace framework. *Cognition* 79, 1–37

Dehaene, S., Sergent, C., and Changeux, J. P. (2003). A neuronal network model linking subjective reports and objective physiological data during conscious perception. *Proceedings of the National Academy of Sciences of the United States of America* 100, 8520–8525. 10.1073/pnas.1332574100

Demertzi, A., Antonopoulos, G., Heine, L., Voss, H. U., Crone, J. S., de Los Angeles, C., et al. (2015). Intrinsic functional connectivity differentiates minimally conscious from unresponsive patients. *Brain : a journal of neurology* 138, 2619–31. 10.1093/brain/awv169

Demertzi, A., Soddu, A., and Laureys, S. (2013). Consciousness supporting networks. *Current Opinion in Neurobiology* 23, 239–244. 10.1016/j.conb.2012.12.003

Demertzi, A., Tagliazucchi, E., Dehaene, S., Deco, G., Barttfeld, P., Raimondo, F., et al. (2019). Human consciousness is supported by dynamic complex patterns of brain signal coordination. *Science Advances* 5, eaat7603. 10.1126/sciadv.aat7603

Demirtaş, M., Burt, J. B., Helmer, M., Ji, J. L., Adkinson, B. D., Glasser, M. F., et al. (2019). Hierarchical Heterogeneity across Human Cortex Shapes Large-Scale Neural Dynamics. *Neuron* 101, 1181–1194. 10.1016/j.neuron.2019.01.017

Deshpande, G., Kerssens, C., Sebel, P. S., and Hu, X. (2010). Altered local coherence in the default mode network due to sevoflurane anesthesia. *Brain Research* 1318, 110–121. 10.1016/j.brainres.2009.12.075

Di Perri, C., Bastianello, S., Bartsch, A. J., Pistarini, C., Maggioni, G., Magrassi, L., et al. (2013). Limbic hyperconnectivity in the vegetative state. *Neurology* 81, 1417–1424. 10.1212/WNL.0b013e3182a43b78

Ding, M., Bressler, S. L., Yang, W., and Liang, H. (2000). Short-window spectral analysis of cortical event-related potentials by adaptive multivariate autoregressive modeling: data preprocessing, model validation, and variability assessment. *Biological cybernetics* 83, 35–45. 10.1007/s004229900137

Donahue, C. J., Sotiropoulos, S. N., Jbabdi, S., Hernandez-Fernandez, M., Behrens, T. E., Dyrby, T. B., et al. (2016). Using diffusion tractography to predict cortical connection strength and distance: A quantitative comparison with tracers in the monkey. *Journal of Neuroscience* 36, 6758–6770. 10.1523/JNEUROSCI.0493-16.2016

Efron, R. (1970). The minimum duration of a perception. *Neuropsychologia* 8, 57–63. 10.1016/0028-3932(70)90025-4

Escrichs, A., Sanjuán, A., Atasoy, S., López-González, A., Garrido, C., Càmara, E., et al. (2019). Characterizing the Dynamical Complexity Underlying Meditation. *Frontiers in Systems Neuroscience* 13, 27. 10.3389/fnsys.2019.00027

Estrada, E. and Hatano, N. (2008). Communicability in complex networks. *Physical Review E - Statistical, Nonlinear, and Soft Matter Physics* 77. 10.1103/PhysRevE.77.036111

Ezaki, T., Watanabe, T., Ohzeki, M., and Masuda, N. (2017). Energy landscape analysis of neuroimaging data. 10.1098/rsta.2016.0287

Fagerholm, E. D., Lorenz, R., Scott, G., Dinov, M., Hellyer, P. J., Mirzaei, N., et al. (2015). Cascades and Cognitive State: Focused Attention Incurs Subcritical Dynamics. *Journal of Neuroscience* 35, 4626–4634. 10.1523/JNEUROSCI.3694-14.2015

Fekete, T., Omer, D. B., O'Hashi, K., Grinvald, A., van Leeuwen, C., and Shriki, O. (2018). Critical dynamics, anesthesia and information integration: Lessons from multi-scale criticality analysis of voltage imaging data. *NeuroImage* 183, 919–933. 10.1016/j.neuroimage.2018.08.026

Fernández-Espejo, D., Soddu, A., Cruse, D., Palacios, E. M., Junque, C., Vanhaudenhuyse, A., et al. (2012). A role for the default mode network in the bases of disorders of consciousness. *Annals of Neurology* 72, 335–343. 10.1002/ana.23635

Ferrarelli, F., Massimini, M., Sarasso, S., Casali, A., Riedner, B. A., Angelini, G., et al. (2010). Breakdown in cortical effective connectivity during midazolam-induced loss of consciousness. *Proceedings of the National Academy of Sciences of the United States of America* 107, 2681–2686. 10.1073/pnas.0913008107

Fiset, P. (1999). Practical pharmacokinetics as applied to our daily anesthesia practice. In *Canadian Journal of Anaesthesia* (Canadian Anaesthetists' Society), vol. 46, R122–R130. 10.1007/BF03013188

Fiset, P., Plourde, G., and Backman, S. B. (2005). Brain imaging in research on anesthetic mechanisms: Studies with propofol. 10.1016/S0079-6123(05)50018-9

FitzHugh, R. (1961). Impulses and Physiological States in Theoretical Models of Nerve Membrane. *Biophysical Journal* 1, 445–466. 10.1016/S0006-3495(61)86902-6

Fox, M. D. and Raichle, M. E. (2007). Spontaneous fluctuations in brain activity observed with functional magnetic resonance imaging. *Nature Reviews Neuroscience* 8, 700–711. 10.1038/nrn2201

Fox, M. D., Snyder, A. Z., Vincent, J. L., Corbetta, M., Van Essen, D. C., and Raichle, M. E. (2005). The human brain is intrinsically organized into dynamic, anticorrelated functional networks. *Proceedings of the National Academy of Sciences of the United States of America* 102, 9673–9678. 10.1073/pnas.0504136102

Fransson, P. (2005). Spontaneous low-frequency BOLD signal fluctuations: An fMRI investigation of the resting-state default mode of brain function hypothesis. *Human Brain Mapping* 26, 15–29. 10.1002/hbm.20113

Friedman, N., Ito, S., Brinkman, B. A. W., Shimono, M., DeVille, R. E. L., Dahmen, K. A., et al. (2012). Universal Critical Dynamics in High Resolution Neuronal Avalanche Data. *Physical Review Letters* 108, 208102. 10.1103/PhysRevLett.108.208102

Fries, P. (2005). A mechanism for cognitive dynamics: neuronal communication through neuronal coherence. *Trends in Cognitive Sciences* 9, 474–480. 10.1016/j.tics.2005.08.011

Friston, K. J., Fletcher, P., Josephs, O., Holmes, A., Rugg, M. D., and Turner, R. (1998). Event-related fMRI: Characterizing differential responses. *NeuroImage* 7, 30–40. 10.1006/nimg.1997.0306

Friston, K. J., Frith, C. D., Liddle, P. F., and Frackowiak, R. S. (1993). Functional connectivity: The principal-component analysis of large (PET) data sets. *Journal of Cerebral Blood Flow and Metabolism* 13, 5–14. 10.1038/jcbfm.1993.4

Friston, K. J., Harrison, L., and Penny, W. (2003). Dynamic causal modelling. *NeuroImage* 19, 1273–1302. 10.1016/S1053-8119(03)00202-7

Garrett, D. D., Kovacevic, N., McIntosh, A. R., and Grady, C. L. (2013). The modulation of BOLD variability between cognitive states varies by age and processing speed. *Cerebral Cortex* 23, 684–693. 10.1093/cercor/bhs055

Gauthier, B., Eger, E., Hesselmann, G., Giraud, A. L., and Kleinschmidt, A. (2012). Temporal tuning properties along the human ventral visual stream. *Journal of Neuroscience* 32, 14433–14441. 10.1523/JNEUROSCI.2467-12.2012

Ghosh, A., Rho, Y., McIntosh, A. R., Kötter, R., and Jirsa, V. K. (2008). Noise during Rest Enables the Exploration of the Brain's Dynamic Repertoire. *PLoS Computational Biology* 4, e1000196. 10.1371/journal.pcbi.1000196

Giacino, J. T. (2005). The minimally conscious state: Defining the borders of consciousness. 10.1016/S0079-6123(05)50027-X

Giacino, J. T., Ashwal, S., Childs, N., Cranford, R., Jennett, B., Katz, D. I., et al. (2002). The minimally conscious state: Definition and diagnostic criteria. *Neurology* 58, 349–353. 10.1212/WNL.58.3.349

Gilson, M., Deco, G., Friston, K. J., Hagmann, P., Mantini, D., Betti, V., et al. (2018). Effective connectivity inferred from fMRI transition dynamics during movie viewing points to a balanced reconfiguration of cortical interactions. 10.1016/j.neuroimage.2017.09.061

Gilson, M., Kouvaris, N. E., Deco, G., Mangin, J. F., Poupon, C., Lefranc, S., et al. (2019a). Network analysis of whole-brain fMRI dynamics: A new framework based on dynamic communicability. *NeuroImage* 201. 10.1016/j.neuroimage.2019.116007

Gilson, M., Kouvaris, N. E., Deco, G., and Zamora-López, G. (2017). A novel framework to analyze complex network dynamics 10.1103/PhysRevE.97.052301

Gilson, M., Moreno-Bote, R., Ponce-Alvarez, A., Ritter, P., and Deco, G. (2016). Estimation of Directed Effective Connectivity from fMRI Functional Connectivity Hints at Asymmetries of Cortical Connectome. *PLoS computational biology* 12, e1004762. 10.1371/journal.pcbi.1004762

Gilson, M., Zamora-López, G., Pallarés, V., Adhikari, M. H., Senden, M., Campo, A. T., et al. (2019b). Model-based whole-brain effective connectivity to study distributed cognition in health and disease. *Network Neuroscience* 4, 338–373. 10.1162/netn_a_00117

Glerean, E., Salmi, J., Lahnakoski, J. M., Jääskeläinen, I. P., and Sams, M. (2012). Functional Magnetic Resonance Imaging Phase Synchronization as a Measure of Dynamic Functional Connectivity. *Brain Connectivity* 2, 91–101. 10.1089/brain.2011.0068

Glomb, K., Mullier, E., Carboni, M., Rubega, M., Iannotti, G., Tourbier, S., et al. (2019). Using structural connectivity to augment community structure in EEG functional connectivity. *bioRxiv* , 83174310.1101/831743

Golesorkhi, M., Gomez-Pilar, J., Tumati, S., Fraser, M., and Northoff, G. (2021). Temporal hierarchy of intrinsic neural timescales converges with spatial core-periphery organization. *Communications Biology* 4, 277. 10.1038/s42003-021-01785-z

Gollo, L. L. (2019). Exploring atypical timescales in the brain. *eLife* 8. 10.7554/eLife.45089

Gollo, L. L., Zalesky, A., Matthew Hutchison, R., Van Den Heuvel, M., and Breakspear, M. (2015). Dwelling quietly in the rich club: Brain network determinants of slow cortical fluctuations. *Philosophical Transactions of the Royal Society B: Biological Sciences* 370. 10.1098/rstb.2014.0165

Gómez-Gardeñes, J., Zamora-López, G., Moreno, Y., and Arenas, A. (2010). From modular to centralized organization of synchronization in functional areas of the cat cerebral cortex. *PLoS ONE* 5, 12313. 10.1371/journal.pone.0012313

Gong, G., He, Y., Concha, L., Lebel, C., Gross, D. W., Evans, A. C., et al. (2009). Mapping Anatomical Connectivity Patterns of Human Cerebral Cortex Using In Vivo Diffusion Tensor Imaging Tractography. *Cerebral Cortex* 19, 524–536. 10.1093/cercor/bhn102

Grayson, D. S., Ray, S., Carpenter, S., Iyer, S., Dias, T. G., Stevens, C., et al. (2014). Structural and functional rich club organization of the brain in children and adults. *PLoS ONE* 9, 88297. 10.1371/journal.pone.0088297

Greicius, M. (2008). Resting-state functional connectivity in neuropsychiatric disorders. *Current opinion in neurology* 21, 424–30. 10.1097/WCO.0b013e328306f2c5

Greicius, M. D., Krasnow, B., Reiss, A. L., and Menon, V. (2003). Functional connectivity in the resting brain: A network analysis of the default mode hypothesis. *Proceedings of the National Academy of Sciences* 100, 253–258. 10.1073/pnas.0135058100

Greicius, M. D., Supekar, K., Menon, V., and Dougherty, R. F. (2009). Resting-State Functional Connectivity Reflects Structural Connectivity in the Default Mode Network. *Cerebral Cortex* 19, 72–78. 10.1093/cercor/bhn059

Griffanti, L., Douaud, G., Bijsterbosch, J., Evangelisti, S., Alfaro-Almagro, F., Glasser, M. F., et al. (2017). Hand classification of fMRI ICA noise components. *NeuroImage* 154, 188–205. 10.1016/j.neuroimage.2016.12.036

Griffanti, L., Salimi-Khorshidi, G., Beckmann, C. F., Auerbach, E. J., Douaud, G., Sexton, C. E., et al. (2014). ICA-based artefact removal and accelerated fMRI acquisition for improved resting state network imaging. *NeuroImage* 95, 232–247. 10.1016/j.neuroimage.2014.03.034

Gu, S., Yang, M., Medaglia, J. D., Gur, R. C., Gur, R. E., Satterthwaite, T. D., et al. (2017). Functional hypergraph uncovers novel covariant structures over neurodevelopment. *Human Brain Mapping* 38, 3823–3835. 10.1002/hbm.23631

Gummadavelli, A., Motelow, J. E., Smith, N., Zhan, Q., Schiff, N. D., and Blumenfeld, H. (2015). Thalamic stimulation to improve level of consciousness after seizures: Evaluation of electrophysiology and behavior. *Epilepsia* 56, 114–124. 10.1111/epi.12872

Haber, S. N. and Calzavara, R. (2009). The cortico-basal ganglia integrative network: The role of the thalamus. 10.1016/j.brainresbull.2008.09.013

Hagmann, P. (2005). *From Diffusion MRI to Brain Connectomics — .* Ph.D. thesis

Hagmann, P., Cammoun, L., Gigandet, X., Meuli, R., Honey, C. J., Wedeen, V. J., et al. (2008). Mapping the Structural Core of Human Cerebral Cortex. *PLoS Biology* 6, e159. 10.1371/journal.pbio.0060159

Hahn, G., Petermann, T., Havenith, M. N., Yu, S., Singer, W., Plenz, D., et al. (2010). Neuronal avalanches in spontaneous activity in vivo. *Journal of neurophysiology* 104, 3312–22. 10.1152/jn.00953.2009

Hahn, G., Ponce-Alvarez, A., Monier, C., Benvenuti, G., Kumar, A., Chavane, F., et al. (2017). Spontaneous cortical activity is transiently poised close to criticality. *PLOS Computational Biology* 13, e1005543. 10.1371/journal.pcbi.1005543

Haken, H., Kelso, J. A., and Bunz, H. (1985). A theoretical model of phase transitions in human hand movements. *Biological Cybernetics* 51, 347–356. 10.1007/BF00336922

Haldeman, C. and Beggs, J. M. (2005). Critical branching captures activity in living neural networks and maximizes the number of metastable States. *Physical review letters* 94, 058101. 10.1103/PhysRevLett.94.058101

Hansen, E. C., Battaglia, D., Spiegler, A., Deco, G., and Jirsa, V. K. (2015). Functional connectivity dynamics: Modeling the switching behavior of the resting state. *NeuroImage* 105, 525–535. 10.1016/j.neuroimage.2014.11.001

Hasson, U., Yang, E., Vallines, I., Heeger, D. J., and Rubin, N. (2008). A hierarchy of temporal receptive windows in human cortex. *Journal of Neuroscience* 28, 2539–2550. 10.1523/JNEUROSCI.5487-07.2008

Haufe, S., Nikulin, V. V., Müller, K. R., and Nolte, G. (2013). A critical assessment of connectivity measures for EEG data: A simulation study. *NeuroImage* 64, 120–133. 10.1016/j.neuroimage.2012.09.036

He, B. J. (2013). Spontaneous and task-evoked brain activity negatively interact. *Journal of Neuroscience* 33, 4672–4682. 10.1523/JNEUROSCI.2922-12.2013

Hellyer, P. J., Shanahan, M., Scott, G., Wise, R. J. S., Sharp, D. J., and Leech, R. (2014). The control of global brain dynamics: opposing actions of frontoparietal control and default mode networks on attention. *The Journal of neuroscience : the official journal of the Society for Neuroscience* 34, 451–61. 10.1523/JNEUROSCI.1853-13.2014

Herbet, G., Lafargue, G., de Champfleur, N. M., Moritz-Gasser, S., le Bars, E., Bonnetblanc, F., et al. (2014). Disrupting posterior cingulate connectivity disconnects consciousness from the external environment. *Neuropsychologia* 56, 239–44. 10.1016/j.neuropsychologia.2014.01.020

Herzog, R., Mediano, P. A., Rosas, F. E., Carhart-Harris, R., Perl, Y. S., Tagliazucchi, E., et al. (2020). A mechanistic model of the neural entropy increase elicited by psychedelic drugs. *Scientific Reports* 10, 17725. 10.1038/s41598-020-74060-6

Hilgetag, C. C. and Goulas, A. (2020). âHierarchyâ in the organization of brain networks. 10.1098/rstb.2019.0319

Hindriks, R., van Putten, M. J., and Deco, G. (2014). Intra-cortical propagation of EEG alpha oscillations. *NeuroImage* 103, 444–453. 10.1016/j.neuroimage.2014.08.027

Hodgkin, A. L. and Huxley, A. F. (1952). A quantitative description of membrane current and its application to conduction and excitation in nerve. *The Journal of Physiology* 117, 500–544. 10.1113/jphysiol.1952.sp004764

Honey, C. J., Kötter, R., Breakspear, M., and Sporns, O. (2007). Network structure of cerebral cortex shapes functional connectivity on multiple time scales. *Proceedings of the National Academy of Sciences of the United States of America* 104, 10240–10245. 10.1073/pnas.0701519104

Honey, C. J., Sporns, O., Cammoun, L., Gigandet, X., Thiran, J. P., Meuli, R., et al. (2009). Predicting human resting-state functional connectivity from structural connectivity. *Proceedings of the National Academy of Sciences of the United States of America* 106, 2035–40. 10.1073/pnas.0811168106

Honey, C. J., Thesen, T., Donner, T. H., Silbert, L. J., Carlson, C. E., Devinsky, O., et al. (2012). Slow Cortical Dynamics and the Accumulation of Information over Long Timescales. *Neuron* 76, 423–434. 10.1016/j.neuron.2012.08.011

Hopfield, J. J. (1982). Neural networks and physical systems with emergent collective computational abilities. *Proceedings of the National Academy of Sciences of the United States of America* 79, 2554–2558. 10.1073/pnas.79.8.2554

Huang, Y. Z., Lu, M. K., Antal, A., Classen, J., Nitsche, M., Ziemann, U., et al. (2017). Plasticity induced by non-invasive transcranial brain stimulation: A position paper. 10.1016/j.clinph.2017.09.007

Hudetz, A. G. (2012). General Anesthesia and Human Brain Connectivity. 10.1089/brain.2012.0107

Hudetz, A. G., Liu, X., and Pillay, S. (2015). Dynamic repertoire of intrinsic brain states is reduced in propofol-induced unconsciousness. *Brain Connectivity* 5, 10–22. 10.1089/brain.2014.0230

Ipiña, I. P., Kehoe, P. D., Kringelbach, M., Laufs, H., Ibañez, A., Deco, G., et al. (2020). Modeling regional changes in dynamic stability during sleep and wakefulness. *NeuroImage* 215, 116833. 10.1016/j.neuroimage.2020.116833

Ito, T., Hearne, L. J., and Cole, M. W. (2020). A cortical hierarchy of localized and distributed processes revealed via dissociation of task

activations, connectivity changes, and intrinsic timescales. *NeuroImage* 221. 10.1016/j.neuroimage.2020.117141

Izhikevich, E. M. and Edelman, G. M. (2008). Large-scale model of mammalian thalamocortical systems. *Proceedings of the National Academy of Sciences of the United States of America* 105, 3593–3598. 10.1073/pnas.0712231105

Jenkinson, M., Bannister, P., Brady, M., and Smith, S. (2002). Improved optimization for the robust and accurate linear registration and motion correction of brain images. *NeuroImage* 17, 825–41. 10.1016/s1053-8119(02)91132-8

Jenkinson, M. and Smith, S. (2001). A global optimisation method for robust affine registration of brain images. *Medical image analysis* 5, 143–56. 10.1016/s1361-8415(01)00036-6

Jennett, B. and Plum, F. (1972). Persistent vegetative state after brain damage. *RN* 35, 1–4

Jeurissen, B., Descoteaux, M., Mori, S., and Leemans, A. (2019). Diffusion MRI fiber tractography of the brain. 10.1002/nbm.3785

Jirsa, V. K., Fuchs, A., and Kelso, J. A. (1998). Connecting cortical and behavioral dynamics: bimanual coordination. *Neural computation* 10, 2019–45

Jobst, B. M., Hindriks, R., Laufs, H., Tagliazucchi, E., Hahn, G., Ponce-Alvarez, A., et al. (2017). Increased Stability and Breakdown of Brain Effective Connectivity During Slow-Wave Sleep: Mechanistic Insights from Whole-Brain Computational Modelling. *Scientific Reports* 7, 4634. 10.1038/s41598-017-04522-x

John, E. R., Prichep, L. S., Kox, W., Valdés-Sosa, P., Bosch-Bayard, J., Aubert, E., et al. (2001). Invariant reversible QEEG effects of anesthetics. *Consciousness and Cognition* 10, 165–183. 10.1006/ccog.2001.0507

Jurd, R., Arras, M., Lambert, S., Drexler, B., Siegwart, R., Crestani, F., et al. (2003). General anesthetic actions in vivo strongly attenuated by a point mutation in the GABA(A) receptor beta3 subunit. *The FASEB*

journal : official publication of the Federation of American Societies for Experimental Biology 17, 250–252. 10.1096/fj.02-0611fje

Kafashan, M. M., Ching, S. N., and Palanca, B. J. (2016). Sevoflurane alters spatiotemporal functional connectivity motifs that link resting-state networks during wakefulness. *Frontiers in Neural Circuits* 10. 10.3389/fncir.2016.00107

Kaiser, M. and Hilgetag, C. C. (2010). Optimal hierarchical modular topologies for producing limited sustained activation of neural networks. *Frontiers in Neuroinformatics* 4. 10.3389/fninf.2010.00008

Kelso, J. A. (1984). Phase transitions and critical behavior in human bimanual coordination. *American Journal of Physiology - Regulatory Integrative and Comparative Physiology* 15. 10.1152/ajpregu.1984.246.6.r1000

Kinouchi, O. and Copelli, M. (2006). Optimal dynamical range of excitable networks at criticality. *Nature Physics* 2, 348–351. 10.1038/nphys289

Kitano, H. (2004). Biological robustness. 10.1038/nrg1471

Kitzbichler, M. G., Smith, M. L., Christensen, S. R., and Bullmore, E. (2009). Broadband Criticality of Human Brain Network Synchronization. *PLoS Computational Biology* 5, e1000314. 10.1371/journal.pcbi.1000314

Kiviniemi, V., Vire, T., Remes, J., Elseoud, A. A., Starck, T., Tervonen, O., et al. (2011). A Sliding Time-Window ICA Reveals Spatial Variability of the Default Mode Network in Time. *Brain Connectivity* 1, 339–347. 10.1089/brain.2011.0036

Kobeleva, X. (2020). Spatiotemporal scales of dynamical functional networks â using whole-brain modelling to identify the optimal resolution. *bioRxiv* , 2020.09.12.27769910.1101/2020.09.12.277699

Kobeleva, X., Varoquaux, G., Dagher, A., Adhikari, M., Grefkes, C., and Gilson, M. (2021). Advancing brain network models to reconcile functional neuroimaging and clinical research. *PsyArXiv* , 1–2310.31234/OSF.IO/SYQPC

Koch, C., Massimini, M., Boly, M., and Tononi, G. (2016). Neural correlates of consciousness: Progress and problems. 10.1038/nrn.2016.22

Koenig, T., Lehmann, D., Merlo, M. C., Kochi, K., Hell, D., and Koukkou, M. (1999). A deviant EEG brain microstate in acute, neuroleptic-naive schizophrenics at rest. *European archives of psychiatry and clinical neuroscience* 249, 205–11

Koenig, T., Prichep, L., Lehmann, D., Sosa, P. V., Braeker, E., Kleinlogel, H., et al. (2002). Millisecond by millisecond, year by year: normative EEG microstates and developmental stages. *NeuroImage* 16, 41–8. 10.1006/nimg.2002.1070

Kringelbach, M. L. and Deco, G. (2020). Brain States and Transitions: Insights from Computational Neuroscience. 10.1016/j.celrep.2020.108128

Kringelbach, M. L., Jenkinson, N., Owen, S. L., and Aziz, T. Z. (2007). Translational principles of deep brain stimulation. 10.1038/nrn2196

Kuznetsov, Y. A. (2004). *Elements of Applied Bifurcation Theory*, vol. 112 of *Applied Mathematical Sciences* (New York, NY: Springer New York). 10.1007/978-1-4757-3978-7

LANDAU and D., L. (1944). On the problem of turbulence. *Dokl. Akad. Nauk USSR* 44, 311

Langlois, J. A., Rutland-Brown, W., and Wald, M. M. (2006). The epidemiology and impact of traumatic brain injury: A brief overview. 10.1097/00001199-200609000-00001

Laufs, H., Krakow, K., Sterzer, P., Eger, E., Beyerle, A., Salek-Haddadi, A., et al. (2003). Electroencephalographic signatures of attentional and cognitive default modes in spontaneous brain activity fluctuations at rest. *Proceedings of the National Academy of Sciences of the United States of America* 100, 11053–11058. 10.1073/pnas.1831638100

Laureys, S. (2005). The neural correlate of (un)awareness: lessons from the vegetative state. *Trends in Cognitive Sciences* 9, 556–559. 10.1016/j.tics.2005.10.010

Laureys, S., Celesia, G. G., Cohadon, F., Lavrijsen, J., León-Carrión, J., Sannita, W. G., et al. (2010). Unresponsive wakefulness syndrome: A new name for the vegetative state or apallic syndrome. *BMC Medicine* 8. 10.1186/1741-7015-8-68

Laureys, S., Goldman, S., Phillips, C., Van Bogaert, P., Aerts, J., Luxen, A., et al. (1999). Impaired effective cortical connectivity in vegetative state: Preliminary investigation using PET. *NeuroImage* 9, 377–382. 10.1006/nimg.1998.0414

Laureys, S., Owen, A. M., and Schiff, N. D. (2004). Brain function in coma, vegetative state, and related disorders. *The Lancet. Neurology* 3, 537–46. 10.1016/S1474-4422(04)00852-X

Leemans, A. and Jones, D. K. (2009). The ¡i¿B¡/i¿ -matrix must be rotated when correcting for subject motion in DTI data. *Magnetic Resonance in Medicine* 61, 1336–1349. 10.1002/mrm.21890

Lehmann, D., Faber, P. L., Galderisi, S., Herrmann, W. M., Kinoshita, T., Koukkou, M., et al. (2005). EEG microstate duration and syntax in acute, medication-naïve, first-episode schizophrenia: a multicenter study. *Psychiatry Research: Neuroimaging* 138, 141–156. 10.1016/j.pscychresns.2004.05.007

Lehmann, D., Ozaki, H., and Pal, I. (1987). EEG alpha map series: brain micro-states by space-oriented adaptive segmentation. *Electroencephalography and clinical neurophysiology* 67, 271–88. 10.1016/0013-4694(87)90025-3

Lehmann, D., Strik, W., Henggeler, B., Koenig, T., and Koukkou, M. (1998). Brain electric microstates and momentary conscious mind states as building blocks of spontaneous thinking: I. Visual imagery and abstract thoughts. *International Journal of Psychophysiology* 29, 1–11. 10.1016/S0167-8760(97)00098-6

Lerner, Y., Honey, C. J., Silbert, L. J., and Hasson, U. (2011). Topographic mapping of a hierarchy of temporal receptive windows using a narrated story. *Journal of Neuroscience* 31, 2906–2915. 10.1523/JNEUROSCI.3684-10.2011

Libet, B. (1993). The Experimental Evidence for Subjective Referral of a Sensory Experience Backwards in Time: Reply to P. S. Churchland. In *Neurophysiology of Consciousness* (Boston, MA: Birkhäuser Boston). 205–220. 10.1007/978-1-4612-0355-1_11

Lin, S., Sun, Q., Wang, H., and Xie, G. (2018). Influence of transcutaneous electrical nerve stimulation on spasticity, balance, and walking speed in stroke patients: A systematic review and meta-analysis. 10.2340/16501977-2266

Lin, Y., Liu, T., Huang, Q., Su, Y., Chen, W., Gao, D., et al. (2019). Electroencephalography and functional magnetic resonance imaging-guided simultaneous transcranial direct current stimulation and repetitive transcranial magnetic stimulation in a patient with minimally conscious state. *Frontiers in Genetics* 10. 10.3389/fnins.2019.00746

Llinás, R. R. and Paré, D. (1991). Of dreaming and wakefulness. *Neuroscience* 44, 521–535. 10.1016/0306-4522(91)90075-Y

Llinás, R. R. and Ribary, U. (1998). Temporal conjunction in thalamocortical transactions. *Advances in neurology* 77, 95–102

Logothetis, N. K., Pauls, J., Augath, M., Trinath, T., and Oeltermann, A. (2001). Neurophysiological investigation of the basis of the fMRI signal. *Nature* 412, 150–157. 10.1038/35084005

Lopes-dos Santos, V., Ribeiro, S., and Tort, A. B. (2013). Detecting cell assemblies in large neuronal populations. *Journal of Neuroscience Methods* 220, 149–166. 10.1016/j.jneumeth.2013.04.010

Lord, L. D., Stevner, A. B., Deco, G., and Kringelbach, M. L. (2017). Understanding principles of integration and segregation using whole-brain computational connectomics: Implications for neuropsychiatric disorders. 10.1098/rsta.2016.0283

Lotze, M., Montoya, P., Erb, M., Hülsmann, E., Flor, H., Klose, U., et al. (1999). Activation of cortical and cerebellar motor areas during executed and imagined hand movements: An fMRI study. *Journal of Cognitive Neuroscience* 11, 491–501. 10.1162/089892999563553

Luppi, A. I., Craig, M. M., Pappas, I., Finoia, P., Williams, G. B., Allanson, J., et al. (2019). Consciousness-specific dynamic interactions of brain integration and functional diversity. *Nature Communications* 10, 1–12. 10.1038/s41467-019-12658-9

Luppi, A. I., Mediano, P. A., Rosas, F. E., Allanson, J., Williams, G. B., Craig, M. M., et al. (2021). Paths to Oblivion: Common Neural Mechanisms of Anaesthesia and Disorders of Consciousness. *bioRxiv* , 2021.02.14.43114010.1101/2021.02.14.431140

Mantini, D., Perrucci, M. G., Del Gratta, C., Romani, G. L., and Corbetta, M. (2007). Electrophysiological signatures of resting state networks in the human brain. *Proceedings of the National Academy of Sciences of the United States of America* 104, 13170–5. 10.1073/pnas.0700668104

Margulies, D. S., Ghosh, S. S., Goulas, A., Falkiewicz, M., Huntenburg, J. M., Langs, G., et al. (2016). Situating the default-mode network along a principal gradient of macroscale cortical organization. *Proceedings of the National Academy of Sciences of the United States of America* 113, 12574–12579. 10.1073/pnas.1608282113

Marinazzo, D., Riera, J. J., Marzetti, L., Astolfi, L., Yao, D., and Valdés Sosa, P. A. (2019). Controversies in EEG Source Imaging and Connectivity: Modeling, Validation, Benchmarking. 10.1007/s10548-019-00709-9

Markram, H., Muller, E., Ramaswamy, S., Reimann, M. W., Abdellah, M., Sanchez, C. A., et al. (2015). Reconstruction and Simulation of Neocortical Microcircuitry. *Cell* 163, 456–492. 10.1016/j.cell.2015.09.029

Marre, O., El Boustani, S., Frégnac, Y., and Destexhe, A. (2009). Prediction of Spatiotemporal Patterns of Neural Activity from Pairwise Correlations. *Physical Review Letters* 102, 138101. 10.1103/PhysRevLett.102.138101

Marshall, N., Timme, N. M., Bennett, N., Ripp, M., Lautzenhiser, E., and Beggs, J. M. (2016). Analysis of Power Laws, Shape Collapses, and Neural Complexity: New Techniques and MATLAB Support via the NCC Toolbox. *Frontiers in physiology* 7, 250. 10.3389/fphys.2016.00250

Martuzzi, R., Ramani, R., Qiu, M., Rajeevan, N., and Constable, R. T. (2010). Functional connectivity and alterations in baseline brain state in humans. *NeuroImage* 49, 823–834. 10.1016/j.neuroimage.2009.07.028

Mashour, G. A., Roelfsema, P., Changeux, J. P., and Dehaene, S. (2020). Conscious Processing and the Global Neuronal Workspace Hypothesis. 10.1016/j.neuron.2020.01.026

Mason, M. F., Norton, M. I., Van Horn, J. D., Wegner, D. M., Grafton, S. T., and Macrae, C. N. (2007). Wandering minds: The default network and stimulus-independent thought. *Science* 315, 393–395. 10.1126/science.1131295

Massimini, M., Ferrarelli, F., Huber, R., Esser, S. K., Singh, H., and Tononi, G. (2005). Breakdown of Cortical Effective Connectivity During Sleep. *Science* 309, 2228–2232. 10.1126/science.1117256

May, R. M. (1972). Will a large complex system be stable? *Nature* 238, 413–414. 10.1038/238413a0

Mazzoni, A., Broccard, F. D., Garcia-Perez, E., Bonifazi, P., Ruaro, M. E., and Torre, V. (2007). On the Dynamics of the Spontaneous Activity in Neuronal Networks. *PLoS ONE* 2, e439. 10.1371/journal.pone.0000439

Messé, A., Rudrauf, D., Benali, H., and Marrelec, G. (2014). Relating Structure and Function in the Human Brain: Relative Contributions of Anatomy, Stationary Dynamics, and Non-stationarities. *PLoS Computational Biology* 10. 10.1371/journal.pcbi.1003530

Mesulam, M. M. (1998). From sensation to cognition. 10.1093/brain/121.6.1013

Michel, C. M. and Koenig, T. (2018). EEG microstates as a tool for studying the temporal dynamics of whole-brain neuronal networks: A review. *NeuroImage* 180, 577–593. 10.1016/j.neuroimage.2017.11.062

Mohr, H., Wolfensteller, U., Betzel, R. F., Mišić, B., Sporns, O., Richiardi, J., et al. (2016). Integration and segregation of large-scale brain networks during short-term task automatization. *Nature Communications* 7. 10.1038/ncomms13217

Monti, M. M., Lutkenhoff, E. S., Rubinov, M., Boveroux, P., Vanhaudenhuyse, A., Gosseries, O., et al. (2013). Dynamic Change of Global and Local Information Processing in Propofol-Induced Loss and Recovery of Consciousness. *PLoS Computational Biology* 9. 10.1371/journal.pcbi.1003271

Moretti, P. and Muñoz, M. A. (2013). Griffiths phases and the stretching of criticality in brain networks. *Nature Communications* 4, 1–10. 10.1038/ncomms3521

Munoz, M. A. (2017). Colloquium: Criticality and dynamical scaling in living systems 10.1103/RevModPhys.90.031001

Muñoz, M. A., Juhász, R., Castellano, C., and Ódor, G. (2010). Griffiths phases on complex networks. *Physical Review Letters* 105, 128701. 10.1103/PhysRevLett.105.128701

Murase, N., Duque, J., Mazzocchio, R., and Cohen, L. G. (2004). Influence of interhemispheric interactions on motor function in chronic stroke. *Annals of Neurology* 55, 400–409. 10.1002/ana.10848

Murray, J. D., Bernacchia, A., Freedman, D. J., Romo, R., Wallis, J. D., Cai, X., et al. (2014). A hierarchy of intrinsic timescales across primate cortex. *Nature Neuroscience* 17, 1661–1663. 10.1038/nn.3862

Musso, F., Brinkmeyer, J., Mobascher, A., Warbrick, T., and Winterer, G. (2010). Spontaneous brain activity and EEG microstates. A novel EEG/fMRI analysis approach to explore resting-state networks. 10.1016/j.neuroimage.2010.01.093

Muthuraman, M., Fleischer, V., Kolber, P., Luessi, F., Zipp, F., and Groppa, S. (2016). Structural Brain Network Characteristics Can Differentiate CIS from Early RRMS. *Frontiers in neuroscience* 10, 14. 10.3389/fnins.2016.00014

Nakagawa, T. T., Woolrich, M., Luckhoo, H., Joensson, M., Mohseni, H., Kringelbach, M. L., et al. (2014). How delays matter in an oscillatory whole-brain spiking-neuron network model for MEG alpha-rhythms at rest. *NeuroImage* 87, 383–394. 10.1016/j.neuroimage.2013.11.009

Newman, M. E. (2006). Modularity and community structure in networks. *Proceedings of the National Academy of Sciences of the United States of America* 103, 8577–8582. 10.1073/pnas.0601602103

Nishida, K., Morishima, Y., Yoshimura, M., Isotani, T., Irisawa, S., Jann, K., et al. (2013). EEG microstates associated with salience and frontoparietal networks in frontotemporal dementia, schizophrenia and Alzheimer's disease. *Clinical Neurophysiology* 124, 1106–1114. 10.1016/j.clinph.2013.01.005

Northoff, G. and Lamme, V. (2020). Neural signs and mechanisms of consciousness: Is there a potential convergence of theories of consciousness in sight? 10.1016/j.neubiorev.2020.07.019

Ódor, G. (2016). Critical dynamics on a large human Open Connectome network. *Physical Review E* 94, 062411. 10.1103/PhysRevE.94.062411

Olejniczak, P. (2006). Neurophysiologic basis of EEG. In *Journal of Clinical Neurophysiology* (J Clin Neurophysiol), vol. 23, 186–189. 10.1097/01.wnp.0000220079.61973.6c

Owen, A. M. (2019). The Search for Consciousness. 10.1016/j.neuron.2019.03.024

Owen, A. M., Coleman, M. R., Boly, M., Davis, M. H., Laureys, S., and Pickard, J. D. (2006). Detecting awareness in the vegetative state. *Science* 313, 1402. 10.1126/science.1130197

Padilla, N., Saenger, V. M., van Hartevelt, T. J., Fernandes, H. M., Lennartsson, F., Andersson, J. L. R., et al. (2019). Breakdown of Whole-brain Dynamics in Preterm-born Children. *Cerebral Cortex* 10.1093/cercor/bhz156

Pallarés, V., Insabato, A., Sanjuán, A., Kühn, S., Mantini, D., Deco, G., et al. (2018). Extracting orthogonal subject- and condition-specific signatures from fMRI data using whole-brain effective connectivity. *NeuroImage* 178, 238–254. 10.1016/j.neuroimage.2018.04.070

Panda, R., Bharath, R. D., Upadhyay, N., Mangalore, S., Chennu, S., and Rao, S. L. (2016). Temporal Dynamics of the Default Mode Network

Characterize Meditation-Induced Alterations in Consciousness. *Frontiers in Human Neuroscience* 10, 372. 10.3389/fnhum.2016.00372

Pasquale, V., Massobrio, P., Bologna, L., Chiappalone, M., and Martinoia, S. (2008). Self-organization and neuronal avalanches in networks of dissociated cortical neurons. *Neuroscience* 153, 1354–1369. 10.1016/j.neuroscience.2008.03.050

Perl, Y. S., Pallavicini, C., Pérez Ipiña, I., Demertzi, A., Bonhomme, V., Martial, C., et al. (2020). Perturbations in dynamical models of whole-brain activity dissociate between the level and stability of consciousness. *ORBi : Université de Liège* , 2020.07.02.18515710.1101/2020.07.02.185157

Peyrache, A., Benchenane, K., Khamassi, M., Wiener, S. I., and Battaglia, F. P. (2010). Principal component analysis of ensemble recordings reveals cell assemblies at high temporal resolution. *Journal of Computational Neuroscience* 29, 309–325. 10.1007/s10827-009-0154-6

Piarulli, A., Bergamasco, M., Thibaut, A., Cologan, V., Gosseries, O., and Laureys, S. (2016). EEG ultradian rhythmicity differences in disorders of consciousness during wakefulness. *Journal of Neurology* 263, 1746–1760. 10.1007/s00415-016-8196-y

Pigorini, A., Sarasso, S., Proserpio, P., Szymanski, C., Arnulfo, G., Casarotto, S., et al. (2015). Bistability breaks-off deterministic responses to intracortical stimulation during non-REM sleep. *NeuroImage* 112, 105–113. 10.1016/j.neuroimage.2015.02.056

Pikovsky, A., Rosenblum, M., Kurths, J., and Hilborn, R. C. (2002). Synchronization: A Universal Concept in Nonlinear Science . *American Journal of Physics* 70, 655–655. 10.1119/1.1475332

Plenz, D. and Thiagarajan, T. C. (2007). The organizing principles of neuronal avalanches: cell assemblies in the cortex? *Trends in Neurosciences* 30, 101–110. 10.1016/j.tins.2007.01.005

Ponce-Alvarez, A., Deco, G., Hagmann, P., Romani, G. L., Mantini, D., and Corbetta, M. (2015). Resting-State Temporal Synchronization Net-

works Emerge from Connectivity Topology and Heterogeneity. *PLOS Computational Biology* 11, e1004100. 10.1371/journal.pcbi.1004100

Ponce-Alvarez, A., Jouary, A., Privat, M., Deco, G., and Sumbre, G. (2018). Whole-Brain Neuronal Activity Displays Crackling Noise Dynamics. *Neuron* 100, 1446–1459. 10.1016/j.neuron.2018.10.045

Ponce-Alvarez, A., Mochol, G., Hermoso-Mendizabal, A., de la Rocha, J., and Deco, G. (2020). Cortical state transitions and stimulus response evolve along stiff and sloppy parameter dimensions, respectively. *eLife* 9. 10.7554/eLife.53268

Ponce-Alvarez, A., Uhrig, L., Deco, N., Signorelli, C. M., Jarraya, B., and Deco, G. (2021). Macroscopic quantities of collective brain activity during wakefulness and anesthesia. *bioRxiv* , 2021.02.03.42957810.1101/2021.02.03.429578

Potjans, T. C. and Diesmann, M. (2014). The cell-type specific cortical microcircuit: Relating structure and activity in a full-scale spiking network model. *Cerebral Cortex* 24, 785–806. 10.1093/cercor/bhs358

Power, J. D., Barnes, K. A., Snyder, A. Z., Schlaggar, B. L., and Petersen, S. E. (2012). Spurious but systematic correlations in functional connectivity MRI networks arise from subject motion. *NeuroImage* 59, 2142–2154. 10.1016/j.neuroimage.2011.10.018

Priesemann, V., Wibral, M., Valderrama, M., Pröpper, R., Le Van Quyen, M., Geisel, T., et al. (2014). Spike avalanches in vivo suggest a driven, slightly subcritical brain state. *Frontiers in Systems Neuroscience* 8, 108. 10.3389/fnsys.2014.00108

Qin, P. and Northoff, G. (2011). How is our self related to midline regions and the default-mode network? 10.1016/j.neuroimage.2011.05.028

Raichle, M. E. (2001). Bold insights. 10.1038/35084300

Raichle, M. E. (2009). A paradigm shift in functional brain imaging. 10.1523/JNEUROSCI.4366-09.2009

Rieger, K., Hernandez, L. D., Baenninger, A., and Koenig, T. (2016). 15 years of microstate research in schizophrenia - Where are we? A meta-analysis. *Frontiers in Psychiatry* 7, 22. 10.3389/fpsyt.2016.00022

Rizkallah, J., Annen, J., Modolo, J., Gosseries, O., Benquet, P., Mortaheb, S., et al. (2019). Decreased integration of EEG source-space networks in disorders of consciousness. *NeuroImage: Clinical* 23, 101841. 10.1016/j.nicl.2019.101841

Rodriguez, E., George, N., Lachaux, J. P., Martinerie, J., Renault, B., and Varela, F. J. (1999). Perception's shadow: long-distance synchronization of human brain activity. *Nature* 397, 430–3. 10.1038/17120

Rosanova, M., Fecchio, M., Casarotto, S., Sarasso, S., Casali, A. G., Pigorini, A., et al. (2018). Sleep-like cortical OFF-periods disrupt causality and complexity in the brain of unresponsive wakefulness syndrome patients. *Nature Communications* 9, 4427. 10.1038/s41467-018-06871-1

Rubega, M., Carboni, M., Seeber, M., Pascucci, D., Tourbier, S., Toscano, G., et al. (2019). Estimating EEG Source Dipole Orientation Based on Singular-value Decomposition for Connectivity Analysis. *Brain Topography* 32, 704–719. 10.1007/s10548-018-0691-2

Rubinov, M. and Sporns, O. (2010). Complex network measures of brain connectivity: Uses and interpretations. *NeuroImage* 52, 1059–1069. 10.1016/J.NEUROIMAGE.2009.10.003

Rubinov, M. and Sporns, O. (2011). Weight-conserving characterization of complex functional brain networks. *NeuroImage* 56, 2068–2079. 10.1016/j.neuroimage.2011.03.069

Rudie, J. D., Brown, J. A., Beck-Pancer, D., Hernandez, L. M., Dennis, E. L., Thompson, P. M., et al. (2012). Altered functional and structural brain network organization in autism. *NeuroImage. Clinical* 2, 79–94. 10.1016/j.nicl.2012.11.006

Saenger, V. M., Kahan, J., Foltynie, T., Friston, K., Aziz, T. Z., Green, A. L., et al. (2017). Uncovering the underlying mechanisms and whole-brain dynamics of deep brain stimulation for Parkinson's disease. *Scientific reports* 7, 9882. 10.1038/s41598-017-10003-y

Saenger, V. M., Ponce-Alvarez, A., Adhikari, M., Hagmann, P., Deco, G., and Corbetta, M. (2018). Linking entropy at rest with the underlying structural connectivity in the healthy and lesioned brain. *Cerebral Cortex* 28, 2948–2958. 10.1093/cercor/bhx176

Salimi-Khorshidi, G., Douaud, G., Beckmann, C. F., Glasser, M. F., Griffanti, L., and Smith, S. M. (2014). Automatic denoising of functional MRI data: Combining independent component analysis and hierarchical fusion of classifiers. *NeuroImage* 90, 449–468. 10.1016/j.neuroimage.2013.11.046

Sanchez-Vives, M. V., Barbero-Castillo, A., Perez-Zabalza, M., and Reig, R. (2021). GABAB receptors: modulation of thalamocortical dynamics and synaptic plasticity. 10.1016/j.neuroscience.2020.03.011

Sanchez-Vives, M. V., Massimini, M., and Mattia, M. (2017). Shaping the Default Activity Pattern of the Cortical Network. 10.1016/j.neuron.2017.05.015

Sarasso, S., Rosanova, M., Casali, A. G., Casarotto, S., Fecchio, M., Boly, M., et al. (2014). Quantifying cortical EEG responses to TMS in (Un)consciousness. *Clinical EEG and Neuroscience* 45, 40–49. 10.1177/1550059413513723

Schartner, M., Seth, A., Noirhomme, Q., Boly, M., Bruno, M. A., Laureys, S., et al. (2015). Complexity of multi-dimensional spontaneous EEG decreases during propofol induced general anaesthesia. *PLoS ONE* 10. 10.1371/journal.pone.0133532

Schiff, N. D. (2010). Recovery of consciousness after brain injury: a mesocircuit hypothesis. 10.1016/j.tins.2009.11.002

Schilling, K. G., Rheault, F., Petit, L., Hansen, C. B., Nath, V., Yeh, F. C., et al. (2020). Tractography dissection variability: what happens when 42 groups dissect 14 white matter bundles on the same dataset? 10.1101/2020.10.07.321083

Schmidt, R., LaFleur, K. J., de Reus, M. A., van den Berg, L. H., and van den Heuvel, M. P. (2015). Kuramoto model simulation of neural

hubs and dynamic synchrony in the human cerebral connectome. *BMC Neuroscience* 16. 10.1186/s12868-015-0193-z

Schneidman, E., Berry, M. J., Segev, R., and Bialek, W. (2006). Weak pairwise correlations imply strongly correlated network states in a neural population. *Nature* 440, 1007–1012. 10.1038/nature04701

Schrouff, J., Perlbarg, V., Boly, M., Marrelec, G., Boveroux, P., Vanhaudenhuyse, A., et al. (2011). Brain functional integration decreases during propofol-induced loss of consciousness. *NeuroImage* 57, 198–205. 10.1016/j.neuroimage.2011.04.020

Scott, G., Fagerholm, E. D., Mutoh, H., Leech, R., Sharp, D. J., Shew, W. L., et al. (2014). Voltage Imaging of Waking Mouse Cortex Reveals Emergence of Critical Neuronal Dynamics. *Journal of Neuroscience* 34, 16611–16620. 10.1523/JNEUROSCI.3474-14.2014

Senden, M., Deco, G., De Reus, M. A., Goebel, R., and Van Den Heuvel, M. P. (2014). Rich club organization supports a diverse set of functional network configurations. *NeuroImage* 96, 174–182. 10.1016/j.neuroimage.2014.03.066

Senden, M., Reuter, N., van den Heuvel, M. P., Goebel, R., and Deco, G. (2017). Cortical rich club regions can organize state-dependent functional network formation by engaging in oscillatory behavior. *NeuroImage* 146, 561–574. 10.1016/j.neuroimage.2016.10.044

Shen, X., Tokoglu, F., Papademetris, X., and Constable, R. (2013). Groupwise whole-brain parcellation from resting-state fMRI data for network node identification. *NeuroImage* 82, 403–415. 10.1016/j.neuroimage.2013.05.081

Shew, W. L. and Plenz, D. (2013). The functional benefits of criticality in the cortex. *The Neuroscientist : a review journal bringing neurobiology, neurology and psychiatry* 19, 88–100. 10.1177/1073858412445487

Siebner, H. R., Bergmann, T. O., Bestmann, S., Massimini, M., Johansen-Berg, H., Mochizuki, H., et al. (2009). Consensus paper: Combining transcranial stimulation with neuroimaging. *Brain Stimulation* 2, 58–80. 10.1016/j.brs.2008.11.002

Signorelli, C. M., Uhrig, L., Kringelbach, M., Jarraya, B., and Deco, G. (2021). Hierarchical disruption in the cortex of anesthetized monkeys as a new signature of consciousness loss. *NeuroImage* 227. 10.1016/j.neuroimage.2020.117618

Simon, H. A. (1962). *The Architecture of Complexity.* Tech. Rep. 6

Smith, S. M. (2002). Fast robust automated brain extraction. *Human Brain Mapping* 17, 143–155. 10.1002/hbm.10062

Sporns, O. (2011). The human connectome: a complex network. *Annals of the New York Academy of Sciences* 1224, 109–125. 10.1111/j.1749-6632.2010.05888.x

Sporns, O. (2013). Network attributes for segregation and integration in the human brain. 10.1016/j.conb.2012.11.015

Sporns, O. (2018). Graph theory methods: applications in brain networks. *Dialogues in clinical neuroscience* 20, 111–121

Sporns, O., Tononi, G., and Kötter, R. (2005). The Human Connectome: A Structural Description of the Human Brain. *PLoS Computational Biology* 1, e42. 10.1371/journal.pcbi.0010042

Spreng, R. N. and Grady, C. L. (2010). Patterns of brain activity supporting autobiographical memory, prospection, and theory of mind, and their relationship to the default mode network. *Journal of Cognitive Neuroscience* 22, 1112–1123. 10.1162/jocn.2009.21282

Stamatakis, E. A., Adapa, R. M., Absalom, A. R., and Menon, D. K. (2010). Changes in resting neural connectivity during propofol sedation. *PLoS ONE* 5. 10.1371/journal.pone.0014224

Stender, J., Gosseries, O., Bruno, M.-A., Charland-Verville, V., Vanhaudenhuyse, A., Demertzi, A., et al. (2014). Diagnostic precision of PET imaging and functional MRI in disorders of consciousness: a clinical validation study. *Lancet (London, England)* 384, 514–22. 10.1016/S0140-6736(14)60042-8

Stender, J., Kupers, R., Rodell, A., Thibaut, A., Chatelle, C., Bruno, M. A., et al. (2015). Quantitative rates of brain glucose metabolism distinguish minimally conscious from vegetative state patients. *Journal of Cerebral Blood Flow and Metabolism* 35, 58–65. 10.1038/jcbfm.2014.169

Stender, J., Mortensen, K. N., Thibaut, A., Darkner, S., Laureys, S., Gjedde, A., et al. (2016). The Minimal Energetic Requirement of Sustained Awareness after Brain Injury. *Current Biology* 26, 1494–1499. 10.1016/j.cub.2016.04.024

Stephens, G. J., Honey, C. J., and Hasson, U. (2013). A place for time: The spatiotemporal structure of neural dynamics during natural audition. *Journal of Neurophysiology* 110, 2019–2026. 10.1152/jn.00268.2013

Storm, J. F., Boly, M., Casali, A. G., Massimini, M., Olcese, U., Pennartz, C. M., et al. (2017). Consciousness Regained: Disentangling Mechanisms, Brain Systems, and Behavioral Responses. *The Journal of Neuroscience* 37, 10882–10893. 10.1523/JNEUROSCI.1838-17.2017

Storti, S. F., Formaggio, E., Nordio, R., Manganotti, P., Fiaschi, A., Bertoldo, A., et al. (2013). Automatic selection of resting-state networks with functional magnetic resonance imaging. *Frontiers in Neuroscience* 10.3389/fnins.2013.00072

Stuart, J. T. (1960). On the non-linear mechanics of wave disturbances in stable and unstable parallel flows Part 1. The basic behaviour in plane Poiseuille flow. *Journal of Fluid Mechanics* 9, 353–370. 10.1017/S002211206000116X

Sutterer, M. J. and Tranel, D. (2017). Neuropsychology and cognitive neuroscience in the fMRI era: A recapitulation of localizationist and connectionist views. *Neuropsychology* 31, 972–980. 10.1037/neu0000408

Suzuki, M. and Larkum, M. E. (2020). General Anesthesia Decouples Cortical Pyramidal Neurons. *Cell* 180, 666–676. 10.1016/j.cell.2020.01.024

Tagliazucchi, E., Chialvo, D. R., Siniatchkin, M., Amico, E., Brichant, J.-F., Bonhomme, V., et al. (2016a). Large-scale signatures of unconsciousness are consistent with a departure from critical dynamics. *Journal of The Royal Society Interface* 13, 20151027. 10.1098/rsif.2015.1027

Tagliazucchi, E., Crossley, N., Bullmore, E. T., and Laufs, H. (2016b). Deep sleep divides the cortex into opposite modes of anatomicalâfunctional coupling. *Brain Structure and Function* 221, 4221–4234. 10.1007/s00429-015-1162-0

Tagliazucchi, E., von Wegner, F., Morzelewski, A., Borisov, S., Jahnke, K., and Laufs, H. (2012). Automatic sleep staging using fMRI functional connectivity data. *NeuroImage* 63, 63–72. 10.1016/j.neuroimage.2012.06.036

Tagliazucchi, E., von Wegner, F., Morzelewski, A., Brodbeck, V., Jahnke, K., and Laufs, H. (2013). Breakdown of long-range temporal dependence in default mode and attention networks during deep sleep. *Proceedings of the National Academy of Sciences* 110, 15419–15424. 10.1073/pnas.1312848110

Thibaut, A., Bruno, M. A., Chatelle, C., Gosseries, O., Vanhaudenhuyse, A., Demertzi, A., et al. (2012). Metabolic activity in external and internal awareness networks in severely brain-damaged patients. *Journal of Rehabilitation Medicine* 44, 487–494. 10.2340/16501977-0940

Thibaut, A., Schiff, N., Giacino, J., Laureys, S., and Gosseries, O. (2019). Therapeutic interventions in patients with prolonged disorders of consciousness. 10.1016/S1474-4422(19)30031-6

Timofeev, I. (2001). Disfacilitation and active inhibition in the neocortex during the natural sleep-wake cycle: An intracellular study. *Proceedings of the National Academy of Sciences* 98, 1924–1929. 10.1073/pnas.041430398

Tkačik, G., Marre, O., Mora, T., Amodei, D., Berry, M. J., and Bialek, W. (2013). The simplest maximum entropy model for collective behavior in a neural network. *Journal of Statistical Mechanics: Theory and Experiment* 2013, P03011. 10.1088/1742-5468/2013/03/P03011

Tkačik, G., Mora, T., Marre, O., Amodei, D., Palmer, S. E., Berry, M. J., et al. (2015). Thermodynamics and signatures of criticality in a network of neurons. *Proceedings of the National Academy of Sciences of the United States of America* 112, 11508–13. 10.1073/pnas.1514188112

Tkacik, G., Schneidman, E., Berry, M. J., and Bialek, W. (2009). Spin glass models for a network of real neurons

Tognoli, E. and Kelso, J. A. (2014). The Metastable Brain. 10.1016/j.neuron.2013.12.022

Tomescu, M. I., Rihs, T. A., Roinishvili, M., Karahanoglu, F. I., Schneider, M., Menghetti, S., et al. (2015). Schizophrenia patients and 22q11.2 deletion syndrome adolescents at risk express the same deviant patterns of resting state EEG microstates: A candidate endophenotype of schizophrenia. *Schizophrenia Research: Cognition* 2, 159–165. 10.1016/j.scog.2015.04.005

Tononi, G. (2004). An information integration theory of consciousness. *BMC Neuroscience* 5, 42. 10.1186/1471-2202-5-42

Tononi, G., Boly, M., Massimini, M., and Koch, C. (2016). Integrated information theory: From consciousness to its physical substrate. 10.1038/nrn.2016.44

Tononi, G. and Edelman, G. M. (1998). Consciousness and complexity. 10.1126/science.282.5395.1846

Tononi, G. and Koch, C. (2008). The neural correlates of consciousness: an update. *Annals of the New York Academy of Sciences* 1124, 239–61. 10.1196/annals.1440.004

Tourbier, S., Aleman-Gomez, Y., Mullier, E., Griffa, A., Bach Cuadra, M., and Hagmann, P. (2020). connectomicslab/connectomemapper3: Connectome Mapper v3.0.0-beta-RC1 10.5281/ZENODO.3727708

Uhrig, L., Sitt, J. D., Jacob, A., Tasserie, J., Barttfeld, P., Dupont, M., et al. (2018). Resting-state Dynamics as a Cortical Signature of Anesthesia in Monkeys. *Anesthesiology* 129, 942–958. 10.1097/ALN.0000000000002336

Vaessen, M. J., Braakman, H. M. H., Heerink, J. S., Jansen, J. F. A., Debeij-van Hall, M. H. J. A., Hofman, P. A. M., et al. (2013). Abnormal modular organization of functional networks in cognitively impaired

children with frontal lobe epilepsy. *Cerebral cortex (New York, N.Y. : 1991)* 23, 1997–2006. 10.1093/cercor/bhs186

Van de Steen, F., Faes, L., Karahan, E., Songsiri, J., Valdes-Sosa, P. A., and Marinazzo, D. (2019). Critical Comments on EEG Sensor Space Dynamical Connectivity Analysis. *Brain Topography* 32, 643–654. 10.1007/s10548-016-0538-7

Van de Ville, D., Britz, J., and Michel, C. M. (2010). EEG microstate sequences in healthy humans at rest reveal scale-free dynamics. *Proceedings of the National Academy of Sciences of the United States of America* 107, 18179–84. 10.1073/pnas.1007841107

van den Heuvel, M. P. and Hulshoff Pol, H. E. (2010). Exploring the brain network: A review on resting-state fMRI functional connectivity. 10.1016/j.euroneuro.2010.03.008

Van Den Heuvel, M. P., Kahn, R. S., Goñi, J., and Sporns, O. (2012). High-cost, high-capacity backbone for global brain communication. *Proceedings of the National Academy of Sciences of the United States of America* 109, 11372–11377. 10.1073/pnas.1203593109

van den Heuvel, M. P. and Sporns, O. (2011). Rich-club organization of the human connectome. *The Journal of neuroscience : the official journal of the Society for Neuroscience* 31, 15775–86. 10.1523/JNEUROSCI.3539-11.2011

van den Heuvel, M. P. and Sporns, O. (2013). Network hubs in the human brain. 10.1016/j.tics.2013.09.012

van den Heuvel, M. P. and Sporns, O. (2019). A cross-disorder connectome landscape of brain dysconnectivity. *Nature Reviews Neuroscience* 20, 435–446. 10.1038/s41583-019-0177-6

van den Heuvel, M. P., Stam, C. J., Kahn, R. S., and Hulshoff Pol, H. E. (2009). Efficiency of functional brain networks and intellectual performance. *The Journal of neuroscience : the official journal of the Society for Neuroscience* 29, 7619–24. 10.1523/JNEUROSCI.1443-09.2009

van Vugt, B., Dagnino, B., Vartak, D., Safaai, H., Panzeri, S., Dehaene, S., et al. (2018). The threshold for conscious report: Signal loss and response bias in visual and frontal cortex. *Science* 360, 537–542. 10.1126/science.aar7186

Vanhaudenhuyse, A., Noirhomme, Q., Tshibanda, L. J., Bruno, M. A., Boveroux, P., Schnakers, C., et al. (2010). Default network connectivity reflects the level of consciousness in non-communicative brain-damaged patients. *Brain* 133, 161–171. 10.1093/brain/awp313

Vincent, J. L., Patel, G. H., Fox, M. D., Snyder, A. Z., Baker, J. T., Van Essen, D. C., et al. (2007). Intrinsic functional architecture in the anaesthetized monkey brain. *Nature* 447, 83–86. 10.1038/nature05758

Wackermann, J., Lehmann, D., Michel, C. M., and Strik, W. K. (1993). Adaptive segmentation of spontaneous EEG map series into spatially defined microstates. *International Journal of Psychophysiology* 14, 269–283. 10.1016/0167-8760(93)90041-M

Wang, Z., Larivière, S., Xu, Q., Vos De Wael, R., Hong, S. J., Wang, Z., et al. (2019). Community-informed connectomics of the thalamocortical system in generalized epilepsy. *Neurology* 93, e1112–e1122. 10.1212/WNL.0000000000008096

Wannez, S., Heine, L., Thonnard, M., Gosseries, O., and Laureys, S. (2017). The repetition of behavioral assessments in diagnosis of disorders of consciousness. *Annals of Neurology* 81, 883–889. 10.1002/ana.24962

Watanabe, T., Hirose, S., Wada, H., Imai, Y., Machida, T., Shirouzu, I., et al. (2013). A pairwise maximum entropy model accurately describes resting-state human brain networks. *Nature Communications* 4, 1370. 10.1038/ncomms2388

Watanabe, T., Rees, G., and Masuda, N. (2019). Atypical intrinsic neural timescale in autism. *eLife* 8. 10.7554/eLife.42256

Werner, G. (2007). Metastability, criticality and phase transitions in brain and its models. *Bio Systems* 90, 496–508. 10.1016/j.biosystems.2006.12.001

White, N. S. and Alkire, M. T. (2003). Impaired thalamocortical connectivity in humans during general-anesthetic- induced unconsciousness. *NeuroImage* 19, 402–411. 10.1016/S1053-8119(03)00103-4

Wijdicks, E. F. (2001). The diagnosis of brain death. 10.1056/NEJM200104193441606

Williams, N. R. and Okun, M. S. (2013). Deep brain stimulation (DBS) at the interface of neurology and psychiatry. 10.1172/JCI68341

Williamson, S. J., Kaufman, L., Curtis, S., Lu, Z. L., Michel, C. M., and Wang, J. Z. (1996). Neural substrates of working memories are revealed magnetically by the local suppression of alpha rhythm. *Electroencephalography and clinical neurophysiology. Supplement* 47, 163–80

Wilson, H. R. and Cowan, J. D. (1972). Excitatory and Inhibitory Interactions in Localized Populations of Model Neurons. *Biophysical Journal* 12, 1–24. 10.1016/S0006-3495(72)86068-5

Wilting, J. and Priesemann, V. (2018). Inferring collective dynamical states from widely unobserved systems. *Nature Communications* 9. 10.1038/s41467-018-04725-4

Wu, G. R., Di Perri, C., Charland-Verville, V., Martial, C., Carrière, M., Vanhaudenhuyse, A., et al. (2019). Modulation of the spontaneous hemodynamic response function across levels of consciousness. *NeuroImage* 200, 450–459. 10.1016/j.neuroimage.2019.07.011

Yang, J. Q., Wang, R., Wang, Z. P., Ma, Q. Y., Mao, J. Y., Ren, Y., et al. (2020). Leaky integrate-and-fire neurons based on perovskite memristor for spiking neural networks. *Nano Energy* 74, 104828. 10.1016/j.nanoen.2020.104828

Yeshurun, Y., Nguyen, M., and Hasson, U. (2017). Amplification of local changes along the timescale processing hierarchy. *Proceedings of the National Academy of Sciences of the United States of America* 114, 9475–9480. 10.1073/pnas.1701652114

Yip, G. M., Chen, Z. W., Edge, C. J., Smith, E. H., Dickinson, R., Hohenester, E., et al. (2013). A propofol binding site on mammalian GABA A receptors identified by photolabeling. *Nature Chemical Biology* 9, 715–720. 10.1038/nchembio.1340

Yuan, H., Zotev, V., Phillips, R., Drevets, W. C., and Bodurka, J. (2012). Spatiotemporal dynamics of the brain at rest - Exploring EEG microstates as electrophysiological signatures of BOLD resting state networks. *NeuroImage* 60, 2062–2072. 10.1016/j.neuroimage.2012.02.031

Zamora-López, G. and Brasselet, R. (2019). Sizing complex networks. *Communications Physics* 2, 1–10. 10.1038/s42005-019-0239-0

Zamora-López, G., Zhou, C., and Kurths, J. (2009). Graph analysis of cortical networks reveals complex anatomical communication substrate. *Chaos* 19. 10.1063/1.3089559

Zamora-López, G., Zhou, C., and Kurths, J. (2010). Cortical hubs form a module for multisensory integration on top of the hierarchy of cortical networks. *Frontiers in Neuroinformatics* 4. 10.3389/neuro.11.001.2010

Zamora-López, G., Zhou, C., and Kurths, J. (2011). Exploring brain function from anatomical connectivity. 10.3389/fnins.2011.00083

Zhang, J., Huang, Z., Chen, Y., Zhang, J., Ghinda, D., Nikolova, Y., et al. (2018). Breakdown in the temporal and spatial organization of spontaneous brain activity during general anesthesia. *Human Brain Mapping* 39, 2035–2046. 10.1002/hbm.23984

Zhou, S. and Mondragón, R. J. (2004). The rich-club phenomenon in the internet topology. *IEEE Communications Letters* 8, 180–182. 10.1109/LCOMM.2004.823426